

**THREE NEUTRINO OSCILLATIONS APPLIED TO SOLAR AND LONG
BASELINE EXPERIMENTS**

By

Scott Kelly Hayward

B. Math. (Applied Mathematics/Computer Science) University of Waterloo

B. Sc. (Physics) University of Waterloo

M. Sc. (Physics) University of British Columbia

A THESIS SUBMITTED IN PARTIAL FULFILLMENT OF
THE REQUIREMENTS FOR THE DEGREE OF
DOCTOR OF PHILOSOPHY

in

THE FACULTY OF GRADUATE STUDIES
PHYSICS

We accept this thesis as conforming
to the required standard

THE UNIVERSITY OF BRITISH COLUMBIA

December 1997

© Scott Kelly Hayward, 1997

In presenting this thesis in partial fulfilment of the requirements for an advanced degree at the University of British Columbia, I agree that the Library shall make it freely available for reference and study. I further agree that permission for extensive copying of this thesis for scholarly purposes may be granted by the head of my department or by his or her representatives. It is understood that copying or publication of this thesis for financial gain shall not be allowed without my written permission.

Department of

PHYSICS

The University of British Columbia
Vancouver, Canada

Date

DEC 24/97

Abstract

Details of the Standard Solar Model and experiments measuring neutrinos produced inside the sun and in the upper atmosphere are reviewed. Inconsistencies between theoretical calculations and experimental measurements are discussed, establishing the need for new physics beyond the Standard Model of Particle Physics.

Neutrino oscillations are introduced as a viable solution and the phenomenology in the two flavour case is reviewed. Calculations of neutrino oscillations at long baseline experiments are performed using realistic spectra and source/detector combinations. Both vacuum and matter enhanced oscillations of solar neutrinos are computed to account for the solar neutrino data, and allowed regions of parameter space are found.

New analytical results are presented which determine the three family hamiltonian in matter. Oscillation probabilities in vacuum are calculated, and methods to account for matter effects are outlined.

A numerical treatment to determine the CKM parameters in matter is shown to be identical to existing analytical results in the literature. Computer codes developed to calculate long baseline neutrino oscillation experiments through the earth's variable density are discussed. Several techniques used in a second set of programs written to determine solar neutrino survival probabilities in the three neutrino case are also reviewed.

Symmetries between four different mass hierarchies which have two well-separated mass scales are studied. A two-fold degeneracy noted in the literature is shown to be inherent in experiments which only measure muon neutrino oscillations, and an expression relating the two sets of CKM parameters is calculated. Detailed computations illustrate how long baseline experiments can determine the CKM parameters. First order matter

effects are included and numerical work shows where matter effects are likely to break some of the symmetries.

The phenomenon of CP violation in both vacuum and matter is studied in the three neutrino scenario. Existing work on first order matter and CP corrections to oscillation probabilities at long baseline experiments is extended to second order. It is argued that since CP effects are very likely to be smaller than matter, second order corrections are necessary. In detailed calculations, second order effects are clearly apparent. At high energies the approximation breaks down, but numerical results yield accurate answers allowing further study. Several strategies to isolate CP violation from competing matter effects are suggested, including tuning the neutrino beam energy and a novel approach which combines data sets from accelerator and reactor based experiments. Finally, new analytical work is presented showing that CP violation may modify the ratio of μ -type to e-type neutrinos in the atmospheric flux. The magnitude of the effect is estimated and found to be significant.

New techniques allow solar neutrino survival probabilities to be calculated including three mixing angles and two mass scales. A preliminary survey is performed assuming one relevant mass scale but including the three angular parameters. A distinct three neutrino solution is found by allowing the large neutrino mass squared difference to drop somewhat below the atmospheric neutrino data's best fit solution of $3 \times 10^{-4} \text{ eV}^2$. Then the high energy tail of the ${}^8\text{B}$ neutrino flux is converted to ν_τ by a second resonance in the sun, leaving unique spectral characteristics to differentiate it from two neutrino models.

Table of Contents

Abstract	ii
List of Figures	ix
List of Tables	xii
Acknowledgement	xiii
1 Theoretical and Experimental Background	1
1.1 Introduction	1
1.2 The Standard Solar Model: A Review	4
1.2.1 Solar Formation	5
1.2.2 Solar Model Assumptions	5
1.2.3 Initial Elemental Abundances	8
1.2.4 Nuclear Reaction Rates	9
1.2.5 The Proton-Proton Chain	12
1.2.6 The CNO Cycle	16
1.2.7 The Equation of State	17
1.2.8 The Opacity	18
1.2.9 Elemental Diffusion	21
1.2.10 The Numerical Model	22
1.2.11 Solar Oscillations	25
1.2.12 Discussion of the Solar Model	26

1.3	The Solar Neutrino Experiments	31
1.3.1	The Homestake ^{37}Cl Experiment	33
1.3.2	The Kamiokande Water Cherenkov Experiment	35
1.3.3	The Gallex ^{71}Ga Experiment	38
1.3.4	The SAGE ^{71}Ga Experiment	40
1.3.5	The Solar Neutrino Problem Almost Independent of the Standard Solar Model	41
1.4	The Atmospheric Neutrino Anomaly	48
1.4.1	Predicting the Flux of Neutrinos from Cosmic Ray Interactions	49
1.4.2	Experimental Measurements of Atmospheric Neutrinos	50
1.4.3	Discussion	52
2	Neutrino Oscillations with Two Flavours	55
2.1	Introduction	55
2.2	Theoretical Background	56
2.2.1	Neutrino Oscillations in Vacuum	56
2.2.2	Neutrino Oscillations in Matter	58
2.2.3	The Mikheyev-Smirnov Approach	62
2.3	Long Baseline Neutrino Oscillations with Two Flavours	64
2.3.1	Experimental Notes	64
2.3.2	Characterising Long Baseline Neutrino Oscillations	67
2.3.3	Existing Experimental Results	71
2.3.4	Future Prospects	74
2.4	Neutrino Oscillations and the Solar Neutrino Problem	83
2.4.1	Early Development and Analytical Results	83
2.4.2	Characterising the results	86

2.4.3	Vacuum Oscillation Solutions	90
3	Analytical Results with Three Neutrinos	95
3.1	Introduction	95
3.2	Developing the Three Neutrino Mass Matrix	98
3.3	Perturbation solutions with small angles	101
3.4	Review of existing three neutrino work	102
3.5	Oscillation probabilities with fixed density	108
3.6	Transition probability across multiple resonances	111
3.6.1	Jump probability with three neutrinos	111
3.6.2	Propagating the neutrino across multiple resonances	112
4	Numerical Methods	119
4.1	Introduction	119
4.2	Numerical Treatment of the CKM Matrix	120
4.3	Long Baseline Calculations	122
4.3.1	Basic Long Baseline Code	122
4.3.2	Approximation of the Earth's Density Structure	126
4.3.3	Runge-Kutta Methods of Solution	128
4.4	Solar Neutrino Calculations	130
4.4.1	Basic Solar Code	130
4.4.2	Treatment of Monte Carlo Parameters	133
4.4.3	Fitting the CKM Parameters	134
4.4.4	Multiple Resonance Possibilities	135
4.4.5	Seasonal and Day/Night Effects	139
4.4.6	Stability of the Results	141

5	Numerical Calculations with Three Neutrinos	145
5.1	Introduction	145
5.2	Preliminary Notes	147
5.2.1	Baselines required for oscillations and matter effects	147
5.2.2	Neutrino mass hierarchies	148
5.3	The One Mass Scale Dominant Structure	149
5.3.1	Two types of OMSD and oscillation probabilities	150
5.3.2	Indirectly coupled $\nu_\mu - \nu_e$ oscillations	151
5.3.3	Symmetries of the $P_{\alpha\beta}(L)$ and measuring the CKM parameters	154
5.3.4	First order matter effects on OMSD parameters	155
5.3.5	OMSD solutions with very long baselines	160
5.4	CP Violation and Neutrino Oscillation	161
5.4.1	Characterising CP Violation in Vacuum	165
5.4.2	Review of the Literature	165
5.4.3	Analytical Results	168
5.4.4	Strategies to Isolate the CP Violation Parameters	175
5.4.5	Combining Reactor and Long Baseline Experiments	185
5.4.6	CP Violation and Atmospheric Neutrinos	190
5.4.7	Discussion	195
5.5	Three Neutrino Solar Results	197
5.5.1	Four Parameter Fits to the Solar Neutrino Problem	199
5.5.2	Combined Atmospheric Best Fit Parameters and Solar Neutrinos	203
5.5.3	Solar Neutrinos with Two Small Mass Parameters	207
5.5.4	Discussion	210
6	Conclusions	213

List of Figures

1.1	Hertzprung-Russel Diagram of Observed Stars	6
1.2	Elemental Abundances in the Sun	10
1.3	Proton-Proton Chain for Energy Generation	13
1.4	S-factor Measurements for ${}^3\text{He} + {}^3\text{He} \rightarrow {}^4\text{He} + 2p$	15
1.5	S-factor Measurements for ${}^3\text{He} + {}^3\text{He} \rightarrow {}^4\text{He} + 2p$	15
1.6	CNO Cycle of Energy Generation	16
1.7	Electron Density Parameters in the Sun	23
1.8	Radial Dependence of Neutrino Production	24
1.9	Time Dependence of the Solar Model	25
1.10	Solar Neutrino Spectrum	32
1.11	Experimental Constraints of Pairs of Neutrino Experiments	46
1.12	Experimental Constraints Combined Neutrino Experiments	47
2.1	Neutrino interactions with electrons	58
2.2	Matter enhancement of $\sin^2(2\theta_V)$	60
2.3	Matter enhancement of Δm_V^2	61
2.4	Accelerator reference flux	66
2.5	Neutrino vacuum oscillations at fixed energy	68
2.6	Neutrino matter oscillations at fixed energy	70
2.7	Electron density profile of the earth	71
2.8	Comparison of Runge-Kutta and exact methods	72
2.9	Best limits on neutrino oscillation parameters.	75

2.10	LSND allowed region with other experimental limits	76
2.11	Neutrino oscillations at 250 km using the reference spectrum	78
2.12	Neutrino interaction rates at 250 km using the reference spectrum	79
2.13	Neutrino energy spectra at 250 km	81
2.14	Probability contours at 10,000 km	82
2.15	Resonant Conversion of Solar Neutrinos	84
2.16	MS Diagram for Dummy Sources	87
2.17	MSW Solutions for Solar Neutrinos	89
2.18	Energy Dependence of Neutrino Conversion	91
2.19	Neutrino Spectra for MSW Best Fit Solutions	91
2.20	Vacuum Oscillation Solutions for Solar Neutrinos	93
2.21	Neutrino Spectra for MSW Best Fit Solutions	94
3.1	Matter enhancement of Δm_0^2 with Three Neutrinos	108
3.2	Path of Double Resonance through Sun	113
4.1	Effective oscillation Parameters in Matter	123
4.2	Structure of Long Baseline Codes	125
4.3	Mean Density along Section of Neutrino Path	127
4.4	Runge-Kutta integration on a discrete path	128
4.5	Structure of Solar Neutrino Codes	131
4.6	Cumulative Distribution Function for 8B Neutrino Energies	134
4.7	Interpolation of Oscillation Parameters in the Solar Interior	136
4.8	Neutrino Resonance with Two Neutrinos	137
4.9	Neutrino Resonance with Three Neutrinos	138
4.10	Seasonal and Day/Night Effect Coordinate System	140
4.11	Statistical Distributions Reproduced by Monte Carlo Method	144

5.1	Three Neutrino Mass Structures	149
5.2	Indirectly Coupled $\nu_\mu - \nu_e$ Oscillations	153
5.3	OMSD-1 and Long Baseline ν_μ Oscillations	157
5.4	OMSD-2 and Long Baseline ν_μ Oscillations	158
5.5	First Order Matter Effects and Mixing Angles	160
5.6	First Order Matter Effects on Spectra	161
5.7	OMSD-1 and Very Long Baseline ν_μ Oscillations	162
5.8	OMSD-2 and Very Long Baseline ν_μ Oscillations	163
5.9	CP Violation at 250 km	179
5.10	Neutrino spectra and CP Violation at 250 km	181
5.11	CP Violation at 732 km	183
5.12	CP Violation at 1500 km	184
5.13	Spectrum of Oscillation Probabilities and CP Violation	186
5.14	Combined Reactors and Accelerator CP Violation Study	189
5.15	Four Parameter Solar Neutrino Fit	200
5.16	Small and Large Angle χ^2 Surface Plots	201
5.17	Small and Large Angle Suppression Spectra	203
5.18	Small Angle Solution to the Solar Neutrino Problem	204
5.19	Large Angle Solution to the Solar Neutrino Problem	205
5.20	Solar Neutrino Fits Using CKM Parameters Implied by Atmospheric Neu- trino Results	206
5.21	Two Mass Scale Solution to the Solar Neutrino Problem	209
5.22	Two Mass Scale Solar Neutrino Suppression Spectra	211

List of Tables

1.1	Standard Solar Models and their Predictions	28
1.2	Percentage Uncertainties for pp chain Neutrino Sources	28
1.3	Summary of Solar Neutrino Experimental Data	33
1.4	Experimental Flux Ratio Measurements of Atmospheric Neutrinos	50
2.1	Experimental Limits on Neutrino Oscillation Parameters	73
2.2	Statistical Significance of MSW Solar Neutrino Solutions	92
4.1	Statistical Study of Standard Solar Model Oscillation Rates	142
5.1	CKM Parameter Sets Implied by Atmospheric Neutrino Experiments . .	176
5.2	Fraction Contribution of CP Terms to Atmospheric Neutrino Ratio . . .	194

Acknowledgement

Many people have contributed to this thesis, both within and outside physics, and without their support it could not have been completed.

I would like to thank my thesis supervisor Nathan Weiss for taking me on as a student, and helping me find an interesting project. He has shown an ability to work with students both on a technical and personal level, and his continued patience and understanding over the years is most appreciated.

I made too many friends to name them all during my time at UBC. I would like to thank the gang at *Club Sedge*, as well as the staff, editors and business office at *The Ubysey* for making the experience enjoyable. Fellow graduate students Dan Peters, Steve Patitsas, Bill Scott and Michael Sofer have all been close friends over the years. Dave Lee and Bob Taylor went well beyond friendship to help me in my time of need and I am deeply indebted to them both.

My family has always been supportive of me, especially in the last several years. My parents, step-parents, sister and nephew have never been more than a telephone call away. Marj Bailey and Francis Latter have been like a family to me their contribution must also be noted.

Last, but certainly not least, I am grateful to my partner Christine Price who has been my daily companion during the difficult final phase of this project. She propped me up when I was down, cared for me when I was sick, shared her strength when mine ran down, and was always a source of inspiration to me. This is as much her accomplishment as it is mine.

Chapter 1

Theoretical and Experimental Background

1.1 Introduction

Since it was first postulated by Pauli in 1930, more as a mathematical convenience than an element of reality, the neutrino has continued to be elusive. Detection did not come until 1953 when Reines and Cowan observed antineutrinos from the nuclear reactor in Hanford, Washington using the reaction $\bar{\nu}_e + p \rightarrow e^+ + n$. Even recently, when the LEP experiment established that there are exactly three light neutrinos, they did so indirectly by measuring the width of the Z^0 resonance.

Neutrinos are a favoured candidate to solve the astrophysical dark matter problem, they may close the universe, and two of them are produced each time four protons are bound together to form a helium atom in the reactions that heat the sun. Their elusive behaviour comes about because they do not interact via either the strong nuclear or electromagnetic forces. But as a result, they also provide a unique probe of the weak force unhindered by other interactions.

Neutrinos are also at the forefront of particle physics today because there are two anomalies in which experimental measurements differ from theoretical calculations: the Solar and Atmospheric Neutrino Problems. Neutrinos produced deep in the interior of the sun propagate out into space in all directions, and some of them are detected by experiments on earth. However, only between one third and one half of those expected are actually seen, depending on the experiment. Interactions of cosmic rays in the upper

atmosphere produce two different types of neutrinos in predictable ratios. But the ratio measured by earth-bound detectors does not match, a discrepancy which defines the Atmospheric Neutrino Problem.

The resolution of these two anomalies is not just a necessary step in furthering our understanding of particle physics, but also opens a window on fields like stellar modelling, cosmology and Big Bang nucleosynthesis. There is a ready theory to explain these phenomena, a minimal extension of the Standard Model of particle physics which in some ways simplifies that model. By assuming that neutrinos have a finite mass and that there is mixing between the leptons, in direct analogy with the quark sector, it may be possible to resolve the Solar and Atmospheric Neutrino Problems. At the same time, an additional parallel between the quarks and leptons would be manifested.

This thesis will develop some of the mathematical details in this extension of the Standard Model. It will use these to calculate how it affects the interpretation of the experiments, and hopefully, move the process a small step forward. Finally, it will offer some new ideas for study, which serve to confirm or refute this extension as a plausible explanation of the behaviour or nature. Neutrino masses, mixing and oscillations will purposely not be mentioned beyond the introduction of this chapter, in order to pursue a purely empirical approach; demonstration of the need for new physics will precede its introduction.

Section two will be a detailed review of the Standard Solar Model, with some discussion of unsuccessful attempts to modify it to explain the Solar Neutrino Problem. Next, section three will discuss the solar neutrino experiments themselves, and an argument will be presented which shows that some of the experiments contradict each other under very general conditions almost independent of the solar model. Finally section four will define and discuss the atmospheric neutrino anomaly.

Chapter two will introduce neutrino masses, mixing and the oscillation formalism in

the simple case of two neutrinos. It will be used to study long baseline neutrino oscillation experiments at accelerators using a realistic simulated neutrino beam. The oscillations will then be applied to solar neutrinos to set constraints on the mixing parameter space based on measurements by the solar neutrino experiments.

Chapter three will discuss the necessity of going beyond the simple two neutrino formalism to consider all three flavours. A formalism will be developed in analogy with the two neutrino case, and several new analytical results will be presented.

Chapter four will discuss the numerical methods used to compute neutrino oscillations, especially in the three flavour scenario. Two distinct set of codes have been developed, one to calculate the oscillation of beams of neutrinos in earth bound experiments, and another to compute detection probabilities for neutrinos originating in the solar interior. Several techniques used will be discussed and, where possible, it will be verified that the numerical calculations can accurately replace analytical ones.

Chapter five will extend some of the analytical results from Chapter three to specific cases and combine them using the numerical methods in Chapter four. Long baseline neutrino oscillation experiments will be studied in four cases in which the neutrinos have a hierarchical mass structure. Detailed numerical calculations will again be performed, and some new analytical work will also be done to interpret them. Similar techniques will be used to study the violation of the CP symmetry using accelerator and reactor experiments. New ideas will be presented to look at the atmospheric neutrinos as a measure of the CP violation effect. Solar neutrino detection rates will be calculated with the three neutrino formalism to show that new regions of parameter space open up with the addition of the third neutrino.

Finally, Chapter six will conclude the discussion.

1.2 The Standard Solar Model: A Review

The sun is a medium sized star about half way through the hydrogen burning or "*Main Sequence*" phase of its life. The Standard Solar Model (hereafter the SSM) consists of a set of assumptions about the physics which takes place in the sun, coupled with the most current experimental inputs and combined in a set of computer codes that calculate the current properties of the sun based on those inputs.

The idea behind the SSM is to begin with a one solar mass protostar and evolve it forward to the sun's current age of 4.5 billion years. The model assumes an initial chemical composition, a hydrostatic equilibrium throughout its life, energy transfer mechanisms its interior and nuclear energy generation networks. Its major predictions are the luminosity, radius, temperature, neutrino spectra, chemical composition and oscillation modes, though a total of about 20 independent parameters are used as constraints [1].

In the section which follows, the Standard Solar Model will be discussed in some detail. The general assumptions of the model and the initial chemical composition will be outlined, the nuclear reaction mechanisms which provide its energy and the thermodynamics of the transfer of that energy will be discussed, and the general ideas of the computer codes which combine these inputs to calculate the model will be reviewed. Results from the recent SSM calculations by Bahcall and Pinsonneault [2] will then be presented. Finally, an overview of the model will be given discussing how modifications to it would affect neutrino fluxes.

This discussion will focus almost exclusively on the solar interior because that is where that the solar neutrinos are produced. Among the most comprehensive SSM calculations are those done by Bahcall and Pinsonneault [2] using the most up to date chemical abundance measurements, state of the art equation of state and opacity computations, and accounting for elemental diffusion in the solar interior. Their model will be used as

an input to all solar neutrino calculations which follow, and will be referred to as *BP95*.

1.2.1 Solar Formation

The Pre-Main Sequence evolution of a star takes place in two stages over about 5×10^7 years, or 1% of the total age of the sun [3]. The first stage is the Dynamic Phase in which a dense cloud collapses to a much smaller object with high density. It is characterised by matter falling inwards freely, and is followed by the Hydrostatic Phase where internal gas pressure provides sufficient support to slow the rate of contraction. This latter stage ends when the fully ignited star enters the Main Sequence.

It is here that most solar models begin. The radius and luminosity are about $0.89R_{\odot}$ and $0.73L_{\odot}$ respectively (R_{\odot} and L_{\odot} are the current values), the central temperature is about 1.3×10^7 K and the convection zone contains about 3% of the mass. Today the sun's central temperature is about 1.5×10^7 K and the convection zone contains about 2% of the mass.

1.2.2 Solar Model Assumptions

Early in this century, astronomers noticed that scatter plots of the surface temperature T_{eff} versus luminosity L of observed stars populated only certain sections of the plot. Scatter plots of stars drawn on axes of $\log(T_{eff})$ and $\log(L/L_{\odot})$ are referred to as Hertzsprung-Russell diagrams, as shown in figure 1.1 [4]. Most stars, including our sun, populate a chord referred to as the "*Main Sequence*" of this diagram, where hydrogen is fused to form helium.

Arthur Eddington realised that neither chemical nor gravitational energy would be sufficient to heat the sun for the several billion years which it had been shining, and wrote in 1926 that the sun must derive its energy from nuclear processes [5, pp. 292-293]. However the temperatures required for a proton to overcome the classical Coulomb barrier

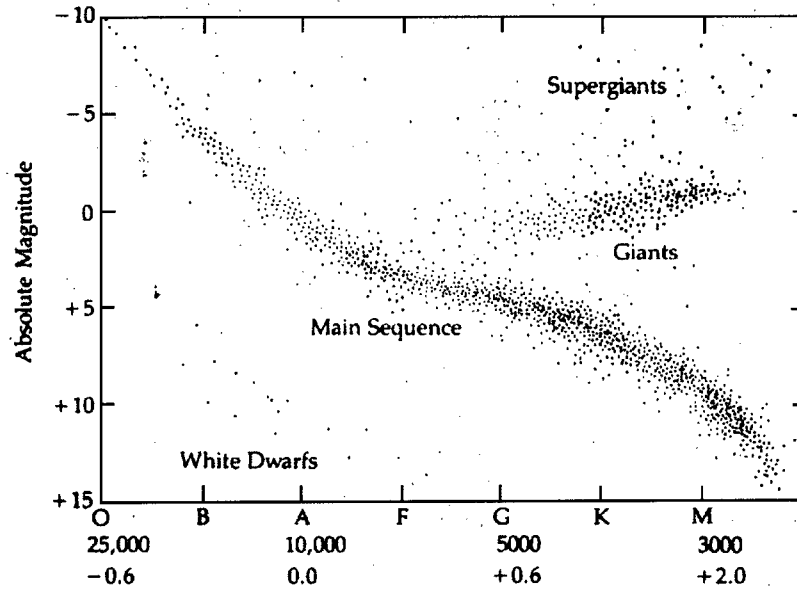


Figure 1.1: Scatter plot of observed stars on a $\log - \log$ plot of temperature (horizontal axis) and luminosity (vertical axis). The region labelled *Main Sequence* denotes those stars which are in their hydrogen burning phase. [4]

were extremely high. In 1928 George Gamow showed quantum tunnelling provided a mechanism to penetrate this barrier at a much more reasonable temperature [6]. By the late 1930's Bethe, Weizsäcker, and Critchfield [7] had determined that the proton-proton (pp) and Carbon-Nitrogen-Oxygen (CNO) cycles were the two possible mechanisms to convert hydrogen to helium producing the nuclear energy which heats the sun. Except for filling in some additional details and improving the estimates of the cross sections, the modern view has not changed. Early models to predict the solar mass, luminosity, and radius have evolved to today's SSM which attempts to accurately predict a much wider variety of properties.

An essential element of any solar model is to predict the current luminosity and radius of the sun given its mass and age. The present age of the sun is estimated to be $4.57 \pm 0.02 \times 10^9$ years [2, Appendix A, by G.J. Wasserburg]. It is determined by placing

upper and lower bounds on objects in the solar system which were present just before and just after the sun's formation. An upper bound of $t_{\odot} < 4.576 \times 10^9$ years is given by the age of *crystallized refractory condensates*, containing different isotopic ratios than terrestrial matter, that were formed from presolar materials. Measuring the age of the oldest "*C1 chondrite*" asteroids which were formed after the sun provides a lower limit $t_{\odot} > 4.563 \times 10^9$ years.

The Standard Solar Model makes four general assumptions [8]:

1. **Hydrostatic Equilibrium:** The model begins by assuming that the sun is spherically symmetric, and that the pressure gradient at each point exactly balances the gravitational force. This equality requires that:

$$\frac{dP(r)}{dr} = -\frac{Gm(r)\rho(r)}{r^2} \quad (1.1)$$

where $P(r)$, $m(r)$, and $\rho(r)$ are the pressure, contained mass, and density of the sun at radius r . The pressure is governed by the Equation of State and will be discussed in section 1.2.7, while the mass and density are related by the continuity equation

$$\frac{dm(r)}{dr} = 4\pi r^2 \rho(r) \quad (1.2)$$

2. **Energy Transport:** Energy in the interior of the sun is transported radiatively by photons with a contribution by electrons in the deep interior. The plasma at the centre of the sun is in a local thermodynamic equilibrium so diffusion approximation can be used to describe energy transport [9],[10]. Nearer the surface of the sun, heat is transported by convection.
3. **Nuclear Energy Generation:** Solar energy is generated by the conversion of hydrogen to helium via two series of nuclear reactions, the *pp chain* and the *CNO*

cycle. A complete description of these mechanisms will be discussed shortly. The rate of energy generation as a function of radius must also satisfy a continuity equation:

$$\frac{dL(r)}{dr} = 4\pi r^2 \rho(r) \epsilon_n(r) \quad (1.3)$$

where $L(r)$ and $\epsilon_n(r)$ are the luminosity and rate of nuclear energy generation at radius r .

4. **Changes in Elemental Abundances:** In most solar models, changes in the radial abundance of all elements in the sun are presumed to be due only to nuclear reactions. Cox *et. al.* [11] showed that other mechanisms such as the gravitational settling of heavier elements and thermal diffusion have a small effect and most SSM codes used to exclude them, however recent models including BP95 do account for elemental diffusion.

1.2.3 Initial Elemental Abundances

The SSM begins with a chemically homogeneous sun and changes to that uniformity over time are calculated by the model. The usual notation for elemental abundances in the SSM are X , Y , and Z which denote the fraction of the solar mass which is made up of *hydrogen*, *helium*, and *heavy elements* respectively. Anders and Grevesse [12] compiled experimental measurements and found the ratio $X : Y : Z$ to be $70.683 \pm 2.5\% : 27.431 \pm 6\% : 1.886 \pm 8.5\%$. Grevesse and Noels later updated the analysis without significant changes [15].

Estimates of the heavy element abundances Z_i are very important to the SSM because they determine the radiative opacity of the solar interior. This affects the central temperature of the sun, and determines the relative rates of different nuclear reactions, which in turn influences the neutrino spectra. Calculations have gradually improved over

the last 20 years [12], [13], [14] and today the state of the art is the work of Grevesse and Noels [15].

Elemental abundances are determined by comparing elemental ratios in C1 chondrite meteorites to independent spectroscopic measurements of the solar photosphere, corona and the solar wind. Recent improvements in the latter method have reduced the systematic errors in important opacity calculations in the SSM, although most authors were already using the meteoritic values where the two measures disagreed [16].

Figure 1.2 taken from Anders and Grevesse compares the meteoritic and solar abundances of different elements showing that of those whose spectroscopic content can be well determined most agree within 10% with some notable exceptions. Lithium and Beryllium are depleted by nuclear interactions at the bottom of the convection zone.

1.2.4 Nuclear Reaction Rates

The SSM calculates the rate at which different reactions occur using a combination of statistical mechanics and nuclear physics. The notation reviewed here is that of Parker [17], but is similar to treatments elsewhere. The rate R_{12} at which reactions between species 1 and 2 occur is given by:

$$R_{12} = \frac{N_1 N_2}{1 + \delta_{12}} \langle \sigma v \rangle_{12} \quad (1.4)$$

where N_1 and N_2 are the number densities of species 1 and 2, δ_{12} is unity if species 1 and 2 are identical and zero if they are not, and $\langle \sigma v \rangle_{12}$ is the cross section multiplied by the relative velocity v between the two particles when averaged over the Maxwell-Boltzmann velocity distribution $\Phi(v)$. This last term is given by the integral:

$$\langle \sigma v \rangle = \int_0^\infty dv [v \sigma(v)] \Phi(v) \quad (1.5)$$

$$\Phi(v) = 4\pi v^2 \left(\frac{\mu}{2\pi kT} \right)^{\frac{3}{2}} \exp \left(-\frac{\mu v^2}{kT} \right) \quad (1.6)$$

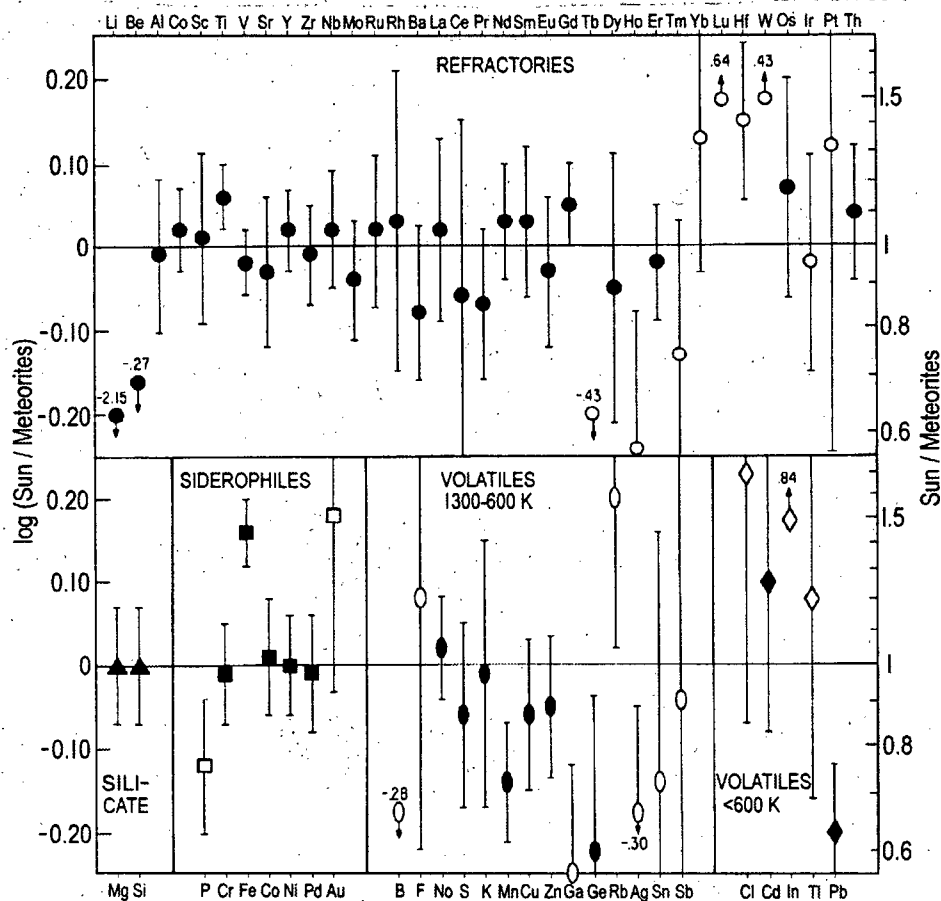


Figure 1.2: Comparison of elemental abundances in the sun using spectroscopic and meteoritic measurements. Open symbols show those elements which are poorly determined from spectroscopic data. *Li* and *Be* are affected by thermonuclear reactions in the sun, while most other elements agree quite well. Of the five (*W*, *Fe*, *Mn*, *Ge* and *Pb*) which do not agree, *Fe* was the most problematic because it is more abundant and has a strong effect on the solar opacity. However, later photospheric measurements improved the discrepancy. [12]

where μ , k , and T are the reduced mass of the two particles, Boltzmann's constant, and temperature respectively. Temperatures at the centre of the sun are much smaller than nuclear masses (on the order of a few keV compared to $m_p = 938$ MeV). Transforming the integral to one over energy using $E = \frac{1}{2}\mu v^2$ results in a more useful expression:

$$\langle \sigma v \rangle = \left[\frac{8}{\pi \mu (kT)^3} \right]^{\frac{1}{2}} \int_0^\infty dE [E \sigma(E)] \exp\left(-\frac{E}{kT}\right) \quad (1.7)$$

The low energy cross section $\sigma(E)$ is dominated by the Coulomb barrier. Its energy dependence can be conveniently expressed through the "*S-factor*" $S(E)$ which is defined by writing the cross section in the form

$$\sigma(E) = \frac{S(E)}{E} \exp\left(-\frac{2\pi e^2 Z_1 Z_2}{\hbar v}\right) \quad (1.8)$$

where the eZ_i are the electric charges of the interacting nuclei. The exponential term is often written as $\exp(-2\pi\eta)$ and referred to as the Gamow barrier penetration factor. By making the substitution $v = (2E/\mu)^{1/2}$ and defining $E_G = 2\mu(\pi Z_1 Z_2 e^2/\hbar)^2$, the energy dependence of the exponential term in $\sigma(E)$ becomes explicit and it can be written as $\exp(\sqrt{E_G/E})$. The velocity average cross section factor in equation 1.7 simplifies to

$$\langle \sigma v \rangle = \left[\frac{8}{\pi \mu (kT)^3} \right]^{\frac{1}{2}} \int_0^\infty dE S(E) \exp\left(-\sqrt{\frac{E_G}{E}} - \frac{E}{kT}\right) \quad (1.9)$$

Experiments measure the energy dependence of the nuclear S-factors at energies as low as possible in the laboratory and the results are extrapolated to zero. When the S-factor is approximated with the first few terms its Taylor expansion at zero energy, equation 1.9 can be evaluated as the sum of standard integrals.

Experiments which determine the S-factor require a correction for the screening by inner electron shells which surround the atomic nucleus. They measure the energy dependence of the cross section for colliding ions, whereas in the solar interior the electrons are stripped from the atomic nuclei. Salpeter [18] first calculated a "*weak-screening*" which

is of the order of a few percent. More recently, Assenbaum et al. [19] have modelled the effect of electron screening in the solar plasma, where electrons tend to cluster around the nuclei. Just as the valence electrons in Salpeter's treatment screen incoming projectiles from the full Coulomb potential of a target nucleus, the electrons in the plasma sea also screen incoming projectiles.

One critical caveat must be considered when extrapolating the S-factor down to zero energy. The above analysis neglects the possibility that a nuclear resonance exists below the lowest energy measured in the laboratory. If such a resonance *does* exist then the cross section for the process can increase dramatically. While it is possible to calculate the effect of such a resonance on $\langle\sigma v\rangle$ [20], if an unknown resonance exists then the extrapolation to zero energy of the experimentally measured S-factor would not be valid. It is therefore important to try to measure the relevant S-factors at energies as low as possible, and then carefully rule out any nuclear resonances which might exist.

1.2.5 The Proton-Proton Chain

The proton-proton chain, which accounts for about 99% of the sun's luminosity, is shown in figure 1.3. The first two reactions in the chain produce deuterium (^2H), with pp occurring about 500 times as often as pep . This is the slowest process in the cycle and therefore dominates the overall rate of energy production. It is very difficult to measure the cross section directly—with a typical experimental apparatus one would expect pp reactions about once every 10^6 years [21]. The idea is that as two protons come into close contact with each other for a short period of time, one undergoes a β -decay to form a neutron and they bind together to form a deuteron. The rate is calculated using electroweak theory with the largest uncertainty being the neutron lifetime.

The next reaction in the pp chain is $^2\text{H} + p \rightarrow ^3\text{He}$. Because it occurs very quickly, it does not affect the overall rate of ^4He production. The ^3He now combines with either

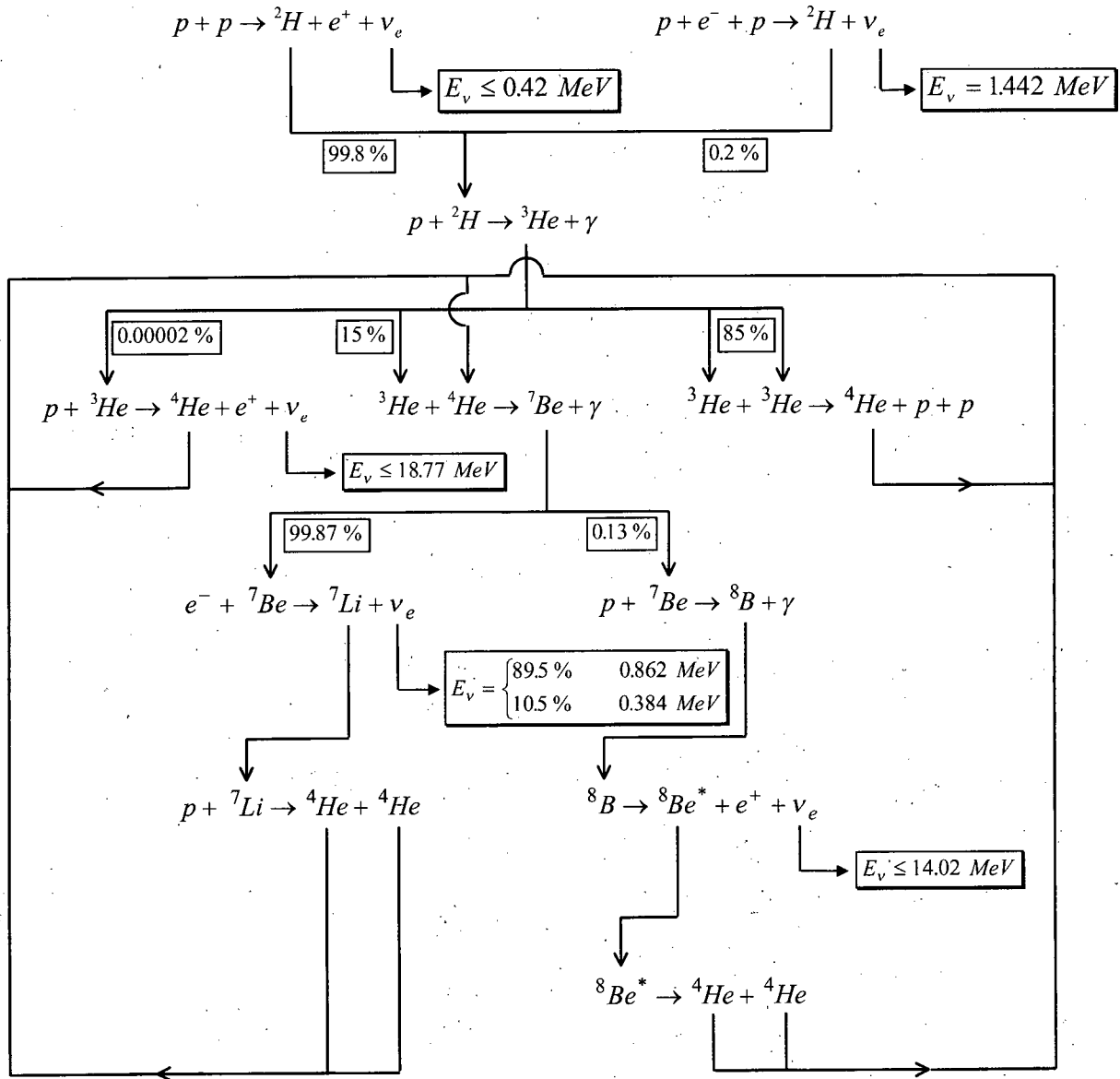


Figure 1.3: The Proton-Proton (pp-chain) reactions for converting hydrogen to helium in the sun, and the energies of the neutrinos produced.

another ${}^3\text{He}$ nucleus or ${}^4\text{He}$. The *hep* reaction $p + {}^3\text{He} \rightarrow {}^4\text{He} + e^+ + \nu$ occurs at a very low rate, but it may be measurable in future precision experiments because the energy of the outgoing neutrino can be as high as 18.77 MeV [2].

The vast majority of ${}^3\text{He}$ in the sun burns via ${}^3\text{He} + {}^3\text{He} \rightarrow {}^4\text{He} + p + p$ and ${}^3\text{He} + {}^4\text{He} \rightarrow {}^7\text{Be} + \gamma$ in an 85 : 15 ratio. The relative rate of these two reactions, once a major source of uncertainty, has very important implications for neutrino fluxes because the ${}^3\text{He}$ - ${}^3\text{He}$ reaction does not produce neutrinos. If there was a nuclear excited state of ${}^6\text{He}$ with energy on the order of 10 – 15 keV, then the rate of ${}^3\text{He}$ - ${}^3\text{He}$ interactions would increase dramatically and the number of ${}^7\text{Be}$ and ${}^8\text{B}$ neutrinos which solar models predict would decrease substantially [21]. Krauss et al. [22] have measured the S-factor for this interaction from 350 keV down to about 25 keV and no resonance was found. Figure 1.4 shows the energy dependence of this S-factor and illustrates that the experiment does probe energies which are relevant to the solar interior. Figure 1.5 taken from Hilgemeier et al. [23] shows the measured energy dependence of the ${}^3\text{He}$ - ${}^4\text{He}$ interaction and a theoretical model on the range 200 – 700 keV. These and similar experiments determine the 85 : 15 ratio.

The last important branch of the *pp* chain are the two mechanisms which destroy its ${}^7\text{Be}$. The reaction $e^- + {}^7\text{Be} \rightarrow {}^7\text{Li} + \nu_e$ burns 99.87 % of the sun's ${}^7\text{Be}$ and $p + {}^7\text{Be} \rightarrow {}^8\text{B} + \gamma$ destroys the remaining 0.13 %. The e^- - ${}^7\text{Be}$ interaction has a 2-body final state including a 0.862 MeV neutrino in 89.5 % of interactions and 0.384 MeV neutrino in the remaining 10.5 % [24]. The p - ${}^7\text{Be}$ reaction destroys only a small fraction of the ${}^7\text{Be}$ but produces the all-important ${}^8\text{B}$ neutrinos in subsequent decays.

A recent study by Johnson et al. [25] carefully reexamined both these rates to account for additional effects. Their study reduced the p - ${}^7\text{Be}$ rate by 7 %, and their analysis has been incorporated into BP95.

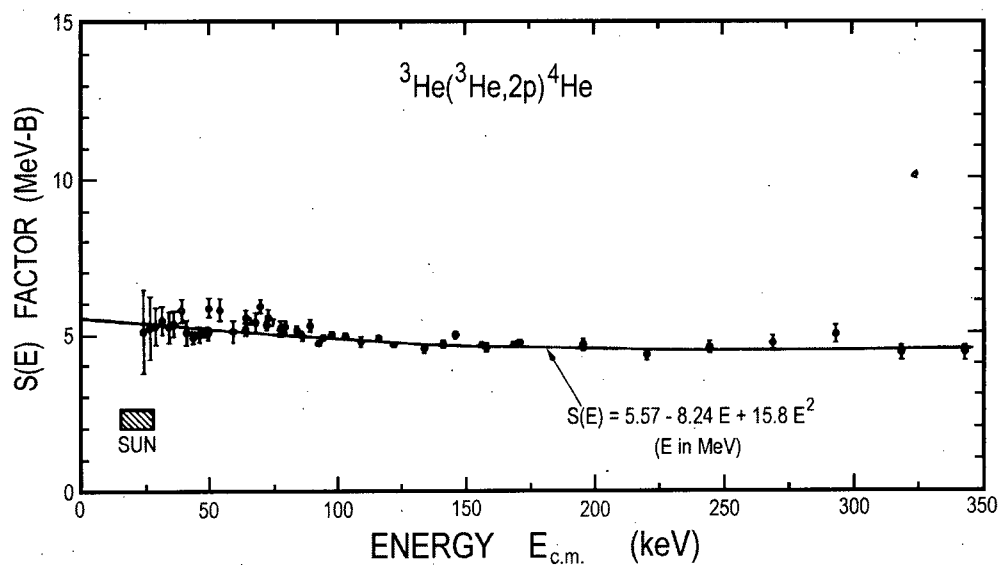


Figure 1.4: Energy dependence of the $S(E)$ factor for the reaction ${}^3\text{He} + {}^3\text{He} \rightarrow {}^4\text{He} + 2p$. The solid line shows a polynomial fit to the data, while the hatched region at the bottom left shows the thermal energy region relevant to the solar interior [22].

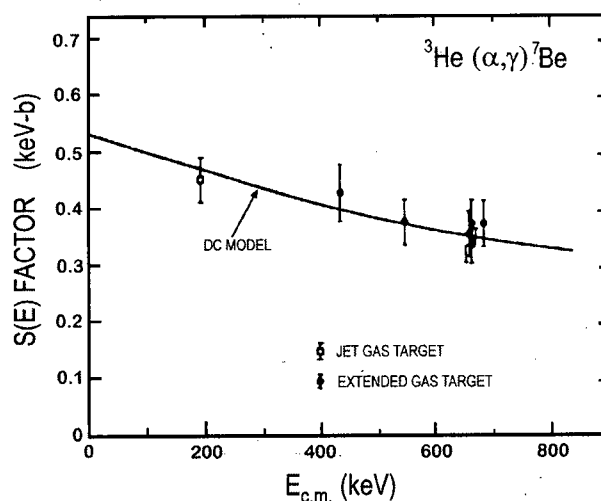


Figure 1.5: Energy dependence of the astrophysical $S(E)$ factor for the reaction ${}^3\text{He} + {}^4\text{He} \rightarrow {}^7\text{Be} + \gamma$. The solid line shows a model prediction fitted to the γ -ray data [23].

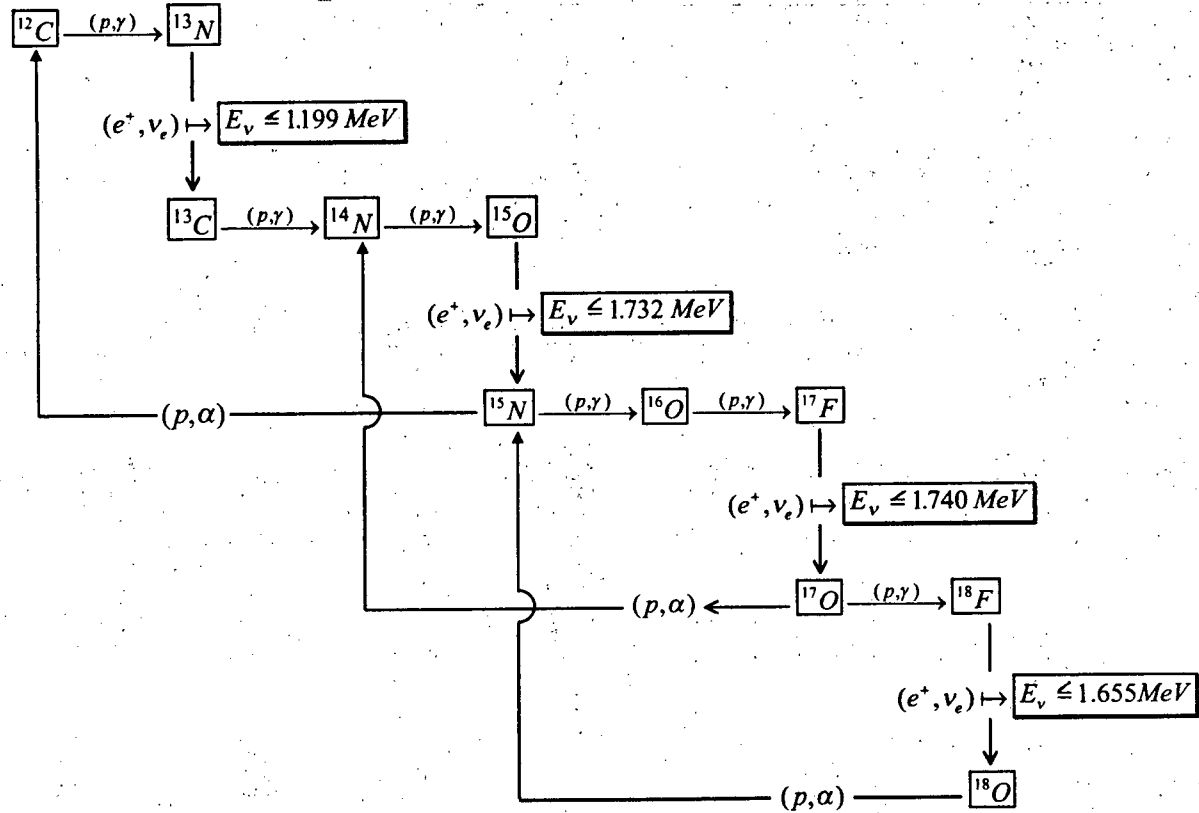


Figure 1.6: The CNO-cycle reactions which catalyze conversion of hydrogen into helium in the sun, with the energies of the neutrinos produced.

1.2.6 The CNO Cycle

The CNO-cycle is a minor reaction in the sun and accounts for only about 1.5 % of its luminosity [26], mainly because the heavier elements have a higher Coulomb barrier to overcome than reactants in the pp chain. It consists of a series of proton capture reactions and β^+ decays involving carbon, nitrogen and oxygen, which act as catalysts to the reaction. There are several “sequences” of interactions as shown in figure 1.6, with the most important cycle involving the six elements in the upper left of the diagram.

The rate at which this mechanism produces energy depends on the abundance of the elements which catalyse the reaction. The slowest CNO reaction is $p + ^{14}\text{N} \rightarrow ^{15}\text{O} + \gamma$

so its S-factor and the ^{14}N abundance largely determine the rate. The cross sections for the interactions in the CNO cycle are fairly well established experimentally, and careful studies which have shown that the effect of low energy resonances is smaller than 1 % [27].

1.2.7 The Equation of State

The general idea of an Equation of State is to relate the density, temperature, and pressure of a gas. The simplest reasonable model for the sun would be to assume that the Equation of State of the solar interior is given by the ideal gas law relating these quantities to the mean molecular weight, and Boltzmann's constant k :

$$P(r) = \frac{k\rho(r)T(r)}{\mu(r)} \quad (1.10)$$

Because the sun is not an ideal gas, this equation must be corrected for several effects, such as Coulomb interactions, partial electron degeneracy, and radiation pressure which can lead to partial ionisation of the plasma. There are two general methods for calculating the Equation of State called the Chemical Picture and the Physical Picture and the two lead naturally to different treatments of the opacity. The two methods do agree quite well, but the latter has recently emerged as the preferred method in solar modelling.

In the Chemical Picture every bound state of every element in the plasma is treated as a separate species. An equation for the free energy of the plasma is constructed based on the "external" parameters temperature, volume, and concentrations of the different elements in the plasma. This free energy is numerically minimized in order to determine the configuration which realises thermodynamic equilibrium, and the temperature, pressure, and entropy are calculated by differentiating the free energy at this minimum. The philosophy behind the Chemical Picture is to construct the free energy based on those *external* parameters which are adjustable by the experimenter, and allow the minimization

procedure to determine the “*internal*” parameters—those which are specified by nature [28].

Until recently, this method had been used in the majority of Equation of State calculations for the solar interior. It has the advantage that all quantities calculated are explicitly thermodynamically consistent by construction. However, it involves a divergent partition function and some cutoff procedure must be applied. At low densities where the gas is nearly ideal, the partition function is independent of the cutoff. However, at very high densities more complicated models must be employed.

In the last few years the Physical Picture has emerged as the preferred method to calculate the Equation of State in solar models. Whereas the Chemical Picture can be considered a thermodynamic approach to the problem, the Physical Picture is a statistical mechanical approach. In this method, only electrons and different nuclei are considered to be different species, and bound states are calculated explicitly using the Hamiltonian describing the interactions between the components of the plasma.

1.2.8 The Opacity

Opacity is a measure of the transport of radiation through matter and may be thought of as the inverse of the mean free path to absorption. In the solar interior most energy is transported via photons, but in the deep interior electrons also play a role. The opacity is dependent upon the chemical species which are present and the different interactions which they have with photons. It is also contingent on the thermodynamic variables of the plasma, and hence it is intimately connected to the Equation of State.

The interior of the sun consists of a plasma which has both high density and high temperature. In these *collision dominated* conditions the free electrons are well described by a Maxwell velocity distribution, and the occupation of bound electrons obeys a Boltzmann distribution. In addition, radiation is nearly in equilibrium with matter so that

both follow a Planck temperature spectrum. These three conditions define a *Local Thermodynamic Equilibrium* [10], and Rosseland showed in 1924 that they are sufficient to permit radiation transport to be approximated by diffusion with a coefficient proportional to the temperature gradient [9]. The Rosseland mean radiative opacity κ_R can be shown to be:

$$\frac{1}{\kappa_R} = \frac{15}{4\pi^4} \int_0^\infty du \frac{1}{\kappa'(u)} \frac{u^4 e^u}{(e^u - 1)^2} \quad (1.11)$$

where the extinction coefficient κ' is a measure of how far a photon travels before it is absorbed by the plasma.

Deep in the interior of the sun where the temperature and density are very high, electron conduction also provides significant resistance to energy transport and an effective opacity κ_{eff} must be used.

The Rosseland mean opacity coefficient measures the least resistance to radiation flow. There are no laboratory experiments which can simulate the details of the interior of the sun so the calculation of this coefficient relies on theoretical models which are based on quantum mechanics, statistical mechanics, atomic spectral properties, and nuclear cross sections.

To determine κ_R in the sun, one needs to know the abundance of all chemical elements in the plasma, as well as their energy levels and radiative transition probabilities. These atomic properties are in turn dependent on the temperature and density of the surrounding plasma. There are two general methods for modelling the plasma which are then used to calculate the radiative opacity: the Explicit Ion Approach and the Mean Ion Model.

The Explicit Ion Approach is used when there are fewer atomic species present and the temperature is relatively low. This method requires comprehensive experimental data detailing all atomic energy levels and splittings. It treats each species of ion separately,

and the partition function of each ionic species is a weighted sum over all excited states of the ion. Additional interactions between the ions and the plasma are calculated as perturbations to the relative populations of each species. This method is reminiscent of the Chemical Picture calculation of the Equation of State and is typically used in conjunction with it. However the calculations are only tractable when there are a smaller number of species in the plasma with well known energy levels, typically elements with $Z \leq 30$ [10].

In order to model plasmas at high temperature and density in which the atomic energy levels are perturbed from their well known laboratory values and where the number of species is too large for the Explicit Ion Approach to be tractable, the Mean Ion Model is employed. The idea behind the model is to construct an *average* ion which will provide a gross indication of the ionization and excitation of ions in the plasma. There are several methods [10, and references therein] of constructing approximate energy levels for each ionization state of the mean ion to make it sufficiently similar to real ions based on statistical mechanical ideas, making it particularly amenable to being used with the Physical Picture of the Equation of State.

In many real calculations of the opacity of stellar plasmas a combination of these two models is used. For low Z elements the known atomic levels are used, while the high Z elements are treated with a Mean Ion Model. This was the method used by the Los Alamos Opacity Library which produced the stellar opacity tables used in most solar models throughout the 1980's and into the early 1990's. The recently developed OPAL code, which was employed to compute the opacities used in BP95, uses the Explicit Ion Approach on a reduced set of elements. The opacity calculation was optimized by removing elements from the plasma mixture (and increasing the abundances of neighbouring elements to conserve the number of particles and molecular weight) to see which elements were important in determining the opacity. Iglesias and Rogers [29] were able to reduce

the number of elements to 15: H, He, C, N, O, Ne, Na, Mg, Al, Si, S, Ar, Ca, Fe, and Ni. In doing the study they found that cutting out the five least significant elements of these 15 (namely Na, Al, Ar, Ca, and Ni) only lead to an change in the opacity of 1 % to 3 %.

Once all of the ionization state abundances and excited state occupation probabilities have been determined the next step in the opacity calculation is to calculate the cross sections of the photon interaction processes which specify the opacity. There are four physical processes which can absorb or emit a photon or change its motion: bound-bound, bound-free and free-free scattering with ions, and Thompson scattering which requires the presence of an ion.

1.2.9 Elemental Diffusion

Cox, Guzik, and Kidman [11] studied diffusion of both light and heavy elements in the sun. The distribution of these elements affects the equation of state, which in turn determines the opacity, temperature, and therefore rates of production of solar neutrinos.

They found increases of less than 1 % in the abundance Y of helium and Z of heavy elements in the core of the sun, its central temperature, and density. Their model did predict an increase in the number of ${}^7\text{Be}$ and ${}^8\text{B}$ solar neutrinos of about 5 % to 7 %. Abundances Y and Z also showed noticeable reductions of just over 10 % in the outer regions, but these surface corrections do not affect neutrino generation.

In their first collaborative effort, Bahcall and Pinsonneault [16] included the effect of helium diffusion but not heavy elements. They found that it increased the number of ${}^7\text{Be}$ and ${}^8\text{B}$ solar neutrinos by about 6 % and 12 % respectively as a result of small increases in the central temperature and a slight shift of energy generation towards the centre of the sun. BP95 includes a more accurate calculation of elemental diffusion, including heavy elements, based on a paper by Thoul, Bahcall, and Loeb [30]. It predicts still larger ${}^7\text{Be}$

and ^8B neutrino fluxes.

1.2.10 The Numerical Model

The SSM begins with a sphere of gas at time $t = 0$ in which the heavy element abundances are given by experimental measurements (the most recent results are those of Grevesse and Noels [15]), and the helium abundance Y is guessed. The assumptions of hydrostatic and thermal equilibrium, and the continuity equations discussed in section 1.2.2 are used to constrain the mass density of the sun at each radius. The nuclear reaction rate formalism developed in section 1.2.4 and the astrophysical S-factors for the different reaction chains determine the rate at which nuclear energy is generated by each process. The rate of diffusion of this energy is then determined by the Equation of State and opacity as a function of radius. The differential equations which define the solar structure are solved subject to the above constraints at the initial time. BP95 does this by integrating from the solar surface inward and from the centre outward and requiring that the two solutions match at some intermediate radius (typically at $r = 0.2 R_\odot$).

Once a consistent model is obtained for the initial time, a later time step is chosen. Based on the rates at which the nuclear reactions are occurring in the first time step, changes in nuclear abundances as a function of radius are calculated for the later time. Then the differential equations at the second time step are used to produce a consistent model at this time. This process is iterated until the current age of the sun $t_\odot = 4.57 \times 10^9$ years is reached, and may take as few as 10 steps or as many as 200 steps depending on the accuracy performed at each step.

The model takes two important variables as inputs: the initial helium abundance Y and an entropy-like parameter that is significant in the convective zone defined as $S = 2.5 \log T - \log P$. Given the initial estimates of Y_i and S_i the model is iterated forward to the present time, and the radius R_\odot and luminosity L_\odot are compared with

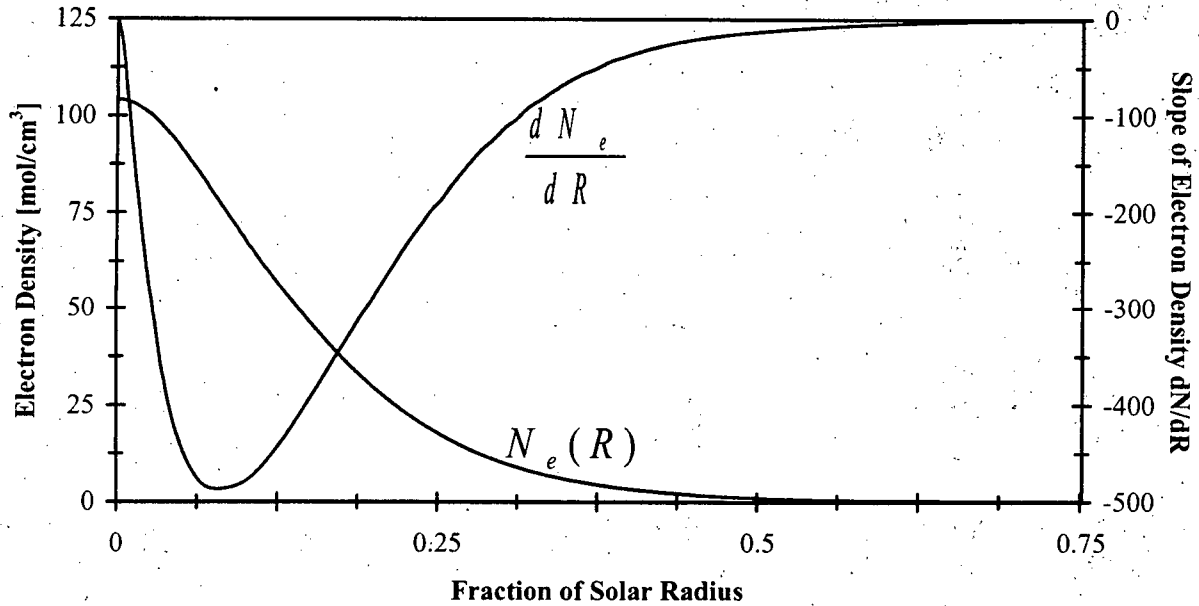


Figure 1.7: Fits to the electron density based on the 1995 model of Bahcall and Pinsonneault [2] with helium and heavy element diffusion. The data beyond $0.4R_{\odot}$ was extrapolated, and the derivative of the density was calculated.

those observed. If the predicted parameters R_{\odot} and L_{\odot} do not match, a new Y_i and S_i are chosen and the process is repeated until R_{\odot} and L_{\odot} are correct within some tolerance, usually on the order of one part in 10^5 [8]. In addition to the primordial values of the parameters Y_i and S_i the SSM model also predicts the current density, elemental abundances, luminosity, temperature and neutrino production rates as a function of radius. Figures 1.7 and 1.8 show the solar electron density and neutrino production as a function of solar radius predicted by BP95. These elements of the model are the most important for neutrino oscillation calculations and will be used later.

Among the predictions of the SSM are the changes which occur throughout the lifetime of the sun. Figure 1.9 shows the time dependence of the radius and luminosity. In addition to those two quantities, the central temperature of the sun also increases: as hydrogen is converted to helium the mean molecular weight μ increases in the solar core, there must

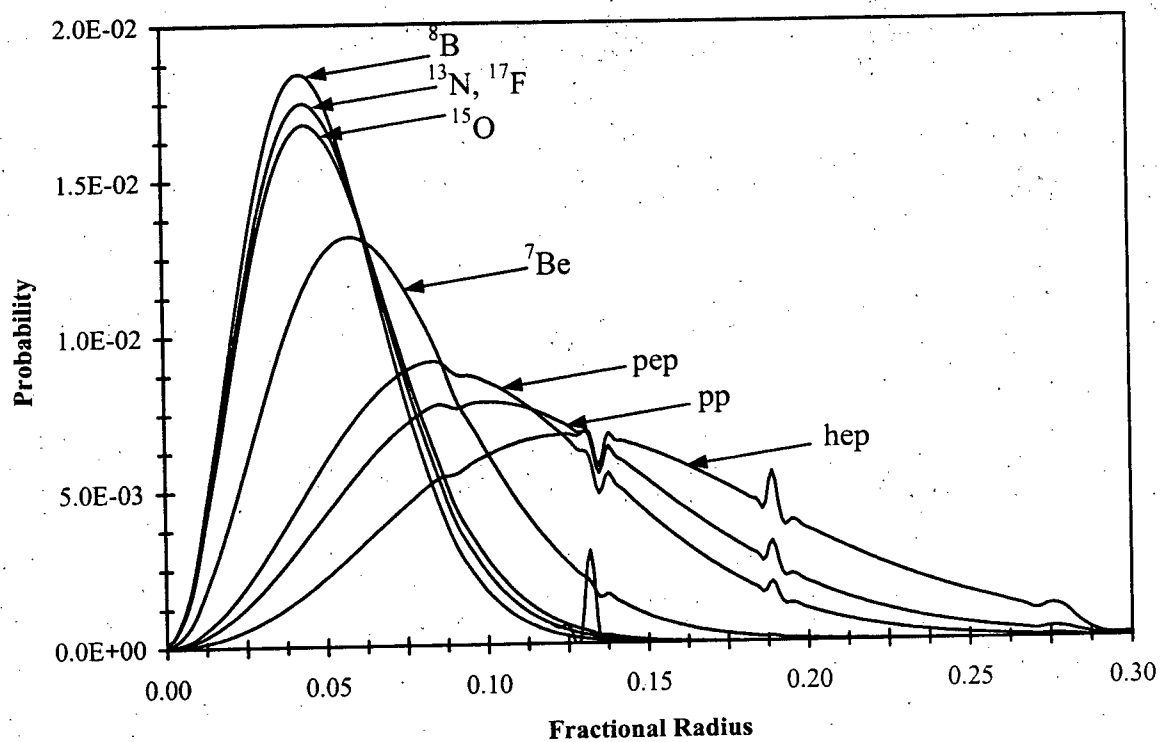


Figure 1.8: Radial dependence of the rate of production of different solar neutrino fluxes.

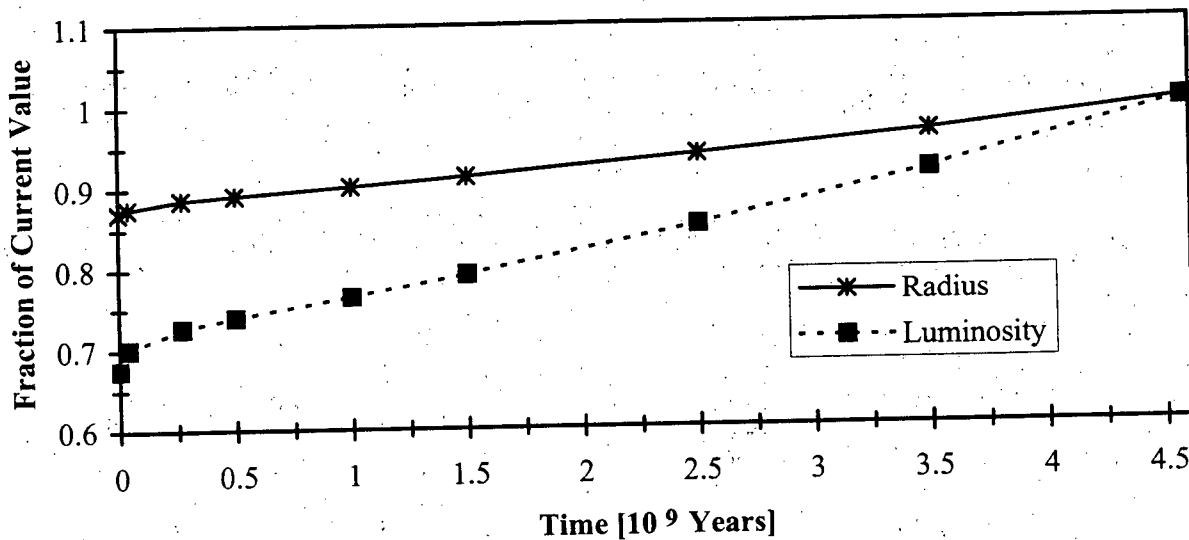


Figure 1.9: Time dependence of the radius and luminosity of the standard solar model.

be a proportional increase in ρT in order to maintain hydrostatic equilibrium (which for an ideal gas requires that $P = k\rho T/\mu$) [31]. This increase in temperature results in an increase in the rate of production of ^8B neutrinos.

1.2.11 Solar Oscillations

Leighton *et. al.* [32] first noticed vertical oscillations in the sun's photosphere by measuring doppler shifts of the matter on its surface. If an acoustic wave travels into the sun at an oblique angle it gradually refracts because the speed of sound v_s increases as it moves to the hotter, more dense interior. When it reaches a point where the local phase velocity is equal to v_s it reverses direction and moves outwards. As it approaches the outer surface of the sun, it is reflected back by surface layers. Standing waves, or *p-modes* are formed at certain frequencies, and the calculation of which stable modes can exist reduces to an eigenvalue problem that is dependent on the speed of sound in the sun [33].

The oscillations can be described by the product of a radial term, a spherical harmonic

term, and a time dependent term and have the form [34]:

$$E(l, m, n) \equiv K_{\ln}(r) Y_l^m(\theta, \varphi) e^{i\omega_{lmn}t} \quad (1.12)$$

The speed of sound in the sun v_s is given by the equation

$$v_s^2 = \frac{P(r)}{\rho(r)} \left(\frac{\partial \ln P}{\partial \ln \rho} \right)_S \quad (1.13)$$

where $P(r)$ and $\rho(r)$ are the pressure and density, and the subscript S implies that the partial derivative is to be taken at constant entropy. The penetration depth of the wave increases with its frequency, so these waves may be used to probe successively deeper into the interior of the sun.

Using numerical techniques, several of which are described by Christensen-Dalsgaard and Berthomieu [35], stable modes can be calculated given the pressure and density profiles of a given model of the sun. Inverting the p-mode data to place constraints on the solar interior is another difficult numerical problem which has been studied in the last several years [36], [37], [38].

These latter investigations showed that the sun is hotter in the outer part of the radiative interior than was previously thought, and the new OPAL opacity tables have produced models in much better agreement with the measured p-mode oscillation frequencies. The BP95 model, which includes both helium and heavy element diffusion and uses the OPAL tables, predicts a convective zone depth of $0.712R_{\odot}$ which compares very favourably with Christensen-Dalsgaard *et al.* [38] who measured it to be $0.713 \pm 0.003R_{\odot}$ using p-mode oscillation data. Without diffusion the same SSM predicts a depth of $0.726R_{\odot}$ and the fit to p-mode data is much less accurate.

1.2.12 Discussion of the Solar Model

There are a number of independently produced Standard Solar Model codes discussed in the literature, using different numerical techniques and slightly different inputs, but the

results show remarkable agreement. Table 1.1 lists several of the principle predictions for different solar models including the neutrino fluxes. Note that different models use slightly different abundances, Equations of State, opacity tables, and nuclear S-factors, but the inputs are generally quite similar. Those models which include elemental diffusion are on the right of the table.

It is apparent that the pp neutrino rates are very stable, while the ${}^7\text{Be}$ and ${}^8\text{B}$ neutrinos are more sensitive to the details of the model, particularly the temperature. However it is clear that the neutrino fluxes of all of the models are far above the measured rates at the four neutrino experiments. It is also notable that in the most up to date model [2] in which heavy element diffusion has been incorporated and which fits the p-mode oscillation data, the neutrino fluxes have increased. The increases come about because elemental diffusion raises the central temperature of the sun by about 2 %, which increases the temperature sensitive ${}^7\text{Be}$ and ${}^8\text{B}$ neutrino production rates.

Bahcall and Pinsonneault calculated the errors in their model from different inputs including different reaction rates, heavy metal abundances Z_i , solar luminosity L_\odot , age of the sun t_\odot , opacity, and diffusion. These results are summarized in table 1.2. Note that the errors from most of the different sources are uncorrelated so they must be combined in quadrature. Moreover, since the theoretical errors in the model are not dominated by one or two errors, it is unlikely that a single major improvement in the model will reduce the overall error substantially.

Neutrino production rates calculated by the SSM are much lower than experiments measure. This discrepancy has been known for over 25 years and was first measured in the Homestake experiment. Since that time many researchers have looked for ways to reduce the predicted neutrino fluxes in the SSM, but no one has found any mechanism to reduce them to a level anywhere nearly consistent with the experimental data. Many of the ideas which have been pursued in the past are now being ruled out by the helioseismological

Model	BU	SBF	BPML	TCL	Pa	BP _a	BP _b	BP _c	Pb
Diffusion	No	No	No	No	No	No	H, He	Yes	Yes
$\phi(pp) \times 10^{-10}$	6.00	6.00	5.93	6.01	6.03	6.01	6.00	5.91	5.91
$\phi(pep) \times 10^{-8}$	1.40	1.29	1.40	1.39	1.43	1.44	143	1.40	1.39
$\phi(hep) \times 10^{-3}$	7.58	6.49	n/a	n/a	1.25	1.27	1.23	1.21	1.20
$\phi(^7Be) \times 10^{-9}$	4.69	4.23	4.47	4.42	4.60	4.53	4.89	5.15	5.18
$\phi(^8B) \times 10^{-6}$	5.76	5.80	5.40	4.71	5.01	4.85	5.69	6.62	6.48
$\phi(^{13}N) \times 10^{-8}$	6.09	3.99	5.71	4.00	4.50	4.07	4.92	6.18	6.40
$\phi(^{15}O) \times 10^{-8}$	5.22	3.09	4.81	3.39	3.81	3.45	4.26	5.45	5.57
$\phi(^{17}F) \times 10^{-6}$	5.16	4.23	4.96	n/a	4.58	4.02	5.39	6.48	6.79
$N(^{37}Cl)$	7.9	7.68	7.43	6.78	7.14	7.0	8.1	9.3	9.02
$N(^{71}Ga)$	132	125	127.7	124	127.3	126	132	137	136.9
T_C (10^7 K)	1.564	1.543	1.555	1.543	1.523	1.556	1.567	1.584	1.581
R_{CZ}/R_\odot	0.74	n/a	0.721	0.725	0.721	0.726	0.707	0.712	0.712
ρ_C ($\frac{10^2 g}{cm^3}$)	1.48	1.466	1.519	1.469	1.633	1.524	1.542	1.562	1.559

Table 1.1: Standard Solar Models and their Predictions. Models referenced are as follows: BU (Bahcall and Ulrich [8], 1989), SBF (Sackman, Boothroyd, and Fowler [39], 1990), BPML (Berthomieu et. al. [40], 1993), TCL (Turck-Chieze and Lopes [41], 1993), Pa (Proffitt [42], 1994), BP_a (Bahcall and Pinsonneault [2], 1995), BP_b (Bahcall and Pinsonneault [16], 1992), BP_c (Bahcall and Pinsonneault [2], 1995), Pb (Proffitt [42], 1994). Fluxes for each solar neutrino source are shown in number neutrinos arriving on earth per cm^2 per second, as well as the rate for ^{37}Cl and ^{71}Ga targets quoted in SNU, central temperature of the sun T_C , radius of the convective zone R_{CZ} , and central solar density ρ_C .

Source of error	pp	pep	7Be	8B
$p - p$ reaction rate	0.2	0.3	1.0	3.0
$^3He - ^3He$ reaction rate	0.2	0.0	2.0	2.0
$^3He - ^4He$ reaction rate	0.2	0.3	3.0	3.0
$p - ^7Be$ reaction rate	0.0	0.0	0.0	9.0
$p - ^{14}N$ reaction rate	0.2	0.2	0.0	0.0
Heavy element abundance Z/X	0.4	0.9	3.0	8.0
Luminosity L_\odot	0.3	0.3	1.0	3.0
Solar Age t_\odot	0.0	0.0	0.0	1.0
Opacity Tables	0.3	0.5	3.0	5.0
Elemental Diffusion	0.6	0.9	4.0	8.0

Table 1.2: Percentage uncertainties in the principle neutrino sources in the Solar pp chain.

constraints made by inverting p-mode oscillation frequencies. Three recent ideas studied to reduce the neutrino output of the SSM include modification of nuclear cross sections, rotation or mixing effects, and changes to the opacity.

Most of the astrophysical S-factors have not been measured under conditions which are equivalent to the centre of the sun so some researchers feel that changes in these quantities could resolve the solar neutrino problem. For example if the pp S-factor was increased, then this interaction could occur more easily and at a lower temperature, and the ^8B and ^7Be neutrino fluxes would drop. However studies such as Castellani et. al. [43] have looked at what constraints can be obtained on solar model parameters, including the S-factors, by looking at the rates measured in the solar neutrino experiments.

For example, using the $^3\text{He} + ^4\text{He}$ reaction as the main mechanism to burn ^3He would reduce the pp neutrino flux by a factor of 2, but would increase the ^8B and ^7Be fluxes markedly, contrary to the Kamiokande data which already finds these rates too low. Reducing the S-factor S_{17} for the $p + ^7\text{Be}$ reaction would reduce the number of ^8B neutrinos, but because Kamiokande is only sensitive to these neutrinos there is a limit to how much this could be reduced, and Berezhinsky et al. [44] concluded that varying both S_{17} and temperature were not sufficient to explain any two types of solar neutrino experiments. The most plausible change in nuclear physics which could reduce the solar neutrino fluxes would be a low energy resonance in the cross section for the reaction $^3\text{He} + ^3\text{He} \rightarrow ^4\text{He} + p + p$. This reaction could then dominate the burning of ^3He and reduce the ^8B and ^7Be fluxes. However section 1.3.5 will show that with assumptions which are almost completely independent of the S-factors and the solar model itself, the different experimental results are irreconcilable with each other.

Experiments have been performed to dramatically reduce the energy region in which such a resonance could occur [22], and the LUNA experiment at Borexino will probe to still lower energies. But because the Kamiokande experiment does see ^8B neutrinos, such

a solution is still a poor fit to the experimental data [43].

If the solar core rotates faster than the exterior, then there would be a change in the equations governing hydrostatic equilibrium which would reduce both the pressure inside the sun and the neutrino fluxes. However calculations have shown that the inner core would have to be rotating 1000 times faster than the exterior, which not only creates very serious dynamical problems, but also leads to predictions of p-mode frequencies which do not match observations [26]. Mixing of the contents of the sun would increase the abundance of hydrogen in its core and allow it to burn at a lower temperature. However no plausible mechanism has been proposed to create mixing to the degree necessary or at a sufficient rate; it has been shown that about $\frac{2}{3}M_{\odot}$ would have to have been mixed in the last $\frac{1}{10}t_{\odot}$ in order to solve the solar neutrino problem [45].

Many ideas to reduce the opacity in the solar interior have been investigated. This would make the sun more transparent and thereby reduce the temperature (for a fixed luminosity), and hence decrease the ^8B and ^7Be fluxes. Possible mechanisms include decreasing the heavy element abundance Z , imposing an overall reduction in the opacity tables, assuming that some of the iron in the solar interior precipitates, or making changes to the Equation of State. However p-mode oscillation data implies that the opacities tables used in the early eighties (LAOL) were too low, and newer models with higher opacities (OPAL) provide much better fits [46]. This view is consistent with the study by Turck-Cheize and Lopes which rules out opacity and Equation of State solutions to the Solar Neutrino Problem [41]. Moreover some authors have concluded that attempts to reduce the neutrino fluxes by decreasing the interior temperature of the sun have been ruled out by experimental results [43].

1.3 The Solar Neutrino Experiments

Among the major predictions of the Standard Solar Model (SSM) are the fluxes of solar neutrinos from the different nuclear interactions. In 1963, the Homestake experiment began measuring the flux of solar neutrinos, and it has continued to do so for over 30 years. The rates measured have consistently been much lower than those predicted by solar models. However, because most of the signal comes from the relatively rare ${}^7\text{Be}$ and ${}^8\text{B}$ neutrinos which are particularly sensitive to the central temperature in solar models, the anomalous results were not taken as seriously as they might otherwise have been.

In 1987 the Kamiokande experiment began taking data and also found a deficit in solar neutrinos although it too, is only sensitive to the high energy tail of the ${}^8\text{B}$ neutrinos. The early 1990's saw the completion of the gallium experiments Gallex and SAGE and they, too, found a deficit in the solar neutrino flux compared to the SSM. What is significant about these latter experiments is that the energy threshold for measuring neutrinos in gallium is low enough that they measure the nearly model independent pp and pep neutrinos. The newer experiments, combined with the progress in the SSM over the last three decades, have made the Solar Neutrino Problem very apparent. Our understanding of particle physics and the sun cannot be considered complete without resolution of this serious discrepancy.

In this section each of the four experiments currently measuring solar neutrino fluxes will be reviewed. Table 1.3 summarizes their results and figure 1.10 shows the solar neutrino fluxes with the energy thresholds for the different detectors marked at the top. The Solar Neutrino Problem, in its simplest form, is that all of the experiments measure fewer neutrinos than predicted by the SSM. However, as will be shown in section 1.3.5, the experiments do not agree with each other under very general conditions almost independent of the solar model.

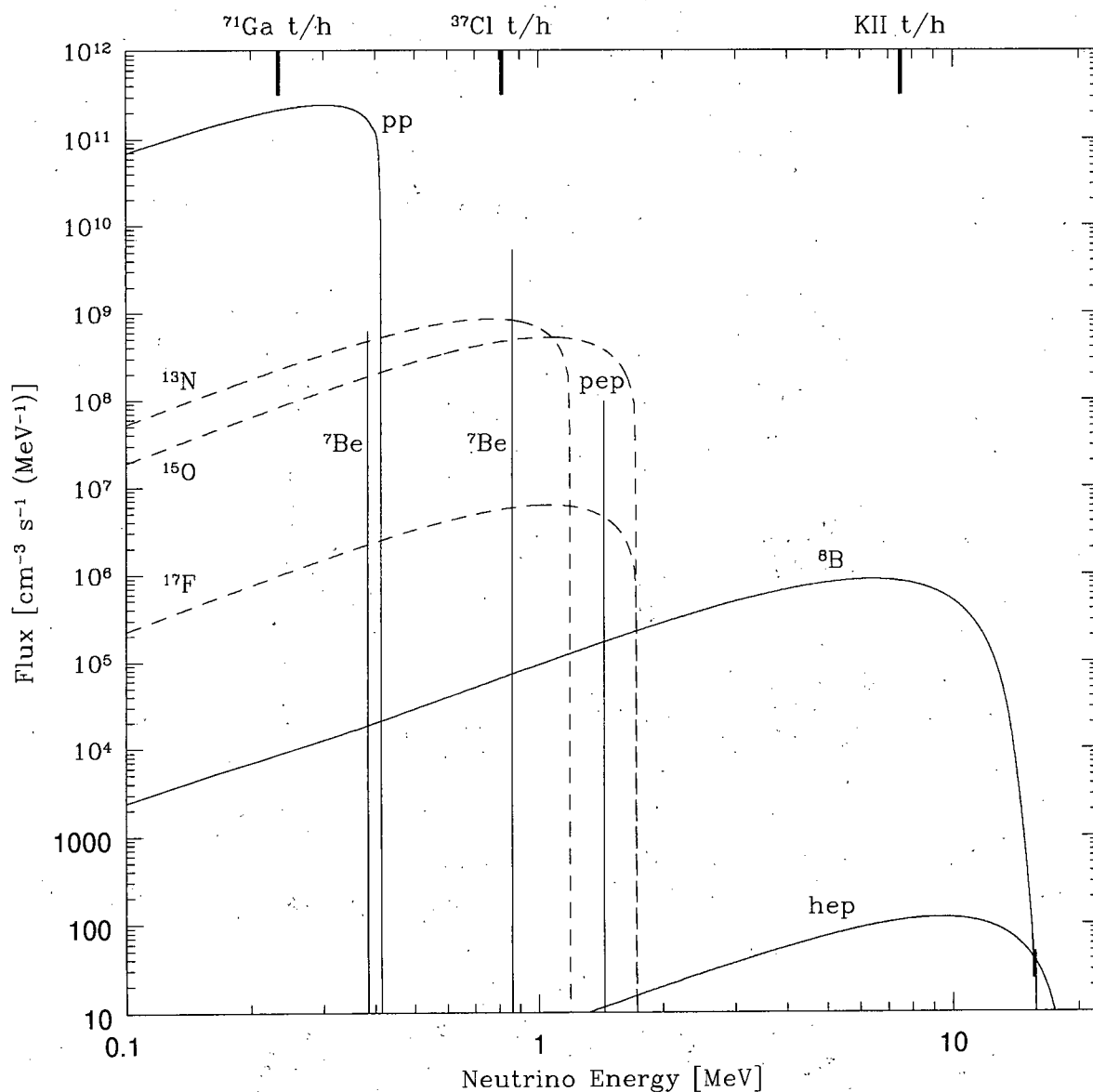


Figure 1.10: Spectrum of all sources of solar neutrinos based on relative rates in [2]. Continuum sources are given in number arriving on earth in units $\text{cm}^{-2}\text{s}^{-1}\text{MeV}^{-1}$, while fixed energy sources are given in $\text{cm}^{-2}\text{s}^{-1}$. Neutrinos from the *pp*-chain are shown with solid lines, while those from the CNO-cycle are shown with dashed lines. Energy thresholds for the different experiments are marked on the top of the figure.

Experiment	Homestake	Kamiokande	Gallex	Sage
Target	^{37}Cl in C_2Cl_4	Hydrogen	^{71}Ga in HCl	metallic ^{71}Ga
Size	$3.8 \times 10^5 \text{ l}$	2,140 t H_2O	30.3 t Ga	57 t
E_{th}	0.814 MeV	7.5 MeV	0.2332 MeV	0.2332 MeV
Reaction	$^{37}\text{Cl}(\nu_e, e^-)^{37}\text{Ar}$	$\nu_e \text{H} \rightarrow \nu_e \text{H}$	$^{71}\text{Ga}(\nu_e, e^-)^{71}\text{Ge}$	$^{71}\text{Ga}(\nu_e, e^-)^{71}\text{Ge}$
Depth [mwe]	4100	2700	3300	4700
$\tau_{1/2}$ (product)	35 days	n/a	11.4 days	11.4 days
Exp. Rate	$2.55 \pm 0.17 \pm 0.18$	1.0	$79 \pm 10 \pm 6$	74^{+13+5}_{-12-7}
No Diff	$7.0^{+0.9}_{-1.0}$	1.64	126^{+6}_{-6}	126^{+6}_{-6}
Diff	$9.3^{+1.2}_{-1.4}$	2.22	137^{+8}_{-7}	137^{+8}_{-7}

Table 1.3: Summary of features of solar neutrino experiments and their rates [49] relative to the BP95 model [2] with and without helium and heavy element diffusion. Note that measured and predicted rates (with and without diffusion) for the geochemical experiments are in SNU's, while the Kamiokande rates are relative to the BP95 model.

1.3.1 The Homestake ^{37}Cl Experiment

The Experiment

Construction of the ^{37}Cl experiment began in 1965 in the Homestake Gold Mine in Lead, South Dakota, and it has been running almost continuously since 1970. The mine is at a depth of 1478 m, or 4100 mwe (metres of water equivalent). It consists of a large tank containing $3.8 \times 10^5 \text{ l}$ of C_2Cl_4 (perchloroethylene) liquid, with a total mass of about 615 tonnes and containing 2.19×10^{30} ^{37}Cl atoms. Solar neutrinos produce about 0.5 atoms per day through the reaction $^{37}\text{Cl} + \nu_e \rightarrow ^{37}\text{Ar} + e^-$.

The threshold for this reaction is $E_{th} = 0.814 \text{ MeV}$ making it mainly sensitive to the ^8B and ^7Be neutrino fluxes, but not the pp and pep fluxes as shown in figure 1.10. The ^{37}Ar produced in the detector has a half life of about 35 days and decays by electron capture, the reverse of the reaction above. While there are many excellent reviews on this experiment, what follows is based on those by Bahcall [26], Davis and Cox [47], and Rowley, Cleveland and Davis [48]. Recent results were presented at Neutrino 94 by Cleveland et. al. [49].

Although the experimental procedure has been refined over the years to reduce backgrounds, the basic method has endured. A typical run begins by adding a known quantity (normally about 0.2 cm^3) of either ^{36}Ar or ^{38}Ar , alternating each run. This stable carrier isotope is used to monitor the efficiency of argon removal from the tank. The tank is then exposed for a period of time, usually on the order of one to three months.

After exposure the tank is pumped with $4 \times 10^5 \text{ l}$ of He gas which removes the argon from the C_2Cl_4 . The gas then passes through a condenser, a molecular sieve, and finally a charcoal trap which is cooled to 70 K. This process removes about 95 % of the argon and collects it in the charcoal. The trap is heated to remove the argon gas and after its volume has been measured, it is combined with low tritium methane gas and placed in a proportional counter to measure the ^{37}Ar .

The two major sources of background in the experiment are high energy interactions caused by cosmic ray muons and fast neutrons produced by uranium decays in the rock walls of the mine. Background events from radioactive uranium and thorium have been removed with H_2O shielding and cosmic ray neutrino interactions have been determined to be negligible.

Results and Discussion

The most recent results published for the chlorine experiment [49] find a neutrino production rate of $2.55 \pm 0.17 \pm 0.18 \text{ SNU}$, which becomes $2.55 \pm 0.25 \text{ SNU}$ when the uncorrelated errors are combined. This compares to a predicted rate of $9.3^{+1.2}_{-1.4} \text{ SNU}$ predicted by BP95 [2]. This difference between the Homestake experiment and the SSM was the first signal of a solar neutrino problem.

Direct calibration of the Homestake experiment with a neutrino source has not been performed to date. There was a proposal in the 1970's to produce a ^{65}Zn source at a nuclear reactor, but the experiment was found to be prohibitively expensive.

There was also some speculation based on limited statistics during the 1980's that there was an anticorrelation between the solar neutrino rates measured by the Homestake experiment and the number of sunspots on the solar surface. Bahcall et. al. [50] demonstrated that the effect was dependent on how the errors were measured, which was a clear inconsistency. It was again tested in the early 1990's when the sunspot number increased from a minimum to a maximum. Neither Homestake nor the Kamiokande experiment [51], which provides real time neutrino data, measured any effect.

1.3.2 The Kamiokande Water Cherenkov Experiment

The Experiment

The Kamiokande detector is located at a depth of 1000 m (2700 mwe), in a mine in Kamioka, Japan. It consists of a large tank containing 2,140 tonnes of water, 680 tonnes of which are used as a fiducial mass for solar neutrino measurements. The water is viewed by 948 photomultiplier tubes (PMTs) on a 1 m×1 m grid which provide about 20 % coverage of the inner surface. The detector has an anticounter layer which consists of 123 outward facing PMTs which monitor background effects. The following review is based on papers by Bahcall [26], Nakamura [52], and Hirata et. al. [53] and [54], with the latter being the most complete review.

The Kamiokande experiment began in 1983 to measure the proton lifetime, and was upgraded to Kamiokande II in 1987 in order to record solar neutrinos. It took 1040 live days of data, and was subsequently upgraded to Kamiokande III which took an additional 700 days of data after 1990.

Neutrinos are detected by elastically scattering with the 2.27×10^{32} electrons in the detector in the reaction $\nu + e \rightarrow \nu' + e'$. After collision, (if the electron is travelling faster than the speed of light in water), a cone of Cherenkov light is produced. This light is

picked up by the PMTs and the opening angle of the cone determines the energy of the electron. The cross section for neutral current interactions is about one sixth that of charged current interactions, so ν_μ 's and ν_τ 's produce fewer events than ν_e 's.

In addition, the direction of the neutrino is correlated with that of the electron and for elastic scattering,

$$\cos(\theta_e) = \frac{1 + m_e/E_\nu}{(1 + 2m_e/T_e)^{1/2}} \quad (1.14)$$

where E_ν and T_e are the energy of the neutrino and electron respectively. From this, Kamiokande confirmed the neutrinos do originate from the direction of the sun. The threshold of the detector has gradually decreased to about 7.0 MeV (see figure 1.10), but it is only sensitive to the ^8B and *hep* neutrinos, the latter having a very small flux.

A major upgrade to the detector has taken place and *SuperKamiokande* began taking data earlier this year. The detector increased in size to 50,000 tonnes total, providing a fiducial mass of 22,000 tonnes for solar neutrino experiments [55]. A total of 11,200 PMTs were placed in an array in the detector, and the energy threshold decreased to about 6.5 MeV. The anticipated event rate is about 100 times greater than Kamiokande.

There are three major backgrounds in the detector which can mimic solar neutrino events: radioactivity from heavy elements such as radon and uranium in the water, photons coming from the rock surrounding the detector, and spallation products from interactions with cosmic ray muons. Steps have been taken to reduce these backgrounds and determine their rates. Directional information is also very useful because backgrounds are isotropic while the solar signal has a definite source.

The detector water was kept hermetically sealed and heavy metals and radon gas are removed using ion exchangers and a degasification system reducing uranium and radon in the system to negligible levels. The detector is also covered with a black plastic sheet and a layer of water surrounds the central part (or fiducial volume) of the detector where the

neutrino signal is measured. Anticounter PMTs veto photons which come from the outer part of the detector towards its centre and, combined with the shielding reduce these events to between one and two per day. Spallation products of high energy cosmic ray muons which interact with oxygen typically include ^{12}B and ^{12}N which β -decay producing photons picked up by the PMTs. However these decays have lifetimes on the order of tens of milliseconds, so they can be correlated both temporally and spatially with muon tracks and cascade showers to discriminate them from signal events.

Energy calibration is done by comparing three known photon sources: an external Ni source introduced into the detector, the known spectrum of cosmic ray muons stopping in the detector, and decays from ^{12}B and ^{12}N spallation products. This combination calibrates the energy within about 3 %.

The measured flux of ^8B events above 7.5 MeV is $3.0 \pm 0.41 \pm 0.35 \text{ cm}^{-2}\text{s}^{-1}$, which corresponds to only 45 % of the flux predicted by BP95 [2]. Preliminary results from the first 306.3 days at SuperKamiokande show a ^8B flux of $2.44 \pm 0.06^{+0.05}_{-0.09}$ for the flux above 6.5 MeV [56]. This represents about 37 % of the BP95 predicted rate.

Kamiokande has taken real time data over a period where the sunspot number went from a minimum to a maximum and has found no correlation with the neutrino flux, nor have they found evidence for either day/night effects or seasonal/semi-annual variations. By assuming that the ^8B neutrino spectrum is not altered by any effect traversing from the point of production to the earth, the Kamiokande rate implies that ^8B neutrinos should contribute 2.8 SNU to the chlorine experiment.

1.3.3 The Gallex ^{71}Ga Experiment

The Experiment

Neither the Homestake nor the Kamiokande experiment is sensitive to the pp neutrino flux which has a peak energy of $E_{\text{max}} = 0.420 \text{ MeV}$, well below their energy thresholds. However, the pp flux is the most basic reaction in the pp chain and solar models are basically in agreement on its rate. Kuz'man realised in 1966 [57] that gallium is a suitable target for a radiochemical solar neutrino experiment which would detect the pp neutrinos via the reaction $^{71}\text{Ga}(\nu, e)^{71}\text{Ge}$. It has a very low energy threshold $E_{th} = 0.2332 \text{ MeV}$, large cross section and ^{71}Ge has a half life of 11.4 days making it suitable for an experiment.

The Gallex experiment is one of two radiochemical experiments which use ^{71}Ga as a target. It is located in the Gran Sasso Underground Laboratory in central Italy about 6 km from the entrance to a mountain tunnel at an effective depth of 3300 mwe (metres of water equivalent) [58]. It has two large cylindrical tanks (only one of which is in use at any given time), 2 m in diameter and 7 m high. The target consists of 30.3 tonnes of gallium in an 8.13 Molar aqueous solution in HCl. The total mass of the target is 101 tonnes, of which about 12 tonnes is ^{71}Ga .

A typical run begins with the introduction of 1 mg of a stable germanium carrier, alternating between ^{72}Ge , ^{74}Ge , and ^{76}Ge . The tank is then exposed for several weeks, then purged with N_2 gas which removes about 99 % of the germanium in the form of gaseous GeCl_4 . A series of chemical scrubbing processes extracts the germanium and it is converted to GeH_4 which is measured and placed in proportional counters to record the Ge decays [59].

Two major backgrounds have to be considered: process which produce ^{71}Ge and those

that mimic ^{71}Ge decay. Cosmic ray muons create fluxes of protons deep underground producing germanium via $^{71}\text{Ga}(p, n)^{71}\text{Ge}$ and adding about 3.7 ± 1.1 SNU to the experiment. This must be subtracted from raw measurements. Radon gas, ^{222}Rn , which enters the detector from the mine air undergoes a series of three α -decays and two β -decays which are picked up by the proportional counters. Because all five decays occur within about three hours they can be vetoed, introducing about 4% dead time to the proportional counters but reducing the background to 2 ± 1 SNU.

Results and Discussion

On completion of the second phase of the experiment, Gallex II, 30 runs gave a combined results of $79 \pm 10 \pm 6$ SNU from solar neutrinos. The results are based on a total of 148 measured events, 136 of which have been attributed to solar neutrinos. This compares to previous SSM predictions in the 125 – 130 SNU range and 137 SNU for BP95.

Gallex also performed 19 blank runs in which the gallium was not exposed for a significant length of time. They measured a signal of -1 ± 7 SNU which is consistent with the expected null result. The data's maximum likelihood fit to the half life of ^{71}Ge is 17 ± 3 days, while the known result is 16.49 days.

Gallex is also the only solar neutrino experiment to date which has been calibrated with an external neutrino source. A 36 kg sample of chromium enriched in ^{50}Cr , depleted in ^{53}Cr and low in impurities, was exposed to neutrons at the Siloé reactor in Grenoble, France. The irradiated sample was rich in ^{51}Cr which decays by e^- capture:



The two-body chromium decay produces a monoenergetic neutrino with energies 4.26, 4.31, 7.46 or 7.51 MeV in known ratios. In eleven runs ranging in length from 3.35 to 21 days exposure time, the ratio of ^{71}Ge produced in the experiment to that predicted from

the activity was found to be $R = 1.04 \pm 0.12$ [60].

1.3.4 The SAGE ^{71}Ga Experiment

The Experiment

The Soviet-American Gallium Experiment SAGE began taking data in 1990. It is located in a laboratory under Mount Andyrchi in the Caucasus mountains in southern Russia at a depth of 4700 mwe. Like Gallex, SAGE employs a ^{71}Ga target which is converted to ^{71}Ge by neutrino interactions and as such, many of the details and backgrounds are similar.

SAGE consists of eight 2 m^3 teflon-lined vessels, which each hold about 7 tonnes of gallium. Heaters and mixers keep the gallium above its 29.8° melting point, and the experimental procedure is described in detail in the literature [61],[62],[63]. It begins with the introduction of about $700\text{ }\mu\text{g}$ of an isotope of Ge (other than ^{71}Ge) in the form of a GaGe alloy, followed by exposure for periods ranging from three to six weeks. The extraction begins with the addition of HCl , H_2O_2 and water to the tanks to remove the germanium, followed by a procedure similar to that used in Gallex to reduce it into a manageable volume. The final product of the extraction, GeH_4 gas, is mixed with Xe and placed in proportional counters. The extraction procedure is about 80 % efficient.

Backgrounds in the experiment are the same as those in Gallex, the main one being external protons which produce germanium by $^{71}\text{Ga}(p,n)^{71}\text{Ge}$. Detector shielding, use of low activity materials, a NaI coincidence/anticoincidence detector and cuts made to the data combine to reduce backgrounds to less than 0.025 events per day.

Results and Discussion

The SAGE experiment began taking data in the middle of 1990, but several problems with the equipment emerged. Data were lost or considered unreliable as a result of instabilities with the electronics, vacuum accidents, counter failures, contamination from radon and ^{68}Ge , and the theft of an unknown quantity of the target gallium [64]. Early results were very low leading to questions about the reliability of the experiment as the rate measured based on the 1990 data was $20^{+15}_{-20} \pm 32$ SNU.

Throughout 1990, problems with the detector were gradually rectified and its reliability increased. The solar neutrino rate measured by SAGE for the 1990-92 data is 74^{+13+5}_{-12-7} SNU [65], which is in agreement with the results from Gallex. Future plans for the detector are to continue to take measurements in order to increase its statistical accuracy, and there are plans to do a direct calibration of the detector using a ^{51}Cr source.

1.3.5 The Solar Neutrino Problem Almost Independent of the Standard Solar Model

The solar neutrino problem was traditionally thought of as the discrepancy between the experimental data and the SSM. However, recent calculations have shown that the different experiments are not in agreement. Bahcall [66] has argued that there are two solar neutrino problems: the incompatibility of the ^{37}Cl and Kamiokande results and the low counting rates in the gallium experiments.

Kamiokande measures the high energy region of the ^8B flux. If it is assumed that no energy dependent mechanism affects those neutrinos, then it provides a measurement of the ^8B flux. That value can then be used to determine how many ^8B neutrinos should be measured by the ^{37}Cl experiment. Kamiokande's result implies that 3.5 ± 0.5 SNU

should be recorded at Homestake, but only 2.55 ± 0.25 SNU are seen, making the two experiments incompatible at level of about 2σ , even if the ${}^7\text{Be}$ neutrinos aren't there.

The gallium experiments do measure the pp neutrinos which have a very strong lower limit on their flux which comes from the solar luminosity—if the pp neutrinos aren't there, then the sun could not be shining as brightly as it is. Using the luminosity constraint, the pp neutrinos alone are able to explain the gallium experiments' signal, not including the solar model independent pep flux or the ${}^8\text{B}$ flux measured by Kamiokande.

Several authors [67] have analyzed the experimental data and compared it to standard and non-standard solar models to highlight these discrepancies. Extending the simplified argument given by Parke [68] to include all neutrino sources and using the newest SSM [2] makes it even more compelling. The analysis makes four assumptions:

- the pp cycle is the dominant source of solar energy,
- the sun is in a quasi-equilibrium a time scale of about 10^6 years,
- neutrinos are not affected propagating from the sun to the detector, and
- the detector cross-sections are well known.

The pp cycle consists of the conversion $4p + 2e^- \rightarrow {}^4\text{He} + 2\nu_e$. The 26.731 MeV of energy liberated is split between the kinetic energy of the neutrinos and the sun in the form of heat. One of the neutrinos converted is either a pp or a pep neutrino, while the second can be any one of pp , pep , ${}^8\text{B}$, ${}^7\text{Be}$, or hep , depending on which of the paths in figure 1.3 is taken. The mean energy taken by these five type of neutrinos is 0.265, 1.442, 0.861, 7.0, and 9.4 MeV respectively. The ratio of the pp to pep neutrinos is given by the relative cross sections and is well understood to be 0.9976 : 0.0024.

The CNO -cycle consists of three possible cycles producing two different neutrinos with energies in the range 1.2 – 1.74 MeV. For simplicity, we will consider only the first of the three cycles which is believed to produce the vast majority of CNO -cycle neutrinos. Note, however, that the argument which follows does not depend on that assumption

because of the similarity in the *CNO*-neutrino energies. In effect, the three cycles are being lumped into one, and the SSM theoretical flux used will be from ^{13}N neutrinos.

Using the different possible paths for producing neutrinos, the quasi-equilibrium solar luminosity L_{\odot} gives the following constraint:

$$\begin{aligned} \frac{L_{\odot}}{4\pi R_{AU}} = & [(0.9976)(25.0 \text{ MeV}) + (0.0024)(23.8 \text{ MeV})] \Phi^{pep} + \\ & [(0.9976)(19.5 \text{ MeV}) + (0.0024)(18.3 \text{ MeV})] \Phi^{8B} + \\ & [(0.9976)(25.6 \text{ MeV}) + (0.0024)(24.4 \text{ MeV})] \Phi^{7Be} + \\ & [(0.9976)(17.1 \text{ MeV}) + (0.0024)(15.9 \text{ MeV})] \Phi^{hep} + \\ & (13.1 \text{ MeV}) [\Phi^{pp} - \Phi^{pep} - \Phi^{8B} - \Phi^{7Be} - \Phi^{hep}] + (23.8 \text{ MeV}) \Phi^{CNO} \end{aligned} \quad (1.16)$$

where $L_{\odot} = 3.844 \times 10^{33} \text{ erg/s}$ and $R_{AU} = 1.496 \times 10^{13} \text{ cm}$. Each pair of terms in the first four lines has one term for the energy produced with a *pp* neutrino and one with a *pep* neutrino. The energy in the *pp* term in the last line is divided by two because two neutrinos are produced, and the *CNO* term uses neutrino energies of the upper cycle in figure 1.6.

Defining the ratio of the actual neutrino fluxes to those given by the BP95 model $\varphi^i = \Phi^i / \Phi_{BP95}^i$, the luminosity constraint can be written as follows:

$$1 = 1.95 \times 10^{-3} \varphi^{pep} + 4.97 \times 10^{-5} \varphi^{8B} + 7.55 \times 10^{-2} \varphi^{7Be} + \quad (1.17)$$

$$5.67 \times 10^{-9} \varphi^{hep} + 0.908 \varphi^{pp} + 1.72 \times 10^{-2} \varphi^{13N} \quad (1.18)$$

Computer programs which will be discussed in the next chapter determine the contribution to the total rate from each source, for each of the three neutrino experiments using the BP95 fluxes (and assuming they do not change as they propagate to earth). The results are:

$$S_{Cl}^{th} = 6.86 \varphi^{8B} + 1.62 \varphi^{7Be} + 0.206 \varphi^{pep} + 0.532 \varphi^{13N} + 4.27 \times 10^{-3} \varphi^{hep} \quad (1.19)$$

$$S_{Ga}^{th} = 16.0\varphi^{8B} + 37.8\varphi^{7Be} + 2.89\varphi^{pep} + 10.1\varphi^{13N} + 8.35 \times 10^{-3}\varphi^{hep} + 78.7 \quad (1.20)$$

$$S_{Kam}^{th} = \Phi^{8B} + 1.28 \times 10^{-5}\Phi^{hep} \quad (1.21)$$

where the ^{37}Cl and ^{71}Ga rates are given in SNU, and the Kamiokande results are normalized so that the Φ^{8B} coefficient is equal to unity. The luminosity constraint has been used to remove the φ^{pp} term from S_{Ga}^{th} . The results are then compared to the best experimental results, with their statistical and systematic errors combined in quadrature:

$$S_{Cl}^{ex} = 2.55 \pm 0.25 \text{ SNU} \quad (1.22)$$

$$S_{Ga}^{ex} = 74 \pm 9.5 \text{ SNU} \quad (1.23)$$

$$S_{Kam}^{ex} = (0.51 \pm 0.072) \Phi_{BP95}^{8B} \quad (1.24)$$

Because the *hep* coefficients in equations 1.19 to 1.21 are about four orders of magnitude smaller than the largest term in the radiochemical experiments they are dropped. They are too small to be relevant and their contribution in these equations would only strengthen the arguments to follow (but by a negligible amount). The *hep* contribution is also dropped from S_{Kam}^{th} because the coefficient is $O(10^{-5})$ that of the ^8B term. Combining the theoretical and experimental results yields:

$$6.86\varphi^{8B} + 1.62\varphi^{7Be} + 0.206\varphi^{pep} + 0.532\varphi^{13N} = 2.55 \pm 0.25 \quad (1.25)$$

$$16.0\varphi^{8B} + 31.9\varphi^{7Be} + 2.74\varphi^{pep} + 8.71\varphi^{13N} = -4.65 \pm 9.5 \quad (1.26)$$

$$\varphi^{8B} = 0.51 \pm 0.072 \quad (1.27)$$

Substituting φ^{8B} from the third of these equations into the first shows the inconsistency between the Kamiokande and ^{37}Cl results discussed by Bahcall [66] because even with $\varphi^{7Be} = \varphi^{pep} = \varphi^{13N} = 0$, the LHS of the equation would be much larger than the RHS. The second problem identified by Bahcall results from the negative value on the

RHS of the second equation especially when the ^8B neutrinos seen by Kamiokande are included, although this effect is not as pronounced.

One can then look for the best fit to the experimental data using the parameters $\varphi^{^8\text{B}}$ and $\varphi^{^7\text{Be}}$ subject to the constraint $\varphi^{^7\text{Be}} \geq 0$. Three different cases will be considered: (i) $\varphi^{pep} = \varphi^{^{13}\text{N}} = 0$, (ii) $\varphi^{pep} = 1$ and $\varphi^{^{13}\text{N}} = 0$, and (iii) $\varphi^{pep} = \varphi^{^{13}\text{N}} = 1$. The first case is the most conservative effort to try explain the lower than expected experimental results independent of the SSM. The second case is almost as conservative, since the pp and pep fluxes are fixed by the luminosity constraint and are therefore almost independent of the details of the solar model given that the relative size of the cross sections for the two reactions are quite well known. The last case will evaluate at what level the experimental results differ with the SSM.

A maximum likelihood estimate of the parameters for each of the three cases above is given by minimizing the parameter χ^2 which is defined by:

$$\chi^2 = \sum_{i=Cl, Ga, Kam} \left[\frac{S_i^{ex} - S_i^{th}}{\sigma_i} \right]^2 \quad (1.28)$$

Figure 1.11 shows contours of constant χ^2 at intervals one standard deviation apart as a function of $\varphi^{^8\text{B}}$ and $\varphi^{^7\text{Be}}$. The standard model with 3σ errors is also shown on the plot, as well as the relative dependence of the two fluxes on the sun's central temperature. In (a), the Homestake-Kamiokande plot rules out the SSM at the 3σ level, even *with* the central temperature at its optimal level *and* the pep and CNO -cycle neutrinos arbitrarily excluded. A similar plot in (b) with Gallex/SAGE and Homestake leads to a similar conclusion at a level of about 2.25σ and in (c), the Kamiokande and Gallex/SAGE data together exclude such a model at greater than 3σ . These results imply that any pair of experiments rules out an unrealistic SSM in which the sun's central temperature is varied to a best fit value, contrary to the solar oscillation data, and the pep and CNO fluxes are removed.

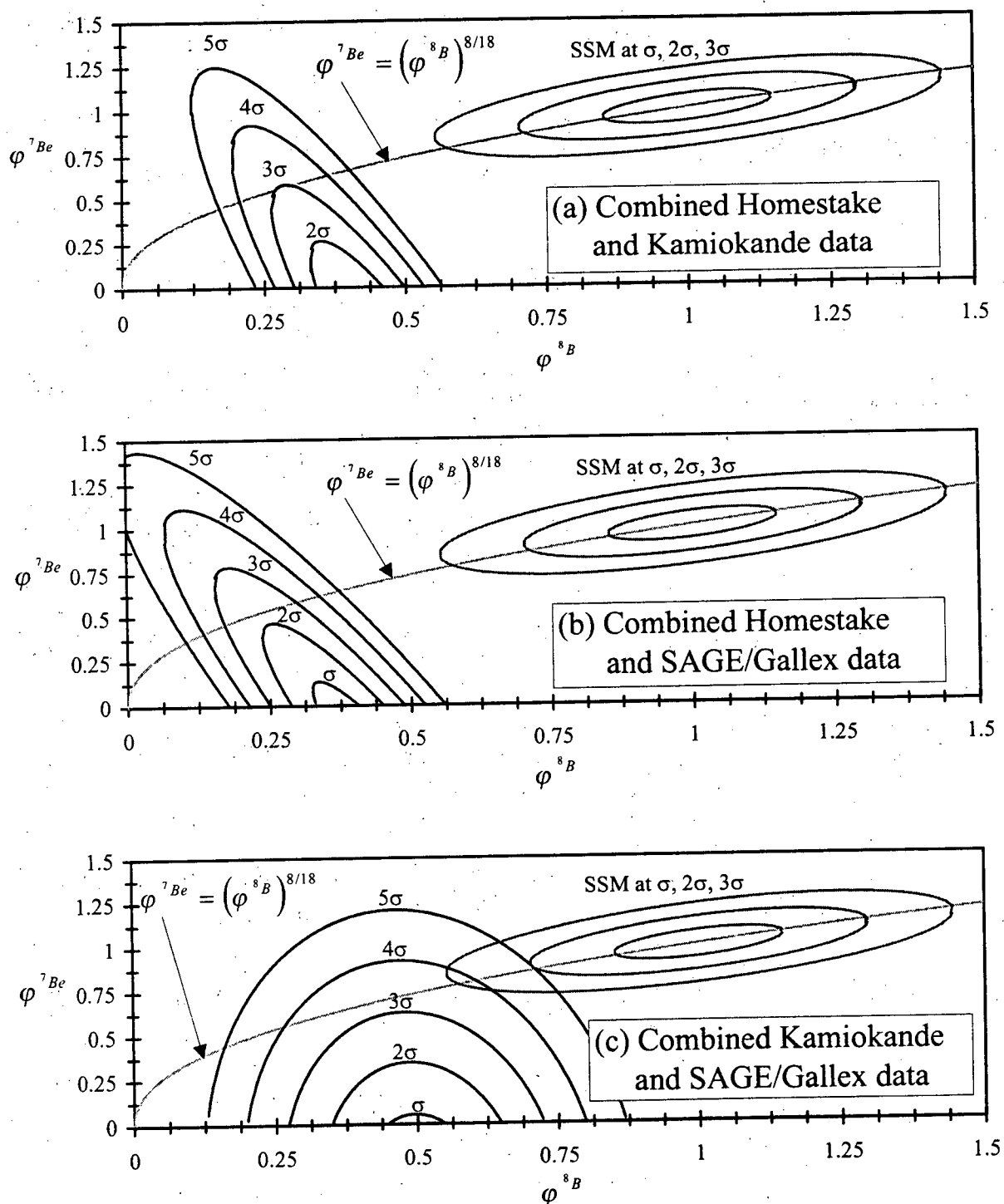


Figure 1.11: Experimental constraints on ϕ^{Be} and ϕ^B of (a) Homestake and Kamiokande data, (b) Homestake and SAGE/Gallex data, and (c) Kamiokande and SAGE/Gallex data. Three standard deviations from the SSM results are shown, as well as the effect on the ratio of the two fluxes resulting from changes in the central temperature of the sun.

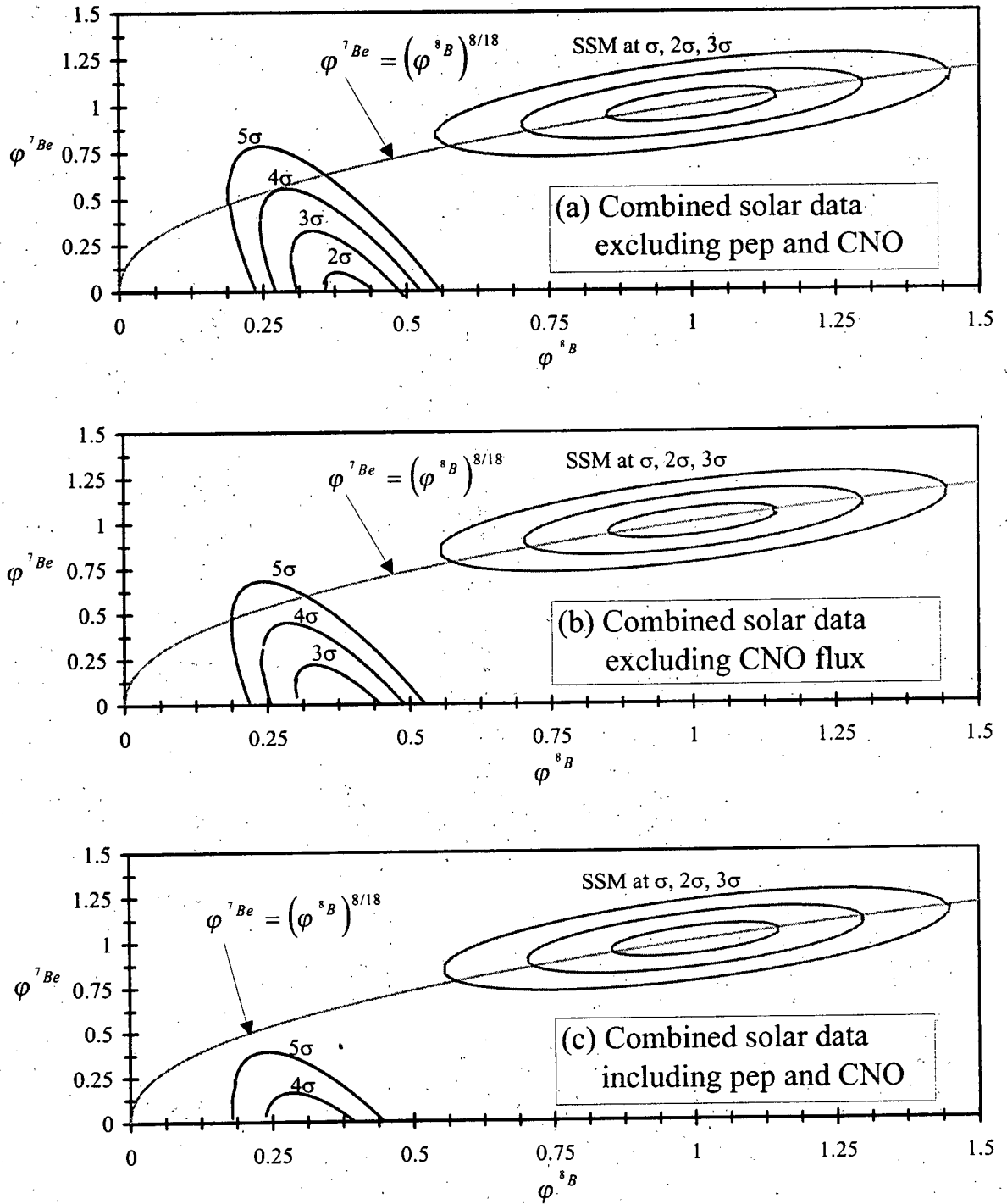


Figure 1.12: Experimental constraints on $\phi^{7\text{Be}}$ and $\phi^{8\text{B}}$ of combined Homestake, Kamiokande and SAGE/Gallex data. Three standard deviations from the SSM results are shown, as well as the effect on the ratio of the two fluxes resulting from changes in the central temperature of the sun. Figure (a) excludes *pep* and *CNO* fluxes, (b) includes *pep* fluxes but excludes *CNO* fluxes, and (c) includes *pep* and *CNO* fluxes predicted by BP95.

Figure 1.12 compares the same contours, except with all three experiments combined. In (a), the same restrictive assumptions above are made, and the experiments rule out a SSM with arbitrary central temperature at a level of 4σ . In (b), the *pep* neutrinos are included—their flux is proportional to the *pp* flux and not the details of the SSM, and the experimental fits are poorer. If the *CNO*-cycle neutrinos are included at SSM levels, then the experiments rule out any type of SSM with a best fit temperature at the 5σ level.

Figure 1.12(b) also shows that the experiments rule out $\varphi^{7Be} \geq 0$ at 2σ for *any* solar model, and any SSM-like model where the temperature varies at 4σ . It should also be noted that the central temperature in the sun is an important determinant of solar oscillation frequencies. The SSM model fits the experimental data well, while models with different central temperatures do not.

1.4 The Atmospheric Neutrino Anomaly

Two large underground water Cherenkov detectors, Kamiokande and IMB, began taking data in the early 1980's in order to measure the lifetime of the proton. At the time, theoretical models which unified the strong force with the electroweak predicted the proton would decay with a time constant on the order of 10^{30} years. While these experiments did not see such a decay and could only set lower limits on the proton lifetime, they did look at other phenomena.

Among them, was the observation of neutrinos produced by cosmic ray interactions in the upper atmosphere. In particular, they found that flux of *e*-type neutrinos (ν_e and $\bar{\nu}_e$) was larger than expected relative to the flux of μ -type neutrinos (ν_μ and $\bar{\nu}_\mu$), and Kamiokande [69] and IMB [70] collected several years worth of data. Three other experiments have also published results. While the statistical significance of the effect is

still up in the air, the disagreement between the predicted and measured fluxes is now referred to as the Atmospheric Neutrino Problem (hereafter the ANP).

1.4.1 Predicting the Flux of Neutrinos from Cosmic Ray Interactions

Many independent groups have modelled the interactions of cosmic rays in the upper atmosphere [71],[72],[73],[74]. The calculations begin by estimating the content, flux and spectra of cosmic rays hitting the upper atmosphere. These are dependent on several factors, including the rate of solar activity and the geomagnetic latitude. The models also estimate the content of the upper atmosphere itself.

Then, using measured nuclear cross sections, Monte Carlo programs simulate the interactions of the cosmic rays with the atmosphere and follow the reaction chains to determine the final neutrino fluxes they ultimately produce. The majority of reactions eventually end up with nuclei, nucleons, pions and kaons. These latter two particles decay to produce a muon and muon type neutrino, either $\pi^+, K^+ \rightarrow \mu^+ + \nu_\mu$ or $\pi^-, K^- \rightarrow \mu^- + \bar{\nu}_\mu$. Some kaons decay to pions, which follow as above. The muons, in turn, decay to electrons producing one μ -type and one e-type neutrino (via $\mu^+ \rightarrow e^+ + \nu_e + \bar{\nu}_\mu$ or $\mu^- \rightarrow e^- + \bar{\nu}_e + \nu_\mu$).

Naively, from the above analysis, one expects that the ratio of μ -type to e-type neutrinos arriving on earth would be 2 : 1. In the more advanced models the ratio turns out to be closer to 1.8 : 1, largely because of the effect of muon polarisation. In addition to the ratio, however, the models calculate the absolute fluxes of neutrinos produced by cosmic rays.

The different analyses only agree on the absolute rates to within about 30 %, depending on the energy. The source of the discrepancies are known—the major difference is how each model treats the production of low energy pions in collisions between protons and nuclei in atmosphere [75]. In spite of differences in the absolute fluxes, the ratio

Experiment	Method	Data Size [kt-yr]	Double Ratio $(R_{\mu/e})_{data} / (R_{\mu/e})_{MC}$
Kamiokande	Water Cherenkov	4.92	$0.60^{+0.07}_{-0.06} \pm 0.05$
SuperKamiokande	Water Cherenkov	300 <i>days</i>	$0.635 \pm 0.033 \pm 0.010 \pm 0.052$
IMB	Water Cherenkov	7.7	$0.71 \pm 0.05 \pm 0.11$
Soudan 2	Iron calorimeter	1.52	$0.72 \pm 0.19^{+0.05}_{-0.07}$
Frejus	Iron calorimeter	1.56	$1.06 \pm 0.18 \pm 0.15$
NUSEX	Iron calorimeter	0.74	$0.96^{+0.32}_{-0.28}$

Table 1.4: Measurements of the double ratio of μ -type to e-type neutrino fluxes by six experiments. Errors are quoted as statistical then systematic, and SuperKamiokande quotes statistical, statistical—Monte Carlo, and systematic respectively.

of the μ -type to e-type fluxes in the calculations all agree within 5 %, again depending on the energy. With the smaller variance, it is this ratio which is normally used by to compare the calculated fluxes to those measured by underground experiments.

1.4.2 Experimental Measurements of Atmospheric Neutrinos

Besides Kamiokande and IMB, atmospheric neutrino fluxes have been measured by two older experiments Frejus and NUSEX, while the new Soudan 2 detector has released preliminary data. The results from the five different experiments are summarised in table 1.4.

NUSEX and Frejus are two iron calorimeter detectors which, like Kamiokande and IMB, were originally built to measure the proton lifetime. NUSEX (nucleon stability experiment) was a 3.5 *m* cube with an active mass of 150 tons located in the Mont Blanc tunnel in eastern France, and took data from 1982 to 1988 [76]. Frejus was a similar but larger detector located in the Laboratoire Souterrain de Modane in the French Alps [77]. Neither detector found a deviation from the predicted ratio of μ -type to e-type neutrinos, however as the table shows, the statistics are very low. In fact, neither experiment is inconsistent with Kamiokande or IMB.

Both water detectors measure rings of Cherenkov light produced by e^\pm and μ^\pm , typically having energies below 1 GeV, created and stopping in the detector. Depending on the interactions of the leptons, either single- or multi-ring events are observed. By analysing the geometry and intensity of the Cherenkov light, the single-ring events can be tagged accurately as either μ -type or e -type by comparing the results of several different algorithms. While μ^\pm produce sharp, well-defined rings, e^\pm tend to produce diffuse ones.

The experiments quote the ratio of μ - to e -type events, $(R_{\mu/e})_{data}$, and compare it to the ratio predicted by Monte Carlo programs using the atmospheric neutrino fluxes discussed in the last section, $(R_{\mu/e})_{MC}$. Table 1.4 shows the double ratio $(R_{\mu/e})_{data} / (R_{\mu/e})_{MC}$ which is typically reported in the literature. This reduces the errors in the Monte Carlo generated fluxes, because ratios of the different groups' calculations models agree much better than their absolute fluxes do.

In addition to the fully contained events, both detectors also record stopping and through-going muons which are produced outside the detector but do enter into it. The muons are produced by neutrinos interacting with rock outside the detector in the reactions $\bar{\nu}_\mu + p \rightarrow \mu^+ + n$ and $\nu_\mu + n \rightarrow \mu^- + p$. They tend to come from neutrinos which are higher in energy than the "fully-contained" events which are created and stop in the detectors. While these events are not used in determining the μ - to e -type ratio, they are used to study the atmospheric neutrino flux, and can be used to constrain some of the explanations for the ANP.

Kamiokande has also measured an anomaly in fully-contained events with energies greater than 1 GeV (multi-GeV), and have studied the dependence of the ratio on the zenith angle [78]. They found an anomaly in $(R_{\mu/e})_{data} / (R_{\mu/e})_{MC}$ similar to their earlier (sub-GeV) results as well as a weak angular correspondence. The double ratio is peaked in the downward direction, although the effect is not statistically overwhelming.

The Soudan 2 detector is another iron calorimeter, but is much larger than NUSEX or

Frejus and has different detection techniques. It consists of 224 modules each weighing 4.3 tons located at a depth of 710 m in the Soudan Underground Mine State Park in Minnesota, USA. Preliminary data presented in table 1.4 was taken between 1989 and 1993 during construction, beginning with 275 tons and ending with the full 963 ton mass [79]. While the data set is not large enough to definitely confirm or oppose the water Cherenkov experiments, future results certainly will be.

Finally, SuperKamiokande has reported some preliminary results based on 300 days of taking data [56]. While the data is based on a small time period, it has more events than the Kamiokande results. The ratio $(R_{\mu/e})_{data} / (R_{\mu/e})_{MC}$ agrees well with previous measurements in both the sub-GeV and multi-GeV ranges, and there is again weak indication of distortion in the zenith angle dependence. Over the coming years, the statistical significance of these results will increase and SuperKamiokande will be able to bin the data by energy to look for spectral distortions.

1.4.3 Discussion

If taken at face value, the atmospheric neutrino results clearly imply physics beyond the standard model. However, some questions about the experiments and statistical significance of the results still need to be worked out.

Initially it was noted that the water Cherenkov detectors saw an anomaly in the double ratio $(R_{\mu/e})_{data} / (R_{\mu/e})_{MC}$ while the iron calorimeters, albeit with very low statistics, did not. Once it has been running for a few years Soudan 2 will resolve this difference. Early indications appear to show an effect similar to that IMB and Kamiokande, but the data so far only shows an anomaly at about 1.5σ .

It has also been suggested that the over-abundance of e-type neutrinos is the result of backgrounds that were not accounted for. Ironically, there was an early suggestion

[80] that the detectors saw additional neutrinos from the proton decay reaction $p \rightarrow e^+ + \nu_e + \bar{\nu}_e$, although this was ruled out [78]. More recently, it was suggested that neutrons enter the detectors and produce pions which mimic e-type neutrino events [81]. Kamiokande has argued that they have accounted for this background in their analysis, and Soudan 2 has studied neutrons entering the detector and concludes that they could not account for the anomalous double ratio results seen by the water detectors.

A second criticism of the statistical significance of the calculations. Perkins studied the models which generate the neutrino fluxes used to compute $(R_{\mu/e})_{MC}$ and argued that the errors have been underestimated. In particular, the spectrum of pions and kaons with large transverse momentum have not been accurately measured, and large extrapolations are built into the calculations. He also argued that there are still significant discrepancies on the order of 15% in vertical muon fluxes measured at sea level, which are used to normalise the neutrino flux calculations. Finally, he suggested that the neutrino cross sections for upward going muons measured by Kamiokande and IMB may not have been estimated correctly, adding an error of 6 – 12%. The conclusion of his paper is that the errors associated with calculations of the atmospheric neutrino fluxes may have been underestimated, thus reducing the statistical significance of the anomaly [82].

More recently, Fogli and Lisi have criticised the statistical analysis of the experimental results [83]. They point out that while taking the ratio of μ -type to e-type neutrinos reduces the errors in the theoretical neutrino flux calculations, it changes the type of distribution of the statistical variate. While the sum, difference and product of two gaussian variates is again gaussian, the ratio of two gaussian variates is described by a Cauchy distribution, and the tail of a Cauchy distributed variate is highly non-gaussian.

Fogli and Lisi went on to carefully reanalyse the atmospheric neutrino data using the absolute neutrino fluxes. They found that the Kamiokande sub-GeV, IMB and Soudan 2 data imply anomalies from the theoretical neutrino fluxes at statistical levels of 3σ , 2σ

and 1σ respectively. As a comparison, the Kamiokande sub-GeV data using the ratio of μ -type to e -type neutrinos, $R_{\mu/e} = 0.61 \pm 0.075$ would erroneously suggest an ANP at a level of more than 5σ .

New measurements of the muon fluxes at different heights in the atmosphere will help refine the theoretical calculations of atmospheric neutrino fluxes in the coming years. The new underground iron calorimeter Soudan 2, with different systematics than Kamiokande and IMB, will confirm (or refute) the anomaly measured by the water Cherenkov detectors. Combined with the large volume SuperKamiokande detector now on line, it will also increase the accuracy of measurements of the atmospheric neutrino fluxes, and hopefully settle the question of the anomaly and its statistical significance once and for all.

Chapter 2

Neutrino Oscillations with Two Flavours

2.1 Introduction

Many different suggestions have been made over the years to account for the solar neutrino problem, some which proposed changing the solar models while others involved new neutrino properties. A fairly obvious extension to the Standard Model of Particle Physics (SMPP) is to allow the neutrinos to have a mass. All other elementary fermions do, and the only reason neutrinos have been considered massless is that to date, no one has been able to measure one. The formalism also provides a natural explanation for the atmospheric neutrino anomaly which was measured years later. The masses that are implied by the SNP and ANP are much less than current experimental limits for direct measurements, so they do not disagree with any existing results.

Upon accepting neutrino mass, it is no longer possible to use linear combinations of the weak eigenstates to diagonalise the Hamiltonian: the weak eigenstates may differ from the mass eigenstates. A similar effect has long been known in the quark sector. It leads to mixing of neutral kaons and B mesons, CP violating effects and many other interesting phenomena, some of which can be expected in the lepton sector with massive neutrinos. But because the neutrinos do not interact as readily as the quarks, the effects are much more difficult to measure.

In this chapter, two massive neutrinos and their effect on both long baseline oscillation experiments and solar neutrinos will be studied. Section two will introduce the

notation used to describe neutrino oscillations in the simple case of two neutrino flavours two different ways: the standard approach and that originally derived by Mikheyev and Smirnov. Section three will apply the theoretical results to long baseline neutrino oscillation experiments using a simulated neutrino beam, and make quantitative statements about what regions of parameter space could be studied with different configurations of detectors. Section four will use the neutrino mass formalism to derive limits on parameters based on the solar neutrino experiments, for both vacuum and MSW enhanced neutrino oscillations.

2.2 Theoretical Background

2.2.1 Neutrino Oscillations in Vacuum

The suggestion that neutrinos may have nonzero mass and undergo oscillations was made as early as 1968 [84]. Although no direct experimental evidence to date has found evidence for nonzero masses, the charged leptons and quarks are all massive Dirac particles. Limits on the masses of the three neutrino flavours are $m_{\nu_e} < 10 - 15 \text{ eV}$ with 95% confidence level, $m_{\nu_\mu} < 170 \text{ keV}$ with 90% confidence level, and $m_{\nu_\tau} < 24 \text{ MeV}$ with 95% confidence level [85].

Early work [86] examined the implications of the assumption of nonzero mass, and showed that oscillations can occur between weak eigenstates as they traverse the vacuum. Several excellent reviews exist, including [26] and [87] which define the notation that has become commonplace in the literature.

The mass eigenstates of massive neutrinos will not, in general, coincide with the eigenstates that participate in weak interactions. These two pairs of basis states are then related by a unitary transformation. For a system of two neutrino states it is common to define the mass eigenstates $|\nu_1\rangle$ and $|\nu_2\rangle$, and weak eigenstates $|\nu_\alpha\rangle$ and $|\nu_\beta\rangle$. The

transformation relating them is described by a single parameter, the mixing angle θ_V as follows:

$$\begin{pmatrix} \nu_\alpha \\ \nu_\beta \end{pmatrix} = \begin{pmatrix} \cos\theta_V & \sin\theta_V \\ -\sin\theta_V & \cos\theta_V \end{pmatrix} \begin{pmatrix} \nu_1 \\ \nu_2 \end{pmatrix} \quad (2.1)$$

The time evolution of diagonal mass eigenstates of momentum k is given by:

$$\begin{aligned} i \frac{d}{dt} \begin{pmatrix} \nu_1 \\ \nu_2 \end{pmatrix} &= \begin{pmatrix} \sqrt{k^2 + m_1^2} & 0 \\ 0 & \sqrt{k^2 + m_2^2} \end{pmatrix} \begin{pmatrix} \nu_1 \\ \nu_2 \end{pmatrix} \\ &\approx k \begin{pmatrix} 1 + \frac{m_1^2}{2k^2} & 0 \\ 0 & 1 + \frac{m_2^2}{2k^2} \end{pmatrix} \begin{pmatrix} \nu_1 \\ \nu_2 \end{pmatrix} \end{aligned} \quad (2.2)$$

where the last step is valid in the ultrarelativistic limit $k^2 \gg m_i^2$. It is customary to subtract $[k + (m_1^2 + m_2^2)/4k]$ times the identity from the Hamiltonian (leaving it traceless and changing only the overall phase of the wavefunction) to obtain

$$i \frac{d}{dt} \begin{pmatrix} \nu_1 \\ \nu_2 \end{pmatrix} = \frac{1}{4E} \begin{pmatrix} -\Delta m_V^2 & 0 \\ 0 & \Delta m_V^2 \end{pmatrix} \begin{pmatrix} \nu_1 \\ \nu_2 \end{pmatrix} \quad (2.3)$$

where $\Delta m_V^2 = m_2^2 - m_1^2$ and $E \approx k$ in the high energy limit.

Neutrino oscillations become apparent upon calculation of the probability that a pure $|\nu_\alpha\rangle$ produced at the origin is still a $|\nu_\alpha\rangle$ after travelling a distance L . Combining the equation above with (2.1) determines the time evolution of a weak eigenstate:

$$|\nu_\alpha(t)\rangle = \cos(\theta_V) e^{i \frac{\Delta m_V^2}{4E} t} |\nu_1\rangle + \sin(\theta_V) e^{-i \frac{\Delta m_V^2}{4E} t} |\nu_2\rangle \quad (2.4)$$

One can then calculate the probability that a weak eigenstate $|\nu_\alpha\rangle$ produced at position $L = 0$ will still be a $|\nu_\alpha\rangle$ after traversing a distance L . The probability is given by calculating $|\langle \nu_\alpha(t) | \nu_\alpha(0) \rangle|^2$ which is easily shown to be:

$$P(\nu_\alpha(0) \rightarrow \nu_\alpha(L)) = 1 - \sin^2(2\theta_V) \sin^2 \left(1.27 \frac{\Delta m_V^2 L}{E} \right) \quad (2.5)$$

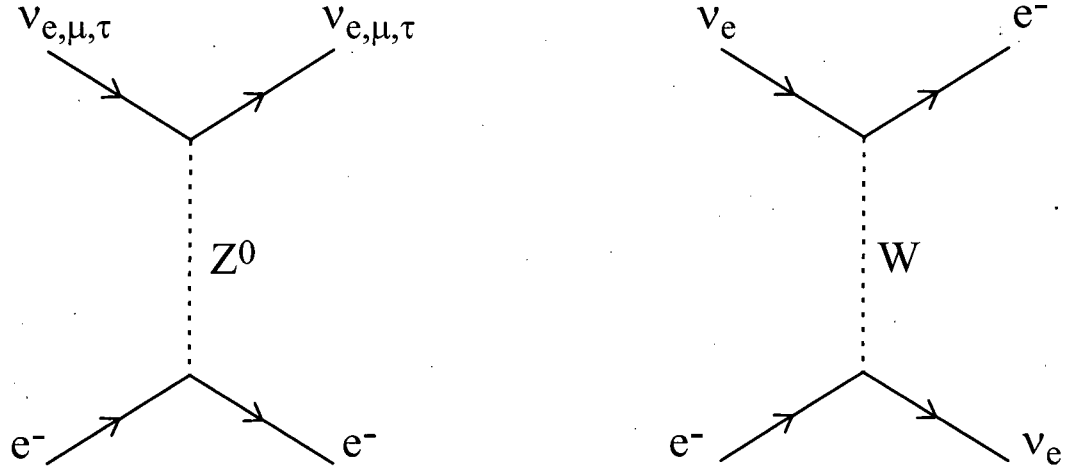


Figure 2.1: Feynman diagrams showing weak current scattering of neutrinos off electrons. At left, all three neutrino flavours participate in neutral current scattering, while the charged current channel on the right is open only to electron neutrinos.

where the constant 1.27 is equal to $(4\hbar c)^{-1}$ expressed in units $[\text{GeV}][\text{eV}]^{-2}[\text{km}]^{-1}$ which prove useful for analyzing the oscillations of typical accelerator produced neutrino beams.

It is also common to write the Hamiltonian in the weak eigenbasis by applying the transformation (2.1) to equation (2.3) to obtain

$$i \frac{d}{dt} \begin{pmatrix} \nu_\alpha \\ \nu_\beta \end{pmatrix} = \frac{\Delta m_V^2}{4E} \begin{pmatrix} -\cos(2\theta_V) & \sin(2\theta_V) \\ \sin(2\theta_V) & \cos(2\theta_V) \end{pmatrix} \begin{pmatrix} \nu_\alpha \\ \nu_\beta \end{pmatrix} \quad (2.6)$$

2.2.2 Neutrino Oscillations in Matter

The next major development in neutrino came with Wolfenstein's realisation [88],[89] that when electron neutrinos pass through matter the H_{ee} component of the Hamiltonian acquires an additional term. Electron neutrinos can scatter off the electrons in matter via *both* the charged *and* neutral currents, whereas muon and tau neutrinos have only neutral current interactions as shown in figure 2.1.

The standard model contribution to the Hamiltonian from charged current part of

the interaction is given by [87]

$$\begin{aligned} H_{ee} &= \frac{G_F}{\sqrt{2}} \bar{e} \gamma^\mu (1 - \gamma^5) \nu \bar{\nu} \gamma_\mu (1 - \gamma^5) e \\ &= \sqrt{2} G_F \bar{\nu} \gamma_\alpha \nu \bar{e} \gamma^\alpha e \end{aligned} \quad (2.7)$$

where Fierz reordering and the assumption that all neutrinos are left-handed while electrons are unpolarised is used to obtain the final expression above. For forward scattering the electron momentum is unchanged so only the γ^0 component contributes leaving $H_{ee} = \sqrt{2} G_F N_e$.

Adding this term to the Hamiltonian in the weak eigenbasis and subtracting one half its value times the identity matrix again yields a traceless matrix which has the form:

$$\begin{aligned} i \frac{d}{dt} \begin{pmatrix} \nu_\alpha \\ \nu_\beta \end{pmatrix} &= \frac{\Delta m_V^2}{4E} \begin{pmatrix} -\cos(2\theta_V) + \frac{2\sqrt{2}G_F N_e E}{\Delta m_V^2} & \sin(2\theta_V) \\ \sin(2\theta_V) & \cos(2\theta_V) - \frac{2\sqrt{2}G_F N_e E}{\Delta m_V^2} \end{pmatrix} \begin{pmatrix} \nu_\alpha \\ \nu_\beta \end{pmatrix} \\ &= \frac{\Delta m_M^2}{4E} \begin{pmatrix} -\cos(2\theta_M) & \sin(2\theta_M) \\ \sin(2\theta_M) & \cos(2\theta_M) \end{pmatrix} \begin{pmatrix} \nu_\alpha \\ \nu_\beta \end{pmatrix} \end{aligned} \quad (2.8)$$

The last step writes the equation in a form where the Hamiltonian in matter is identical to that in vacuum, except that the mixing angle and mass squared difference have been modified in matter. The new parameterisation is dependent on the energy E of the neutrino and the number density N_e of the electrons. It is conveniently expressed by defining the quantity

$$D_M = \left[1 - 2 \left(\frac{L_V}{L_e} \right) \cos(2\theta_0) + \left(\frac{L_V}{L_e} \right)^2 \right]^{\frac{1}{2}} \quad (2.9)$$

where the vacuum oscillation length in dimensionful units L_V and neutrino interaction length L_e are given by

$$L_V = 4\pi E \hbar c / \Delta m_V^2 c^4 \quad (2.10)$$

$$L_e = \sqrt{2} \pi \hbar c / G_F N_e \quad (2.11)$$

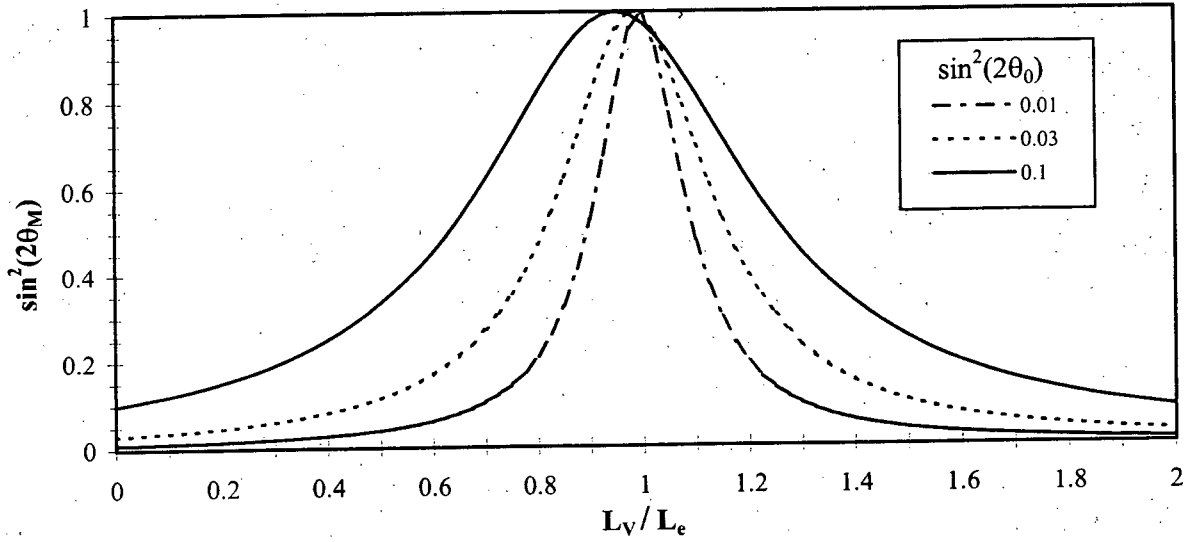


Figure 2.2: Matter enhancement of the neutrino mixing parameter $\sin^2(2\theta_M)$. The resonance occurs when $L_V/L_e = \cos(2\theta_M)$, and its width increases with $\sin^2(2\theta_V)$.

Using these definitions, the mixing parameters in matter can be easily related to those in vacuum using as follows:

$$\Delta m_M^2 = D_M \times \Delta m_V^2 \quad (2.12)$$

$$\sin(2\theta_M) = \frac{\sin(2\theta_V)}{D_M} \quad (2.13)$$

What is notable about the matter oscillations is that there is a resonant density. When $N_e = \frac{\Delta m_V^2 \cos(2\theta_V)}{2\sqrt{2}G_F E}$, then $L_V/L_e = \cos(2\theta_V)$, equation (2.9) reduces to $D_M = \sin(2\theta_V)$ and $\sin(2\theta_M) = 1$ which implies that mixing is maximal.

The matter enhanced mixing angle is illustrated as a function of electron density in figure (2.2), which shows that the width of the resonance increases as $\sin(2\theta_V)$ increases. The behaviour of the two squared masses is shown in figure (2.2). The minimum difference between the masses occurs at resonance, when $(\Delta m_M^2)_{\min} = \sin(2\theta_V)\Delta m_V^2$.

The mixing angle θ_M defined above diagonalises the Hamiltonian and provides a unitary transformation to the effective mass eigenstates in matter. Applying the inverse

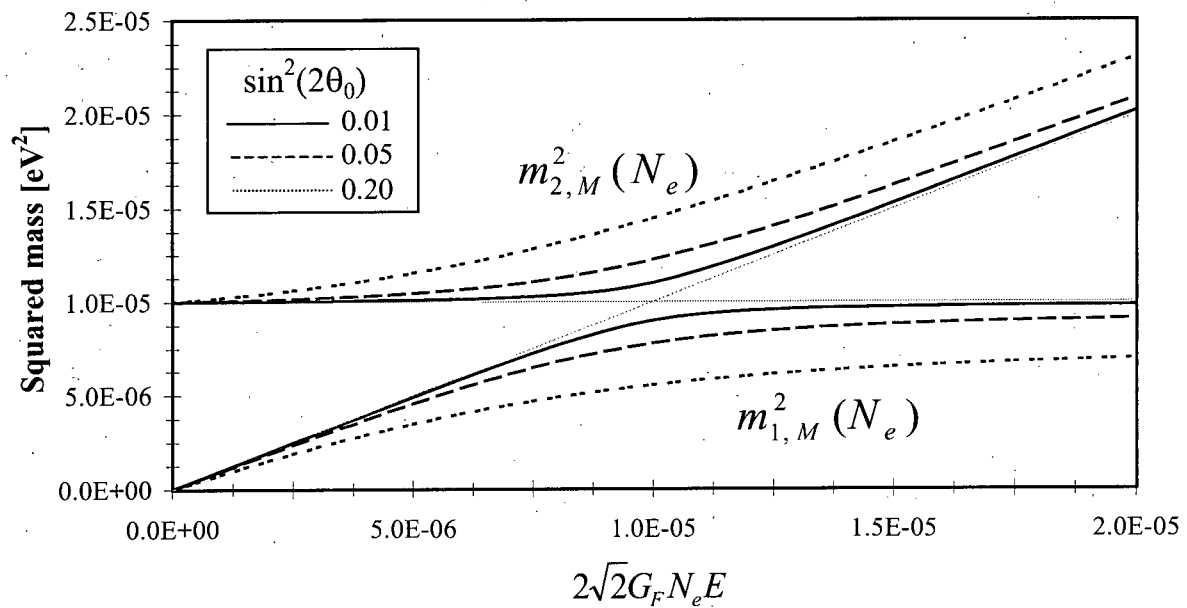


Figure 2.3: Matter enhancement of the mass eigenstates as a function of electron density. Note that the vertical scale has been set so that $m^2_{1,V} = 0$. The masses approach $m^2_{2,V}$ and $m^2_{1,V} + 2\sqrt{2}G_F N_e E$ asymptotically at large density. As $\sin^2(2\theta_V)$ increases, the difference between the masses at resonance increases.

of the analogous transformation in vacuum 2.1, a new basis can be defined as follows:

$$\begin{pmatrix} \nu_{1,M} \\ \nu_{2,M} \end{pmatrix} = \begin{pmatrix} \cos\theta_M & -\sin\theta_M \\ \sin\theta_M & \cos\theta_M \end{pmatrix} \begin{pmatrix} \nu_\alpha \\ \nu_\beta \end{pmatrix} \quad (2.14)$$

In this new basis, the Hamiltonian equation has the same form as it did in vacuum except that the mass squared difference now takes its modified form:

$$i \frac{d}{dt} \begin{pmatrix} \nu_{1,M} \\ \nu_{2,M} \end{pmatrix} = \frac{1}{4E} \begin{pmatrix} -\Delta m_M^2 & 0 \\ 0 & \Delta m_M^2 \end{pmatrix} \begin{pmatrix} \nu_{1,M} \\ \nu_{2,M} \end{pmatrix} \quad (2.15)$$

and the probability that a neutrino produced in the weak eigenstate $|\nu_\alpha\rangle$ which is measured after propagating a distance L through matter at constant electron density is then given by:

$$P(\nu_\alpha(0) \rightarrow \nu_\alpha(L)) = 1 - \sin^2(2\theta_M) \sin^2 \left(1.27 \frac{\Delta m_M^2 L}{E} \right) \quad (2.16)$$

2.2.3 The Mikheyev-Smirnov Approach

In their series of early papers [90],[91],[92], Mikheyev and Smirnov took a different approach to solving the system which is presented here for completeness. They defined two parameters $M(L_V, L_e)$ and $m(L_V, L_e, Ne)$ as follows:

$$2M = \frac{2\pi}{L_V} \sin(2\theta_V) \quad ; \quad m = \frac{2\pi}{L_V} \left(\cos(2\theta_V) - \frac{L_V}{L_e} \right) \quad (2.17)$$

Next they wrote the probability P that a ν_e produced at time $t = 0$ will still be a ν_e at a later time t , and two transition amplitudes as follows:

$$P = \langle \nu_e(t) | \nu_e \rangle \langle \nu_e | \nu_e(t) \rangle \quad (2.18)$$

$$R_1 + iI_1 = \langle \nu_\mu | \nu_e(t) \rangle \quad (2.19)$$

$$R_2 + iI_2 = \langle \nu_\mu | \nu_\mu(t) \rangle \quad (2.20)$$

where the amplitudes have been explicitly broken up into their real and imaginary parts and the time dependence is expressed in the obvious way. Differentiating these quantities with respect to time and using 2.8 above gives a series of equations:

$$\frac{dP}{dt} = -2M(R_2 I_1 + R_1 I_2) \quad (2.21)$$

$$\frac{d^2 P}{dt^2} = 2M^2(R_1^2 + I_1^2 - R_2^2 - I_2^2) + 4Mm(R_1 R_2 + I_1 I_2) \quad (2.22)$$

$$\frac{dR_1}{dt} = -mI_1 + MI_2 \quad ; \quad \frac{dI_1}{dt} = mR_1 - MR_2 \quad (2.23)$$

$$\frac{dR_2}{dt} = MI_1 + mI_2 \quad ; \quad \frac{dI_2}{dt} = -MR_1 - mR_2 \quad (2.24)$$

By taking successively higher order derivatives of these quantities, the amplitude terms can be eliminated, leaving a differential equation for P :

$$m \frac{d^3 P}{dt^3} - \frac{dm}{dt} \frac{d^2 P}{dt^2} + 4m(m^2 + M^2) \frac{dP}{dt} - 2M^2 \frac{dm}{dt} (2P - 1) = 0 \quad (2.25)$$

The initial conditions come from the definitions in 2.18 to 2.20 and are $P(0) = 1$, $\dot{P}(0) = 0$ and $\ddot{P}(0) = -2M^2$. This general form of the equation can be used to calculate neutrino oscillations in a variable density medium. In a fixed density medium, $\frac{dm}{dt} = 0$ and it reduces to

$$\frac{d^3 P}{dt^3} + 4(m^2 + M^2) \frac{dP}{dt} = 0 \quad (2.26)$$

which admits a periodic solution of the form

$$\dot{P}(t) = A \sin\left(\frac{2\pi t}{L_M}\right) + B \cos\left(\frac{2\pi t}{L_M}\right) \quad (2.27)$$

where the matter oscillation length is given by $L_M = 4\pi E \hbar c / \Delta m_M^2 c^4$ in analogy with that in vacuum. Applying two initial conditions determines $A = \sin^2(2\theta_M)$ and $B = 0$. Integrating this solution and including the last initial condition produces a result identical to 2.16 upon applying $t = \frac{L}{c}$:

$$P(t) = 1 - \sin^2(2\theta_M) \sin^2\left(\frac{\pi t}{L_M}\right) \quad (2.28)$$

2.3 Long Baseline Neutrino Oscillations with Two Flavours

Computer codes developed by the author calculated oscillations for neutrinos passing through the earth and displayed the results. Unless otherwise specified, *all* calculations in this section were done with these codes. For fixed densities, exact evaluation of equation 2.16 was possible. However Runge-Kutta methods were also employed to integrate equation 2.8 and take into account the variable density of the earth. Details of the code and the Runge-Kutta methods are given in the next chapter.

2.3.1 Experimental Notes

Early long baseline experiments were based at nuclear reactors which provide copious fluxes of electron antineutrinos [93],[94],[95]. Detectors which measured the reaction $\bar{\nu}_e + p \rightarrow e^+ + n$ were placed at different distances from the source to determine whether the rate drops off as the inverse square of the distance from the detector. The longest baselines for reactor experiments to date are on the order of 100 m, although new ones up to 1 km will be coming on line soon and proposals for lengths as high as 13 km have been made [96].

Reactor-based investigations have the advantage that the neutrino energy is very low, in the range of several MeV which is about three orders of magnitude below typical accelerator-based neutrino energies. This means that it is possible to probe to much lower mass-squared differences because, as is evident from equations (2.5) and (2.16), neutrino oscillations become apparent when $1.27 \frac{\Delta m^2 L}{E}$ is on the order of $\pi/4$.

However such experiments also have several disadvantages. Because nuclear reactors are isotropic sources of antineutrinos, only a fraction of those produced actually enter the detector. The cross-section for the antineutrino reaction $\sigma(\bar{\nu}_l N \rightarrow l^+ X) \approx 3.25 \times 10^{-38} \text{ cm}^2 \frac{E}{\text{GeV}}$ at low energies is less than one half of the corresponding neutrino reaction

$\sigma(\nu_l N \rightarrow l^- X)$. Moreover, the sign of the matter contribution to the Hamiltonian is opposite that of neutrino and as a result, matter suppresses antineutrino oscillations rather than enhancing them.

Several accelerator-based experiments have also been performed to date, while many others have been discussed [97],[98],[99],[100] with baselines ranging from less than one kilometre to substantial fractions of the diameter of the earth. In these experiments, neutrino beams are produced by focusing a high energy particle beam at a target in order to produce copious numbers of secondary hadrons, mostly pions and kaons [101]. Those with positive electric charge are then focused into a well collimated beam and enter a long decay tunnel where the mesons can decay via the reaction $\pi^+, K^+ \rightarrow \mu^+ \nu_\mu$. Since $c\tau_{\mu^+} = 659$ m, a relativistic muon (which would also include a time dilation factor) is unlikely to decay in a tunnel on the order of 100 m. Contamination of a typical ν_μ beam by ν_e is generally on the order of about one half of one percent.

In the calculations presented, oscillations are calculated for a *typical* accelerator-produced neutrino flux. The fluxes computed were based [99] on the AGS accelerator at Brookhaven National Lab. Calculations were redone assuming a higher proton current which would have been available at the then proposed KAON factory, but with the same 28.3 GeV beam energy. While neither the BNL oscillation experiment nor the KAON factory will be constructed, the neutrino fluxes are typical for low energy accelerator neutrino beams so they serve as a reference beam from which to work. Figure 2.4 shows the ν_μ , $\bar{\nu}_\mu$, ν_e and $\bar{\nu}_e$ fluxes used in the calculations which follow.

The neutrino energy spectra in the figure peak at about 1.7 GeV. Since the neutrinos are produced in the decay of kaons ($m_{K^+} = 494$ MeV) and pions ($m_{\pi^+} = 139.6$ MeV) into muons ($m_{\mu^+} = 105.7$ MeV), such a flux is approaching the lower limit in energy at which a well collimated ν_μ beam can be produced. At much lower energies it becomes difficult to focus the kaons and pions, and the energy released in their decays will spread

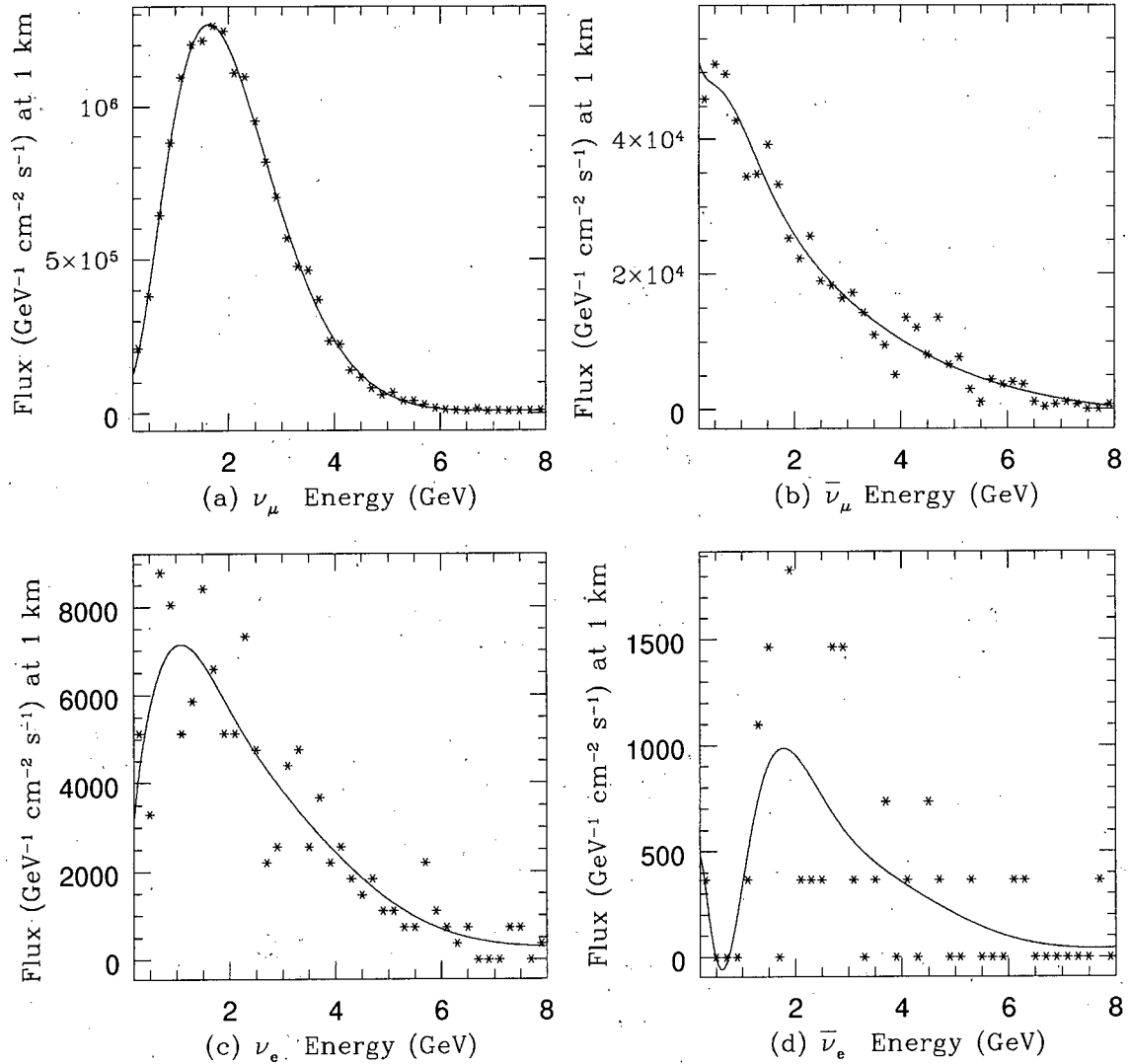


Figure 2.4: Neutrino and antineutrino fluxes produced by an intense 28.3 GeV primary proton beam and focussing pions and kaons into a 200 m decay tunnel. Raw fluxes from the Monte Carlo program were scaled to $\text{GeV}^{-1}\text{cm}^{-2}\text{s}^{-1}$. Note that the apparently poor fit in the $\bar{\nu}_e$ fit is a result of low statistics in the Monte Carlo.

out the beam. This observation, coupled with the fact that the fluxes were generated using a very high current machine, will provide an estimate of what regions of neutrino oscillation parameter space could possibly be ruled out with today's technology.

Accelerator experiments consist of generating a neutrino beam and measuring its flux and content with two or more detectors. One detector is located near the end of the decay tunnel and calibrates the neutrino beam at its source, while distant detector(s) look for changes in that beam farther downstream. These experiments look at two channels: one disappearance and one appearance. The former signal would be apparent if a measurable reduction in the ν_μ flux at the distant detector (beyond the $1/L^2$ factor as the beam spreads out). The latter signal would be an increase in the ν_e or ν_τ flux.

2.3.2 Characterising Long Baseline Neutrino Oscillations

Bernstein and Parke [97],[98] discussed long baseline experiments, noting that the probability of a transition in a long baseline experiment is given by

$$P_{\alpha\alpha} = 1 - \sin^2(2\theta_M) \sin^2 \left(1.27 \frac{\Delta m_M^2 L}{E} \right) \quad (2.29)$$

They defined ε as the limit that a particular experiment can put on $P_{\alpha\beta} = 1 - P_{\alpha\alpha}$, assuming that it does not find positive evidence for oscillations. The value of ε depends on the level of contamination of the neutrino beam, uncertainty in flux calculations, experimental acceptance, and backgrounds.

In the limit of large Δm_V^2 (in vacuum, the subscripts M in equation 2.29 revert to V), many oscillations take place along the baseline and the second sinusoidal term in the equation averages to $1/2$. Such an experiment can then probe $\sin^2(2\theta_V) \geq 2\varepsilon$. If $\varepsilon \ll 1$, then in the limit of maximal mixing when $\sin^2(2\theta_V) = 1$ the experiment can rule out $\Delta m_V^2 \geq \frac{\sqrt{\varepsilon} E}{1.27 L}$.

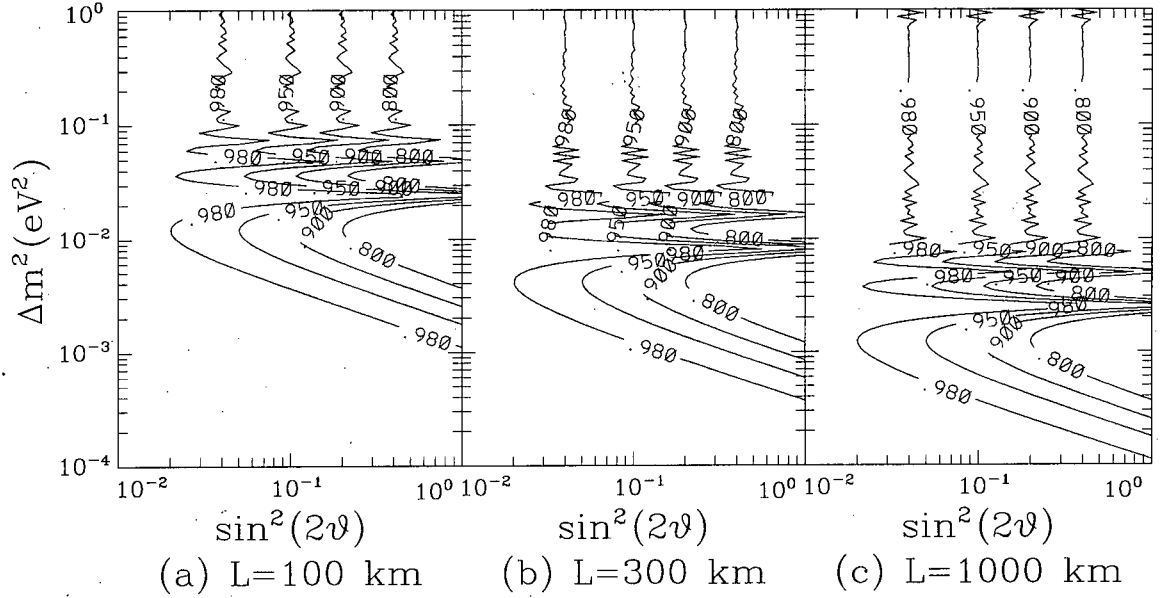


Figure 2.5: Contours of $P_{\alpha\alpha}(\Delta m_V^2, \sin^2(2\theta_V))$ for neutrinos in vacuum, with a flat spectrum and energy on the range 0.9 to 1.1 GeV.

Figure 2.5 shows calculations of contours of constant probability for $P_{\alpha\alpha}$ in vacuum on a $(\Delta m_V^2, \sin^2(2\theta_V))$ plane for four different values of the parameter ε , assuming a *flat* neutrino spectrum on the range $E \in [0.9, 1.1]$ GeV. Varying the baseline (and therefore L/E) illustrates that the contours shift vertically in proportion to $\frac{1}{L}$. Also, when $\frac{1.27\Delta m_V^2 L}{E} = \frac{\pi}{2}$, $P_{\alpha\alpha}$ reaches the first minimum and the contour extends down to $\sin^2(2\theta_V) = 1 - \varepsilon$.

Figure 2.6 shows similar plots for oscillations of neutrinos and antineutrinos in vacuum and in matter. As L increases towards the length of one oscillation at resonance, and provided that Δm_V^2 is small enough that $\frac{L_V}{L_e} \rightarrow \frac{2\sqrt{2}G_F N_e E}{\Delta m_V^2}$, matter effects enhance the neutrino oscillations. This enhancement manifests itself in the middle column of figure 2.6 as the contours jut out to the left at the resonance mass, especially at the $L = 10,000$ km baseline. This allows an experiment to probe to a much smaller mixing angle.

In the column on the right, it is apparent that matter suppresses mixing of antineutrinos compared with vacuum. The matter term in the Hamiltonian has opposite sign in the antineutrino case and $D_M > 1$ grows with larger density. As a result, the mass difference between the two states *increases* and the mixing angle *decreases*.

Figure 2.7 plots the electron density of the earth as a function of radius based on a code provided by Stephen Parke [102], as well as the length of a baseline tangent to that radius. The figure illustrates that N_e varies slowly except at several radii where jumps occur. The most pronounced increase occurs at the transition to the liquid iron core, where the density rises by about 80 percent over a very short distance. However, the figure also shows that any baseline less than 10,700 km in length would not probe deep enough to encounter that core, so most calculations in this field have estimated the average density along the path and assumed that it is constant. This usually provides an accurate estimate because in order to probe to the lowest possible Δm_V^2 , experiments involve a small number of oscillations along their baseline.

As a neutrino traverses along an arc through the earth, N_e gradually increases until it reaches the midpoint, after which it slowly decreases. The matter oscillation length will be slightly longer at the beginning and end of the path and shorter in the middle, or vice versa depending on whether its energy places it above or below the resonance density. However because there are only a few oscillations, one can usually approximate N_e with its mean value, and the neutrino will undergo almost the same few oscillations.

Figure 2.8 plots $P_{\alpha\alpha}(\Delta m_V^2, \sin^2(2\theta_V))$ contours with two different baselines using the reference neutrino spectrum on the range 0.9 to 1.1 GeV, assuming constant N_e and one which varies with the radius of the earth. In the former case, an exact calculation can be performed very quickly while in the latter, a fourth-order Runge-Kutta method must be used to integrate the neutrino wave function along its path. The two methods yield very similar results at 10,000 km. At 12,800 km (the diameter of the earth), there

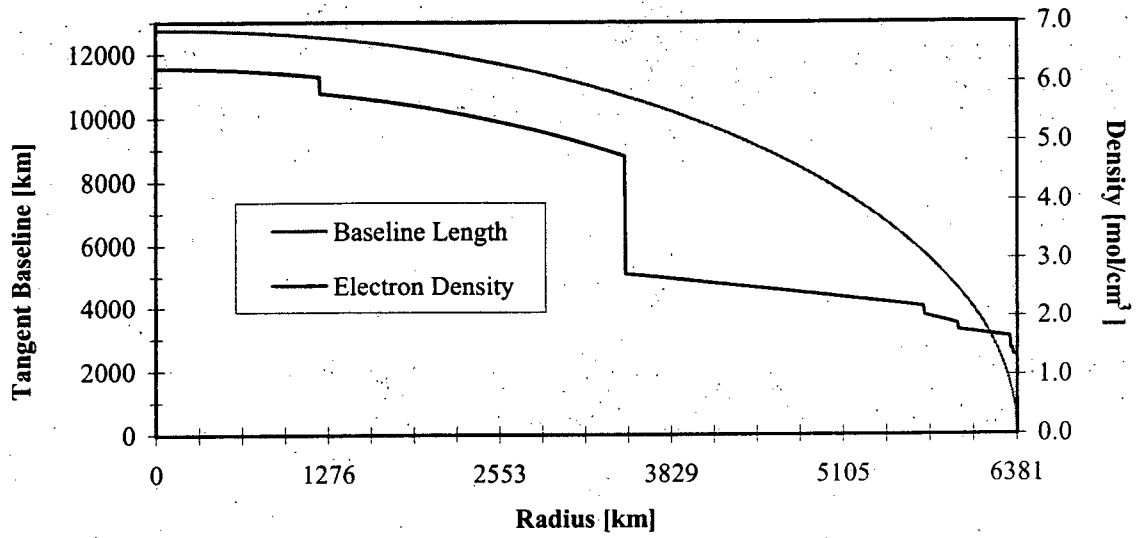


Figure 2.7: Electron density of the earth as a function of radius (right axis), and length of a baseline through the earth which is tangent to that density (left axis). The latter function is given by the formula $2\sqrt{\rho_{\text{earth}}^2 - \rho^2}$.

is a noticeable change. There are two resonant densities—one inside the core and one outside, so there are two different Δm_V^2 's which match the resonant condition causing the contours jut out to the left in the figure. However this effect will be smoothed out in any real experiment because a wider distribution of energies which will wash it out.

2.3.3 Existing Experimental Results

Many long baseline experiments running over the past decade have gradually lowered the limits on possible values of the parameters Δm_V^2 and $\sin^2(2\theta_V)$. They have examined both appearance and disappearance channels and considered oscillations between all three flavours of neutrinos. Except for the LSND detector at LAMPF, no experiment to date has reported positive evidence for neutrino oscillations, and so far the LSND results have not been confirmed. Table 2.1 lists several characteristics of some of the more significant recent programs.

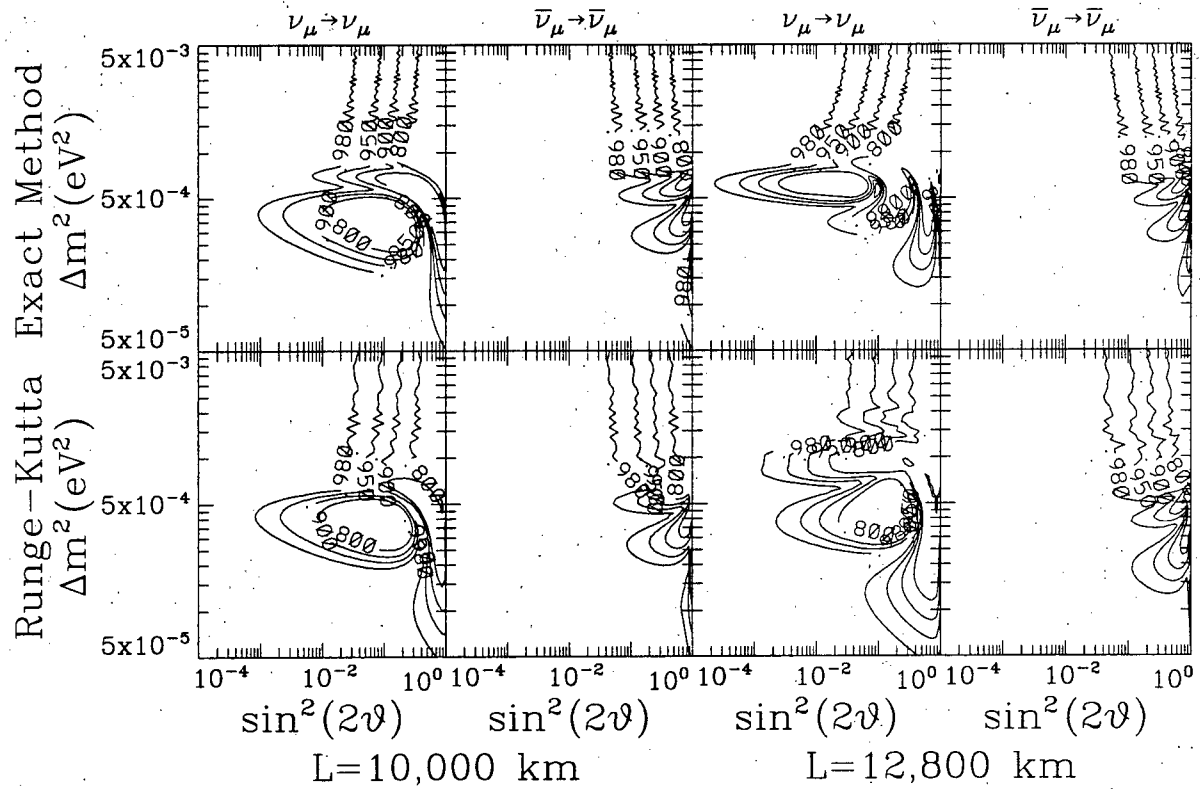


Figure 2.8: Comparison of contours for $P_{\alpha\alpha}(\Delta m_V^2, \sin^2(2\theta_V))$ using an exact solution and assuming fixed density and numerical solution with Runge-Kutta method and using the variable density of the earth. The exact solution assumes $N_e = 2.3$ and 4.0 g/cm^3 at $L = 10,000$ and $12,800 \text{ km}$ respectively.

Experiment	E_ν [GeV]	Baseline [m]	Reaction	$(\Delta m_V^2)_{\min}$ [eV ²]	Minimum $(\sin^2(2\theta_V))_{\min}$
Gösgen	0.0035	38, 46, 65	$\bar{\nu}_e D$	0.02	0.14
Bugey	0.0035	15, 40, 95	$\bar{\nu}_e D$	0.01	0.04
Krasnoyarsk	0.0035	57, 231	$\bar{\nu}_e D$	7.5×10^{-3}	0.05
LAMPF	0.05	30	$\bar{\nu}_\mu \rightarrow \bar{\nu}_e A$	n/a	n/a
BNL E776	3.0	1000	$\nu_\mu, \bar{\nu}_\mu \rightarrow \nu_e, \bar{\nu}_e A$	7.5×10^{-2}	0.03
CCFR	140	900, 1400	$\nu_\mu, \bar{\nu}_\mu \rightarrow \nu_e, \bar{\nu}_e D$	1.0	4×10^{-3}
CCFR	140	900, 1400	$\nu_\mu, \bar{\nu}_\mu \rightarrow \nu_\tau, \bar{\nu}_\tau D$	1.0	0.01
CDHSW	3.2	130, 885	$\bar{\nu}_\mu D$	0.26	0.053
FNAL 531	30	440	$\nu_\mu \rightarrow \nu_\tau A$	0.9	4×10^{-3}
FNAL 531	30	440	$\nu_e \rightarrow \nu_\tau A$	9.0	0.12
NOMAD	25	820	$\nu_\mu \rightarrow \nu_\tau A$	0.7	3×10^{-4}
CHORUS	25	820	$\nu_\mu \rightarrow \nu_\tau A$	0.6	3×10^{-4}
KARMEN	25	17.5	$\nu_\mu \rightarrow \nu_e A$	0.2	0.1
KARMEN	25	17.5	$\bar{\nu}_\mu \rightarrow \bar{\nu}_e A$	0.1	0.02

Table 2.1: Best limits set on neutrino oscillation parameters by recent and future long baseline experiments. Gösgen [95], Bugey [103] and Krasnoyarsk [104] are reactor-based, while LAMPF [105], BNL E776 [106], CCFR [107], CDHSW [108], FNAL 531 [109], NOMAD [110], CHORUS [111], and KARMEN [112] use accelerator produced neutrinos. Note that D and A in the reaction column refer to disappearance and appearance experiments respectively.

Figure 2.9 shows the excluded regions for the newest experiments. The reactor experiments are still among the best experiments at excluding low Δm_V^2 because the antineutrino energy is relatively low, on the order of a few MeV. Accelerator based experiments with focussed beams have higher statistics and can probe lower mixing angles and newer, more sensitive experiments are now taking data. The KARMEN experiment is setting new limits in the $\nu_e \nu_\mu$ domain, while CHORUS and NOMAD use muon neutrinos from CERN to investigate $\nu_\mu \nu_\tau$ oscillations and should reduce current limits on $\sin^2(2\theta_V)$ by an order of magnitude [110].

The LAMPF experiment did issue two papers [113], [114] with new data claiming to have a positive signal for the appearance channel of $\bar{\nu}_\mu \rightarrow \bar{\nu}_e$. The result is surprising because it implies an allowed region with mass-squared difference in the range above 10^{-1} eV^2 , more than four orders of magnitude greater than the regions implied by the solar neutrino results and well above the Δm^2 suggested by the atmospheric neutrino experiments. Moreover, it has been noted [115] that much of the allowed region has been ruled out by other experiments. Figure 2.10 shows the LAMPF allowed regions along with the best exclusion regions from other experiments. However, to date, their results have not been confirmed.

2.3.4 Future Prospects

Accelerator-based neutrino oscillation experiments are limited in the range of Δm_V^2 which they can probe. The baseline cannot be longer than the diameter of the earth, and the energy of a well focussed ν_μ beam cannot drop far below 1 GeV. However it is instructive to see just how low in Δm^2 such an experiment might be able to probe. Using the reference spectrum from the proposed BNL/KAON beam, it is possible to predict the best limits such an experiment could be expected to see. Two possible experiments will be examined: a 250 km baseline with a 5 kT detector and a 10,000 km baseline with a

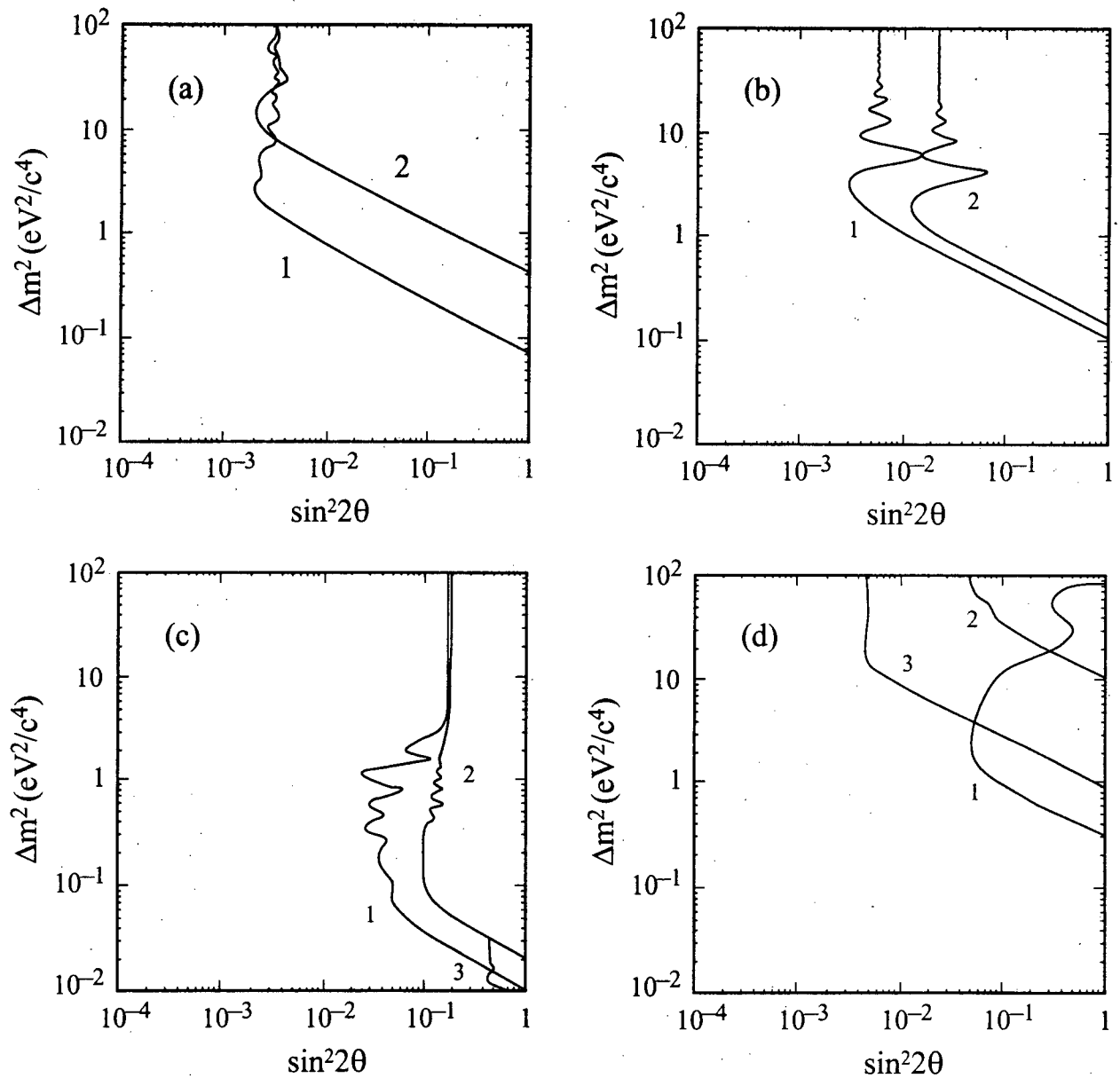


Figure 2.9: Most sensitive limits on neutrino oscillations at 90% C.L. (a) $\nu_\mu \rightarrow \nu_e$ appearance from the (1) E776 and (2) E734 experiments at BNL. (b) $\bar{\nu}_\mu \rightarrow \bar{\nu}_e$ appearance from the (1) KARMEN and (2) E645 experiments. (c) $\bar{\nu}_e$ disappearance from the (1) Bugey, (2) Gösgen and (3) Krasnoyarsk reactor experiments. (d) ν_μ disappearance from the (1) CDHS and (2) CCFR experiments. Also shown is the limit from the (3) E531 $\nu_\mu \rightarrow \nu_\tau$ appearance experiment [113].

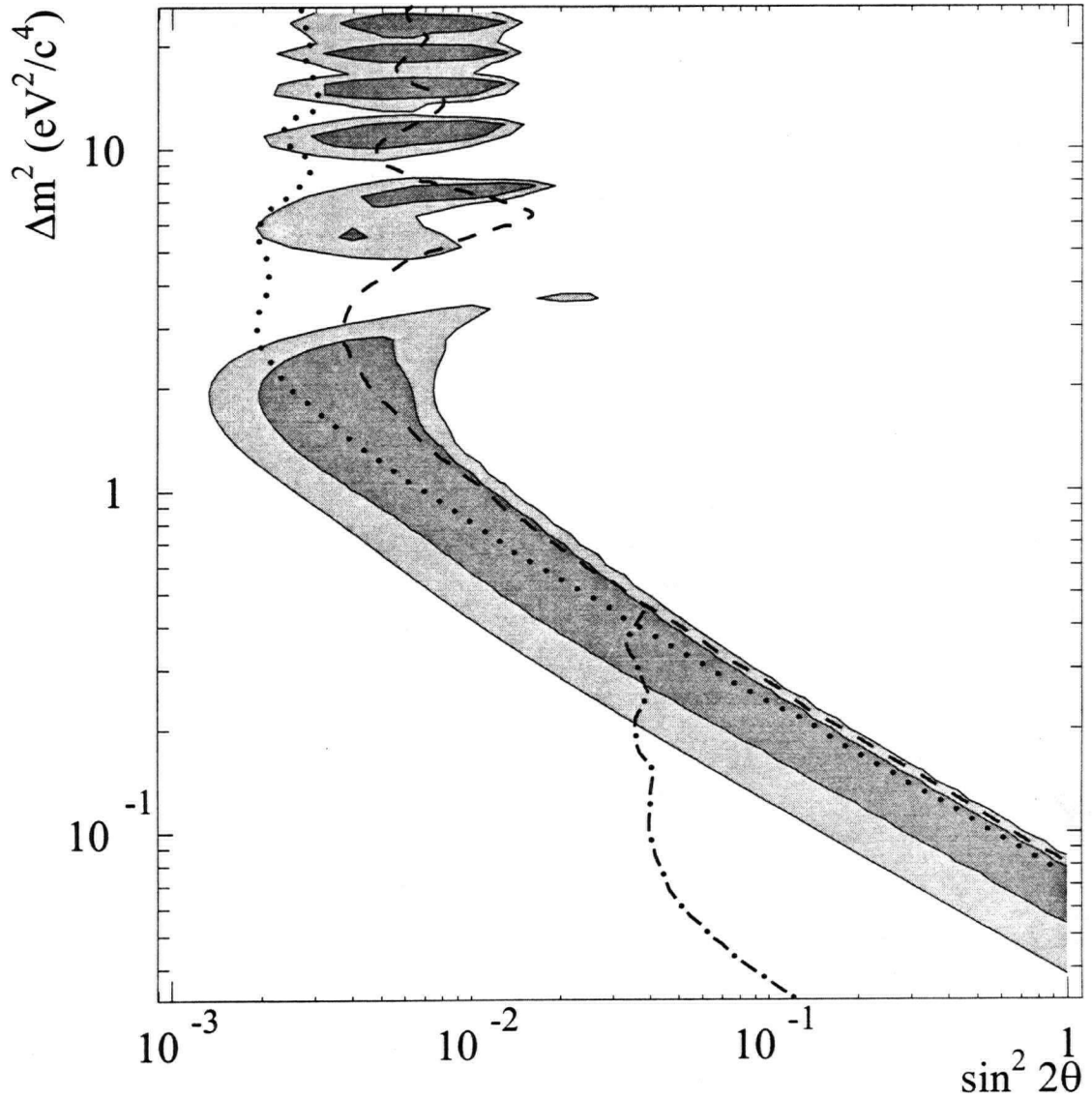


Figure 2.10: Plot of the LSND Δm^2 vs $\sin^2(2\theta)$ favoured regions. The method used to obtain these is described in [113]. The darkly-shaded and lightly-shaded regions correspond to 99% and 90% likelihood regions after the inclusion of the effects of systematic errors. Also shown are the 90% C.L. limits from KARMEN at ISIS (dashed curve), E776 at BNL (dotted curve), and the Bugey reactor experiment (dot-dashed curve) [113].

32 kT detector.

The first of these experiments would involve building a reasonable sized single purpose detector on the same order as ones which have been proposed for other experiments. The statistics from such a configuration would provide sufficient data, provided that oscillations were found, to *accurately* determine the mixing parameters. This could be achieved by examining the spectrum of the detected neutrinos.

The second experiment has a baseline of 78 % of the diameter of the earth, but its path misses the liquid iron core where the electron density jumps. The detector size was chosen to match the fiducial volume of the SuperKamiokande detector. This should provide an accurate estimate of the lowest possible Δm_V^2 which is accessible to accelerator-based long baseline experiments.

Figure 2.11 plots $P_{\alpha\alpha}(\Delta m_V^2, \sin^2(2\theta_V))$ contours for $\nu_\alpha \rightarrow \nu_\alpha$ in both vacuum and matter and $\bar{\nu}_\alpha \rightarrow \bar{\nu}_\alpha$ in matter, with constant $N_e = 1.34 \text{ mol/cm}^3$. From the figure it is clear that matter effects are very small, so the plots which follow at the 250 km baseline assume vacuum oscillations.

Figure 2.12 shows the rates for different interactions assuming 100 % efficiency in the detector. With 70,000 μ^- events per year, one can naively estimate a standard deviation of $\sigma \approx 1/\sqrt{70,000} = 0.3 \%$, so that $\varepsilon \approx 3\sigma$ would be on the order of 1 %. From figure 2.11, at large mixing, this experiment could rule out $\sin^2(2\theta_V) \geq 3 \times 10^{-3} \text{ eV}^2$ for $\Delta m_V^2 \geq 4 \times 10^{-3} \text{ eV}^2$, while in the limit $\sin^2(2\theta_V) = 1$ it could probe down to $\Delta m_V^2 = 5 \times 10^{-4} \text{ eV}^2$.

What is perhaps more interesting about this experiment, however, is that if oscillations were found with, say, $\Delta m_V^2 \geq 0.01 \text{ eV}^2$ then the statistics are sufficient to bin the data by energy. The left-hand column of figure 2.13 shows $P_{\alpha\alpha}(E)$ for three different values of Δm_V^2 . The right-hand column plots the spectrum of the muons with and without

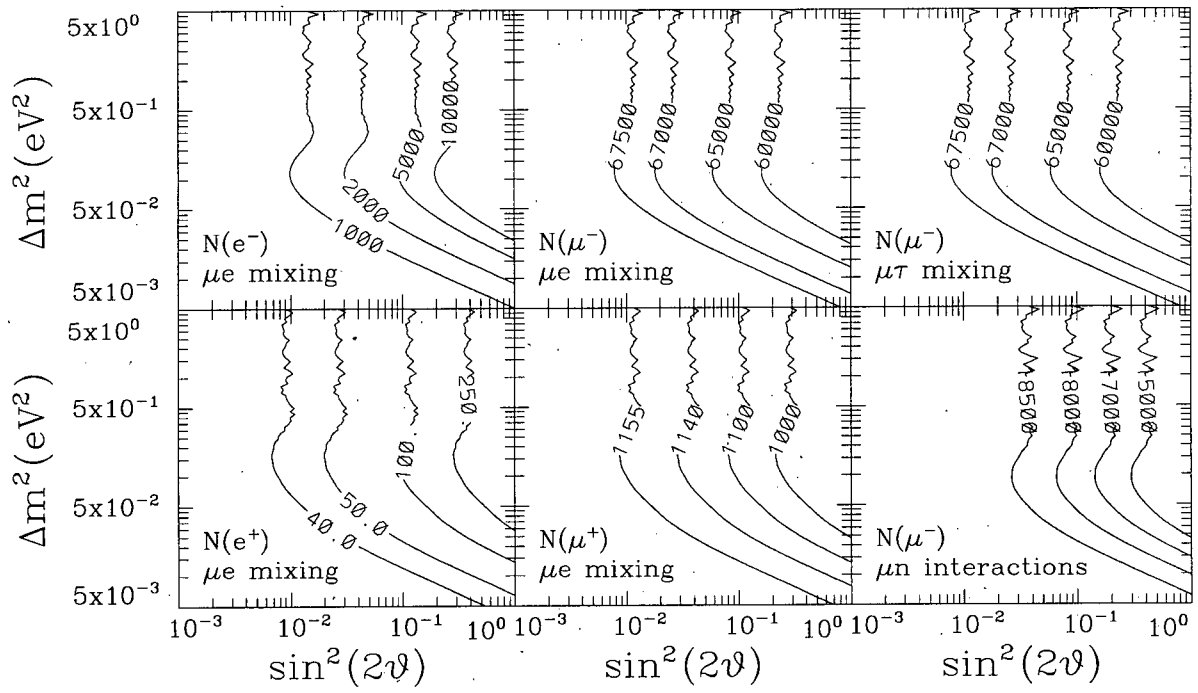


Figure 2.12: Yearly rates for neutrino interactions from the reference flux hitting a 5 kT target at 250 km. The bottom right figure gives the rate for $\nu_\mu n \rightarrow \mu^- p$, while all others are for the inclusive reaction $\nu N \rightarrow lX$.

oscillations, with rates per year based on bin widths of 1/8 GeV. Because neutrino oscillation models predict a well-defined energy dependence, the structure of this spectrum could be used to confirm the theory and provide precision measurements of the masses and mixing angles, as apparent in the figure.

To probe to the lowest possible Δm_V^2 with a long baseline experiment, it is necessary to extend the baseline to a substantial fraction of the diameter of the earth. Figure 2.14 plots $P_{\alpha\alpha}(\Delta m_V^2, \sin^2(2\theta_V))$ using the reference flux and a 10,000 km baseline. With vacuum oscillations, the experiment rules out $\sin^2(2\theta_V) > 0.1$ for $\Delta m_V^2 > 2 \times 10^{-4} \text{ eV}^2$ and $\Delta m_V^2 > 3 \times 10^{-5} \text{ eV}^2$ in the limit of large mixing, in both cases assuming that $\varepsilon = 0.05$.

Matter enhancement of the oscillations is apparent down to a few times 10^{-4} eV^2 , somewhat below the resonance at $2 \times 10^{-3} \text{ eV}^2$. The reference flux would produce about 270 events per year in the detector (assuming no oscillations). In order to make the experiment more feasible, a neutrino flux four times as great would be required. This would raise the rate to about 1,000 events per year. However the experiment would not be able to detect $\nu_e - \nu_\mu$ oscillations in the 10^{-5} eV^2 range implied by the solar neutrino experiments, and it is unlikely that an experiment this large will be performed in the foreseeable future.

The reference flux spectrum peaks at about 1.7 GeV, and it is very difficult to produce a *focussed* neutrino beam below 0.5 GeV because the kinetic energy released in the decay which produces the neutrino would perturb its direction. Reducing the peak energy by a factor of three would move the contours in figure 2.14 down by a factor of three, still not approaching 10^{-5} eV^2 , but the cross section would also drop by a factor of three. Thus, even with a lower energy and much higher flux (or larger detector), accelerator-based long baseline experiments are unlikely to confirm or rule out the regions of parameter space implied by the solar neutrino experiments.

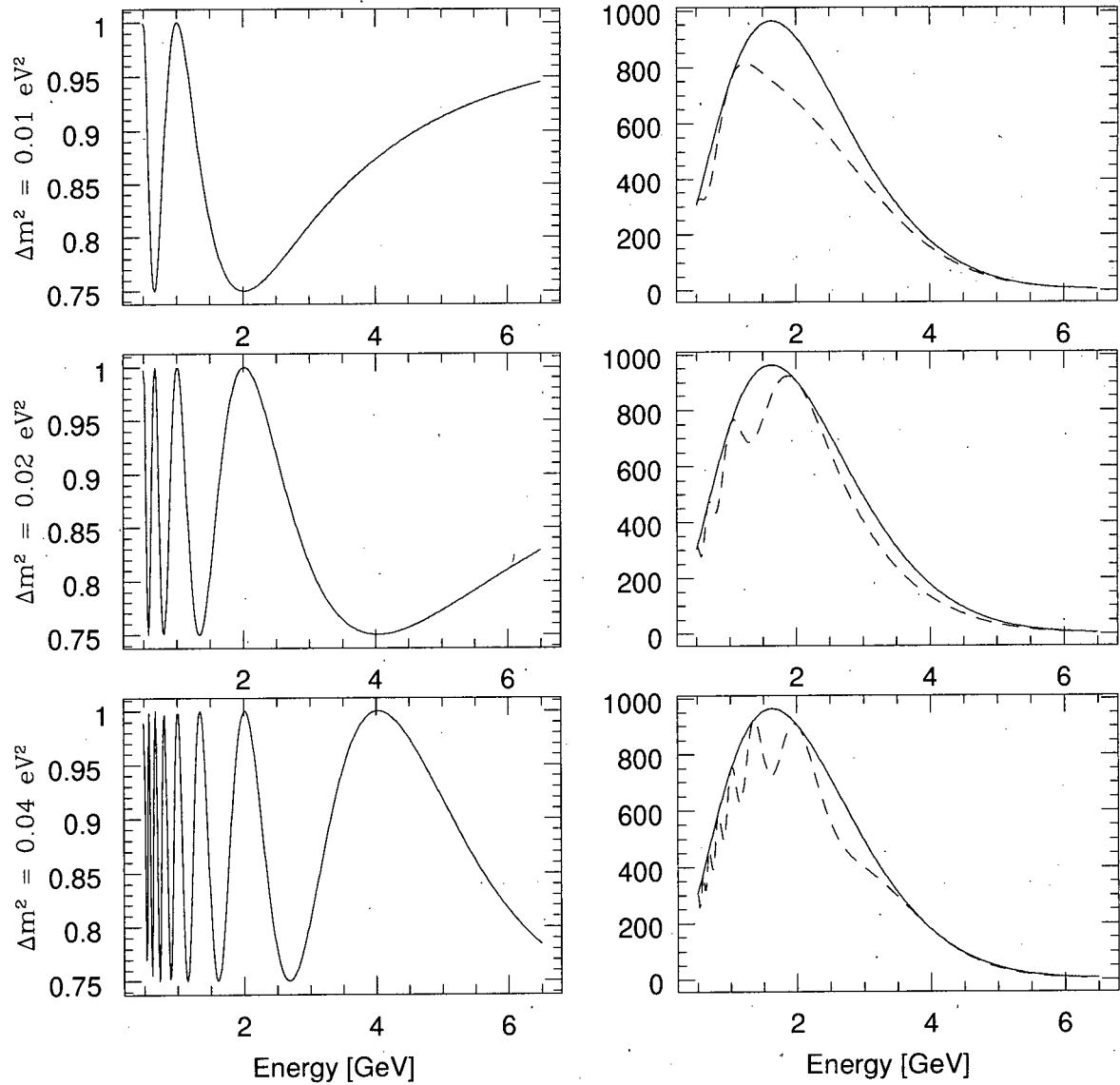


Figure 2.13: Energy spectrum for muon neutrinos measured in a 5 kT detector and a 250 km baseline with mixing $\sin^2(2\theta_V) = 0.25$ for $\Delta m_V^2 = 0.01, 0.02$ and 0.04 eV^2 . Figures in the left column show $P_{\alpha\alpha}(E)$, while the right column plots the neutrino spectrum without oscillations (solid lines) and with oscillations (dashed lines). The rates in column two are normalised assuming bin widths of 0.125 GeV.

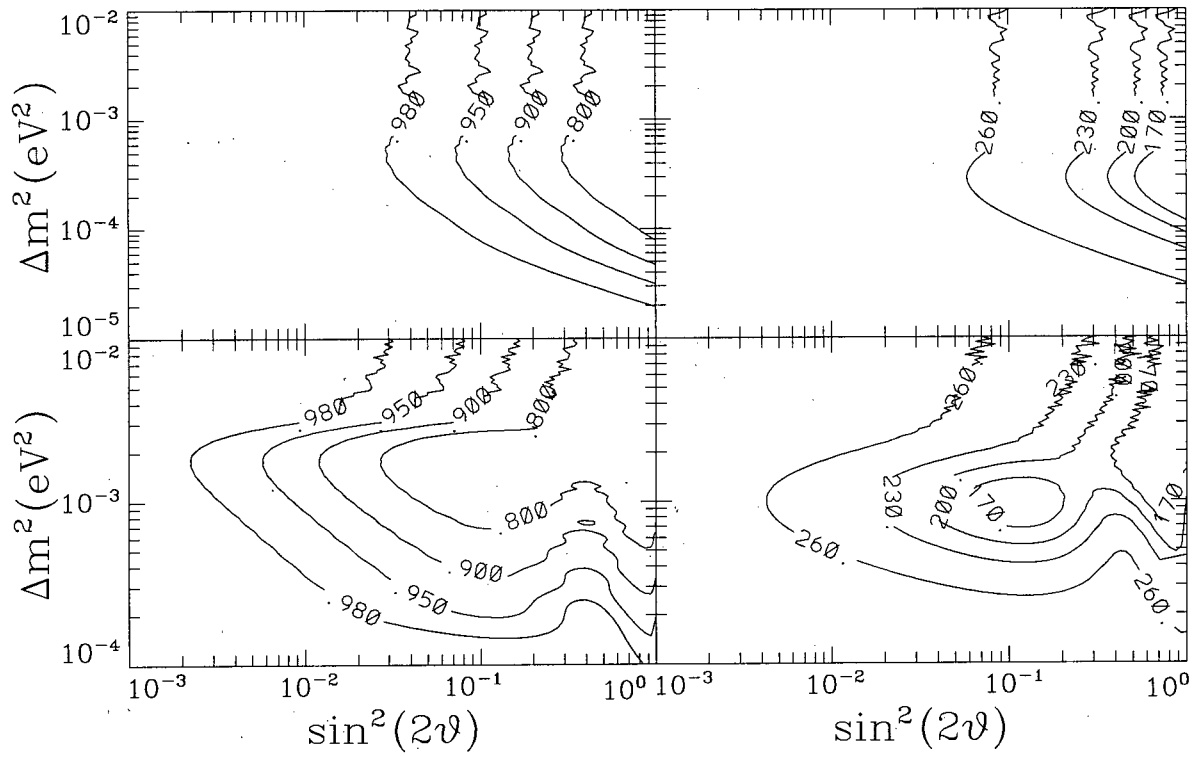


Figure 2.14: Neutrino oscillations on a 10,000 km baseline. Top row shows vacuum oscillations (relevant to $\nu_\mu \rightarrow \nu_\tau$), while bottom row includes matter effects. Left column plots $P_{\alpha\alpha}$ while right column plots number of interactions per year assuming a detector with 32 kT fiducial mass.

2.4 Neutrino Oscillations and the Solar Neutrino Problem

2.4.1 Early Development and Analytical Results

In one of the two early papers in which Wolfenstein revolutionised neutrino physics by introducing matter enhancement of the oscillation parameters [88],[89], the sign of the matter term was reversed. Unfortunately, in their early work, Mikheyev and Smirnov used the incorrect sign and concluded that if neutrino oscillations were to solve the solar neutrino problem, it was necessary to assume that $m_{\nu_e} > m_{\nu_\mu}$. Langacker [117] clarified the situation, and a paper by Bethe [118] in 1986 renewed interest in neutrino oscillations as a plausible explanation for the observed deficit in solar neutrinos.

In his paper Bethe noted that if $m_{\nu_\mu} > m_{\nu_e}$ in vacuum are in the right range, such that $m_{\nu_e} > m_{\nu_\mu}$ at the centre of the sun, then the ν_e may emerge from the sun as a ν_μ . Figure 2.15 shows that at large density, the electron neutrino produced closely corresponds to the heavier mass eigenstate ν_2 . If the density of the sun changes gradually enough that the neutrino eigenstate propagates out of the sun as a ν_2 (the adiabatic condition), then it will emerge from the sun in the mass eigenstate which approximately corresponds to ν_μ in vacuum.

A more realistic possibility is that there is some probability that the neutrino jumps from the ν_2 state to the ν_1 state. If so, it is much more likely to happen near resonance when the difference in the masses is the smallest. Parke [119] calculated the amplitude for a ν_e produced in matter at high density at time t , which propagates through a resonance at time t_r , and is detected as a ν_e in vacuum at time t' to be:

$$\begin{aligned} \langle \nu_e(t) | \nu_e \rangle = & A_1(t) \exp \left(-\frac{i}{4E} \int_{t_r}^{t'} dt \Delta m^2(t) \right) + \\ & A_2(t) \exp \left(\frac{i}{4E} \int_{t_r}^{t'} dt \Delta m^2(t) \right) \end{aligned} \quad (2.30)$$

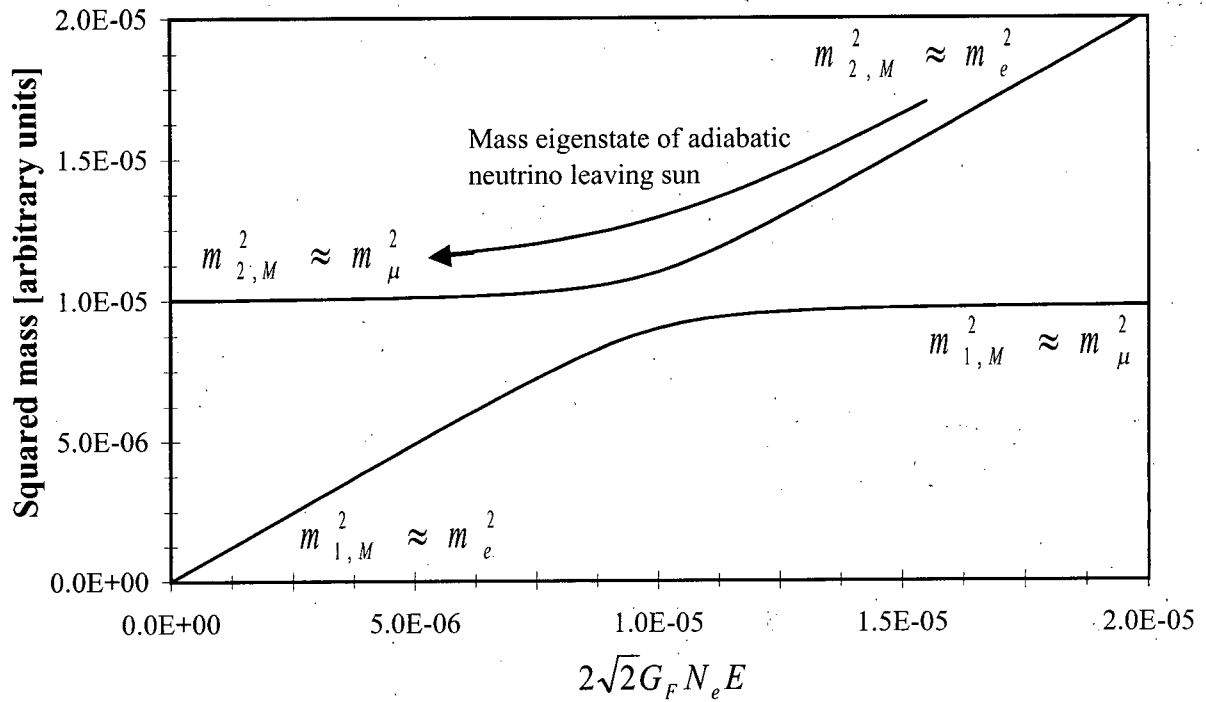


Figure 2.15: A ν_e produced at very high density at the centre of the sun corresponds approximately to the ν_2 eigenstate. If the density changes slowly enough, it will remain a ν_2 as it propagates outwards and will emerge in a state which closely corresponds to the ν_μ weak eigenstate.

$$A_1(t) = \cos \theta_V [a_1 \cos \theta_N \exp \left(\frac{i}{4E} \int_{t_r}^t dt \Delta m^2(t) \right) - a_2^* \sin \theta_N \exp \left(-\frac{i}{4E} \int_{t_r}^t dt \Delta m^2(t) \right)] \quad (2.31)$$

$$A_2(t) = \sin \theta_V [a_2 \cos \theta_N \exp \left(\frac{i}{4E} \int_{t_r}^t dt \Delta m^2(t) \right) + a_1^* \sin \theta_N \exp \left(-\frac{i}{4E} \int_{t_r}^t dt \Delta m^2(t) \right)] \quad (2.32)$$

The exponential terms come about by applying phases of $\exp \pm \frac{i}{2} \int dt \Delta E$ to the effective mass eigenstates $|\nu_{1,M}\rangle$ and $|\nu_{2,M}\rangle$ when they propagate far from resonance. Here the dependence of Δm_M^2 on the changing density as the neutrino passes through the sun is expressed by the parameter t . The coefficients a_1 and a_2 are the amplitudes for a pure ν_1 state to remain a ν_1 or transform to a ν_2 as the neutrino passes through the resonance, so they satisfy $|a_1|^2 + |a_2|^2 = 1$. The term $a_1 \cos \theta_N \cos \theta_0 \exp \left(\frac{i}{4E} \int_{t_r}^t dt \Delta m^2(t) \right) \exp \left(-\frac{i}{4E} \int_{t_r}^{t'} dt \Delta m^2(t) \right)$ is the product of five terms which come about as follows:

- $\cos \theta_N$ is the amplitude for the ν_e being initially projected onto ν_2 ,
- $\exp \left(\frac{i}{4E} \int_{t_r}^t dt \Delta m^2(t) \right)$ is the phase the ν_2 picks up moving from t to t_r ,
- a_1 is the amplitude for remaining a ν_2 when crossing resonance,
- $\exp \left(-\frac{i}{4E} \int_{t_r}^{t'} dt \Delta m^2(t) \right)$ is the phase the ν_2 picks up moving from t_r to t' , and
- $\cos \theta_V$ is the amplitude for the ν_2 to be projected onto a ν_e on detection.

Upon squaring the amplitude Parke found two complex phases which represent the phase of the wavefunction when it enters the resonance and when it is detected. By averaging the result over the resonance and detection positions he found the probability simplified to

$$P(\nu_e \rightarrow \nu_e) = \frac{1}{2} + \left(\frac{1}{2} - P_{jump} \right) \cos(2\theta_N) \cos(2\theta_V) \quad (2.33)$$

where $P_{jump} = |a_2|^2$ is the probability that the neutrino jumps from one mass eigenstate to the other when it crosses the resonance.

The calculation of P_{jump} for a simple level crossing was solved simultaneously in 1932 by Landau [120] and Zener [121] in reference to the crossing of atomic levels. The derivation requires that the off-diagonal terms in the Hamiltonian at resonance are much smaller than the kinetic energy, the transition region is sufficiently small that the mass differences can be approximated by a linear function and all other quantities are constant. The Hamiltonian can then be expressed as a second order ODE which can be converted to Weber's equation by a change of variables, solved for the initial conditions, and converted back. Parke applied the result to the neutrino resonance crossing and showed that [119]:

$$P_{jump} = \exp \left[-\frac{\pi \Delta m_V^2 \sin^2(2\theta_V)}{4E \cos(2\theta_V)} \left(\frac{N_e}{|dN_e/dr|} \right)_{res} \right] \quad (2.34)$$

2.4.2 Characterising the results

A Monte Carlo computer code written by the author calculated solar neutrino survival probabilities, and some details of it are given in the next chapter. All results presented in this section were produced using that code. It first calculates the probability that a neutrino emerges from the sun as a ν_e depending on where it was produced in the sun. It then computes vacuum oscillations of neutrinos as they travel from the sun to the earth, including corrections for the eccentricity of the earth. Finally, it accounts for the regeneration of neutrinos as they pass through the earth on the way to the detector.

Figure 2.16 shows the contours of constant probability for two different *hypothetical* sources with discrete energy spectra at 1 MeV and 10 MeV, in which the neutrinos are always produced at the centre of the sun. The contours are identical except that the 1 MeV curves are shifted down the Δm^2 axis by a factor 10. In the centre of the triangular contour, a large percentage of neutrinos are converted even though $\sin^2(2\theta)/\cos(2\theta) \sim O(10^{-2})$. Mikheyev and Smirnov identified the different regions of the MS diagram and labelled them accordingly [123].

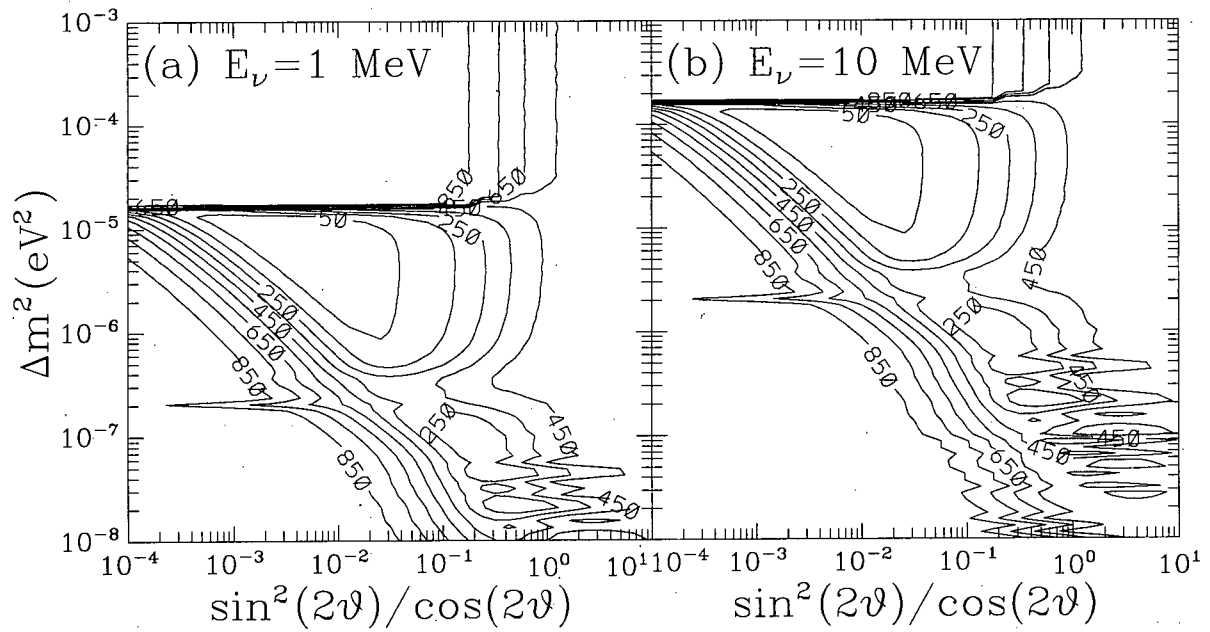


Figure 2.16: Probability that neutrinos from hypothetical sources with (a) $E = 1 \text{ MeV}$ and (b) $E = 10 \text{ MeV}$ will arrive in an underground detector as electron neutrinos. All neutrinos from both sources are assumed to be produced at the centre of the sun. Contours in the figure have been scaled by a factor of 1000.

The horizontal contours along the top define the adiabatic limit—as Δm^2 drops, it reaches a point where the solar density is large enough for MSW conversion to take place. The adiabatic regions in figure 2.16 are compressed in the vertical direction because the hypothetical neutrino sources used have fixed energy and their radial production distribution is fixed at the centre of the sun. The vertical contours on the right occur because at very large mixing, half of the neutrinos arriving on earth will be ν_e irrespective of what happened in the sun. The diagonal line from upper left to lower right is referred to as the non-adiabatic line. It determines how low Δm^2 can drop (depending on $\sin^2(2\theta)/\cos(2\theta)$), before adiabaticity breaks down and neutrinos jump from one state to the other when they cross the resonance.

The spike jutting out to the left in the bottom left contour is a result of neutrino regeneration in the earth. It occurs at a value of Δm^2 which matches the resonance condition for the earth's density and the neutrino's energy. The sharpness of the contour is a result of the fixed energy of the neutrino source. The region at the bottom right of the diagram shows very rapid vacuum oscillations as the neutrino travels from the sun to the earth.

Figure 2.17(a) to (c) plots contours of constant neutrino detection for the different experiments. The Kamiokande results are given as a fraction of the no MSW hypothesis while the Homestake and SAGE/Gallex results are given in SNU. With no conversion, these latter experiments would produce 9.22 and 138 SNU respectively. The adiabatic limits for the ^8B , ^7Be and pp neutrinos are apparent, and the density of contour lines provides an estimate of the relative contribution of the different sources. It is also clear that Kamiokande only sees ^8B neutrinos, Homestake sees both ^8B and ^7Be , while SAGE and Gallex see ^8B , ^7Be and pp neutrinos.

In 2.17(d), the χ^2 parameter is calculated for the combined results of the four experiments. There are three local minima with $\chi^2 = 1.37$ in the upper left, $\chi^2 = 2.75$ in the

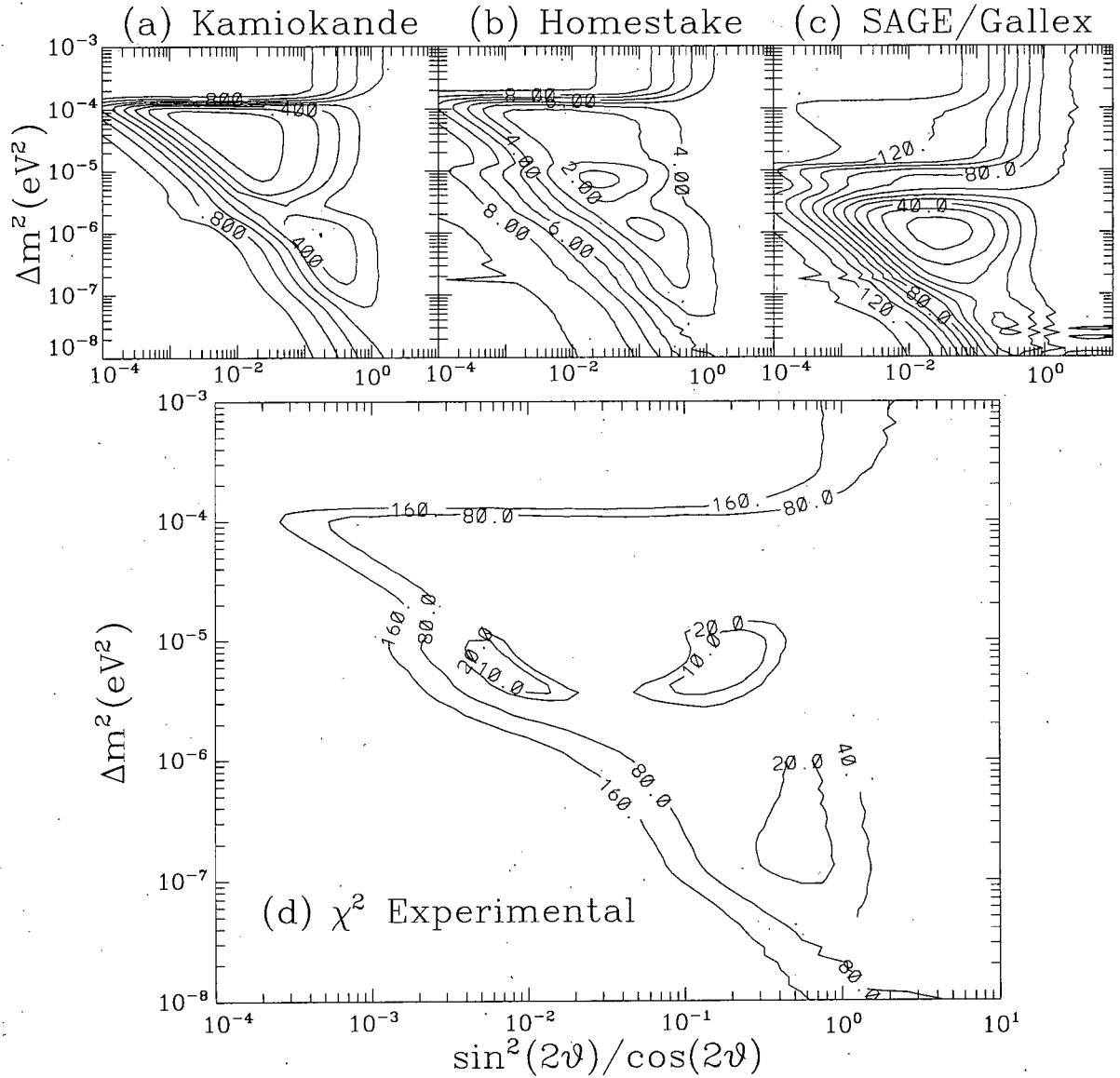


Figure 2.17: Contours of ν_e survival probability for the neutrino experiments as a function of the matter enhanced oscillation parameters. Kamiokande results (a) shown are a fraction of the total predicted by the SSM, while Homestake (b) and SAGE/Gallex (c) are absolute rates in SNU. In (d), the χ^2 parameter is calculated at each point using the rates measured by the four experiments.

upper right, and $\chi^2 = 12.9$ in the lower right region of the diagram. The probabilities that a χ^2 variable with two degrees of freedom (four experiments less two parameters) would yield values larger than 1.37, 2.75 and 12.9 are 0.50, 0.25 and 0.0016 respectively. Thus, the two upper minima provide very good fits to the data while the lower one does not. If the hypothesis corresponding to the $\chi^2 = 1.37$ minimum is accepted, then the contour line $\chi^2 = 10$ approximately corresponds to a 98.7% confidence level, while for the region around the $\chi^2 = 2.75$ minimum, the same contour represents a 97.3% confidence level.

The MSW mechanism is an energy dependent effect, so the spectrum can be used to differentiate solutions. In figure 2.18, the spectra of solar neutrinos on a gallium detector are shown assuming $\sin^2(2\theta)/\cos(2\theta) = 0.01$ with $\Delta m^2 = 10^{-7}, 3 \times 10^{-7}, 10^{-6}, 3 \times 10^{-6}, 10^{-5}, 3 \times 10^{-5}$ and 10^{-4} eV^2 . It is clear that as Δm^2 decreases from a large value, first the ^8B then the ^7Be and finally the pp neutrinos are suppressed as their respective adiabatic limits are crossed. Then as Δm^2 continues to drop, the ^8B , ^7Be and pp fluxes return in that order as the nonadiabatic limits are crossed. Unfortunately, none of the radiochemical experiments provide any spectral information.

Figure 2.19 shows the neutrino spectra for the three minima in χ^2 using a water Cherenkov detector with a threshold of 5 MeV which will be achieved at SuperKamiokande. While there are minor differences in the three spectra, very high statistics would be required to differentiate the three solutions.

2.4.3 Vacuum Oscillation Solutions

Before Wolfenstein showed that matter could enhance the neutrino oscillation parameters, vacuum oscillations were considered as a solution to the solar neutrino problem. Most authors today prefer the MSW effect because there is a small angle solution and vacuum oscillations require the earth-sun distance to be on the order of the oscillation length for

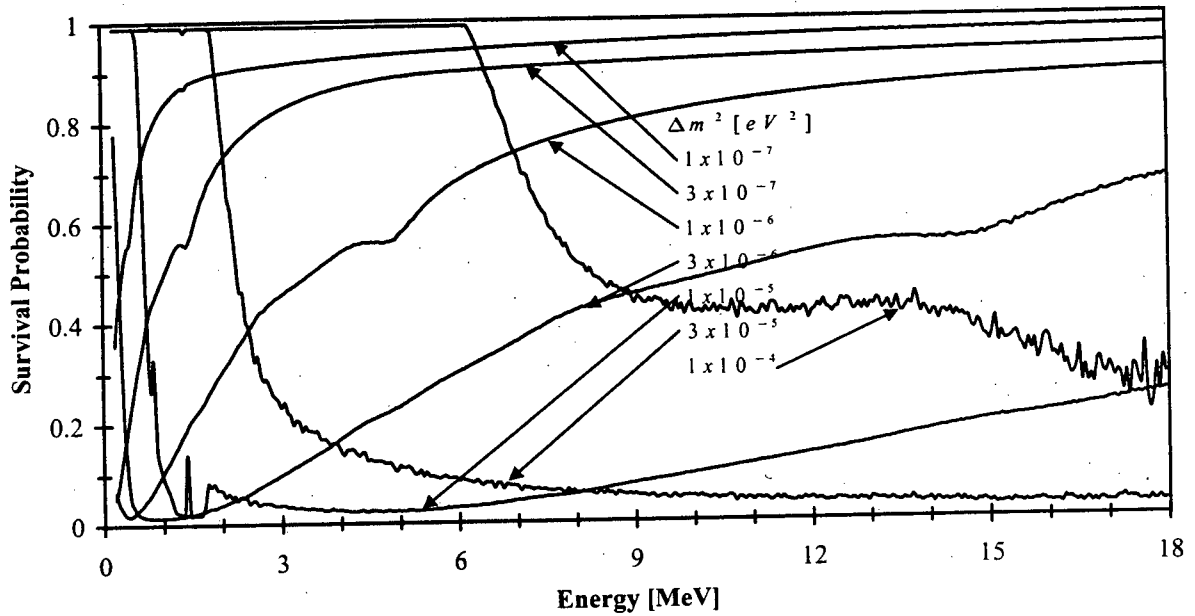


Figure 2.18: Neutrino conversion probability as a function of energy for different values of Δm_V^2 with a fixed value $\sin^2(2\theta_V)/\cos^2(2\theta_V) = 0.01$. Notice that as Δm_V^2 drops, first the high energy then successively lower energy neutrinos cross the adiabatic limits. Similarly, as it continues to drop first the high energy then successively lower energy neutrinos hit the non-adiabatic limit and are no longer converted.

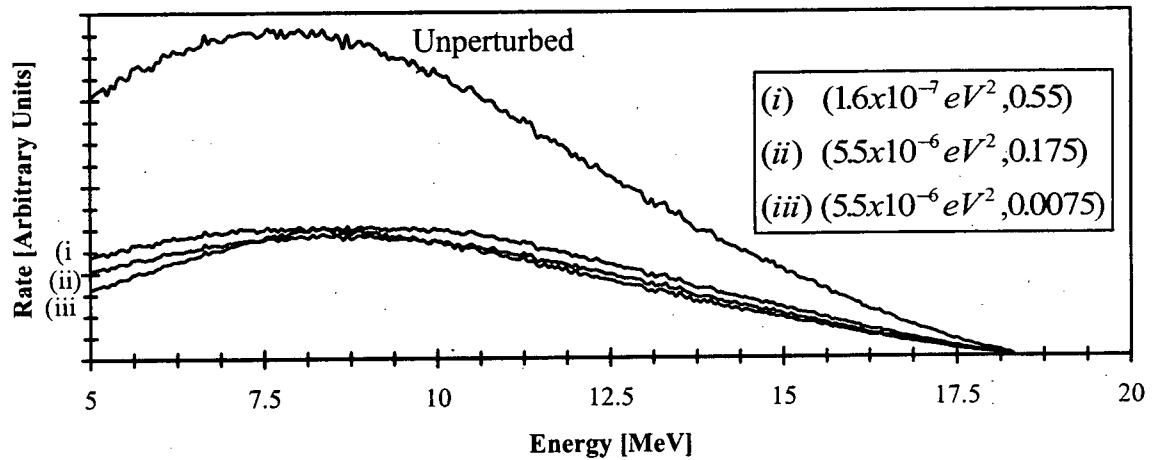


Figure 2.19: Neutrino energy spectra for the three parameter sets $(\Delta m_V^2, \sin^2(2\theta_V)/\cos(2\theta_V))$ defined by the local minima in figure 2.17.

Solution Type	Δm_V^2 [eV ²]	Angular Parameter	χ_{min}^2	$P(\chi^2) > \chi_{min}^2$
MSW	5.5×10^{-6}	0.0075	1.37	0.50
MSW	5.5×10^{-6}	0.175	2.75	0.25
MSW	1.6×10^{-7}	0.55	12.9	0.0016
Vacuum	5.20×10^{-11}	31	10.2	0.0061
Vacuum	9.00×10^{-11}	5	4.79	0.091
Vacuum	1.05×10^{-10}	25	4.62	0.099
Vacuum	2.45×10^{-10}	62	11.7	0.0029

Table 2.2: Local minima for the χ^2 variable for the solar neutrino experiments using the MSW and vacuum oscillation models. The column *Angular Parameter* refers to $\sin^2(2\theta_V)/\cos(2\theta_V)$ for the MSW solutions and $\sin^2(2\theta_V)/\cos^2(2\theta_V)$ for the vacuum oscillation solutions. The last column in the table gives the probability that a χ^2 would have a value greater than the local minimum by chance.

⁸B neutrinos, which seems somewhat unnatural. However, there are still regions of parameter space where vacuum oscillations provide a plausible solution [124].

Figures 2.20(a) to (c) show rates of neutrinos measured at the four experiments as a function of the vacuum oscillation parameters. Note that the horizontal axis is now $\sin^2(2\theta_V)/\cos^2(2\theta_V)$ —the additional factor of $\cos(2\theta_V)$ in the denominator further stretches out the large angle region. The Kamiokande contours shown are the first two oscillation envelopes, so that the ⁸B neutrinos would have to reach the earth near the first minimum for vacuum oscillations to solve the solar neutrino problem.

Figure 2.20(d) shows contours for the χ^2 parameter, and table 2.2 shows the details of the local minima for both the MSW and vacuum oscillation hypotheses. Only the two smallest local minima in the vacuum calculation provide plausible solutions to the data with two degrees of freedom. A χ^2 variate with two degrees of freedom larger than 4.62 and 4.79 would be produced by chance in about 10 % of experiments. Thus the vacuum oscillation model should not be ruled out, but the fit which it provides to the data is much less impressive than the MSW fit.

Figure 2.21 shows the energy spectrum of the four fits vacuum oscillations in table 2.2.

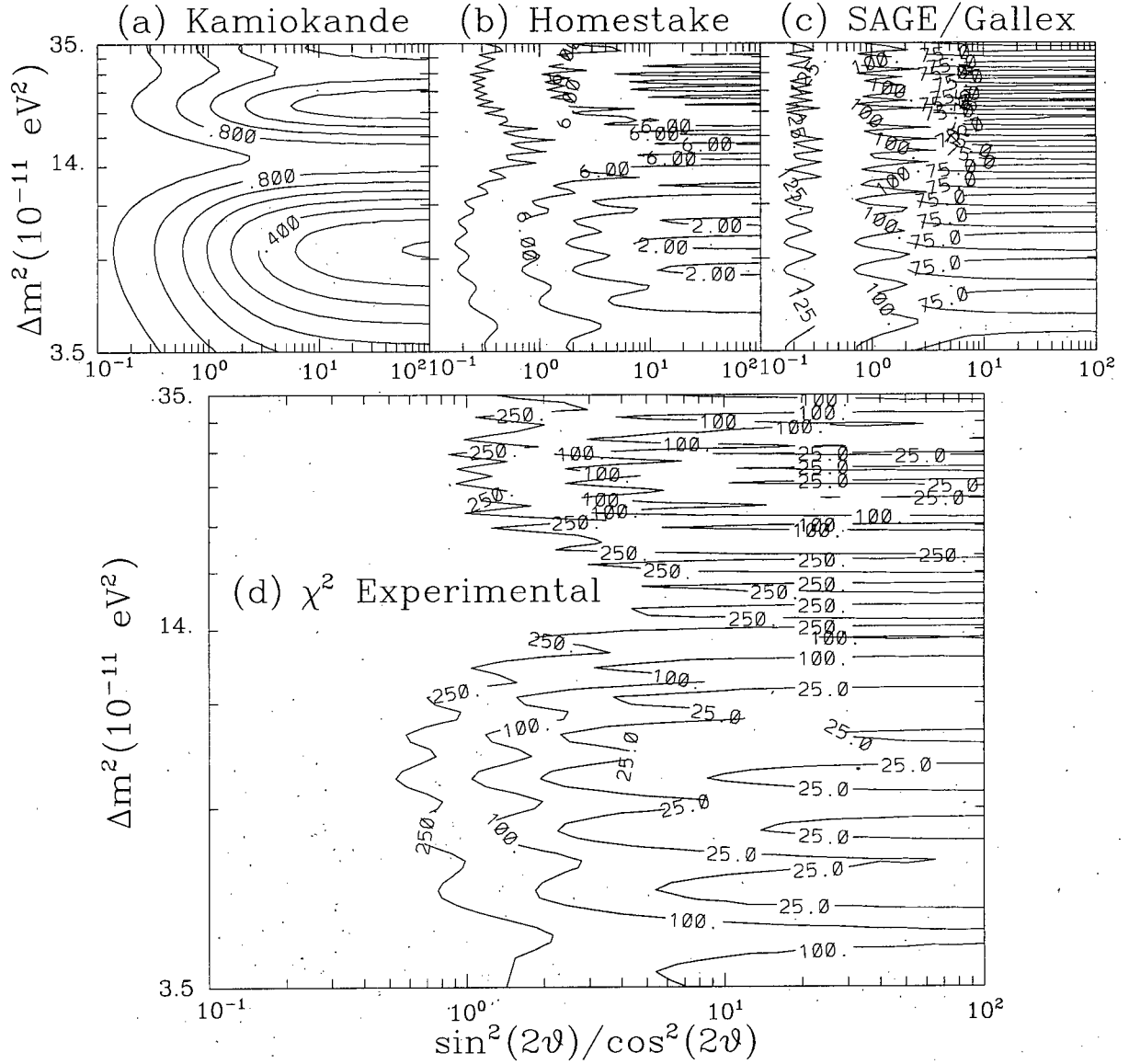


Figure 2.20: Contours of ν_e survival probability for the neutrino experiments as a function of the vacuum oscillation parameters. Kamiokande results (a) shown are a fraction of the total predicted by the SSM, while Homestake (b) and SAGE/Gallex (c) are absolute rates in SNU. In (d), the χ^2 parameter is calculated at each point using the rates measured by the four experiments.

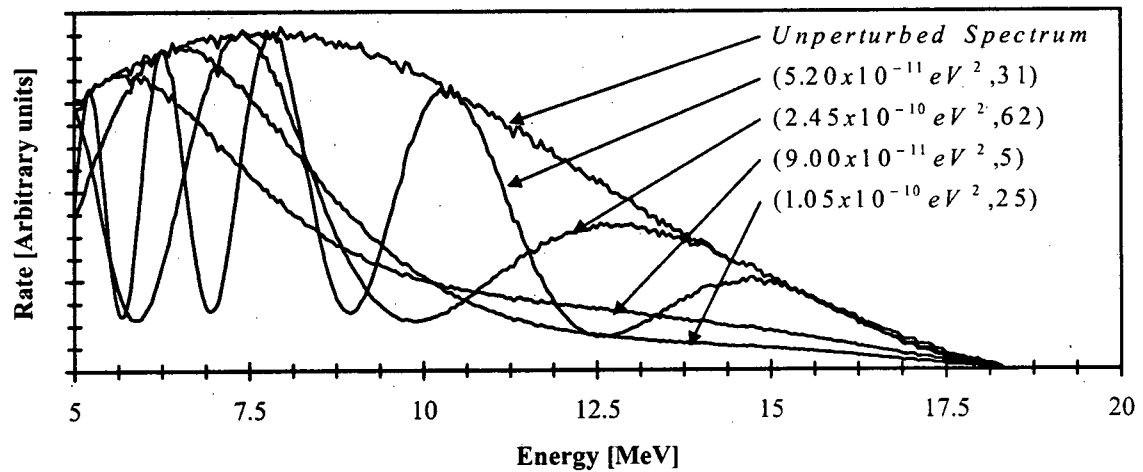


Figure 2.21: Neutrino energy spectra for the four best vacuum oscillation fits to the solar neutrino data identified in table 2.2.

The two most plausible parameter sets have similar spectra but could be differentiated by an experiment with sufficient statistics. More importantly, differences between this figure and 2.19 are very apparent and spectral information from SuperKamiokande will eventually be able to differentiate the two solutions.

Chapter 3

Analytical Results with Three Neutrinos

3.1 Introduction

In spite of experimental evidence that there are three light neutrinos, most early work on neutrino oscillations assumed that just two families were present. The reason was simple practicality; the first investigations examined the feasibility of neutrino oscillations as a solution to the Solar and (later) Atmospheric Neutrino Problems, and early attempts at solving the three neutrino case were wrought with mathematical difficulties.

The two neutrino case has one independent mass difference, and the mixing matrix contains one angular parameter. However with three neutrinos, there are two independent mass differences and a mixing matrix which contains four angular parameters. To determine the mass differences in matter, it is necessary to first solve a complicated cubic equation. While this is possible in principle, it is not easy to obtain a simple solution which algebraically isolates the mass differences and angular parameters in matter as a function of the corresponding parameters in vacuum and the matter density.

In 1980, Barger *et. al.* considered three neutrinos in a medium of uniform density, and concluded that “unfortunately, the algebra is rather impenetrable” [125]. They wrote formal solutions for the mass eigenstates in matter but not the angular parameters, and then constructed approximate solutions in the two cases when the matter density is very small and very large relative to the mass differences, but neither case is useful for the SNP. Kuo and Pantaleone wrote in 1986 that “The expression for the mass matrix, analogous

to [the two neutrino case], is quite complicated. The exact solution can be written down, but its implications are not transparent" [126]. Petcov and Toshev noted in 1987 that "the physical interpretation of these [analytical] expressions is rather difficult" [127].

Even today, authors make extensive simplifications in order to make the analytical calculations tractable. The most common is the *one mass-scale dominant* (OMSD) case, in which the heaviest neutrino is assumed to be larger than any other mass scale in the problem: $m_3^2 \gg m_2^2, m_1^2, A$, where A is the electron density at the centre of the sun. This removes the heaviest neutrino from the solar neutrino problem, and removes two angular parameters from relevance. It will be discussed later in this chapter.

Pantaleone [128] was among the first to discuss reasons for going beyond two families in the analysis of neutrino oscillations. The obvious one is that there are three known families in the standard model and, as the LEP experiment has confirmed, three light neutrinos, so the system should be analysed as such. In spite of its difficulties, the three neutrino solution has a much more robust structure and can therefore accommodate a much wider variety of phenomena.

The two neutrino solutions for the atmospheric data indicate that at least one of the mixing angles is large. In addition, the vacuum and one of the two matter enhanced oscillation solutions to the SNP also have a large mixing angle. Pantaleone pointed out that the reduction of the three neutrino system to a pair of two neutrino systems treated separately is only valid in the case when the mixing angles are small. Since the data do not indicate that this assumption is necessarily valid, more investigation is in order. He also noted that theoretical work into neutrino masses and mixings using the group $SO(10)$ does not necessarily produce small angle mixings.

By itself, the ANP suggests consideration of three neutrinos. Early analyses have always looked at either $\nu_\mu \rightarrow \nu_\tau$ or $\nu_\mu \rightarrow \nu_e$ oscillations separately, but clearly there may be a combination of both. Pantaleone also proposed looking for ν_e appearance at

long baseline experiments, which would be a signature of $\nu_\mu \rightarrow \nu_\tau \rightarrow \nu_e$, a strictly three neutrino effect [129].

In order to determine whether or not neutrino oscillations present a viable solution to experimental data, to accurately measure the values of the parameters using existing and future experiments, and to decide what new experiments should be done to further our understanding, a full three neutrino analysis is absolutely necessary.

There are also compelling reasons to analyse the three neutrino case without the constraints of OMSD. Recent results by Fogli et. al. [130] show that combining all the existing upward-going muon data with both the sub-GeV and multi-GeV atmospheric neutrino data does not rule out Δm_{31}^2 on the order of $5 \times 10^{-4} \text{ eV}^2$ or even slightly lower. This would place that mass squared almost within an order of magnitude of that favoured for Δm_{21}^2 to solve the SNP, thus invalidating the OMSD assumption. Moreover if Δm_{31}^2 is that small, some ν_e 's produced at the centre of the sun may cross two separate resonances on the way to the surface, and solar neutrino parameter spaces would have to be reexamined. Alternately, the SNP might be solved by a combination of, for example, a $\nu_e \rightarrow \nu_\mu$ resonant solution in the sun followed by $\nu_e \leftrightarrow \nu_\mu \leftrightarrow \nu_\tau$ vacuum oscillations as it travels from the sun to earth.

In what follows, new work on the three neutrino Hamiltonian will be developed. While an exact expression for it in the weak eigenbasis will be presented, difficulties in making use of the result in practical problems will become clear. A perturbative solution for small mixing angles will be presented. Then the existing literature on the analytical treatment of three neutrinos will be reviewed, detailing the various assumptions including OMSD which are made by other authors. Next, exact expressions for all neutrino oscillation probabilities at fixed density will be calculated without any simplifications. Finally, some comments will be made on how to do MSW oscillations with three neutrinos, and a neutrino wave function will be propagated from the point of production in the sun across

two resonances and then through space arriving at the earth. An expression to describe it will be shown to simplify to a classical one when averaged over the phase at the points of production, resonance and detection.

3.2 Developing the Three Neutrino Mass Matrix

Several different parameterisations of the mixing matrix are commonly used. Kuo and Pantaleone popularised one in their important 1989 review of the field [87]. It has the advantage of being a product of four matrices, the first two of which commute with the matrix added to the Hamiltonian in the presence of matter. As a result, two parameters can be explicitly rotated away when the matter term is added.

The parameterisation chosen here, which is more common in the literature, is the classic Cabibbo-Kobayashi-Maskawa (CKM) matrix. It is chosen for consistency with the quark sector and because most authors use it. If CP is conserved in nature, so that the complex phase δ in the matrix is set to zero, then all standard choices of mixing matrices used in the literature are the same. Calculations of probabilities from the various mixing matrices are also identical.

Harari and Leurer [131] recommended a standard parameterisation for $N \times N$ mixing matrices which can be simply extended to any number of generations. When $N = 3$ it is the CKM matrix, and can be decomposed as follows:

$$\begin{aligned}
 V_{\alpha i} &= \begin{pmatrix} 1 & 0 & 0 \\ 0 & c_{23} & s_{23} \\ 0 & -s_{23} & c_{23} \end{pmatrix} \begin{pmatrix} c_{13} & 0 & s_{13}e^{-i\delta_{13}} \\ 0 & 1 & 0 \\ -s_{13}e^{i\delta_{13}} & 0 & c_{13} \end{pmatrix} \begin{pmatrix} c_{12} & s_{12} & 0 \\ -s_{12} & c_{12} & 0 \\ 0 & 0 & 1 \end{pmatrix} \\
 &= \begin{pmatrix} c_{12}c_{13} & s_{12}c_{13} & s_{13}e^{-i\delta_{13}} \\ -s_{12}c_{23} - c_{12}s_{23}s_{13}e^{i\delta_{13}} & c_{12}c_{23} - s_{12}s_{23}s_{13}e^{i\delta_{13}} & s_{23}c_{13} \\ s_{12}s_{23} - c_{12}c_{23}s_{13}e^{i\delta_{13}} & -c_{12}s_{23} - s_{12}c_{23}s_{13}e^{i\delta_{13}} & c_{23}c_{13} \end{pmatrix} \quad (3.1)
 \end{aligned}$$

where $c_{ij} \equiv \cos(\theta_{ij})$ and $s_{ij} \equiv \sin(\theta_{ij})$. Each of the three mixing angles is in the range $0 \leq \theta_{ij} \leq \frac{\pi}{2}$ while the complex phase δ_{13} can have any value from 0 to 2π . Clearly if any two of the mixing angles vanish (and $\delta_{13} = 0$ if $s_{12} = s_{23} = 0$), then one neutrino decouples and $V_{\alpha i}$ reduces to a normal two-dimensional mixing matrix.

The weak neutrino eigenstates can now be related to the mass eigenstates via the CKM matrix:

$$\begin{pmatrix} \nu_e \\ \nu_\mu \\ \nu_\tau \end{pmatrix} = V_{\alpha i} \begin{pmatrix} \nu_1 \\ \nu_2 \\ \nu_3 \end{pmatrix} \quad (3.2)$$

By definition, the mass eigenstates diagonalise the Hamiltonian, so the time evolution is given by:

$$i \frac{d}{dt} \begin{pmatrix} \nu_1 \\ \nu_2 \\ \nu_3 \end{pmatrix} = \begin{pmatrix} E_1 & 0 & 0 \\ 0 & E_2 & 0 \\ 0 & 0 & E_3 \end{pmatrix} \begin{pmatrix} \nu_1 \\ \nu_2 \\ \nu_3 \end{pmatrix} \quad (3.3)$$

In analogy with the two neutrino case, assuming the neutrinos are ultrarelativistic, one can approximate $E_i = \sqrt{k^2 + m_i^2} \approx k(1 + \frac{m_i^2}{2k^2})$. Subtracting k times the identity matrix from the Hamiltonian only adds an overall phase to the wavefunction and replaces each E_i in equation 3.3 with $\frac{m_i^2}{2k} \approx \frac{m_i^2}{2E}$. Then subtracting a further $\frac{1}{3} \left[\frac{1}{2E} (m_1^2 + m_2^2 + m_3^2) \right]$ times the identity, again changing only the phase, renders Hamiltonian traceless. Using 3.2 to switch bases, the time evolution equation for the weak eigenstates can be written as:

$$i \frac{d}{dt} \begin{pmatrix} \nu_e \\ \nu_\mu \\ \nu_\tau \end{pmatrix} = \frac{1}{6E} V_{\alpha i} \begin{pmatrix} -\Delta m_{31}^2 - \Delta m_{21}^2 & 0 & 0 \\ 0 & 2\Delta m_{21}^2 - \Delta m_{31}^2 & 0 \\ 0 & 0 & 2\Delta m_{31}^2 - \Delta m_{21}^2 \end{pmatrix} V_{\alpha i}^{-1} \begin{pmatrix} \nu_e \\ \nu_\mu \\ \nu_\tau \end{pmatrix} \quad (3.4)$$

where $\Delta m_{ij}^2 \equiv m_i^2 - m_j^2$. Calculating the Hamiltonian in matter, using the definitions given in 3.1 is a straightforward task, but one which is non-trivial because of the number of terms. Defining $H_{e\mu\tau}$ to be the Hamiltonian operator on the right hand side of equation 3.4 one can write its components as follows:

$$(H_{e\mu\tau})_{ee} = \left(s_{12}^2 c_{13}^2 - \frac{1}{3}\right) \frac{\Delta m_{21}^2}{2E} + \left(s_{13}^2 - \frac{1}{3}\right) \frac{\Delta m_{31}^2}{2E} \quad (3.5)$$

$$(H_{e\mu\tau})_{\mu\mu} = \left(c_{12}^2 c_{23}^2 - \frac{1}{3} + s_{12}^2 s_{13}^2 s_{23}^2 - 2s_{12}c_{12}s_{13}s_{23}c_{23}c_\delta\right) \frac{\Delta m_{21}^2}{2E} + \left(c_{13}^2 s_{23}^2 - \frac{1}{3}\right) \frac{\Delta m_{31}^2}{2E} \quad (3.6)$$

$$(H_{e\mu\tau})_{\tau\tau} = \left(c_{12}^2 s_{23}^2 - \frac{1}{3} + s_{12}^2 s_{13}^2 c_{23}^2 + 2s_{12}c_{12}s_{13}s_{23}c_{23}c_\delta\right) \frac{\Delta m_{21}^2}{2E} + \left(c_{13}^2 c_{23}^2 - \frac{1}{3}\right) \frac{\Delta m_{31}^2}{2E} \quad (3.7)$$

$$(H_{e\mu\tau})_{e\mu} = s_{12}c_{13} \left(c_{12}c_{23} - s_{12}s_{13}s_{23}e^{-i\delta}\right) \frac{\Delta m_{21}^2}{2E} + s_{13}c_{13}s_{23}e^{-i\delta} \frac{\Delta m_{31}^2}{2E} \quad (3.8)$$

$$(H_{e\mu\tau})_{e\tau} = -s_{12}c_{13} \left(c_{12}s_{23} + s_{12}s_{13}c_{23}e^{-i\delta}\right) \frac{\Delta m_{21}^2}{2E} + s_{13}c_{13}c_{23}e^{-i\delta} \frac{\Delta m_{31}^2}{2E} \quad (3.9)$$

$$(H_{e\mu\tau})_{\mu\tau} = [s_{23}c_{23}(s_{12}^2 s_{13}^2 - c_{12}^2) + s_{12}c_{12}s_{13}((s_{23}^2 - c_{23}^2)c_\delta + i s_\delta)] \frac{\Delta m_{21}^2}{2E} + c_{13}^2 s_{23}c_{23} \frac{\Delta m_{31}^2}{2E} \quad (3.10)$$

where $s_{ij} = \sin(\theta_{ij})$ and $c_{ij} = \cos(\theta_{ij})$ as before, $c_\delta = \cos(\delta)$ and $s_\delta = \sin(\delta)$. Noting that $(H_{e\mu\tau})_{\alpha\beta} = (H_{e\mu\tau})_{\beta\alpha}^\dagger$, this defines the Hamiltonian in vacuum in the weak eigenbasis.

What is obvious is the complexity of the matrix compared to the two neutrino case. Following the analogy with the last chapter, one would then add a term $\sqrt{2}G_F N_e$ to $(H_{e\mu\tau})_{ee}$ and solve the cubic equation. Many authors note that, at least formally, this procedure solves the system in matter. However, even when Zaglauer and Schwarzer wrote explicit expressions for $(s_{ij}^2)_M$, $(\Delta m_{ij}^2)_M$, δ_M as functions of the vacuum parameters Δm_{ij}^2 , s_{ij}^2 , δ and N_e [132], it was not obvious how to apply the unwieldy result to experiments.

3.3 Perturbation solutions with small angles

The majority of work in three neutrino oscillations has assumed that the heaviest neutrino mass is much larger than any other in the problem, so that perturbations can be calculated assuming a fixed Δm_{31}^2 . However, another perturbative solution assumes that the mixing angles are small and the matter density does not place the system at resonance. It puts no other restrictions on the size or hierarchy of the masses. The mixing angles in the quark sector are small and there is a small angle solution to the solar neutrino data, although atmospheric experiments seem to suggest at least one large angle. Then the Hamiltonian can be diagonalised to fixed orders of the $\sin(\theta_{ij})$'s.

The CKM matrix can be written, to first order in the mixing angles, as

$$V_{\alpha i} = \begin{pmatrix} 1 & 0 & 0 \\ 0 & 1 & 0 \\ 0 & 0 & 1 \end{pmatrix} + \varepsilon \begin{pmatrix} 0 & 1 & xe^{-i\delta_{13}} \\ -1 & 0 & y \\ -xe^{i\delta_{13}} & -y & 0 \end{pmatrix} + O(\varepsilon^2) \quad (3.11)$$

where $\varepsilon \equiv s_{12}$, $x\varepsilon \equiv s_{13}$ and $y\varepsilon \equiv s_{23}$. Now converting the mass eigenstate Hamiltonian to weak basis version and adding a matter term to $H_{ee} \rightarrow H_{ee} + A$, the modified masses in matter can be shown to be:

$$(\Delta m_{21}^2)_M = (\Delta m_{21}^2)_V - A + \frac{2s_{12}^2 (\Delta m_{21}^2)_V A}{(\Delta m_{21}^2)_V - A} + \frac{s_{13}^2 (\Delta m_{31}^2)_V A}{(\Delta m_{31}^2)_V - A} + O(\varepsilon^4) \quad (3.12)$$

$$(\Delta m_{31}^2)_M = (\Delta m_{31}^2)_V - A + \frac{2s_{13}^2 (\Delta m_{31}^2)_V A}{(\Delta m_{31}^2)_V - A} + \frac{s_{12}^2 (\Delta m_{21}^2)_V A}{(\Delta m_{21}^2)_V - A} + O(\varepsilon^4) \quad (3.13)$$

where the assumption that A is not close to either mass squared difference in vacuum is used in the calculation. Note that neither θ_{23} nor δ enters at this level—matter is only dependent on those mixing angles which are directly coupled to the ν_1 state at this order.

3.4 Review of existing three neutrino work

In order to make additional progress in three neutrino solutions, some assumptions have been made. The difficulty these calculations face is that with too many simplifications, the system becomes little more than a two neutrino analysis; too few make any useful calculation, like an estimate of the number of solar neutrinos seen by experiments, analytically unfeasible. A second challenge is to illustrate the results of calculations—with six parameters it is not obvious how to present the data.

Early work by Barger *et. al.* [125] looked at two approximations, one in the limit of small matter density and one at very large density. The former may be relevant to long baseline experiments and the latter may be of use in neutron stars, but neither case is important to solar neutrinos.

Toshev and Petcov did some analytical work to determine matter enhanced parameterisations in the limit of small mixing angles [133], [127]. In the second of these studies, they assumed the mass hierarchy $m_1 < m_2 < m_3$ and examined three cases when the matter oscillation length $L_e = \frac{2\pi}{\sqrt{2}G_F N_e}$ was smaller, in between, and larger than the two vacuum oscillation lengths $L_V^{12} = \frac{4\pi E}{\Delta m_{21}^2}$ and $L_V^{31} = \frac{4\pi E}{\Delta m_{31}^2}$. But with little experimental data, few quantitative statements could be made.

Vacuum mixing of three neutrino flavours has also been studied. Acker *et. al.* [134] considered two regions of parameter space which provided solutions to the solar and atmospheric neutrino problems. With three large mass squared differences, they found that $P(\nu_e \rightarrow \nu_e) \approx \frac{1}{3}$ is allowed by solar neutrino experiments with a 90% confidence level. Then dropping δ dependence, they found a solution with $0.48 < |\sin \theta_{13}| < 0.65$ and $0.6 < |\sin \theta_{12}| < 0.8$. A second solution assumes that $\Delta m_{21}^2 \leq 10^{-6} \text{ eV}^2$. In that case they find that the atmospheric neutrino experiments set limits $0.44 < |\sin \theta_{23}| < 1.0$ and $0 < |\sin \theta_{13}| < 0.92$ while the solar neutrinos are solved by essentially two neutrino

oscillations with $0.55 < |\sin \theta_{12}| < 0.70$.

Maximal mixing solutions have also been studied by C.W. Kim and collaborators [135], [136]. They found that the mass hierarchy splits so that $\Delta m_{21}^2 \simeq 10^{-10} \text{ eV}^2$ solves the SNP while $\Delta m_{31}^2 = 10^{-3} - 10^{-1} \text{ eV}^2$ solves the ANP. These results are essentially vacuum oscillation results. Joshipura and Murthy showed that with three neutrinos, if maximal mixing exists between any two eigenstates at resonance, then the problem reduces to a two neutrino case with the third neutrino decoupled [137].

Petcov studied the three neutrino problem with two different situations: the *large neutrino mass hierarchy* (LNMH) case in which $m_1 \ll m_2 \ll m_3$ and the *small vacuum mixing angle* (SMVA) case in which $s_{12}, s_{13} \ll 1$, $\Delta m_{31}^2 - \Delta m_{21}^2 \gg s_{12}\Delta m_{21}^2 + s_{13}\Delta m_{31}^2$ [138]. Under these conditions, Petcov wrote a formal, analytical expression for the probability that a ν_e produced at the centre of the sun emerges as a ν_e . He noted that the probability does not depend on either the complex phase δ or the mixing angle θ_{23} , although regeneration effects in the earth were not included. Because of the complexity of the expression, however, no numerical result related to rates at real solar neutrino experiments were presented.

Shi and Schramm [139] calculated allowed regions of parameter space in the LNMH case based on the solar neutrino experiments. They, too, showed that the angles δ and θ_{23} can be dropped, and plotted MS-type diagrams for fixed values of θ_{13} . Bilenky *et. al.* also studied oscillations with this assumption [140], and found constraints on parameters from the atmospheric neutrino experiments assuming that Δm_{21}^2 is the relevant squared mass to solve the solar neutrino problem.

A more popular treatment of the three neutrino case involves the assumption that $\frac{\Delta m_{31}^2}{2E} > \sqrt{2}G_F N_e, \frac{\Delta m_{21}^2}{2E}$ which has been dubbed the *one-mass scale dominant* (OMSD) scenario. The mass condition is chosen so that neutrinos leaving the solar interior only cross one resonance, not two, which simplifies the calculation. The rationale for this

choice is that if $m_1 < m_2 < m_3$, then m_3^2 must be on the order of 10^{-3} eV^2 or larger in order to account for the atmospheric anomaly. The matter induced mass at the centre of the sun is less than 10^{-4} eV^2 , so choosing m_3^2 that large effectively prevents it from being relevant to solar neutrino calculations.

This has been the choice of two of the groups doing the most advanced work to date in this area. Narayan *et. al.* considered OMSD solar oscillations with three neutrinos [141]. They dropped the angles θ_{23} and δ , and assumed that $\Delta m_{31}^2 \gg \Delta m_{21}^2$, A where A is the matter term. Next, they subtracted $m_1^2 I_3$ from the diagonal mass matrix, multiplied it by the two-parameter CKM matrix, and added the matter term. They decomposed the result into the form $M_m^2 = \Delta m_{31}^2 M_{31} + AM_A + \Delta m_{21}^2 M_{21}$ as follows:

$$M_m^2 = \Delta m_{31}^2 \begin{pmatrix} s_{13}^2 & 0 & s_{13}c_{13} \\ 0 & 0 & 0 \\ s_{13}c_{13} & 0 & c_{13}^2 \end{pmatrix} + A \begin{pmatrix} 1 & 0 & 0 \\ 0 & 0 & 0 \\ 0 & 0 & 0 \end{pmatrix} + \Delta m_{21}^2 \begin{pmatrix} c_{13}^2 s_{12}^2 & c_{13}s_{12}c_{12} & -c_{13}s_{13}s_{12}^2 \\ c_{13}s_{12}c_{12} & c_{12}^2 & -s_{13}s_{12}c_{12} \\ -c_{13}s_{13}s_{12}^2 & -s_{13}s_{12}c_{12} & s_{13}^2 s_{12}^2 \end{pmatrix} \quad (3.14)$$

Now rather than solving the eigenvalue problem algebraically, they treated AM_A and $\Delta m_{21}^2 M_{21}$ as small corrections to $\Delta m_{31}^2 M_{31}$ and solved the system perturbatively. The eigenvectors thus obtained specify the matter enhanced mixing matrix, and expressions relating the matter enhanced parameters in terms of the vacuum values and A were calculated.

With this formalism, Narayan *et. al.* found two solutions to the solar neutrino data in which θ_{13} is small, in analogy with the two solutions present in the two neutrino analysis. In addition, they found three new solutions with larger θ_{13} —these are non-trivial three neutrino effects.

In another paper, Narayan *et. al.* [142] used a similar formalism to examine the ANP. In that case they dropped the complex phase δ for simplicity, and argued that $\Delta m_{21}^2 \ll 10^{-3} \text{ eV}^2$ is too small to be relevant for earth-bound oscillations, so they also dropped the mixing angle θ_{12} . They calculated the new mass eigenvalues m_2^2 and m_3^2 as well as the matter enhanced θ_{13} , and noted that θ_{23} is not affected by the presence of matter. Regions of allowed parameter space to explain the ANP were analysed, and the group found that $8^\circ \leq \theta_{13} \leq 40^\circ$, $0 \leq \theta_{23} \leq 90^\circ$ and $0.005 \text{ eV}^2 \leq \Delta m_{31}^2 \leq 5 \text{ eV}^2$.

Fogli *et. al.* [144] assumed that the CKM matrix is diagonally dominant, in particular $s_{ij}^2 \leq \frac{1}{2}$, which guarantees a unique determination of $\sin(\theta_{ij})$ given a value for $\sin^2(2\theta_{ij})$. In later work they relaxed these angular conditions, but did assume that $m_1 = 0$, $\delta m^2 \equiv m_2^2 \leq 10^{-4} \text{ eV}^2$, $m^2 \equiv m_3^2 \geq 10^{-3} \text{ eV}^2$ [145]. They also argued that CP-violating effects are unobservable, so δ is not relevant. In this framework, the solar neutrino problem is a function of δm^2 , θ_{12} , and θ_{13} , while m^2 oscillations are “averaged out.” The atmospheric neutrino problem is a function of m^2 , θ_{13} , and θ_{23} while δm^2 oscillations are “frozen out.” They went on to analyse the solar neutrino problem with one additional angular parameter, δ , and found that although there are no solutions with $\theta_{12} > \frac{\pi}{4}$, there are solutions with $\theta_{13} > \frac{\pi}{4}$.

Fogli and Lisi [146] also considered the LBNO experiments, and defined the quantities $n_{0\mu}$, $n_{1\mu}$, $N_{0\mu}$, $N_{1\mu}$ to be the number of events with zero or one muon produced at near (n) and far (N) detectors. Next they defined $t = \frac{n_{1\mu}}{n_{1\mu} + n_{0\mu}}$, $T = \frac{N_{1\mu}}{N_{1\mu} + N_{0\mu}}$ and proposed two tests to describe long baseline neutrino oscillations: the *T-test* $Q_T = 1 - \frac{T}{t}$ and the far/near-test $Q_{f/n} = 1 - \frac{N_{1\mu}}{n_{1\mu}} \frac{L_{far}^2}{L_{near}^2}$. Both quantities deviate from unity if oscillations are present.

In a more recent paper, Fogli *et. al.* [147] carefully analysed the ANP results with a Cauchy distribution. They found that $\nu_\mu - \nu_e$ oscillations provide a better fit to the experimental data than $\nu_\mu - \nu_\tau$, while three neutrino oscillations marginally improve the

fit with $6 \times 10^{-4} \text{ eV}^2 < m^2 < 6 \times 10^{-2} \text{ eV}^2$. Finally, they noted that regions of parameter space which solve the SNP and ANP don't necessarily satisfy the *OMSD* assumption that $\delta m^2 \ll m^2$.

Kuo and Pantaleone have written extensively on this subject over the years. They use a parameterisation of the mixing matrix based on the Gell-Mann λ matrices of the form $U = \exp(i\psi\lambda_7)\Gamma\exp(i\phi\lambda_5)\exp(i\omega\lambda_2)$, where $\Gamma = \text{diag}(1, e^{i\delta}, e^{-i\delta})$. With this choice, ψ , ϕ and ω correspond to θ_{23} , θ_{13} and θ_{12} respectively. The first two terms of this parameterisation commute with the induced mass term, so the mass of the ν_e in matter is independent of both ψ and δ [148].

In their early work, Kuo and Pantaleone looked at the three neutrino problem in the small mixing angle approximation [126], and later at a case where the mass scales are well separated or the mixing angles are large [149]. This latter paper also plotted contours of constant probability for the chlorine experiment with fixed mixing angles as a function of the two mass differences, and as a function of m_2 and $|U_{e2}|^2$ when the ratios m_2/m_3 and $|U_{e2}|^2/|U_{e3}|^2$ were held constant. In a subsequent paper, Harley, Kuo, and Pantaleone calculated the survival probability of neutrinos leaving the sun as a function of m_2^2 , m_3^2 and $|U_{e2}|^2$ for fixed $|U_{e3}|^2$ and m_2^2 , $|U_{e2}|^2$ and $|U_{e3}|^2$ for fixed m_3^2 [150]. These calculations assumed that the angle δ vanishes, and did not include vacuum oscillations on the path from the sun to earth or the regeneration effect, so θ_{23} is not relevant either.

Zaglaur and Schwarzer [132] were able to calculate analytical expressions for the matter enhanced parameters. The complexity of these solutions has prevented them from being used in many practical calculations in the literature. However, they will be used extensively in Chapter 5 to calculate oscillation probabilities to second order in $\frac{2\sqrt{2}G_F N_e}{\Delta m_{31}^2}$ and $\frac{\Delta m_{21}^2}{\Delta m_{31}^2}$.

They wrote the matter term as $D = 2\sqrt{2}G_F N_e E$ (note the change in notation—thus far A has been used for the matter term, while Zaglauer and Schwarz used A as

defined below), and quote the following expressions for the matter enhanced squared mass differences:

$$m_{1,M}^2 = m_1^2 + \frac{A}{3} - \frac{1}{3}\sqrt{A^2 - 3BS} - \frac{\sqrt{3}}{3}\sqrt{A^2 - 3B}\sqrt{1 - S^2} \quad (3.15)$$

$$m_{2,M}^2 = m_1^2 + \frac{A}{3} - \frac{1}{3}\sqrt{A^2 - 3BS} + \frac{\sqrt{3}}{3}\sqrt{A^2 - 3B}\sqrt{1 - S^2} \quad (3.16)$$

$$m_{3,M}^2 = m_1^2 + \frac{A}{3} + \frac{2}{3}\sqrt{A^2 - 3BS} \quad (3.17)$$

where quantities A , B , C and S are given by

$$A = (\Delta m_{21}^2)_V + (\Delta m_{31}^2)_V + D \quad (3.18)$$

$$B = (\Delta m_{21}^2)_V (\Delta m_{31}^2)_V + D \left[(\Delta m_{31}^2)_V c_{13}^2 + (\Delta m_{21}^2)_V (c_{13}^2 c_{12}^2 + s_{13}^2) \right] \quad (3.19)$$

$$C = D (\Delta m_{31}^2)_V (\Delta m_{21}^2)_V c_{13}^2 c_{12}^2 \quad (3.20)$$

$$S = \cos \left[\frac{1}{3} \arccos \left(\frac{2A^3 - 9AB + 27C}{2(A^2 - 3B)^{3/2}} \right) \right] \quad (3.21)$$

These solutions were previously written by Barger *et. al.* [125]. However Zaglauer and Schwarzer continued the calculation and obtained the eigenvectors and therefore the mixing angles in matter [132]. Their work will be applied to help obtain the numerical solution of the mass matrix in the next chapter, as well as to test that solution. Their results are as follows:

$$s_{12,M}^2 = \frac{-(m_{2,M}^4 - \alpha m_{2,M}^2 + \beta) (\Delta m_{31}^2)_M}{(\Delta m_{32}^2)_M (m_{1,M}^4 - \alpha m_{1,M}^2 + \beta) + (\Delta m_{31}^2)_M (m_{2,M}^4 - \alpha m_{2,M}^2 + \beta)} \quad (3.22)$$

$$s_{13,M}^2 = \frac{m_{3,M}^4 - \alpha m_{3,M}^2 + \beta}{(\Delta m_{31}^2)_M (\Delta m_{32}^2)_M} \quad (3.23)$$

$$s_{23,M}^2 = \frac{E^2 s_{23}^2 + F^2 c_{23}^2 + 2EF c_{23} s_{23} c_\delta}{E^2 + F^2} \quad (3.24)$$

$$e^{-i\delta_M} = \frac{(E^2 e^{-i\delta} - F^2 e^{i\delta}) s_{23} c_{23} + EF (c_{23}^2 - s_{23}^2)}{\sqrt{(E^2 s_{23}^2 + F^2 c_{23}^2 + 2EF c_{23} s_{23} c_\delta) (E^2 c_{23}^2 + F^2 s_{23}^2 - 2EF c_{23} s_{23} c_\delta)}} \quad (3.25)$$

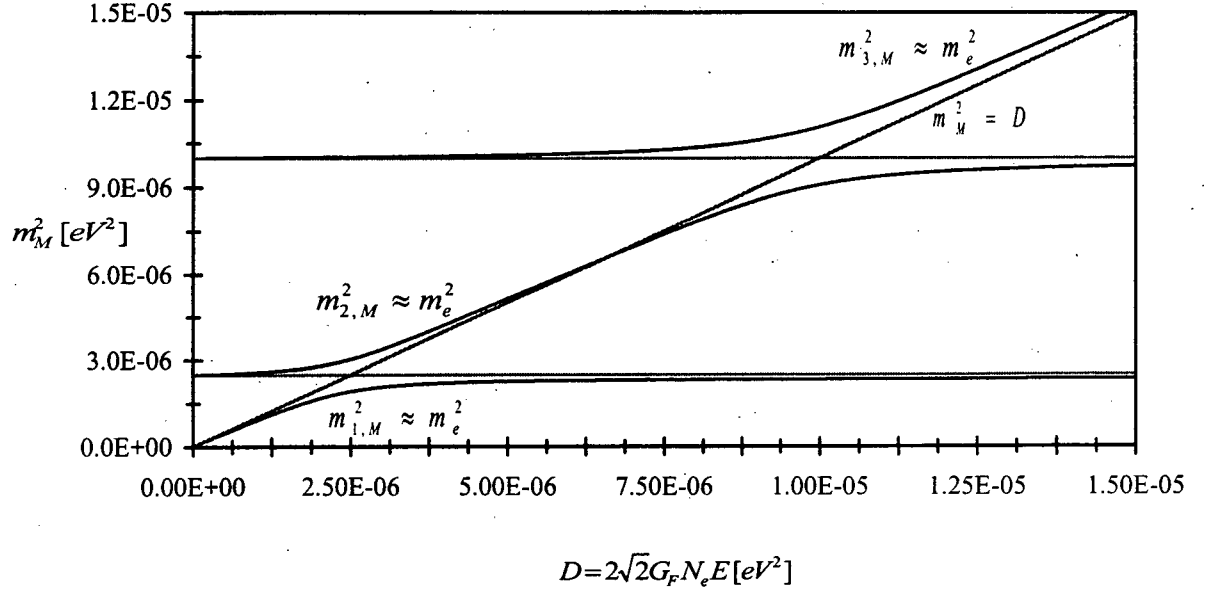


Figure 3.1: Matter enhancement of the mass eigenstates as a function of electron density with three neutrinos. It is assumed that the electron neutrino corresponds most closely to m_1 in vacuum and the mixing angles are given by $\sin^2(2\theta_{13}) = 0.01$ and $\sin^2(2\theta_{12}) = 0.05$.

where the quantities α , β , E and F are given by:

$$\alpha = m_3^2 c_{13}^2 + m_2^2 (c_{13}^2 c_{12}^2 + s_{13}^2) + m_1^2 (c_{13}^2 s_{12}^2 + s_{13}^2) \quad (3.26)$$

$$\beta = m_3^2 c_{13}^2 (m_2^2 c_{12}^2 + m_1^2 s_{12}^2) + m_2^2 m_1^2 s_{13}^2 \quad (3.27)$$

$$E = [\Delta m_{31}^2 (m_{3,M}^2 - m_2^2) - \Delta m_{21}^2 (m_{3,M}^2 - m_3^2) s_{12}^2] c_{13} s_{13} \quad (3.28)$$

$$F = (m_{3,M}^2 - m_3^2) \Delta m_{21}^2 c_{12} s_{12} c_{13} \quad (3.29)$$

3.5 Oscillation probabilities with fixed density

The existing work analytical work in the literature can be extended, and exact expressions for neutrino oscillation probabilities at zero or fixed density will be given. In certain situations, particularly earth-bound long baseline experiments, it is possible to assume

that the electron density is either zero or constant. The last chapter found that, at least with two neutrinos, matter effects do not come into play except at very long baselines on the order of hundreds of kilometres. So for shorter baselines, it should be possible to calculate the probability of neutrino flavour conversion with three neutrinos using vacuum oscillations.

Moreover, it was also found that fairly accurate predictions could be obtained for very long baseline oscillation experiments by assuming an average density over the entire path. Thus, if the oscillation parameters at fixed density are calculated, oscillation probabilities in matter can be obtained from the vacuum results by inserting the effective parameters (modified by matter) in place of their vacuum counterparts. Either the analytical calculation of the CKM parameters in matter by Zaglauer and Schwarzer [132] can be substituted, or the numerical solution presented in the next chapter. While the exact solution is much faster to calculate, the numerical result is more stable because it was designed for the approximate floating point arithmetic performed by computers.

Analytical calculation of the neutrino oscillations with three neutrinos has been done in the literature in several *limited* cases in which some simplifications are made to reduce the number of CKM parameters. What is presented here, however, extends that work by calculating neutrino oscillation probabilities in vacuum without any assumptions about the values of those parameters. The results can be extended to fixed electron density by replacing all parameters with the corresponding effective values in matter.

The amplitude and probability for a neutrino produced as a ν_α at time $t = 0$, propagating through space and being detected as a ν_β at a later time t is given by:

$$\begin{aligned} \langle \nu_\beta(t) | \nu_\alpha \rangle &= \sum_{i,j=1}^3 \langle \nu_i | V_{\beta i}^\dagger e^{iE_j t} V_{\alpha j} | \nu_j \rangle \\ &= \sum_{j=1}^3 V_{\beta j}^\dagger V_{\alpha j} e^{iE_j t} \end{aligned} \quad (3.30)$$

$$P_{\alpha\beta} \equiv P(\nu_\alpha \rightarrow \nu_\beta; t) = |\langle \nu_\beta(t) | \nu_\alpha \rangle|^2 \quad (3.31)$$

where the CKM matrix $V_{\alpha i}$ given in equations 3.1 and 3.2 defines the relation between the weak and mass eigenbases. Converting time parameter from t to length parameter L , the individual probabilities can be shown to be:

$$P_{ee}(L) = 1 - 4s_{12}^2 c_{12}^2 c_{13}^4 \mathbf{S}_{21}^2 - 4c_{12}^2 s_{13}^2 c_{13}^2 \mathbf{S}_{31}^2 - 4s_{12}^2 s_{13}^2 c_{13}^2 \mathbf{S}_{32}^2 \quad (3.32)$$

$$\begin{aligned} P_{\mu\mu}(L) = & 1 - 4[s_{12}^2 c_{12}^2 (c_{23}^2 - s_{13}^2 s_{23}^2)^2 + s_{13}^2 s_{23}^2 c_{23}^2 - 4s_{12}^2 c_{12}^2 s_{13}^2 s_{23}^2 c_{23}^2 c_\delta^2 \\ & - 2s_{12} c_{12} s_{13} s_{23} c_{23} c_\delta (s_{12}^2 - c_{12}^2) (c_{23}^2 - s_{13}^2 s_{23}^2)] \mathbf{S}_{21}^2 \\ & - 4c_{13}^2 s_{23}^2 [s_{12}^2 c_{23}^2 + c_{12}^2 s_{13}^2 s_{23}^2 + 2s_{12} c_{12} s_{13} s_{23} c_{23} c_\delta] \mathbf{S}_{31}^2 \\ & - 4c_{13}^2 s_{23}^2 [c_{12}^2 c_{23}^2 + s_{12}^2 s_{13}^2 s_{23}^2 - 2s_{12} c_{12} s_{13} s_{23} c_{23} c_\delta] \mathbf{S}_{32}^2 \end{aligned} \quad (3.33)$$

$$\begin{aligned} P_{\tau\tau}(L) = & 1 - 4[s_{12}^2 c_{12}^2 (s_{23}^2 - s_{13}^2 c_{23}^2)^2 + s_{13}^2 s_{23}^2 c_{23}^2 - 4s_{12}^2 c_{12}^2 s_{13}^2 s_{23}^2 c_{23}^2 c_\delta^2 \\ & + 2s_{12} c_{12} s_{13} s_{23} c_{23} c_\delta (s_{12}^2 - c_{12}^2) (s_{23}^2 - s_{13}^2 c_{23}^2)] \mathbf{S}_{21}^2 \\ & - 4c_{13}^2 c_{23}^2 [s_{12}^2 s_{23}^2 + c_{12}^2 s_{13}^2 c_{23}^2 - 2s_{12} c_{12} s_{13} s_{23} c_{23} c_\delta] \mathbf{S}_{31}^2 \\ & - 4c_{13}^2 c_{23}^2 [c_{12}^2 s_{23}^2 + s_{12}^2 s_{13}^2 c_{23}^2 + 2s_{12} c_{12} s_{13} s_{23} c_{23} c_\delta] \mathbf{S}_{32}^2 \end{aligned} \quad (3.34)$$

$$\begin{aligned} P_{e\mu}(L) = & 4s_{12}^2 c_{12}^2 c_{13}^2 (c_{23}^2 - s_{13}^2 s_{23}^2) \mathbf{S}_{21}^2 + 4c_{12}^2 s_{13}^2 c_{13}^2 s_{23}^2 \mathbf{S}_{31}^2 \\ & + 4s_{12}^2 s_{13}^2 c_{13}^2 s_{23}^2 \mathbf{S}_{32}^2 + 4s_{12} c_{12} s_{13} c_{13}^2 s_{23} c_{23} \times \\ & [(s_{12}^2 - c_{12}^2) \mathbf{S}_\delta^2 + c_{12}^2 \mathbf{S}_{21+\delta}^2 - s_{12}^2 \mathbf{S}_{21-\delta}^2 + \mathbf{S}_{31-\delta}^2 - \mathbf{S}_{32-\delta}^2] \end{aligned} \quad (3.35)$$

$$\begin{aligned} P_{e\tau}(L) = & 4s_{12}^2 c_{12}^2 c_{13}^2 (s_{23}^2 - s_{13}^2 c_{23}^2) \mathbf{S}_{21}^2 + 4c_{12}^2 s_{13}^2 c_{13}^2 c_{23}^2 \mathbf{S}_{31}^2 \\ & + 4s_{12}^2 s_{13}^2 c_{13}^2 c_{23}^2 \mathbf{S}_{32}^2 - 4s_{12} c_{12} s_{13} c_{13}^2 s_{23} c_{23} \times \\ & [(s_{12}^2 - c_{12}^2) \mathbf{S}_\delta^2 + c_{12}^2 \mathbf{S}_{21+\delta}^2 - s_{12}^2 \mathbf{S}_{21-\delta}^2 + \mathbf{S}_{31-\delta}^2 - \mathbf{S}_{32-\delta}^2] \end{aligned} \quad (3.36)$$

$$\begin{aligned} P_{\mu\tau}(L) = & 4[s_{12}^2 c_{12}^2 s_{13}^2 + s_{13}^2 s_{23}^2 c_{23}^2 - s_{12}^2 c_{12}^2 s_{23}^2 c_{23}^2 (1 + s_{13}^2)^2 \\ & + 2s_{12} c_{12} s_{13} s_{23} c_{23} c_\delta (s_{12}^2 - c_{12}^2) (s_{23}^2 - c_{23}^2) - 4s_{12}^2 c_{12}^2 s_{13}^2 s_{23}^2 c_{23}^2 c_\delta^2] \mathbf{S}_{21}^2 \\ & + 4c_{13}^2 s_{23}^2 c_{23}^2 (s_{12}^2 - c_{12}^2 s_{13}^2) \mathbf{S}_{31}^2 + 4c_{13}^2 s_{23}^2 c_{23}^2 (c_{12}^2 - s_{12}^2 s_{13}^2) \mathbf{S}_{32}^2 \\ & + 4s_{12} c_{12} s_{13} c_{13}^2 s_{23} c_{23} [(s_{12}^2 - c_{12}^2) (s_{23}^2 - c_{23}^2) \mathbf{S}_\delta^2 + s_{23}^2 (\mathbf{S}_{31-\delta}^2 - \mathbf{S}_{32-\delta}^2) \\ & - c_{23}^2 (\mathbf{S}_{31+\delta}^2 - \mathbf{S}_{32+\delta}^2) + (s_{12}^2 c_{23}^2 + c_{12}^2 s_{23}^2) \mathbf{S}_{21+\delta}^2 - (s_{12}^2 s_{23}^2 + c_{12}^2 c_{23}^2) \mathbf{S}_{21-\delta}^2] \end{aligned} \quad (3.37)$$

$$P_{\alpha\beta}(\delta, L) = P_{\beta\alpha}(-\delta, L) \quad (3.38)$$

where $s_{ij} \equiv \sin(\theta_{ij})$, $c_{ij} \equiv \cos(\theta_{ij})$, $s_\delta \equiv \sin(\delta)$, $c_\delta \equiv \cos(\delta)$ and $S_{ji\pm\delta}^2 \equiv \sin^2 \left(\frac{1.27\Delta m_{ji}^2 L}{E} \pm \frac{\delta}{2} \right)$.

Note that these probabilities are valid in the ultrarelativistic limit where $E_\nu^2 \gg m_i^2$.

While the algebra required is tedious and might otherwise be prone to error, there are several independent checks for accuracy. First, the unitarity condition $\sum_{\beta=e\mu\tau} P_{\alpha\beta} = 1 \quad \forall \alpha$ was verified. Second, all nine oscillation probabilities were calculated and the relation 3.38 was used to compare $P_{e\mu}$, $P_{e\tau}$ and $P_{\mu\tau}$ to $P_{\mu e}$, $P_{\tau e}$ and $P_{\tau\mu}$ respectively. Third, a CKM matrix symmetry $V_{\mu\alpha}(s_{23}, c_{23}) = V_{\tau\alpha}(c_{23}, -s_{23})$ admits two more conditions, $P_{\mu\mu}(s_{23}, c_{23}, L) = P_{\tau\tau}(c_{23}, -s_{23}, L)$ and $P_{e\mu}(s_{23}, c_{23}, L) = P_{e\tau}(c_{23}, -s_{23}, L)$. Thus $P_{ee}(L)$, the easiest term to calculate has one check, while all other results have either two or three independent checks. Finally, simplifying the calculated probabilities to the OMSD scenario and setting $\delta = 0$ allows them to be verified against other results in the literature.

3.6 Transition probability across multiple resonances

3.6.1 Jump probability with three neutrinos

Following Parke's application [119] of Landau and Zener's results [120],[121] for the transition probability at a level crossing, the problem of level crossing is considered assuming three neutrinos. Figure 3.1 showed the three masses as a function of electron density based on equations 3.15 to 3.17. It is clear that if the mass hierarchy in vacuum follows $m_1 < m_2 < m_3$ and $m_e \approx m_1$ in vacuum then there may be two resonance crossings.

Kuo and Pantaleone modified the the jump formula and applied it to the three neutrino case, assuming that the two resonances can be treated separately [149]. They found

that at the $\nu_1 - \nu_2$ and $\nu_1 - \nu_3$ resonances are given by:

$$P_{jump}^{12} = \exp \left[-\frac{\sqrt{2}\pi \Delta m_{21}^4 s_{12}^2 c_{12}^2}{2(1 + c_{13}^2) E^2 G_F \hbar c |dN_e/dr|_{res}} \right] \quad (3.39)$$

$$P_{jump}^{13} = \exp \left[-\frac{\sqrt{2}\pi \Delta m_{31}^4 s_{13}^2 c_{13}^2}{4E^2 G_F \hbar c |dN_e/dr|_{res}} \right] \quad (3.40)$$

The condition $L = ct \gg \frac{2E\hbar c}{\Delta m^2 c^4}$ ensures that they do not cross. For a typical 15 MeV neutrino with $\Delta m^2 = 10^{-5} \text{ eV}^2$ this implies that the extent of the resonance region is

$$L \gg \frac{2E\hbar c}{\Delta m^2} = \frac{2(1.5 \times 10^7 \text{ eV})(1.97 \times 10^{-7} \text{ eV} \cdot \text{m})}{10^{-5} \text{ eV}^2} \approx 6 \times 10^5 \text{ m} \approx 9 \times 10^{-4} R_\odot \quad (3.41)$$

It should be noted, however, that as the mass difference Δm^2 decreases the resonance region increases. If $\Delta m^2 \approx 10^{-7} \text{ eV}^2$ (corresponding to the weak third solution to the SNP which was ruled out by the two neutrino analysis in Chapter two), the condition on the resonance region in 3.41 becomes $L \gg 0.09 R_\odot$, which would not be possible to satisfy if a third neutrino were present. Thus, if a second resonance exists inside the sun, it is not necessarily valid to treat the two resonances separately.

3.6.2 Propagating the neutrino across multiple resonances

It has now been established that, as long as the two resonances are well separated, a neutrino crossing a resonance in the three neutrino system can be treated in a manner identical to the two neutrino case. Now consider a neutrino propagating across more than one resonance in succession, but still provided that they are sufficiently well separated. In particular, suppose that a neutrino produced at the centre of the sun propagates outward and that the electron density at the point of production is large enough that it crosses two resonances on its way out of the sun.

This situation is illustrated in figure 3.2 in which a neutrino is produced at time t_i at density ρ_i in the top right of the figure. It propagates downward to the left and passes

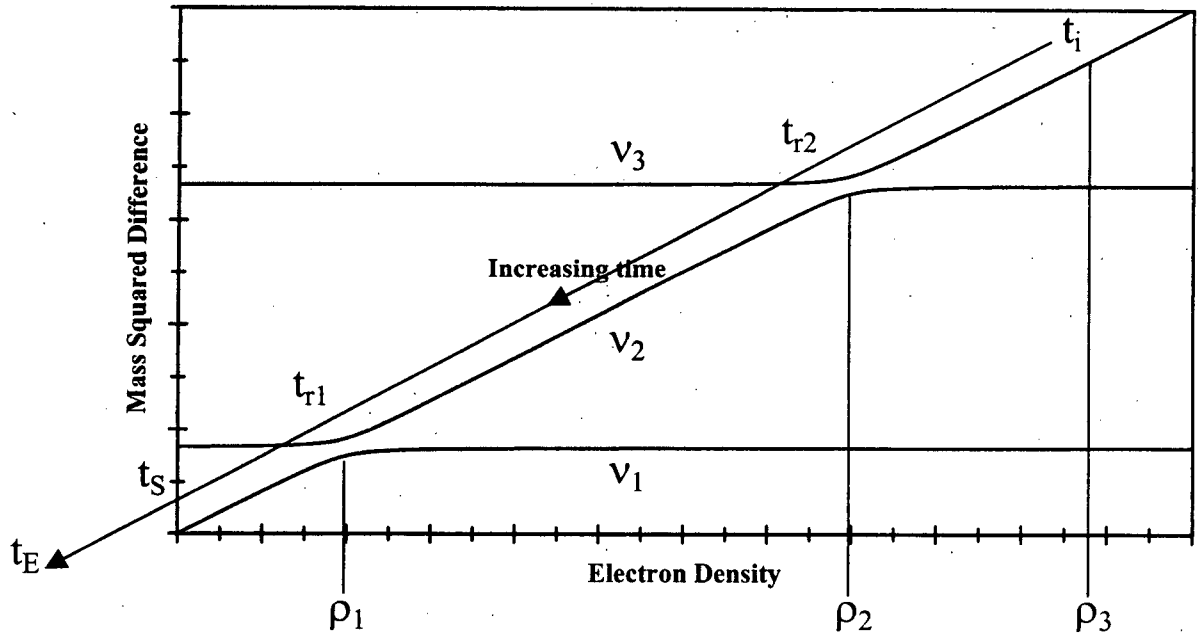


Figure 3.2: Path of a neutrino which crosses two resonances, beginning at high density at the top right and moving downward to the left as it leaves the sun.

resonance density ρ_2 at time t_{r2} . It continues traversing the solar interior and passes the outer resonant density ρ_1 at time t_{r1} , after which it exits the sun at t_s and arrives on earth at t_E . Beginning at t_i we write the neutrino wave function at successive times as it travels to the earth at t_E :

$$\begin{aligned} |\nu(t_i)\rangle &= |\nu_e\rangle = V_{e1}(\rho_3)|\nu_1\rangle + V_{e2}(\rho_3)|\nu_2\rangle + V_{e3}(\rho_3)|\nu_3\rangle \\ &\equiv A_1(t_i)|\nu_1\rangle + A_2(t_i)|\nu_2\rangle + A_3(t_i)|\nu_3\rangle \end{aligned} \quad (3.42)$$

Propagating to a time $t_{r2} - \frac{\tau}{2}$ just outside the resonance at density ρ_2 , where τ is the width of the resonance, yields

$$|\nu(t_{r2} - \frac{\tau}{2})\rangle = A_1(t_i) \exp \left\{ -i \int_{t_i}^{t_{r2} - \tau/2} dt \frac{m_1^2(\rho)}{2E} \right\} |\nu_1\rangle \quad (3.43)$$

$$+ A_2(t_i) \exp \left\{ -i \int_{t_i}^{t_{r2} - \tau/2} dt \frac{m_2^2(\rho)}{2E} \right\} |\nu_2\rangle \quad (3.44)$$

$$\begin{aligned}
& + A_3(t_i) \exp \left\{ -i \int_{t_i}^{t_{r2}-\tau/2} dt \frac{m_3^2(\rho)}{2E} \right\} |\nu_3\rangle \\
& \equiv A_1 \left(t_{r2} - \frac{\tau}{2} \right) |\nu_1\rangle + A_2 \left(t_{r2} - \frac{\tau}{2} \right) |\nu_2\rangle + A_3 \left(t_{r2} - \frac{\tau}{2} \right) |\nu_3\rangle
\end{aligned} \tag{3.45}$$

When the neutrino crosses the resonance at ρ_{r2} there will be an amplitude for level crossing between the $|\nu_2\rangle$ and $|\nu_3\rangle$ states, parameterised by coefficients a_1 and a_2 where $|a_1|^2 + |a_2|^2 = 1$. The off resonance neutrino $|\nu_1\rangle$ does not participate, so that

$$|\nu(t_{r2} + \frac{\tau}{2})\rangle = A_1 \left(t_{r2} - \frac{\tau}{2} \right) \exp \left\{ -i \int_{t_{r2}-\tau/2}^{t_{r2}+\tau/2} dt \frac{m_1^2(\rho)}{2E} \right\} |\nu_1\rangle \tag{3.46}$$

$$+ \left[a_1 A_2(t_{r2} - \frac{\tau}{2}) + a_2 A_3(t_{r2} - \frac{\tau}{2}) \right] |\nu_2\rangle \tag{3.47}$$

$$+ \left[-a_2^* A_2(t_{r2} - \frac{\tau}{2}) + a_1^* A_3(t_{r2} - \frac{\tau}{2}) \right] |\nu_3\rangle \tag{3.48}$$

$$\equiv A_1 \left(t_{r2} + \frac{\tau}{2} \right) |\nu_1\rangle + A_2 \left(t_{r2} + \frac{\tau}{2} \right) |\nu_2\rangle + A_3 \left(t_{r2} + \frac{\tau}{2} \right) |\nu_3\rangle$$

The neutrino then propagates to the edge of the outer resonance at density ρ_1 at time t_{r1} , where σ is the (temporal) width, and

$$|\nu(t_{r1} - \frac{\sigma}{2})\rangle = A_1 \left(t_{r2} + \frac{\tau}{2} \right) \exp \left\{ -i \int_{t_{r2}+\tau/2}^{t_{r1}-\sigma/2} dt \frac{m_1^2(\rho)}{2E} \right\} |\nu_1\rangle \tag{3.49}$$

$$+ A_2 \left(t_{r2} + \frac{\tau}{2} \right) \exp \left\{ -i \int_{t_{r2}+\tau/2}^{t_{r1}-\sigma/2} dt \frac{m_2^2(\rho)}{2E} \right\} |\nu_2\rangle \tag{3.50}$$

$$+ A_3 \left(t_{r2} + \frac{\tau}{2} \right) \exp \left\{ -i \int_{t_{r2}+\tau/2}^{t_{r1}-\sigma/2} dt \frac{m_3^2(\rho)}{2E} \right\} |\nu_3\rangle \tag{3.51}$$

$$\equiv A_1 \left(t_{r1} - \frac{\sigma}{2} \right) |\nu_1\rangle + A_2 \left(t_{r1} - \frac{\sigma}{2} \right) |\nu_2\rangle + A_3 \left(t_{r1} - \frac{\sigma}{2} \right) |\nu_3\rangle$$

At the second resonance, the $|\nu_1\rangle$ and $|\nu_2\rangle$ states come in close contact while the $|\nu_3\rangle$ does not participate. Parameterising the transition between the two states with coefficients b_1 and b_2 such that $|b_1|^2 + |b_2|^2 = 1$, the neutrino state after passing through the resonance is

$$|\nu(t_{r1} + \frac{\sigma}{2})\rangle = \left[b_1 A_1(t_{r1} - \frac{\sigma}{2}) + b_2 A_2(t_{r1} - \frac{\sigma}{2}) \right] |\nu_1\rangle \tag{3.52}$$

$$+ \left[-b_2^* A_1 \left(t_{r1} - \frac{\sigma}{2} \right) + b_1^* A_2 \left(t_{r1} - \frac{\sigma}{2} \right) \right] |\nu_2\rangle \quad (3.53)$$

$$+ A_3 \left(t_{r1} - \frac{\sigma}{2} \right) \exp \left\{ -i \int_{t_{r1}-\sigma/2}^{t_{r1}+\sigma/2} dt \frac{m_3^2(\rho)}{2E} \right\} |\nu_3\rangle \quad (3.54)$$

$$\equiv A_1 \left(t_{r1} + \frac{\sigma}{2} \right) |\nu_1\rangle + A_2 \left(t_{r1} + \frac{\sigma}{2} \right) |\nu_2\rangle + A_3 \left(t_{r1} + \frac{\sigma}{2} \right) |\nu_3\rangle$$

After passing through the last resonance the neutrino propagates to the surface of the sun at t_S

$$|\nu(t_S)\rangle = A_1 \left(t_{r1} + \frac{\sigma}{2} \right) \exp \left\{ -i \int_{t_{r1}+\sigma/2}^{t_S} dt \frac{m_1^2(\rho)}{2E} \right\} |\nu_1\rangle \quad (3.55)$$

$$+ A_2 \left(t_{r1} + \frac{\sigma}{2} \right) \exp \left\{ -i \int_{t_{r1}+\sigma/2}^{t_S} dt \frac{m_2^2(\rho)}{2E} \right\} |\nu_2\rangle \quad (3.56)$$

$$+ A_3 \left(t_{r1} + \frac{\sigma}{2} \right) \exp \left\{ -i \int_{t_{r1}+\sigma/2}^{t_S} dt \frac{m_3^2(\rho)}{2E} \right\} |\nu_3\rangle \quad (3.57)$$

$$\equiv A_1(t_S) |\nu_1\rangle + A_2(t_S) |\nu_2\rangle + A_3(t_S) |\nu_3\rangle$$

Finally, the neutrino state propagates from the surface of the sun to the earth at time t_E . Because the masses are constant, the integral in the exponent can be evaluated exactly to obtain

$$|\nu(t_E)\rangle = A_1(t_S) \exp \left\{ -i \frac{m_{1,V}^2}{2E} (t_E - t_S) \right\} |\nu_1\rangle \quad (3.58)$$

$$+ A_2(t_S) \exp \left\{ -i \frac{m_{2,V}^2}{2E} (t_E - t_S) \right\} |\nu_2\rangle \quad (3.59)$$

$$+ A_3(t_S) \exp \left\{ -i \frac{m_{3,V}^2}{2E} (t_E - t_S) \right\} |\nu_3\rangle \quad (3.60)$$

$$\equiv A_1(t_E) |\nu_1\rangle + A_2(t_E) |\nu_2\rangle + A_3(t_E) |\nu_3\rangle$$

Although each step is straightforward, the algebra has only been kept manageable by redefining the amplitudes A_i at each time. The full expression can be simplified somewhat by assuming that the resonance regions are small compared to the total distance travelled

through the sun. Then the resonance crossings are completely parameterised by the coefficients a_1 , a_2 , b_1 and b_2 , and the widths of the resonances τ and σ vanish.

Introducing the notation $U_{ei} = V_{ei}(\rho_3)$, $\eta_i \equiv \frac{m_{i,V}^2}{2E}(t_E - t_S)$ and $\chi_i(t_1, t_2) \equiv \int_{t_1}^{t_2} dt \frac{m_i^2(\rho)}{2E}$ the neutrino wavefunction on arrival at earth can be simplified to

$$\begin{aligned}
 |\nu(t_E)\rangle = & e^{-i\eta_1} [b_1 U_{e1} e^{-i\chi_1(t_i, t_S)} + b_2 a_1 U_{e2} e^{-i\chi_1(t_{r1}, t_S)} e^{-i\chi_2(t_i, t_{r1})} \\
 & + b_2 a_2 U_{e3} e^{-i\chi_1(t_{r1}, t_S)} e^{-i\chi_2(t_{r2}, t_{r1})} e^{-i\chi_3(t_i, t_{r2})}] |\nu_1\rangle \\
 & + e^{-i\eta_2} [-b_2^* U_{e1} e^{-i\chi_2(t_{r1}, t_S)} e^{-i\chi_1(t_i, t_{r1})} + b_1^* a_1^* U_{e2} e^{-i\chi_2(t_i, t_S)} \\
 & + b_1^* a_2 U_{e3} e^{-i\chi_2(t_{r2}, t_S)} e^{-i\chi_3(t_i, t_{r2})}] |\nu_2\rangle \\
 & + e^{-i\eta_3} [-a_2^* U_{e2} e^{-i\chi_3(t_{r2}, t_S)} e^{-i\chi_2(t_i, t_{r2})} + a_1^* U_{e3} e^{-i\chi_3(t_i, t_S)}] |\nu_3\rangle
 \end{aligned} \tag{3.61}$$

The probability that the neutrino arrives on earth as an electron neutrino state is given by

$$P(\nu_e \rightarrow \nu_e) = |[\langle \nu_1 | V_{e1}^*(0) + \langle \nu_2 | V_{e2}^*(0) + \langle \nu_3 | V_{e3}^*(0) +] |\nu(t_E)\rangle|^2 \tag{3.62}$$

The details of the calculation are quite tedious, but can be performed. It can be shown that the result takes the form:

$$\begin{aligned}
 P(\nu_e \rightarrow \nu_e) = & |V_{e1}|^2 \{ (1 - P_2) |U_{e1}|^2 + (1 - P_1) P_2 |U_{e2}|^2 + P_1 P_2 |U_{e3}|^2 \} \\
 & + |V_{e2}|^2 \{ P_2 |U_{e1}|^2 + (1 - P_1)(1 - P_2) |U_{e2}|^2 + P_1(1 - P_2) |U_{e3}|^2 \} \\
 & + |V_{e3}|^2 \{ P_1 |U_{e2}|^2 + (1 - P_1) |U_{e3}|^2 \} \\
 & + 2 \sum_{i=1}^9 A_i \cos(\arg(A_i) + \sum_k \chi) \\
 & + 2 \sum_{i=1}^9 B_{i3} \cos(\eta_2 - \eta_1 + \arg(B_{i3}) + \sum_k \chi) \\
 & + 2 \sum_{i=1}^6 B_{i2} \cos(\eta_3 - \eta_1 + \arg(B_{i2}) + \sum_k \chi) \\
 & + 2 \sum_{i=1}^6 B_{i1} \cos(\eta_3 - \eta_2 + \arg(B_{i1}) + \sum_k \chi)
 \end{aligned} \tag{3.63}$$

where $V_{ei} \equiv V_{ei}(0)|_{\rho=0}$ is the CKM matrix in vacuum, and $P_1 = |a_2|^2$ and $P_2 = |b_2|^2$ are the jump probabilities at the two resonances. The coefficients A_i and B_{ij} are different

products of the form $V_{ei}V_{ej}^*U_{ek}U_{el}^* \times a_m^{(*)}b_n^{(*)}$. The terms expressed $\sum_k \chi$ are sums of terms of the form $\chi_i(t_1, t_2)$ which come from integrating the neutrino wavefunction as it propagates through the sun.

However, the $\chi_i(t_1, t_2) = \int_{t_1}^{t_2} dt \frac{m_i^2(\rho)}{2E}$ terms each have endpoints of the integration which are two of: the point of production, inner resonance, outer resonance, and point of measurement. The probability calculated above is therefore dependent on the phase of the wavefunction at these points, and it is necessary to average over them. In doing so, all cosine terms in the expression drop out (they average to zero), and the probability is simply given by

$$\begin{aligned}
 P(\nu_e \rightarrow \nu_e) = & |V_{e1}|^2 \left\{ (1 - P_2) |U_{e1}|^2 + (1 - P_1) P_2 |U_{e2}|^2 + P_1 P_2 |U_{e3}|^2 \right\} \\
 & + |V_{e2}|^2 \left\{ P_2 |U_{e1}|^2 + (1 - P_1)(1 - P_2) |U_{e2}|^2 + P_1(1 - P_2) |U_{e3}|^2 \right\} \\
 & + |V_{e3}|^2 \left\{ P_1 |U_{e2}|^2 + (1 - P_1) |U_{e3}|^2 \right\}
 \end{aligned} \tag{3.64}$$

In practice, solar neutrinos are even less coherent. The point of production varies spatially, so neutrinos travel different distances before encountering the resonances (or encounter different resonance structures as will be discussed in the next chapter) reducing coherence. Because the solar density varies, the V_{ei} terms in equation 3.63 will be vary from neutrino to neutrino. In addition, the oscillation lengths are also dependent on energy, and since most neutrino reactions have a distribution of energies, any coherence is washed out even more.

The important thing to glean from this section is that there are no coherent effects. To calculate the probability that the ν_e has been converted to any flavour along the way, compute probabilities. First compute the projection of the wavefunction at production into the mass eigenbasis, then apply the probability of jumps at each resonance successively, calculate vacuum oscillation probabilities for a neutrino propagating from the sun to earth, and project the result onto the weak eigenbasis at the point of measurement. All

coherent effects are washed out not only because of the distribution of points of production and energies, but also due to averaging over the phase at the points of production, at each resonance and at the point of measurement.

Chapter 4

Numerical Methods

4.1 Introduction

Two different types of neutrino phenomena are studied: oscillations by neutrinos through vacuum and/or the earth's interior where the neutrinos are produced by accelerators, and oscillations by neutrinos created in the solar interior which emerge from the sun and travel to earth. The first of these is a straight oscillation problem with either fixed or variable density, while the second has the additional effect of crossing up to four resonances on the way out of the sun (the neutrino may cross each of two resonances twice if it is produced outside the resonance radii on the side of the sun opposite the earth).

Two sets of computer codes were developed to calculate rates for these two different situations. This chapter briefly details those programs, discusses some of the numerical techniques used, and addresses the accuracy of the calculations. In the Section Two, numerical treatment of the CKM matrix is discussed, and results are compared to the analytical solutions presented by Zaglauer and Schwarz [132]. It will be shown that the two different methods produce exactly the same results. While the analytical solution is much faster to calculate, it does break down for certain values of the parameters and when the mass differences become large. The numerical solution was designed for approximate floating point arithmetic and does not break down. So in practice, a combination of the two methods is used to maximise speed of calculation while maintaining stability of the solutions. The two sections following that outline the long baseline and solar numerical

calculations, and discuss some of the details of the algorithms used.

4.2 Numerical Treatment of the CKM Matrix

The hamiltonian operator in the weak eigenbasis in matter is given by

$$(H_{e\mu\tau})_M = \frac{1}{2E} V \begin{pmatrix} m_1^2 & 0 & 0 \\ 0 & m_2^2 & 0 \\ 0 & 0 & m_3^2 \end{pmatrix} V^{-1} + \sqrt{2} G_F N_e \begin{pmatrix} 1 & 0 & 0 \\ 0 & 0 & 0 \\ 0 & 0 & 0 \end{pmatrix} \quad (4.1)$$

There are well known numerical methods for determining the eigenvectors and eigenvalues of an $n \times n$ matrix, especially hermitian matrices which have distinct eigenvectors associated with distinct, real eigenvalues. Hermitian matrices are particularly well behaved because the eigenvalues and eigenvectors are not sensitive to small changes in the original matrix, thereby making numerical routines more stable.

Diagonalisation of the hamiltonian was performed with the EISPACK subroutines *ch*, *htribk*, *htridi*, *tql2*, *tqlrat*, *pythag* and *epsilon*. The method of solution, called the Householder algorithm, involves performing a series of similarity transformations to reduce the matrix to tridiagonal form, after which a transformation can be used to diagonalise it. The product of the matrices used to diagonalise the hamiltonian define a non-unique similarity transformation relating the weak eigenstates to the mass eigenstates in matter. The EISPACK procedure decomposes the hamiltonian as follows:

$$\begin{aligned} (H_{e\mu\tau})_M &= W \begin{pmatrix} d_1 & 0 & 0 \\ 0 & d_2 & 0 \\ 0 & 0 & d_3 \end{pmatrix} W^{-1} \\ &\approx \frac{1}{2E} V_M \begin{pmatrix} m_{1,M}^2 & 0 & 0 \\ 0 & m_{2,M}^2 & 0 \\ 0 & 0 & m_{3,M}^2 \end{pmatrix} V_M^{-1} \end{aligned} \quad (4.2)$$

where V_M and $d_i = \frac{m_{i,M}^2}{2E}$ define the CKM matrix and mass eigenstates in matter. The approximation in the last step comes about because the EISPACK routines do not necessarily produce a matrix identical to the standard CKM matrix, which has positive determinant, four positive real elements in the first row and third column, and a particular structure for the complex phase.

The mixing angles can, however, be determined directly from W as follows:

$$\sin^2(2\theta_{13,M}) = |W_{e3}|^2 \quad (4.3)$$

$$\sin^2(2\theta_{12,M}) = \frac{|W_{e2}|^2}{1 - \sin^2(2\theta_{13,M})} \quad (4.4)$$

$$\sin^2(2\theta_{23,M}) = \frac{|W_{\mu 3}|^2}{1 - \sin^2(2\theta_{13,M})} \quad (4.5)$$

Zaglauer and Schwarzer suggest a transformation of the form $e^{i(aT_3+bY)}We^{-i(cT_3+dY)}$ which helps to determine the phase parameter $\cos(\delta)$. The constants a , b , c and d must be determined and the matrices T_3 and Y are given by

$$T_3 = \begin{pmatrix} 1 & 0 & 0 \\ 0 & 0 & 0 \\ 0 & 0 & -1 \end{pmatrix} \quad \text{and} \quad Y = \begin{pmatrix} 1 & 0 & 0 \\ 0 & -2 & 0 \\ 0 & 0 & 1 \end{pmatrix} \quad (4.6)$$

Correctly choosing the parameters a through d does not, however, recover the CKM matrix in its original form. In addition to multiplication by an overall phase factor, the form of equation 4.2 allows multiplication of any row or column of the matrix W by a factor of -1 . Noticing that the form of the CKM matrix is such that $(V_{\mu 1}V_{\tau 2} - V_{\tau 1}V_{\mu 2})V_{e3} = \sin^2(\theta_{13})$, suggests multiplying W by an additional overall phase factor of $\omega_\delta = \frac{1}{3} \arg[(V_{\mu 1}V_{\tau 2} - V_{\tau 1}V_{\mu 2})V_{e3}]$.

By writing the elements of the matrix as $W_{\alpha i} = w_{\alpha i}e^{i\delta_{\alpha i}}$ it can be shown that choosing

$$a = -\frac{1}{2}(\omega_{e1} + \omega_{e2} + \omega_{\mu 3} + 3\omega_\delta) \quad (4.7)$$

$$\begin{aligned}
b &= \frac{1}{6}(-\omega_{e1} - \omega_{e2} + \omega_{\mu3} - 2\omega_{\tau3} - 3\omega_{\delta}) \\
c &= -\frac{1}{2}(\omega_{e2} + \omega_{\mu3} + \omega_{\tau3} + 3\omega_{\delta}) \\
d &= \frac{1}{6}(2\omega_{e1} - \omega_{e2} + \omega_{\mu3} + \omega_{\tau3} + 3\omega_{\delta})
\end{aligned}$$

produces real terms in the elements V_{e1} , V_{e2} , $V_{\mu2}$ and $V_{\tau3}$. The range of the angular parameters θ_{12} , θ_{13} and θ_{23} always admits positive, real elements in these positions of the matrix. Multiplying one of the first two columns or the second or third rows of the matrix by -1 can render each of these real elements positive. Finally, if the determinant of the resulting matrix is -1 , then multiplying the first row and first and second columns of the matrix by -1 will flip the parity of the matrix while leaving the real elements positive. This completes the process of putting the raw similarity transformation into CKM matrix form and the last parameter, $\cos \delta$ is given by

$$\cos(\delta_M) = \frac{V_{e3}}{\sin(2\theta_{13,M})} \quad (4.8)$$

Figure 4.1 compares the mass differences and CKM parameters calculated numerically using the methods presented above to the analytical formulae given by Zaglauer and Schwarzer, which have been shifted upward slightly in each plot to differentiate them. It is clear from the figure that the numerical method correctly calculates all parameters. As a result, the two methods of obtaining the matter enhanced CKM matrix are used interchangeably in the codes which generate the results in the chapters which follow.

4.3 Long Baseline Calculations

4.3.1 Basic Long Baseline Code

Figure 4.2 gives a conceptual view of the code used to calculate long baseline neutrino oscillations. The program incorporates details of the neutrino spectra, and given a range

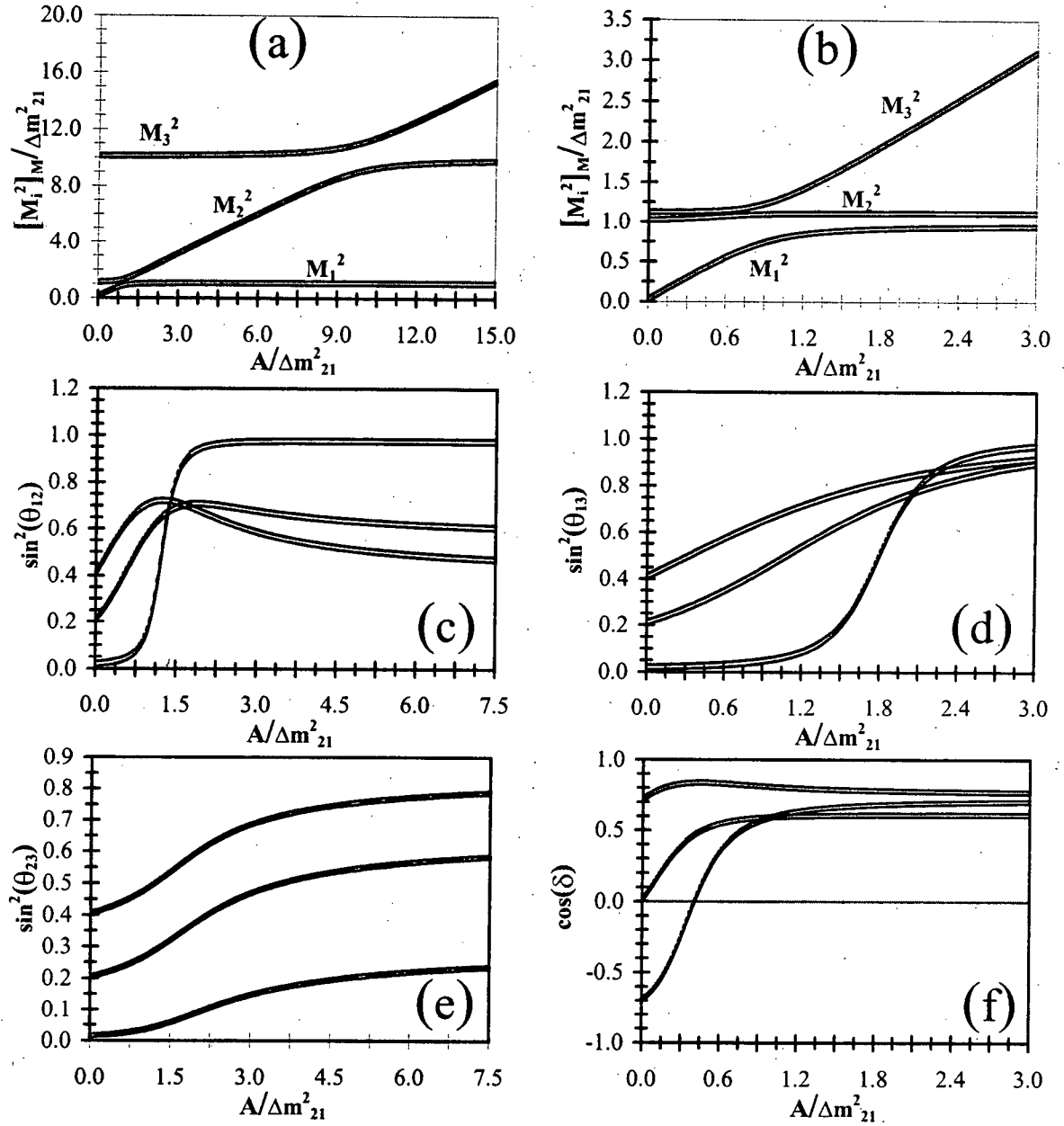


Figure 4.1: Effective neutrino masses and CKM parameters in matter as a function of the matter term A . Analytical results of Zaglauer and Schwarzer are shifted upwards for readability. (a) $M_{i,M}^2$ with $\Delta m_{31,V}^2 = 10\Delta m_{21,V}^2$, $s_{12}^2 = 0.05$ and $s_{13}^2 = 0.01$. (b) $M_{i,M}^2$ with $\Delta m_{31,V}^2 = 1.1\Delta m_{21,V}^2$, $s_{12}^2 = 0.05$ and $s_{13}^2 = 0.01$. (c) $s_{12,M}^2$ with $\Delta m_{31,V}^2 = 2\Delta m_{21,V}^2$ and $s_{13}^2 = 0.1$. (d) $s_{13,M}^2$ with $\Delta m_{31,V}^2 = 2\Delta m_{21,V}^2$ and $s_{12}^2 = 0.1$. (e) $s_{23,M}^2$ with $\Delta m_{31,V}^2 = 2\Delta m_{21,V}^2$ and $s_{12}^2 = s_{13}^2 = 0.1$. (f) $c_{\delta,M}$ with $\Delta m_{31,V}^2 = 2\Delta m_{21,V}^2$, $s_{12}^2 = s_{13}^2 = 0.1$ and $s_{23}^2 = 0.2$.

of CKM parameters and mass squared differences, a range of neutrino energies, and a path, it calculates neutrino oscillation probabilities and rates for different reactions at a distant water based detector. Oscillation probabilities as a function of distance along the path can also be calculated.

The code steps through the CKM parameters and energy in small gradations and calculates the probability at each step. The earth's electron density can be treated as constant, as a series of step functions, or a gradually changing function. If the constant density is chosen, then the CKM matrix in matter is calculated and an exact formula is used to determine the probability. The step function model is treated as a series of constant densities, and the solved sequentially in a similar manner. If a variable density is chosen, then a numerical integration is performed to calculate the final oscillation probabilities. This last approach, while more realistic, takes much longer to compute. Fortunately, for many practical problems the other two methods are sufficient.

The treatment of sudden density changes was carefully examined because there are several sharp variations in the earth's density. The Runge-Kutta method was modified so that when it encountered a large density change across one step, that step was broken up into many small ones across which the density change was very small, and the integration proceeded. The results were compared to two simpler methods: one in which the normal Runge-Kutta method integrated across the large density change in a single step, and a sudden approximation across the interface. The modified Runge-Kutta showed that the sudden approximation did not produce correct results while the unmodified Runge-Kutta method did. The conclusion was that because the neutrinos interact very weakly, sudden changes in the density do not noticeably affect the oscillation probabilities—it is almost as if the oscillations average over the densities encountered. This also explains the results found in Chapter Two that using an exact solution with an average density along the path produces results which are almost identical to integrating along the neutrino path

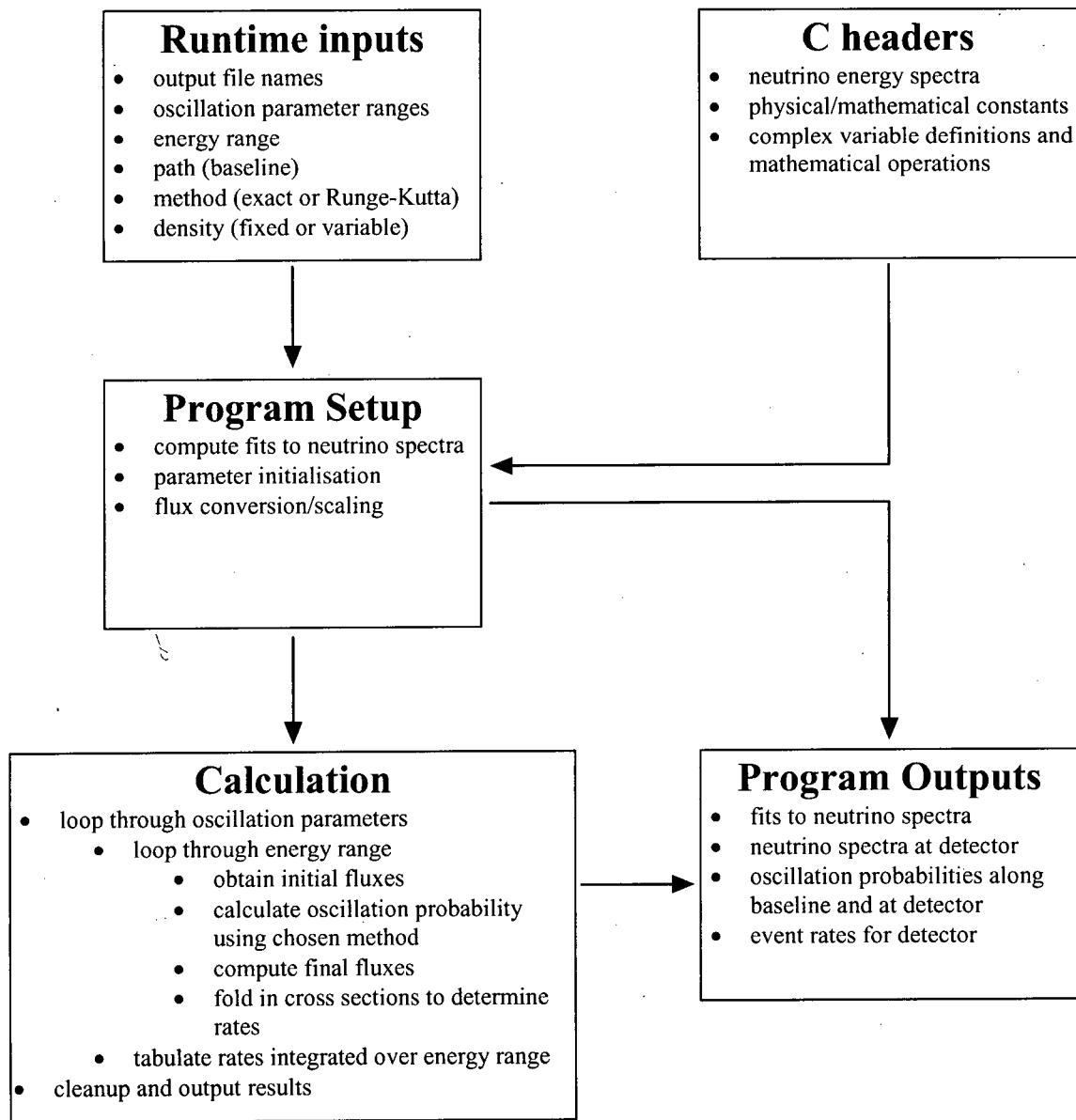


Figure 4.2: Structure of the long baseline neutrino oscillation code showing inputs, outputs, and basic organisation.

using the earth's varying density.

4.3.2 Approximation of the Earth's Density Structure

The earth's density structure, seen in figure 2.7, can be approximated by a series of step functions. The simplest of these would be to assume a single density across the entire path of the neutrino from production point to detection. Then, once the eigenstates and CKM matrix in matter are determined, the exact solution for constant density is easy to calculate. The amplitude for neutrino flavour conversion is given by the matrix A , where $A_{\alpha\beta} = A(\nu_\alpha \rightarrow \nu_\beta)$ is given by

$$\begin{pmatrix} A_{ee} & A_{\mu e} & A_{\tau e} \\ A_{e\mu} & A_{\mu\mu} & A_{\tau\mu} \\ A_{e\tau} & A_{\mu\tau} & A_{\tau\tau} \end{pmatrix} = V_M \begin{pmatrix} e^{-i\frac{2.54\Delta m_1^2 L}{E}} & 0 & 0 \\ 0 & e^{-i\frac{2.54\Delta m_2^2 L}{E}} & 0 \\ 0 & 0 & e^{-i\frac{2.54\Delta m_3^2 L}{E}} \end{pmatrix} V_M^{-1} \quad (4.9)$$

and the probability of conversion is given by $P(\nu_\alpha \rightarrow \nu_\beta) = |A_{\alpha\beta}|^2$.

This simple model proved to be effective in most cases when analysing two neutrino oscillations in chapter two. The method does, however, break down when the neutrino path probes deep into the earth where liquid iron core has much higher density. The three neutrino code has an intermediate solution between the constant and variable density cases. In it, the earth is divided into eight spherical shells, and the mean density along the path through each shell is calculated as shown in figure 4.3. The infinitesimal length element dl is given by

$$dl = \frac{R d\alpha}{\sin(\alpha_i + \theta_i)} = \frac{R_i \sin(\theta_i) d\alpha}{\sin^2(\alpha_i + \theta_i)} \quad (4.10)$$

where the symbols are as defined in the figure. Applying a change of variables $\alpha \rightarrow \alpha - \theta_i$, the path length L_i and mean electron density $\langle N_e(L_i) \rangle$ can be written as

$$L_i = R_i \sin(\theta_i) \int_{\theta_i}^{\theta_i + \alpha_i} d\alpha \frac{1}{\sin^2(\alpha)} = \frac{R_i \sin(\alpha_i)}{\sin(\alpha_i + \theta_i)} \quad (4.11)$$

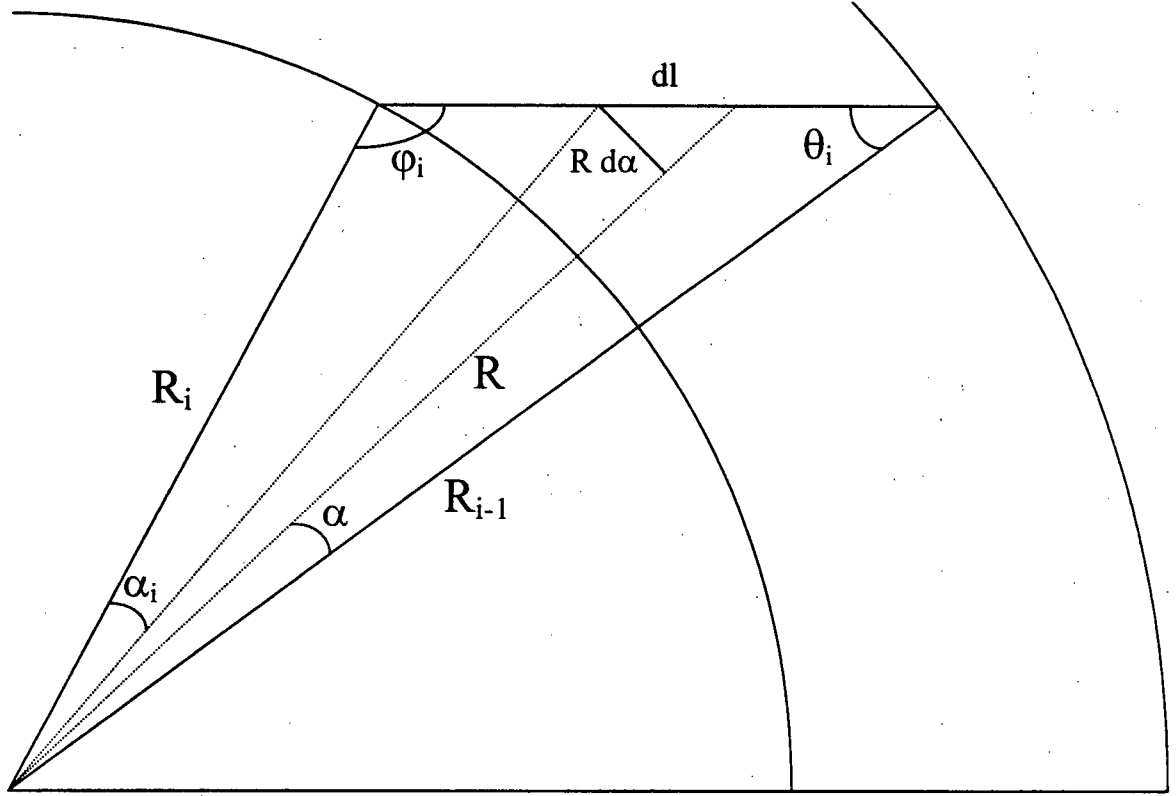


Figure 4.3: Geometry used to calculate the mean density along a path through a spherical shell in the earth.

$$\langle N_e(L_i) \rangle = \frac{R_i \sin(\theta_i)}{L_i} \int_{\theta_i}^{\theta_i + \alpha_i} d\alpha \frac{N_e(R)}{\sin^2(\alpha)} \quad (4.12)$$

The electron density used, which was provided by Stephen Parke [102] consists of a series of eight cubic functions of the radial parameter. Substituting a cubic for $N_e(R)$ in equation 4.12 yields a series of integrals of the form $\frac{1}{\sin^n(\alpha)}$, which can be evaluated exactly to determine the mean density along the neutrino's path.

The neutrino wavefunction is then calculated along a sequence of up to 16 separate paths at different densities, before it is squared to give the individual oscillation probabilities. This method will prove to be more accurate than assuming a single density, while requiring much less calculation time than a full numerical integration.

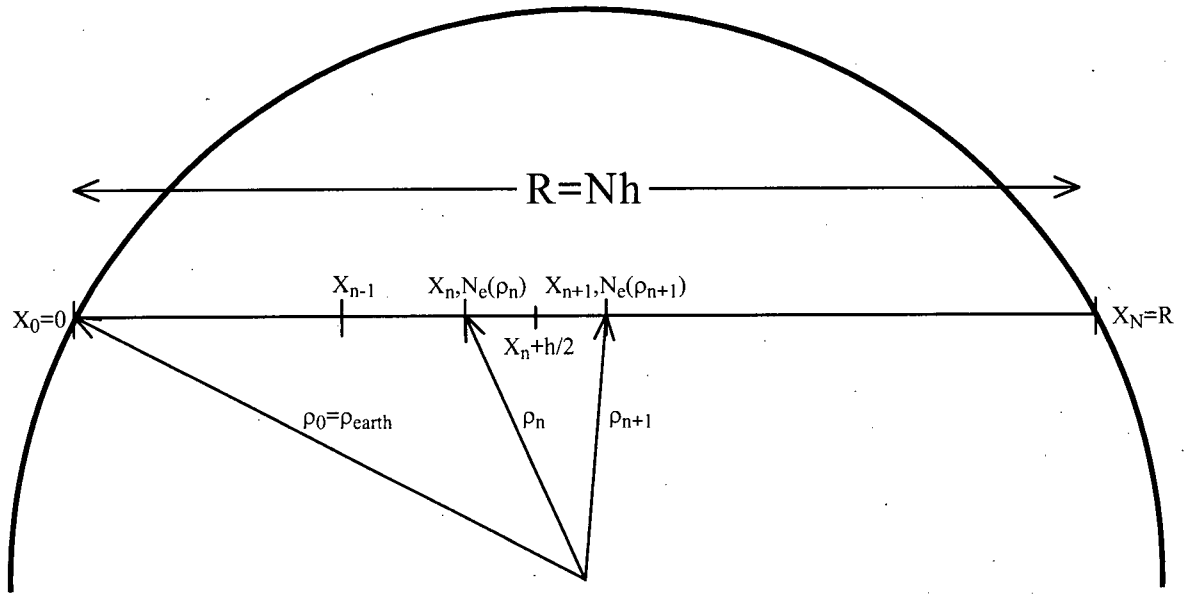


Figure 4.4: Division of the path of a neutrino beam through the earth into N discrete subsections. The Runge-Kutta method uses the electron density at the midpoint and at both ends of the segment in order to integrate the differential equation from x_n to x_{n+1} .

4.3.3 Runge-Kutta Methods of Solution

In contrast to an exact solution along a path of one or more *fixed* densities, Runge-Kutta iterative techniques have been employed to calculate neutrino oscillations on paths through the earth's *gradually varying* density profile. Equation 2.8 can be written as:

$$\frac{d\vec{\psi}(r)}{dr} = \tilde{H}(r)\vec{\psi}(r); \quad \vec{\psi}(r) = \begin{pmatrix} \nu_e(r) \\ \nu_\mu(r) \\ \nu_\tau(r) \end{pmatrix} \quad (4.13)$$

where the dependent parameter has been switched to $r = ct$, the distance along the neutrino's path. The electron density is determined by finding the distance ρ from the centre of the earth at point r along the path, so that $N_e = N_e(\rho(r))$ as shown in figure (4.4).

In order to integrate the D.E. on a path from $r = 0$ to $r = R$, the path is divided

into N sections of length $h = R/N$, such that $\widetilde{H}(r)$ is almost constant over any single segment. The functions are discretised by defining $\vec{\psi}_n(r_n) \approx \vec{\psi}(nh)$ for $n = 0, 1, \dots, N$. Beginning with the initial conditions $\vec{\psi}_0(r_0)$, Runge-Kutta methods integrate the system one step at a time along the path, normally using a combination of $\vec{\psi}_n$, $\widetilde{H}(r_n)$, $\widetilde{H}(r_n + \frac{h}{2})$ and $\widetilde{H}(r_n + h)$ in order to calculate $\vec{\psi}_{n+1}$. A general first order Runge-Kutta method [151, §15.1], defines the vectors \vec{k}_1 and \vec{k}_2 and iteratively calculates $\vec{\psi}_{n+1}$ as follows:

$$\vec{k}_1 = h \widetilde{H}(r_n) \vec{\psi}_n; \quad \vec{k}_2 = h \widetilde{H}\left(r_n + \frac{h}{2}\right) \left(\vec{\psi}_n + \frac{\vec{k}_1}{2}\right) \quad (4.14)$$

$$\vec{\psi}_{n+1} = \vec{\psi}_n + \vec{k}_2 + O(h^2) \quad (4.15)$$

By making h very small, the error in each iteration is small, and after N iterations $\vec{\psi}_N \approx \vec{\psi}(R)$ is determined. As $h = R/N$ decreases, the error at each step decreases as h^2 while the number of steps only increases by $1/h$, so the total error decreases linearly with h .

A fourth order Runge-Kutta method can be used to eliminate higher order error terms in h and reduce the number of steps, but requiring increased calculation at each step. It defines four vectors \vec{k}_1 to \vec{k}_4 and determines $\vec{\psi}_{n+1}$ as follows:

$$\vec{k}_1 = h \widetilde{H}(r_n) \vec{\psi}_n; \quad \vec{k}_2 = h \widetilde{H}\left(r_n + \frac{h}{2}\right) \left(\vec{\psi}_n + \frac{\vec{k}_1}{2}\right) \quad (4.16)$$

$$\vec{k}_3 = h \widetilde{H}\left(r_n + \frac{h}{2}\right) \left(\vec{\psi}_n + \frac{\vec{k}_2}{2}\right); \quad \vec{k}_4 = h \widetilde{H}(r_n + h) \left(\vec{\psi}_n + \vec{k}_3\right) \quad (4.17)$$

$$\vec{\psi}_{n+1} = \vec{\psi}_n + \frac{\vec{k}_1}{6} + \frac{\vec{k}_2}{3} + \frac{\vec{k}_3}{3} + \frac{\vec{k}_4}{6} + O(h^5) \quad (4.18)$$

The error at each step decreases as h^5 while the number of steps still increases as $1/h$, so that the overall error decreases as h^4 .

Because the Hamiltonian \widetilde{H} is not explicitly dependent on $\vec{\psi}_n$, it is possible to replace the 3×1 column vector $\vec{\psi}_0$ with a 3×3 identity matrix as “initial conditions.” The Runge-Kutta iterations then reduce to a series of matrix multiplications with the result that the components of the final result are oscillation amplitudes

$$\vec{\psi}_N = \begin{pmatrix} A(\nu_e \rightarrow \nu_e) & A(\nu_\mu \rightarrow \nu_e) & A(\nu_\tau \rightarrow \nu_e) \\ A(\nu_e \rightarrow \nu_\mu) & A(\nu_\mu \rightarrow \nu_\mu) & A(\nu_\tau \rightarrow \nu_\mu) \\ A(\nu_e \rightarrow \nu_\tau) & A(\nu_\mu \rightarrow \nu_\tau) & A(\nu_\tau \rightarrow \nu_\tau) \end{pmatrix} \quad (4.19)$$

The probability for oscillations is then given by $P(\nu_\alpha \rightarrow \nu_\beta) = |A(\nu_\alpha \rightarrow \nu_\beta)|^2$.

4.4 Solar Neutrino Calculations

4.4.1 Basic Solar Code

In contrast to the LBNO code, the solar neutrino code is a hybrid between two distinct styles of calculation. Probabilities are computed at each discrete grid point of over a range of squared mass differences and CKM parameters, but many random neutrinos at each grid point are generated by choosing random energies and production points within SSM distributions in the style of a Monte Carlo program. The reason for the approach is that there are too many parameters to take the sequential approach with all of them. The mass squared differences and CKM parameters—those which are explicitly plotted in figures—are treated by calculating rates in discrete steps along a range of values. A runtime input number of iterations for each neutrino reaction at each grid point determines the number of random neutrino events which are generated and propagated to the underground detector. A conceptual view of the program is shown in figure 4.5.

For each sample neutrino event, an energy, radius and azimuthal angle is chosen at random. The CKM matrix at the point of production is estimated, and the locations of

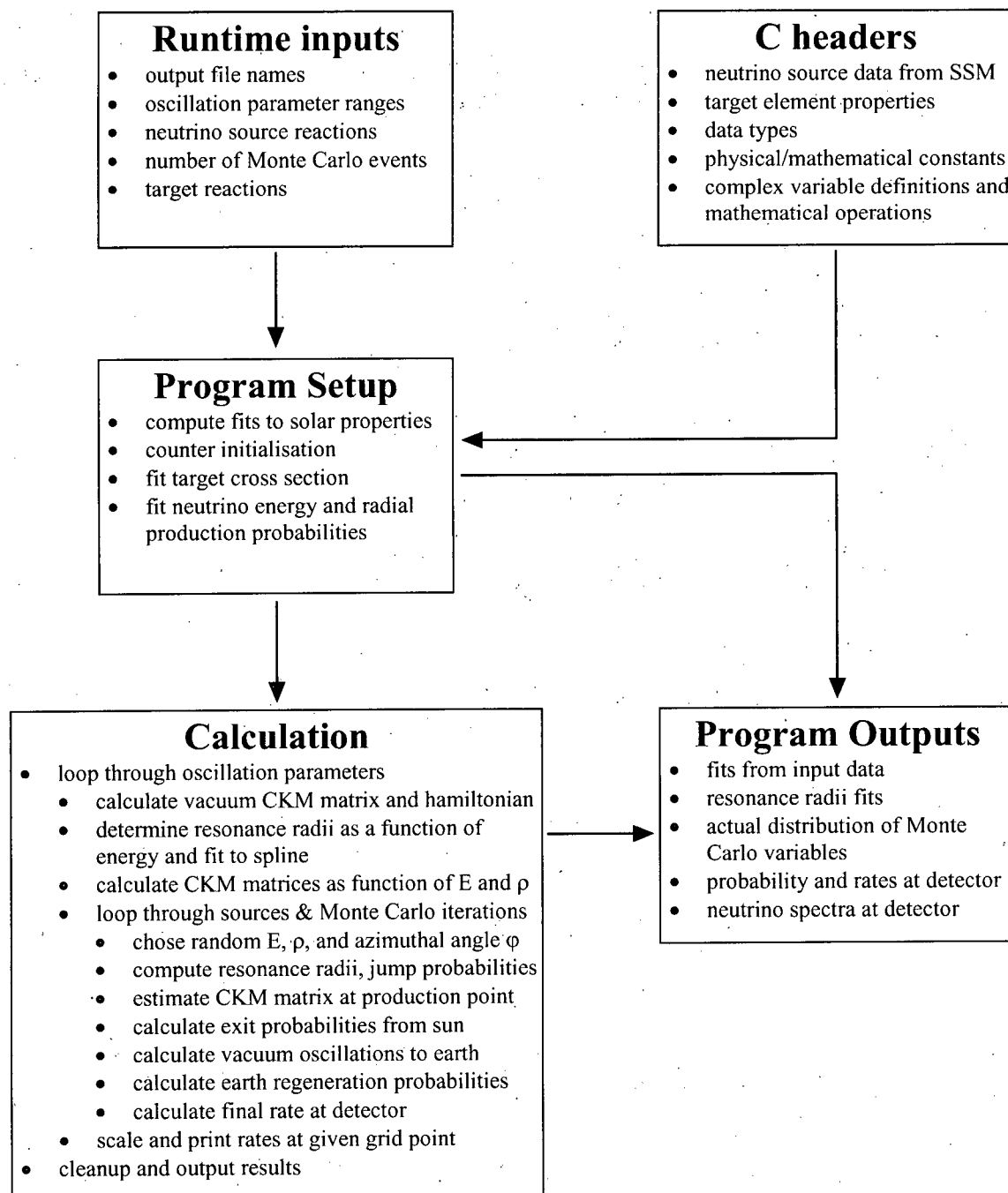


Figure 4.5: Structure of the solar neutrino oscillation code showing inputs, outputs, and basic organisation.

the resonance crossings are calculated. The ν_e is projected into the mass eigenspace, and the probability of being a ν_1 , ν_2 or ν_3 is determined. The components are propagated outwards across resonance crossings to determine the probability of each mass eigenstate when it leaves the sun. As discussed in the previous chapter, coherent effects are washed out so only probabilities need to be evaluated. Then the length of the path from the surface of the sun to the earth is calculated, including a correction for the eccentricity of the earth's orbit. The vacuum oscillations traveling from the sun to the earth are factored in to determine the probability of each neutrino flavour on arrival at the earth's surface.

In the two neutrino code used in Chapter two, a path from the point of entry into the earth to the detector is also calculated, assuming random seasonal variation and time of day (to average the seasonal and day/night effects). The neutrino is propagated through the earth at fixed density, and the detector characteristics are then used to determine the effective rate with and without an MSW effect. It was shown in Chapter Three that averaging the phase of the wavefunction over the point of production, at resonance crossings and at the point of measurement removes coherent effects, which is why probabilities are calculated at each step.

In order to reduce the time to do what are extensive calculations, some parameters are fitted with natural cubic splines, and the fits are used to interpolate the parameters in later calculations. The electron density and its first derivative in the sun, which are used in determining the resonance radii and jump probabilities are fit. The resonance radii for a given set of oscillation parameters are fit as a function of neutrino energy so in the three neutrino code the resonance parameters can be quickly interpolated, and the CKM matrix itself is fit as a function of energy and density. Finally, the cross section for interaction in the detector is fit as a function of energy. Because these functions are smooth, the interpolation is accurate. Natural cubic splines, which consist of a series of

quadratic functions connected sequentially, were chosen to fit the functions. While they are slower to calculate, they provide extremely smooth fits if the data points are very accurate.

4.4.2 Treatment of Monte Carlo Parameters

Each “event” consists of randomly choosing several parameters. The azimuthal angle φ of the neutrino production point relative to the centre of the sun and axis passing through the centres of the sun and earth is chosen. As will be shown in a later section, this angle will determine the resonance crossing structure and affect the jump probabilities. Because neutrino production in the sun is spherically symmetric, φ has a flat probability distribution.

Next, a random energy and radius of production are chosen. The probability distribution function (PDF) for each solar neutrino source reaction as a function of energy and fraction of the solar radius have been calculated and are among the outputs of BP95. These PDFs have been summed to produce cumulative distribution functions (CDFs), and the results are stored in C header files. The CDF for the energy distribution $C(E)$, for example, is a monotonic increasing function whose domain is the span of energies of neutrinos produced by a given reaction, and whose range is from zero to one. $C(E)$ is the probability that a neutrino produced by the reaction has energy less than or equal to E . By choosing a random number $C_R \in [0, 1]$ and interpolating the CDF to determine the unique E_R such that $C(E_R) = C_R$, a random energy is obtained which conforms to the distribution defined by the corresponding PDF. A similar procedure is used to choose a radius of production. The situation is illustrated in figure 4.6 which shows the fit to the ${}^8\text{B}$ neutrino energy spectrum.

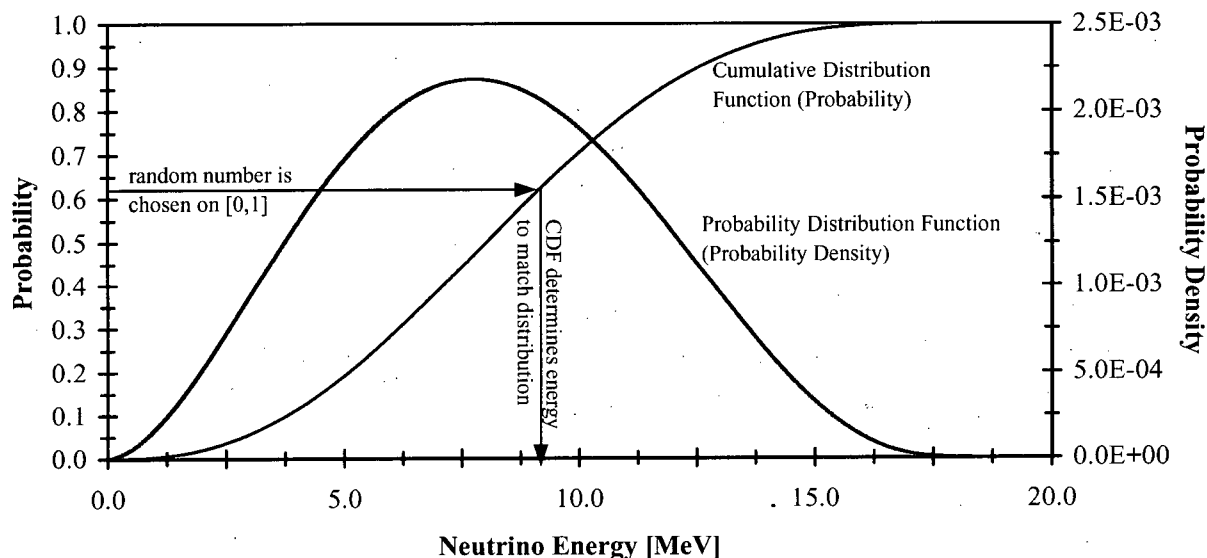


Figure 4.6: Cumulative distribution function for neutrino energy in 8B neutrinos. Given a random number between zero and one, determining the energy at which the CDF has that value will produce a random energy which is distributed with the 8B spectrum.

4.4.3 Fitting the CKM Parameters

With on the order of 10^4 events generated at each grid point in MS diagrams in a typical run of the solar neutrino code, it is impractical to diagonalise the CKM matrix for each event. Instead, a 50×50 array of 3×3 CKM matrices is generated and diagonalised for 50 neutrino energies and 50 densities. The energies are linearly spaced on the minimum range needed, based on the detector threshold and neutrino sources being used, while the densities range linearly from zero to the density at the centre of the sun.

Then for each event generated, elements of the CKM matrix are interpolated linearly inside the array. The formula used to determine $V_{\alpha\beta,M}(E, \rho)$ for $E_i < E < E_{i+1}$ and $\rho_j < \rho < \rho_{j+1}$ where E_i , E_{i+1} , ρ_j and ρ_{j+1} are nodes at which the CKM matrix was

diagonalised is given by

$$\begin{aligned}
 V_{\alpha\beta,M}(E, \rho) = & \frac{E_{i+1}-E}{E_{i+1}-E_i} \frac{\rho_{j+1}-\rho}{\rho_{j+1}-\rho_j} V_{\alpha\beta,M}(E_i, \rho_j) \\
 & + \frac{E_{i+1}-E}{E_{i+1}-E_i} \frac{\rho-\rho_j}{\rho_{j+1}-\rho_j} V_{\alpha\beta,M}(E_i, \rho_{j+1}) \\
 & + \frac{E-E_i}{E_{i+1}-E_i} \frac{\rho_{j+1}-\rho}{\rho_{j+1}-\rho_j} V_{\alpha\beta,M}(E_{i+1}, \rho_j) \\
 & + \frac{E-E_i}{E_{i+1}-E_i} \frac{\rho-\rho_j}{\rho_{j+1}-\rho_j} V_{\alpha\beta,M}(E_{i+1}, \rho_{j+1})
 \end{aligned} \tag{4.20}$$

The interpolation is a weighted average of the four nodes which is a two-dimensional extension of linear interpolation in one dimension. Figure 4.7 shows the interpolation for a typical set of parameters with a grid which is coarser than that used in the calculations by a factor of two in both directions. Clearly all parameters are sufficiently smooth that the interpolation will accurately estimate the CKM parameters in matter.

4.4.4 Multiple Resonance Possibilities

For each neutrino event, there are multiple possible resonance structures. With two neutrinos there is only one resonance radius, and the structure is fairly simple. If the neutrino is produced outside the resonance radius, then either it does not cross any resonance or it crosses the resonance radius twice on the way to the earth. If it is produced inside the resonance radius then it necessarily traverses a level crossing once. The situation is illustrated in figure 4.8 which shows the three possible paths and the effective jump probability for each. It also demonstrates how the path affects $\left[\frac{dN}{dr}\right]_{res}$ which modifies the jump probability. In particular, the density gradient is given by $\left[\frac{dN}{dr}\right]_{eff} = \left[\frac{dN}{dr}\right]_{res} \cos(\alpha)$ because the neutrino does not cross the resonance in the radial direction.

Circumstances are much more complex with three neutrinos. There can be two resonant radii with six distinct paths possible, and the ν_e which is produced has three components instead of two. Figure 4.9 illustrates the different paths a neutrino event can

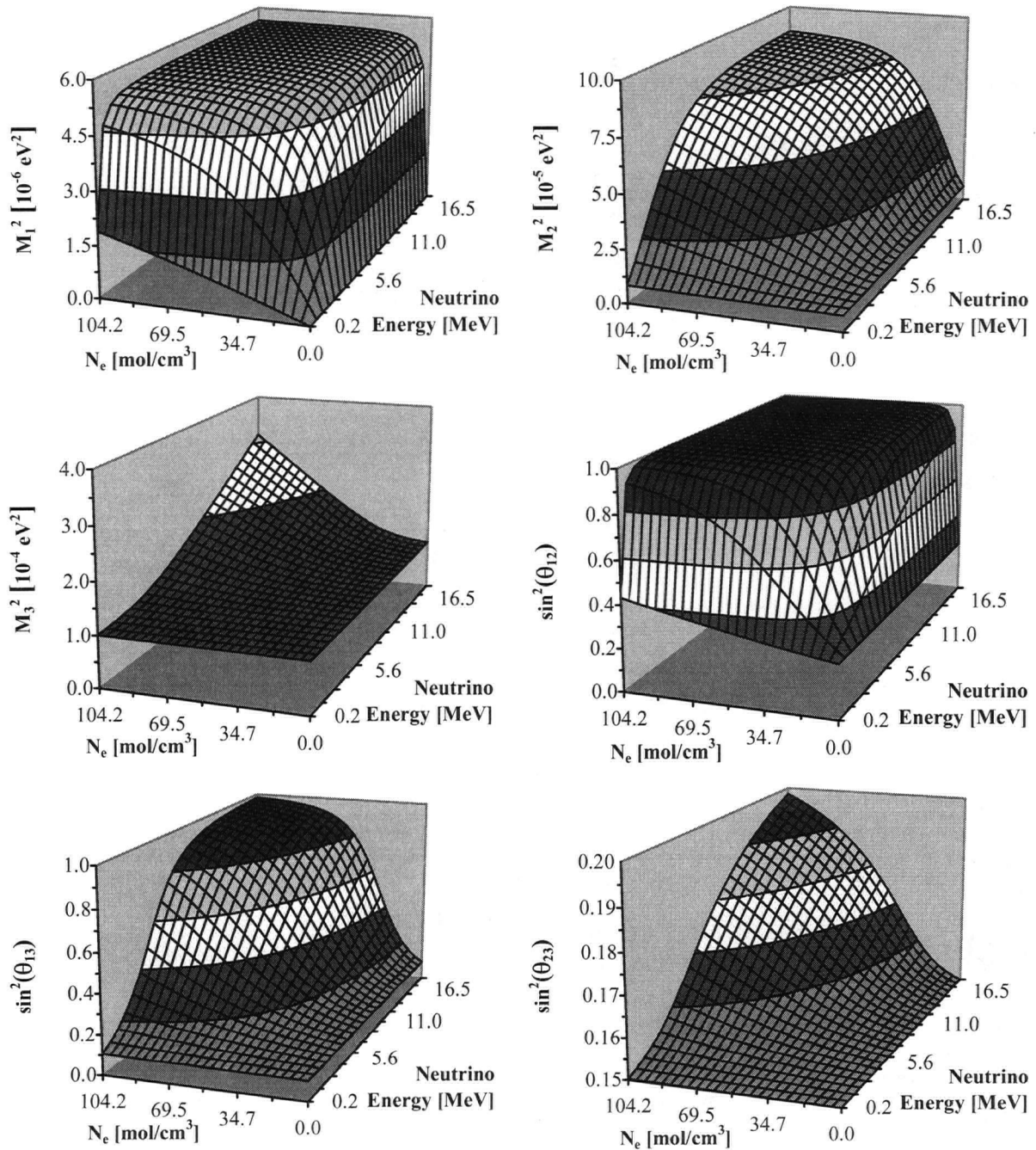


Figure 4.7: Oscillation parameters as a function of neutrino energy and electron density for ranges relevant to the solar interior. Mesh size used in interpolating parameters in solar neutrino calculations is one half the size shown in both the E_ν and N_e directions. Vacuum parameters for the plots are $m_1^2 = 0 \text{ eV}^2$, $m_2^2 = 7.5 \times 10^{-6} \text{ eV}^2$, $m_3^2 = 1.0 \times 10^{-4} \text{ eV}^2$, $s_{12}^2 = 0.25$, $s_{13}^2 = 0.10$, $s_{23}^2 = 0.15$ and $s_\delta = 0.5$.

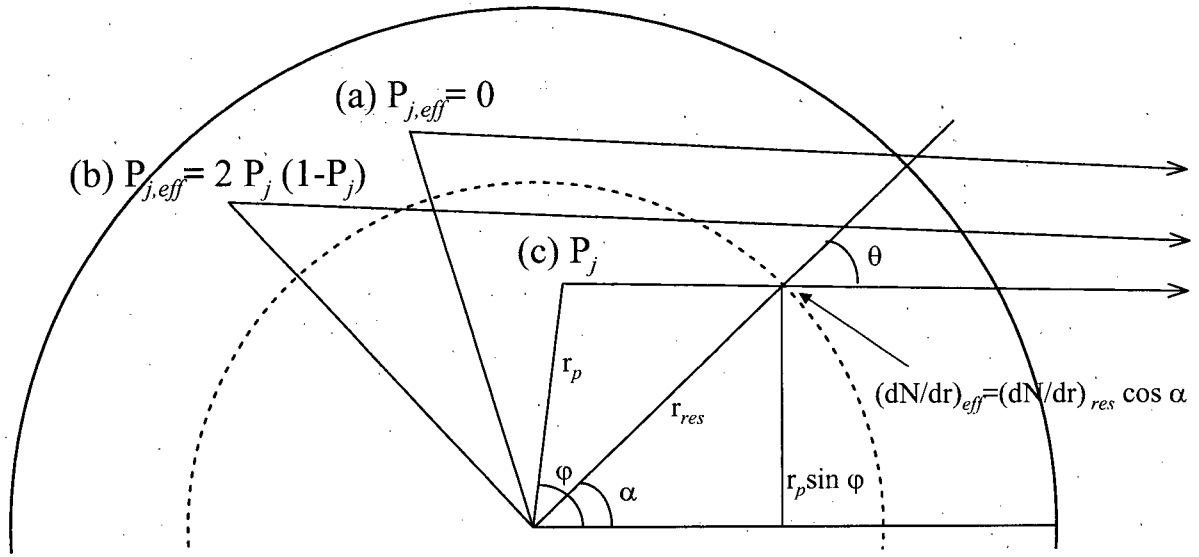


Figure 4.8: Three possible paths with the effective jump probability for each one. Note the $\cos(\alpha)$ term which modifies the neutrino density gradient at the resonance crossing. The angle is defined by $\sin(\alpha) = \frac{r_p \sin(\varphi)}{r_{res}}$.

have when it leaves the sun. The jump probability at each resonance is again modified because the effective density gradient has an added factor of $\cos(\alpha_i)$ as in the previous case.

Defining $V_{\alpha i}$ and $U_{\alpha i}$ to be components of the CKM matrix in vacuum and in matter at the point of production respectively, and P_1 and P_2 to be the jump probabilities at each of the two resonances modified by the terms $\cos(\alpha_1)$ and $\cos(\alpha_2)$, the probability that a ν_e produced in the sun emerges as a ν_e along the six possible paths is given by:

$$P_{ee,(i)} = |U_{e1}|^2 |V_{e1}|^2 + |U_{e2}|^2 |V_{e2}|^2 + |U_{e3}|^2 |V_{e3}|^2 \quad (4.21)$$

$$\begin{aligned} P_{ee,(ii)} = & |U_{e1}|^2 \left\{ (1 - 2P_2 + 2P_2^2) |V_{e1}|^2 + 2P_2 (1 - P_2) |V_{e2}|^2 \right\} + \\ & |U_{e2}|^2 \left\{ 2P_2 (1 - P_2) |V_{e1}|^2 + (1 - 2P_2 + 2P_2^2) |V_{e2}|^2 \right\} + \\ & |U_{e3}|^2 |V_{e3}|^2 \end{aligned} \quad (4.22)$$

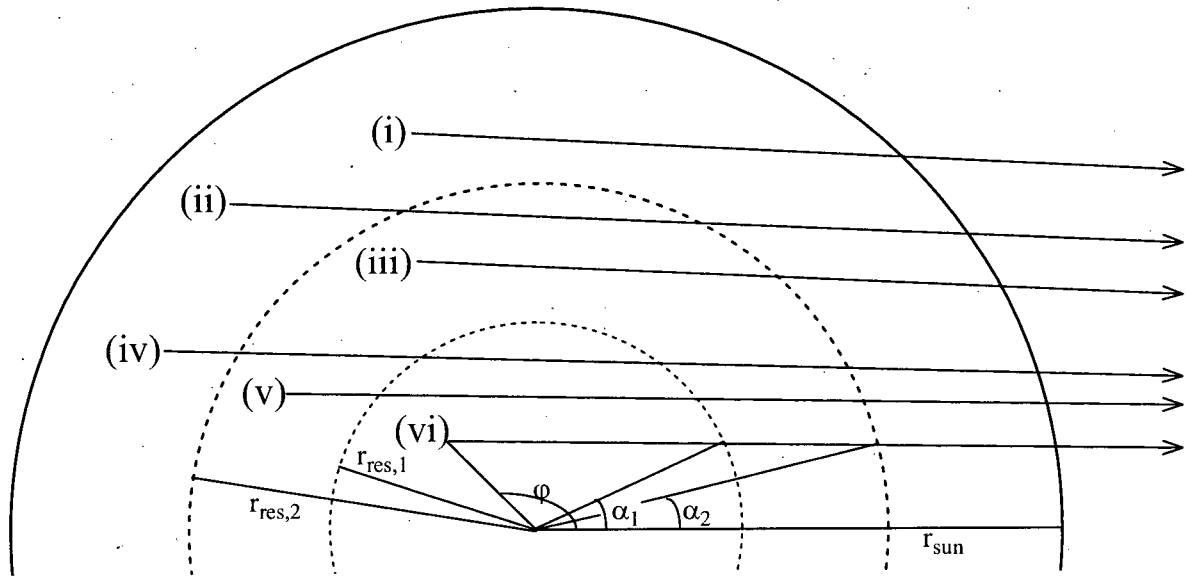


Figure 4.9: Six possible paths which a neutrino can take when leaving the sun with two resonance radii. The density gradient at the two resonances is modified by factors of $\cos(\alpha_1)$ and $\cos(\alpha_2)$ just as it was in the two neutrino case.

$$P_{ee,(iii)} = |U_{e1}|^2 \left\{ (1 - P_2) |V_{e1}|^2 + P_2 |V_{e2}|^2 \right\} + \quad (4.23)$$

$$|U_{e2}|^2 \left\{ P_2 |V_{e1}|^2 + (1 - P_2) |V_{e2}|^2 \right\} + |U_{e3}|^2 |V_{e3}|^2$$

$$P_{ee,(iv)} = |U_{e1}|^2 \left\{ \left[(1 - P_2)^2 + P_2^2 (1 - 2P_1 + 2P_1^2) \right] |V_{e1}|^2 + \quad (4.24)$$

$$2P_2 (1 - P_2) (1 - P_1 + P_1^2) |V_{e2}|^2 + 2P_2 P_1 (1 - P_1) |V_{e3}|^2 \right\} +$$

$$|U_{e2}|^2 \left\{ 2P_2 (1 - P_2) (1 - P_1 + P_1^2) |V_{e1}|^2 + \right.$$

$$\left[P_2^2 + (1 - P_2)^2 (1 - 2P_1 + 2P_1^2) \right] |V_{e2}|^2 + 2(1 - P_2) P_1 (1 - P_1) |V_{e3}|^2 \right\} +$$

$$|U_{e3}|^2 \left\{ 2P_1 (1 - P_1) P_2 |V_{e1}|^2 + 2P_1 (1 - P_1) (1 - P_2) |V_{e2}|^2 + \right.$$

$$\left. (1 - 2P_1 + 2P_1^2) |V_{e3}|^2 \right\}$$

$$P_{ee,(v)} = |U_{e1}|^2 \left\{ (1 - P_2) |V_{e1}|^2 + P_2 |V_{e2}|^2 \right\} + \quad (4.25)$$

$$|U_{e2}|^2 \left\{ (1 - 2P_1 + 2P_1^2) P_2 |V_{e1}|^2 + \right.$$

$$\begin{aligned}
& \left(1 - 2P_1 + 2P_1^2\right) (1 - P_2) |V_{e2}|^2 + 2P_1 (1 - P_1) |V_{e3}|^2 \} + \\
& |U_{e3}|^2 \{ 2P_1 (1 - P_1) P_2 |V_{e1}|^2 + \\
& 2P_1 (1 - P_1) (1 - P_2) |V_{e2}|^2 + (1 - 2P_1 + 2P_1^2) |V_{e3}|^2 \} \\
P_{ee,(vi)} = & |U_{e1}|^2 \{ (1 - P_2) |V_{e1}|^2 + P_2 |V_{e2}|^2 \} + \\
& |U_{e2}|^2 \{ (1 - P_1) P_2 |V_{e1}|^2 + (1 - P_1) (1 - P_2) |V_{e2}|^2 + P_2 |V_{e3}|^2 \} + \\
& |U_{e3}|^2 \{ P_1 P_2 |V_{e1}|^2 + P_1 (1 - P_2) |V_{e2}|^2 + (1 - P_2) |V_{e3}|^2 \}
\end{aligned} \tag{4.26}$$

After averaging out the phase of the neutrino wave functions across each resonance crossing and the point at which it leaves the sun, each term in the formulae above can be interpreted as the product of a series of probabilities at each step—phase effects are not present. The neutrino point of production relative to the resonance radii determines the path across resonances in the sun, and it is a geometric problem to determine which of the six probabilities above to use to translate the neutrino out of the sun.

4.4.5 Seasonal and Day/Night Effects

Seasonal and day/night effects are included in the calculation of neutrino oscillations, as illustrated in figure 4.10. Neutrinos which arrive on earth at night have much longer paths through the earth's interior and may undergo matter enhanced oscillations. Two coordinate systems XYZ and $X'Y'Z'$ are defined as shown, such that Z is perpendicular to the plane of the solar system, Z' is the axis of rotation of the earth and $X = X'$. The $Y'Z'$ axes are rotated $\theta = 23^\circ$ relative to the YZ axes.

Given the azimuthal angle γ of the detector with respect to Z' (90° minus latitude), the angles α in the $X'Y'$ plane and β in the XY plane define the time of day and time of year respectively fully parameterise a neutrino path from the sun to the earth. The position vector of the detector is rotated from the primed coordinates to the unprimed

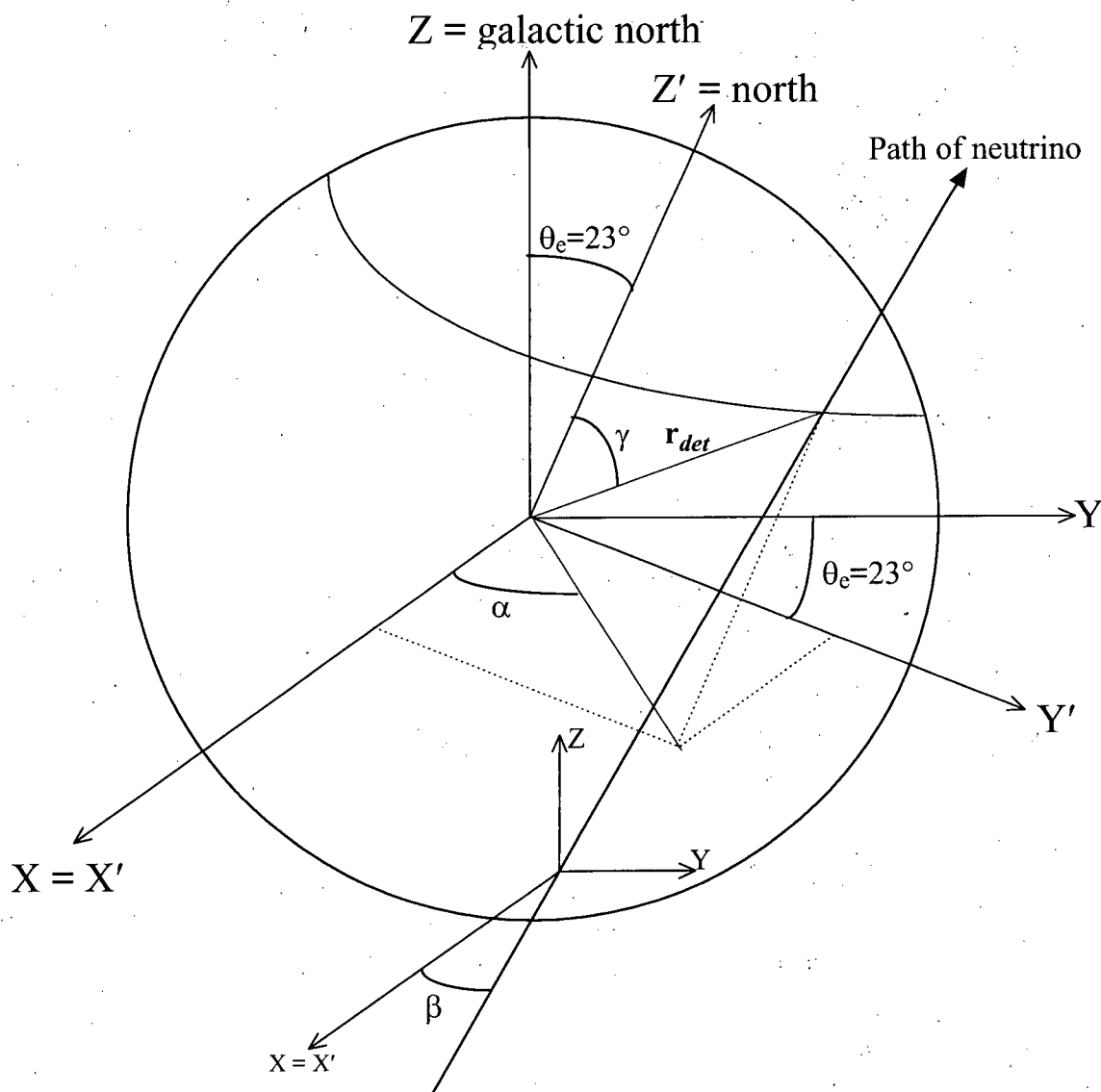


Figure 4.10: Coordinate systems used to determine the path length of the neutrino through the earth. The XY axes define the plane of the ecliptic, while the $X'Y'$ define the equatorial plane. The angle γ is the azimuthal angle of the detector about the axis of rotation of the earth. The angle α defines the degree of freedom in the earth's rotation and determines the time of day at which the neutrino arrives. The angle β defines the angle which the earth makes relative to the sun, and determines the time of year.

as follows:

$$\begin{pmatrix} r_x \\ r_y \\ r_z \end{pmatrix} = r_{\text{det}} \begin{pmatrix} 1 & 0 & 0 \\ 0 & c_\theta & s_\theta \\ 0 & -s_\theta & c_\theta \end{pmatrix} \begin{pmatrix} s_\gamma c_\alpha \\ s_\gamma s_\alpha \\ c_\gamma \end{pmatrix} = r_{\text{det}} \begin{pmatrix} s_\gamma c_\alpha \\ c_\theta s_\gamma s_\alpha + s_\theta c_\gamma \\ -s_\theta s_\gamma s_\alpha + c_\theta c_\gamma \end{pmatrix} \quad (4.27)$$

where s_η and c_η are defined to be the sine and cosine of the angle η . The path of a neutrino through the detector when the earth is at angle β in the XY plane is defined by the line

$$c_\beta x + s_\beta y = c_\beta r_x + s_\beta r_y \quad (4.28)$$

$$z = r_z$$

Combining these equations with $x^2 + y^2 + z^2 = r_{\text{earth}}^2$ determines two solutions (x, y, z) which define the two points where the neutrino path crosses the earth's surface. Eliminating x and z using equations 4.28 yields the equation

$$y^2 - 2s_\beta (c_\beta r_x + s_\beta r_y) y + c_\beta^2 (r_z^2 - r_{\text{earth}}^2) + (c_\beta r_x + s_\beta r_y)^2 = 0 \quad (4.29)$$

The discriminant for this quadratic equation can be reduced to

$$b^2 - 4ac = 4c_\beta^2 [r_{\text{earth}}^2 - r_{\text{det}}^2 + (s_\beta r_x - c_\beta r_y)^2] > 0 \quad (4.30)$$

which is positive definite and guarantees two real solutions, one short path and one long path. If the neutrino arrives in the *daytime* (the short path solution) the constant density $N_e = 1.34 \text{ mol/cm}^3$ is used in regeneration calculations corresponding to the electron density of the earth crust. For *nighttime* neutrinos, a density closer to the average through the earth is used, and regeneration is calculated with $N_e = 2.1 \text{ mol/cm}^3$.

4.4.6 Stability of the Results

One last question which must be addressed is the level of statistics required for the Monte Carlo method to generate accurate results—how many *events* are required to accurately

Source Reaction	Chlorine			Gallium		
	R_{Cl} [SNU]	σ_{Cl}	σ_{Cl}/R_{Cl}	R_{Ga} [SNU]	σ_{Ga}	σ_{Ga}/R_{Ga}
hep	4.27×10^{-3}	2.4×10^{-5}	0.55 %	8.33×10^{-3}	7.0×10^{-5}	0.84 %
8B	6.87	8.9×10^{-2}	1.3 %	15.9	0.13	0.81 %
pep	0.204	5.6×10^{-9}	0.0 %	2.86	4.0×10^{-8}	0.0 %
7Be	1.60	3.9×10^{-3}	0.25 %	37.7	8.2×10^{-2}	0.22 %
pp	0.0	0.0	<i>n/a</i>	71.4	0.43	0.61 %
${}^{13}N$	0.156	1.1×10^{-3}	0.71 %	3.85	1.7×10^{-2}	0.44 %
${}^{15}O$	0.371	2.8×10^{-3}	0.75 %	6.24	3.2×10^{-2}	0.52 %
${}^{17}F$	4.47×10^{-3}	3.3×10^{-5}	0.74 %	7.47×10^{-2}	3.7×10^{-4}	0.49 %
<i>Total</i>	9.21	8.7×10^{-2}	0.95 %	138.1	0.41	0.30 %

Table 4.1: Mean standard model neutrino rates for chlorine and gallium detectors from ten different trials generating 10,000 events for each neutrino source with different pseudo-random number generator seeds.

calculate neutrino oscillation probabilities on earth? In addition, how accurately are the energy and radial distributions of the neutrino sources reproduced by a given number of events?

The first of these questions can be answered by calculating the event rate for a given number of events using different initial random number seeds. Table 4.1 shows the mean and standard deviations in event rates for each of the eight neutrino sources on both chlorine and gallium targets based on 10,000 neutrino events with ten different random number seeds. Almost all of the sources have standard deviations which are less than one percent of the mean, and the discrete energy neutrinos have much more accurately determined rates. The rates for the chlorine and gallium experiments have errors of 0.95 % and 0.30 % respectively.

In calculating the MSW effect in a plot with *typically* a 41×41 grid, the average standard model (no MSW) event rate is calculated over *all* events and all eight neutrino sources ($41 \times 41 \times 10,000 \times 8 = 1.34 \times 10^8$ events). Then the MSW rate at the ij grid point $rate_{ij,MSW}$ is multiplied by the ratio of the overall standard model result with the

standard model rate $r_{ij,STM}$ at that grid point.

$$rate_{ij,MSW,corrected} = rate_{ij,MSW} \frac{\frac{1}{41^2} \sum_{i,j} rate_{ij,STM}}{rate_{ij,STM}} \quad (4.31)$$

This further reduces the statistical error in the calculation. Grid points where the MSW rate is low as a result of statistical variations will also produce low standard model results, but the multiplication factor corrects this.

The second possible concern with the Monte Carlo procedure is that the energy and radial distributions will not be correctly reproduced, either by coding errors or by problems with the pseudo-random number generator. Figure 4.11 shows the actual frequencies for random numbers and neutrino production as a function of the solar radius and energy with the actual distributions. It is clear from the figure that the frequency of pseudo-random numbers generated is consistent with a flat distribution, and that the Monte Carlo reproduces both the radial and energy distributions of neutrino production.

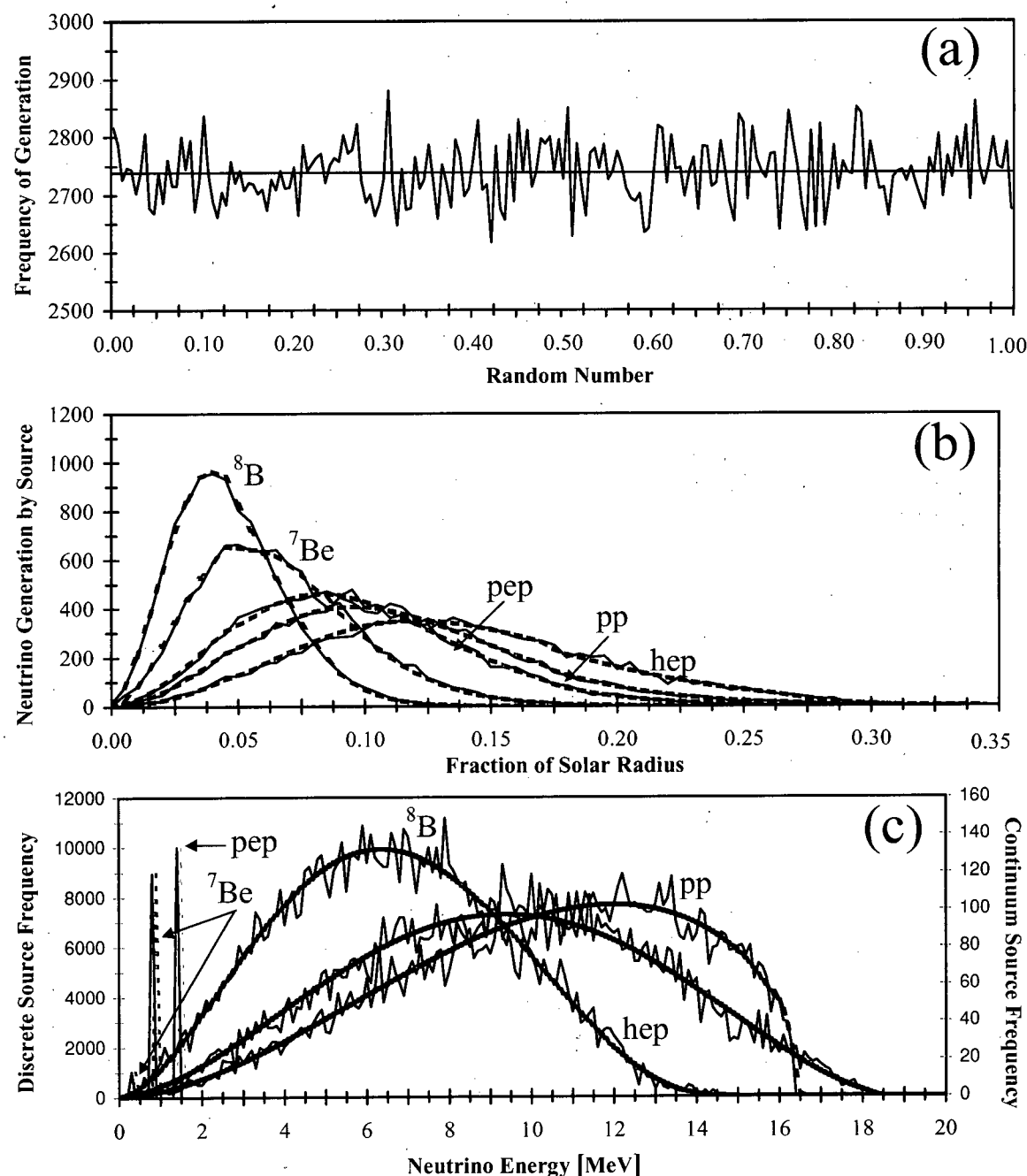


Figure 4.11: Monte Carlo reproduction of statistical distributions based on 10,000 events for each of five pp -cycle neutrino sources. (a) Frequency of generation of random numbers between 0 and 1. (b) Frequency of generation of neutrinos as a function of solar radius for five different neutrino sources. Thick smooth lines show actual probability distributions. (c) Frequency of generation of neutrinos as a function of energy, with actual distributions shown as dotted lines. Note that discrete source lines have been separated horizontally to differentiate them, and that values on the energy axis must be divided by 40 for the pp distribution which has a maximum energy of 0.42 MeV .

Chapter 5

Numerical Calculations with Three Neutrinos

5.1 Introduction

Chapter three introduced the notation to describe mixing of three neutrinos and discussed reasons why two neutrino analyses may not be sufficient to describe nature. This chapter will extend that analytical work in specific cases, and study three neutrino phenomena using the computer codes developed and described in Chapter four.

Section two will make some preliminary notes on oscillation lengths and mass hierarchies that will be used later on. Section three will study neutrinos oscillations in the one mass scale dominant mass hierarchy, but without the assumption of small matter effects. Indirect oscillations of $\nu_\mu \rightarrow \nu_e$ will be shown to be possible even when Δm_{21}^2 is very small—a distinctly three neutrino effect.

Symmetries of the oscillation probabilities will be studied, and it will be shown that normal accelerator experiments will find a two-fold degeneracy in the neutrino oscillation parameters. While this effect has been noted in the literature, it is described here analytically and the relation between the degenerate parameter sets is derived. Regions of parameter space that can be surveyed in four possible OMSD scenarios will be illustrated, and detailed calculations will show that matter effects may become apparent at relatively short baselines (250 km) in some schemes. Finally, matter effects which occur on very long baselines will be plotted.

Section four will look at the phenomenon of CP violation, and discuss where it might

be seen. Conditions required for the next generation of neutrino oscillation experiments to be able to make quantitative inferences will be discussed. After defining the notation used to describe CP violation the existing literature, most of which is less than a year old, will be reviewed. New analytical results describing CP violation to second order in two small parameters (matter effects and ratio of the neutrino mass scales) will be presented. Second order effects will be apparent in the data presented, and it will be argued that because matter effects are likely to be larger than CP, the additional accuracy is needed to correctly interpret future experiments.

These results will be applied to long baseline experiments to make accurate estimates of the magnitude of CP violation likely to be seen at the KEK to SuperKamiokande and MINOS experiments, which has not been done to date. Strategies to isolate CP violating effects from larger matter effects will be applied to these experiments. Using the second order terms presented, measurement of CP violation in the matter dominated regime—a phenomenon which cannot be described at first order—will be discussed. However, numerical calculations will allow CP violation to be studied even when the second order approximation breaks down, a regime thus far unexplored in the literature. It will be shown that nuclear reactor results can be combined with accelerator experiments to isolate CP violation from matter analytically, an effect which will also be studied numerically. Finally, calculations showing that CP violation does impact the ratio of μ -type to e -type neutrinos measured in the atmospheric flux, and the magnitude will be estimated to be up to several percent for reasonable estimates of the neutrino masses and related parameters.

In section five, three neutrino effects on solar neutrino experiments will be discussed. Existing work with two mixing angles and one mass squared difference will be extended to include three mixing angles and two mass squared differences. New calculations will modify the allowed regions of Δm_{21}^2 and s_{12}^2 as a result of the third neutrino, in accordance

with experimental results on atmospheric neutrinos. Through three neutrino vacuum oscillations on the way to the earth, the mixing parameter s_{23}^2 will be shown to materially affect the solar neutrino results. In addition, the possibility that the third neutrino converts some of the high energy ^8B neutrinos will be quantitatively considered.

5.2 Preliminary Notes

5.2.1 Baselines required for oscillations and matter effects

The vacuum oscillation length between two neutrino flavours is given by $L_V = \frac{4\pi E \hbar c}{\Delta m^2}$. Multiplying the constants and putting factors in typical dimensional units gives

$$L_V = 2.48 \text{ km} \frac{E}{\text{GeV}} \frac{\text{eV}^2}{\Delta m^2} \quad (5.1)$$

Or put another way, an experiment with baseline $L = L_V/4$ and neutrino peak energy E which is capable of measuring the first minimum in a neutrino oscillation will rule out

$$\Delta m^2 \geq 0.62 \text{ eV}^2 \frac{E}{\text{GeV}} \frac{\text{km}}{L} \quad (5.2)$$

Further, if a neutrino travels straight down and arrives at its first minimum when emerging on the other side of the earth, then $L = 2R_\oplus$. Substituting this gives an approximation of the smallest mass scale which can be probed on an earth bound experiment:

$$\Delta m_{\min}^2 = 4.8 \times 10^{-5} \text{ eV}^2 \frac{E}{\text{GeV}} \quad (5.3)$$

In order to probe to masses differences below these limits, it is necessary to have: (i) sufficient statistics to allow measurement of an effect before the first oscillation minimum is reached, (ii) neutrino energies below the 1 GeV level, or (iii) some observable matter effect which increases the mass difference.

The effect of matter on neutrino masses can be estimated by writing the matter term added to the hamiltonian in dimensional units to obtain

$$\begin{aligned} H_{ee}^{mat} &= \frac{2\sqrt{2}G_F N_A N_e E}{(\hbar c)^3} \\ &= 1.5 \times 10^{-4} \text{ eV}^2 \frac{E}{\text{GeV}} \frac{N_e}{\text{mol/cm}^3} \end{aligned} \quad (5.4)$$

Except at baselines above 10,000 km, the earth's density is below 2.5 mol/cm³. Using an average of 2.0 mol/cm³ and substituting H_{ee}^{mat} for Δm^2 in equation 5.1 produces an estimate of the baseline at which matter effects would clearly be evident:

$$\frac{L^{mat}}{4} \approx 2050 \text{ km} \quad (5.5)$$

At this length, the matter-induced mass of the electron is equal to mass which reaches a minimum at the detector, so some effect must occur. However, matter dependence does become apparent on much shorter baselines.

5.2.2 Neutrino mass hierarchies

The experimental data suggests that there are two different neutrino mass scales—one which is in either the 10⁻¹⁰ eV² (vacuum) or 10⁻⁵ eV² (MSW) range to solve the solar neutrino problem, and another in the 10⁻⁴–10⁻² eV² range to account for the atmospheric neutrino anomaly. In the work which follows the masses which are considered will go somewhat outside those suggested by the strict interpretation of the experimental results in order to allow for possible changes in them, and because the intuition from two neutrino oscillations may not always apply in the three neutrino situation where six parameters are present.

The mass of the electron neutrino will be assumed to be slightly smaller than one other neutrino, and the third neutrino mass will be left arbitrary. If vacuum oscillations solve the SNP, then the ν_e mass must be within about 10⁻¹⁰ eV² of one of the other masses.

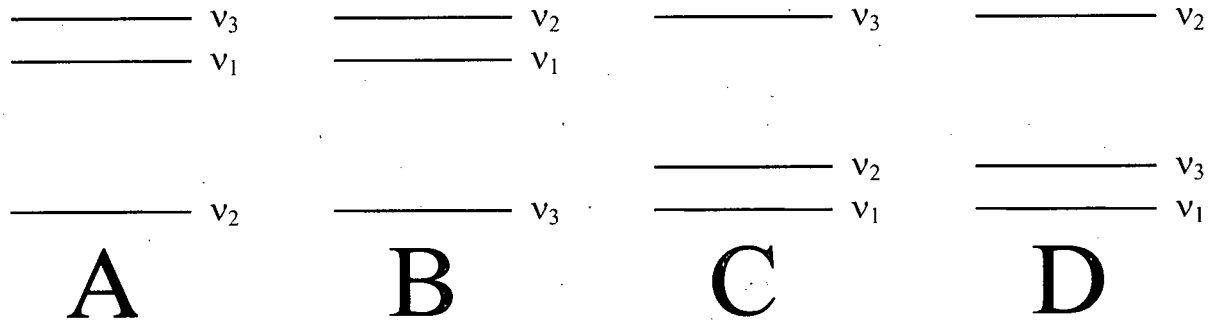


Figure 5.1: Four possible mass structures for three neutrinos given that the ν_1 mass must be slightly less than one of the other neutrino masses.

Whether it is just above or just below is irrelevant in terrestrial experiments because the oscillation length given by equation 5.1 would be orders of magnitude larger than the diameter of the earth at any measurable energy. In this case, an inverted hierarchy with $m_{\nu_1} = m_{\nu_i} + O(10^{-10} \text{ eV}^2)$ would produce results identical to $m_{\nu_1} = m_{\nu_i} - O(10^{-10} \text{ eV}^2)$. Alternately, if the MSW effect explains the SNP, the ν_e mass must be smaller than at least one other neutrino, by an amount on the order of a few times 10^{-5} eV^2 or less. These restrictions reduce the number of unique mass structures to four cases, labelled A, B, C and D and illustrated in figure 5.1.

5.3 The One Mass Scale Dominant Structure

If one mass squared difference in the neutrino mass hierarchy is so small that the oscillation length is many times the diameter of the earth, then the system simplifies greatly. Most authors further simplify the problem by assuming that the complex phase δ vanishes and that matter effects are small. In what follows, however, the situation will be clarified and it will be shown that the first of these assumptions is unnecessary and the second will not be valid on baselines on the order of a few hundred kilometres where matter effects will be apparent.

5.3.1 Two types of OMSD and oscillation probabilities

The four mass structures in figure 5.1 each give rise to distinct OMSD scenarios. Setting $\Delta m_{21}^2 = 0$ in hierarchies B and C reduces the probabilities in equations 3.32 to 3.37 to the following simplified form:

$$P_{ee}^{OMS D-1}(L) = 1 - 4s_{13}^2 c_{13}^2 \mathbf{S}_{31}^2 \quad (5.6)$$

$$P_{\mu\mu}^{OMS D-1}(L) = 1 - 4c_{13}^2 s_{23}^2 (1 - c_{13}^2 s_{23}^2) \mathbf{S}_{31}^2 \quad (5.7)$$

$$P_{\tau\tau}^{OMS D-1}(L) = 1 - 4c_{13}^2 c_{23}^2 (1 - c_{13}^2 c_{23}^2) \mathbf{S}_{31}^2 \quad (5.8)$$

$$P_{e\mu}^{OMS D-1}(L) = 4s_{13}^2 c_{13}^2 s_{23}^2 \mathbf{S}_{31}^2 \quad (5.9)$$

$$P_{e\tau}^{OMS D-1}(L) = 4s_{13}^2 c_{13}^2 c_{23}^2 \mathbf{S}_{31}^2 \quad (5.10)$$

$$P_{\mu\tau}^{OMS D-1}(L) = 4c_{13}^4 s_{23}^2 c_{23}^2 \mathbf{S}_{31}^2 \quad (5.11)$$

Note that none of the oscillation probabilities depend on either the mixing parameter s_{12} or the complex phase δ , so that six parameters have been reduced to three. Fogli et. al. [147] have correctly noted that since $\mathbf{S}_{31}^2 = \sin^2\left(1.27 \frac{\Delta m_{31}^2 L}{E}\right)$ is an even function of Δm_{31}^2 , hierarchies B and C are indistinguishable in vacuum. However, matter enhances neutrino oscillations and suppresses antineutrino oscillations in scenario C, and will have the opposite affect in scenario B.

A similar reduction in the oscillation probabilities occur in hierarchies A and D when $\Delta m_{31}^2 = 0$. However, naively applying these equalities to equations 3.32 to 3.37 produces only slightly simplified expressions which depend on all three mixing angles and the complex phase. Symmetry of the mass structure intuitively suggests that it should be possible to write the oscillation probabilities with expressions with a similar functional form to those in equations 5.6 to 5.11. It turns out that the more complex expressions

come from the form of the CKM matrix which was defined in equation 3.1. The oscillation probabilities can be simplified with a redefinition of the parameters so that

$$P_{ee}^{OMSD-2}(L) = 1 - 4\bar{s}_{12}^2 \bar{c}_{12}^2 S_{21}^2 \quad (5.12)$$

$$P_{\mu\mu}^{OMSD-2}(L) = 1 - 4\bar{c}_{12}^2 \bar{c}_{23}^2 (1 - \bar{c}_{12}^2 \bar{c}_{23}^2) S_{21}^2 \quad (5.13)$$

$$P_{\tau\tau}^{OMSD-2}(L) = 1 - 4\bar{c}_{12}^2 \bar{s}_{23}^2 (1 - \bar{c}_{12}^2 \bar{s}_{23}^2) S_{21}^2 \quad (5.14)$$

$$P_{e\mu}^{OMSD-2}(L) = 4\bar{s}_{12}^2 \bar{c}_{12}^2 \bar{c}_{23}^2 S_{21}^2 \quad (5.15)$$

$$P_{e\tau}^{OMSD-2}(L) = 4\bar{s}_{12}^2 \bar{c}_{12}^2 \bar{s}_{23}^2 S_{21}^2 \quad (5.16)$$

$$P_{\mu\tau}^{OMSD-2}(L) = 4\bar{c}_{12}^4 \bar{s}_{23}^2 \bar{c}_{23}^2 S_{21}^2 \quad (5.17)$$

where the redefined angular parameters are given by:

$$\bar{s}_{12} = s_{12} c_{13} \quad (5.18)$$

$$\bar{c}_{12} = [1 - s_{12}^2 c_{13}^2]^{1/2} \quad (5.19)$$

$$\bar{s}_{23} = \left[\frac{c_{12}^2 s_{23}^2 + 2s_{12} c_{12} s_{13} s_{23} c_{23} c_\delta + s_{12}^2 s_{13}^2 c_{23}^2}{1 - s_{12}^2 c_{13}^2} \right]^{1/2} \quad (5.20)$$

$$\bar{c}_{23} = \left[\frac{c_{12}^2 c_{23}^2 - 2s_{12} c_{12} s_{13} s_{23} c_{23} c_\delta + s_{12}^2 s_{13}^2 s_{23}^2}{1 - s_{12}^2 c_{13}^2} \right]^{1/2} \quad (5.21)$$

5.3.2 Indirectly coupled $\nu_\mu - \nu_e$ oscillations

Pantaleone [129] has suggested that one purely three neutrino effect would be ν_e appearance without direct $\nu_e - \nu_\mu$ mixing. His result will be reproduced for completeness and to verify the computer codes written. In the *OMSD-1* scenario above, Δm_{21}^2 is too small to be of consequence, but $P_{\mu e}(L)$ is non-zero because $\nu_\mu \rightarrow \nu_\tau \rightarrow \nu_e$ oscillations can occur. The contours are identical to those in two neutrino mixing, except that $P_{\mu e}^{OMSD-1}(L)$ has the additional factor of s_{23}^2 which could be absorbed into an *effective* θ_{13} . Figure

5.2 shows an attempt to roughly reproduce the figures in that paper in order to test the three neutrino long baseline code.

The figure shows contours of constant $P_{\mu e}(L)$ as a function of $\sin^2(2\theta_{13})$ and Δm_{31}^2 for both neutrinos and antineutrinos, with $\sin^2(\theta_{23}) = 0.03$ and 0.3 . The reference neutrino spectrum is used with the neutrino energy is tripled so that its peak is closer to the 6 GeV peak of the FNAL neutrino spectrum. The probabilities are scaled by the neutrino flux and energy (the latter because $\sigma \propto E$). The first and second rows show contours at 6400 km and 11,400 km respectively. The results compare favourably to Pantaleone's, with the only visible difference being the height of region where matter enhancement occurs. This difference stems from the wide energy spectrum of the FNAL neutrino beam, compared to the relatively sharp peaked reference spectrum used to generate this figure.

The method of calculation is varied in each column, and the results are more accurate (but take longer to compute) moving from left to right. In the left column, a constant density along the path through the earth is assumed. In the middle column, the earth's density profile is divided into eight shells and the mean density along the neutrino's path through each shell is determined as discussed in Chapter 4. In the rightmost column, the hamiltonian is integrated using a fourth order Runge-Kutta iterative calculation to obtain $P_{\mu e}(L)$. The figure shows that on shorter baselines, both approximate methods reproduce the numerically integrated calculation. On the longer baseline, the shell method does a better job of reproducing the correct result than the fixed density method, although it is not perfect either.

It is also notable that increasing the baseline does not necessarily provide a probe to lower Δm^2 in this case because at increased depths, the earth's electron density increases. Going from $L = 6400$ km to $L = 11,400$ km, $\Delta m_{res}^2 \propto N_e$ has increased about as much as the baseline, so the minimum mass difference probed does not change. However, the longer baseline would survey smaller mixing angles.

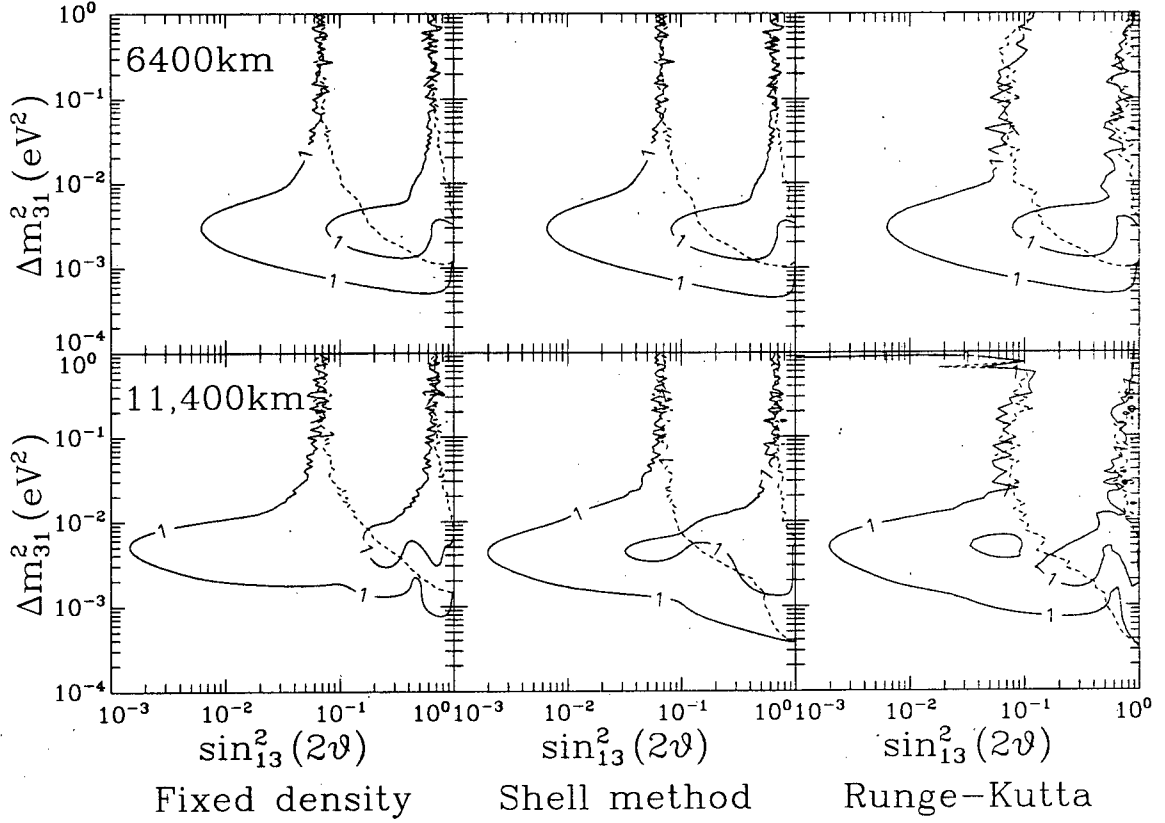


Figure 5.2: Contours for $P_{\mu e} = 1\%$ (solid lines) and $P_{\mu \bar{e}} = 1\%$ (dotted lines) at $L = 6400$ km and $L = 11,400$ km with mixing parameter $s_{23}^2 = 0.03$ and 0.3 . In the left column, a fixed electron density along the path is used (2.1 mol/cm^3 at 6400 km and 4.0 mol/cm^3 at $11,400$ km). In the middle column, the earth's density profile is divided into eight shells, and the mean value along the neutrino's path through each shell is calculated, as discussed in Chapter 4. In the right column, the neutrino wavefunction is integrated along 2048 steps using a fourth-order Runge-Kutta method. Note that this method eventually breaks down at large Δm^2 as the number of steps per oscillation gets too small.

5.3.3 Symmetries of the $P_{\alpha\beta}(L)$ and measuring the CKM parameters

Several symmetries in the oscillation probabilities are apparent. For example, notice that the probability $P_{\alpha\beta}^{OMSD-2}(\bar{s}_{12}^2, \bar{c}_{12}^2, \bar{s}_{23}^2, \bar{c}_{23}^2, \Delta m_{21}^2, L, E)$ is functionally identical to the probability $P_{\alpha'\beta'}^{OMSD-1}(s_{13}^2, c_{13}^2, s_{23}^2, c_{23}^2, \Delta m_{31}^2, L, E)$ where $\alpha' = e, \mu, \tau$ when $\alpha = e, \tau, \mu$ respectively and similarly for β' (i.e. the role of μ and τ are reversed). The redefinition of the *OMSD-2* oscillation parameters restored this symmetry. Moreover, since accelerators produce beams of ν_μ ($\bar{\nu}_\mu$) and measure $P_{\mu e}$, $P_{\mu\mu}$ and $P_{\mu\tau}$, making inferences in the *OMSD-2* scenario is equivalent to making inferences based on $P_{\tau e}$, $P_{\tau\tau}$ and $P_{\tau\mu}$ with *OMSD-1*.

There are two additional symmetries which are of interest. The first comes from the observation that $P_{\alpha\beta}^{OMSD-1}(s_{23}^2, c_{23}^2) = P_{\alpha'\beta'}^{OMSD-1}(c_{23}^2, s_{23}^2)$ where again $\alpha' = e, \mu, \tau$ when $\alpha = e, \tau, \mu$ respectively and similarly for β' . Combining these two symmetries gives the relation:

$$P_{\alpha\beta}^{OMSD-2}(\bar{s}_{12}^2, \bar{c}_{12}^2, \bar{s}_{23}^2, \bar{c}_{23}^2, \Delta m_{21}^2, L, E) = P_{\alpha\beta}^{OMSD-1}(s_{13}^2, c_{13}^2, c_{23}^2, s_{23}^2, \Delta m_{31}^2, L, E) \quad (5.22)$$

Because these probabilities are what the experiments measure, it is not possible to differentiate between the two different *OMSD* scenarios using oscillations in vacuum or, as will be shown shortly, first order matter effects. For each set of parameters and confidence level in *OMSD-1*, there is an equivalent set of parameters with an identical confidence level in *OMSD-2*. In effect, scenarios *A* and *B* are indistinguishable from each other, and so are *C* and *D*.

A more ‘accidental’ symmetry occurs when measuring oscillations of muon neutrinos or antineutrinos—typical of accelerator based experiments. In a recent paper Fogli and Lisi [146] found a two-fold ambiguity in the allowed region when results from $\nu_\mu \rightarrow \nu_e$ and $\nu_\mu \rightarrow \nu_\tau$ experiments were combined. The parallel solution can be calculated by looking for a second set of angles which produce the same oscillation probabilities $P_{\mu\alpha}^{OMSD-1}(L)$

for $\alpha = e, \mu, \tau$. Since these three probabilities sum to unity, it is only necessary to find $\tilde{\theta}_{13}$ and $\tilde{\theta}_{23}$ which satisfy

$$P_{\mu e}^{OMSD-1}(L) = 4s_{13}^2 c_{13}^2 s_{23}^2 \mathbf{S}_{31}^2 = 4\tilde{s}_{13}^2 \tilde{c}_{13}^2 \tilde{s}_{23}^2 \mathbf{S}_{31}^2 \quad (5.23)$$

$$P_{\mu \tau}^{OMSD-1}(L) = 4s_{13}^2 c_{13}^2 c_{23}^2 \mathbf{S}_{31}^2 = 4\tilde{s}_{13}^2 \tilde{c}_{13}^2 \tilde{c}_{23}^2 \mathbf{S}_{31}^2 \quad (5.24)$$

Combining these equations and yields a quadratic equation which admits two solutions, the trivial one in which the new angular parameters are equal to the original ones and a second one:

$$\tilde{s}_{13}^2 = \frac{s_{13}^2 c_{13}^2 s_{23}^2}{1 - c_{13}^2 s_{23}^2} ; \quad \tilde{c}_{13}^2 = \frac{1 - 2c_{13}^2 s_{23}^2 + c_{13}^4 s_{23}^2}{1 - c_{13}^2 s_{23}^2} \quad (5.25)$$

$$\tilde{s}_{23}^2 = \frac{(1 - c_{13}^2 s_{23}^2)^2}{1 - 2c_{13}^2 s_{23}^2 + c_{13}^4 s_{23}^2} ; \quad \tilde{c}_{23}^2 = \frac{c_{13}^4 s_{23}^2 c_{23}^2}{1 - 2c_{13}^2 s_{23}^2 + c_{13}^4 s_{23}^2} \quad (5.26)$$

Thus, even with accurate measurements of both $\nu_\mu \rightarrow \nu_e$ and $\nu_\mu \rightarrow \nu_\tau$ oscillations, the two mixing angles cannot be uniquely determined. Writing $P_{e\tau}^{OMSD-1}$ in terms of the second solution shows that the symmetry does not carry over to the other oscillation channels.

$$4\tilde{s}_{13}^2 \tilde{c}_{13}^2 \tilde{c}_{23}^2 \mathbf{S}_{31}^2 = 4s_{13}^2 c_{13}^2 c_{23}^2 \mathbf{S}_{31}^2 \frac{c_{13}^2 s_{23}^2}{1 - c_{13}^2 s_{23}^2} = \frac{c_{13}^2 s_{23}^2}{1 - c_{13}^2 s_{23}^2} P_{e\tau}^{OMSD-1} \quad (5.27)$$

Unless the CKM parameters conspire to satisfy $c_{13}^2 s_{23}^2 = \frac{1}{2}$, then this two-fold symmetry will be broken, and the two solutions can be differentiated by measuring any one of P_{ee}^{OMSD-1} , $P_{e\tau}^{OMSD-1}$ or $P_{\tau\tau}^{OMSD-1}$.

5.3.4 First order matter effects on OMSD parameters

At baselines greater than about 100 km, which will be probed in the next generation of long baseline neutrino oscillation experiments, first order matter effects do come into play. Such effects can be used to differentiate mass structures A and B, where the ν_1 and

its nearly degenerate mass partner are heavier than the other neutrino, from structures C and D, where the ν_1 is the lightest neutrino. In the latter case matter enhances oscillations as the ν_1 mass approaches the third neutrino while in the former, it inhibits neutrino oscillations and enhances those of antineutrinos.

Assuming that $m_{1,V}^2 = m_{2,V}^2 = 0$, $m_{3,V}^2 = M^2$ and $A = 2\sqrt{2}G_F N_e E$, the mixing parameters can be calculated to first order using equations 3.15 to 3.27:

$$m_{1,M}^2 = 0 \quad (5.28)$$

$$m_{2,M}^2 = c_{13}^2 A \quad (5.29)$$

$$m_{3,M}^2 = M^2 \left[1 + s_{13}^2 \frac{A}{M^2} \right] \quad (5.30)$$

$$s_{23,M}^2 = s_{23}^2 \quad (5.31)$$

$$s_{13,M}^2 = s_{13}^2 \left[1 + 2c_{13}^2 \frac{A}{M^2} \right] \quad (5.32)$$

$$S_{31,M}^2 = \sin^2 \left(\frac{1.27 M^2 L}{E} \right) = S_{31}^2 + \frac{1.27 s_{13}^2 A L}{E} \sin \left(\frac{2.54 M^2 L}{E} \right) \quad (5.33)$$

The parameter most likely to show matter effects is $s_{13,M}^2$ which, assuming that s_{13}^2 is quite small, has a first order coefficient of about 2. Figures 5.3 and 5.4 show contours of equal $P_{\mu e}$, $P_{\mu\mu}$ and $P_{\mu\tau}$ in the OMSD-1 and OMSD-2 scenarios (the latter was actually calculated as $P_{\tau e}$, $P_{\tau\tau}$ and $P_{\tau\mu}$ in OMSD-1). The plots in the two scenarios are very similar, and are identical under the transformation $s_{23}^2 \leftrightarrow \bar{c}_{23}^2$ when the fixed value $s_{23}^2 = 0.1$ and logarithmic scale on the horizontal axes are taken into consideration.

Note that the figures also give an indication of where contours for vacuum oscillations would occur in other experiments (ie. between the solid and dotted lines). For example, the Palo Verde experiment will search for $\bar{\nu}_e$ oscillations using a 12 ton detector at a distance of 800 m from the Palo Verde generating station outside Phoenix, USA. The

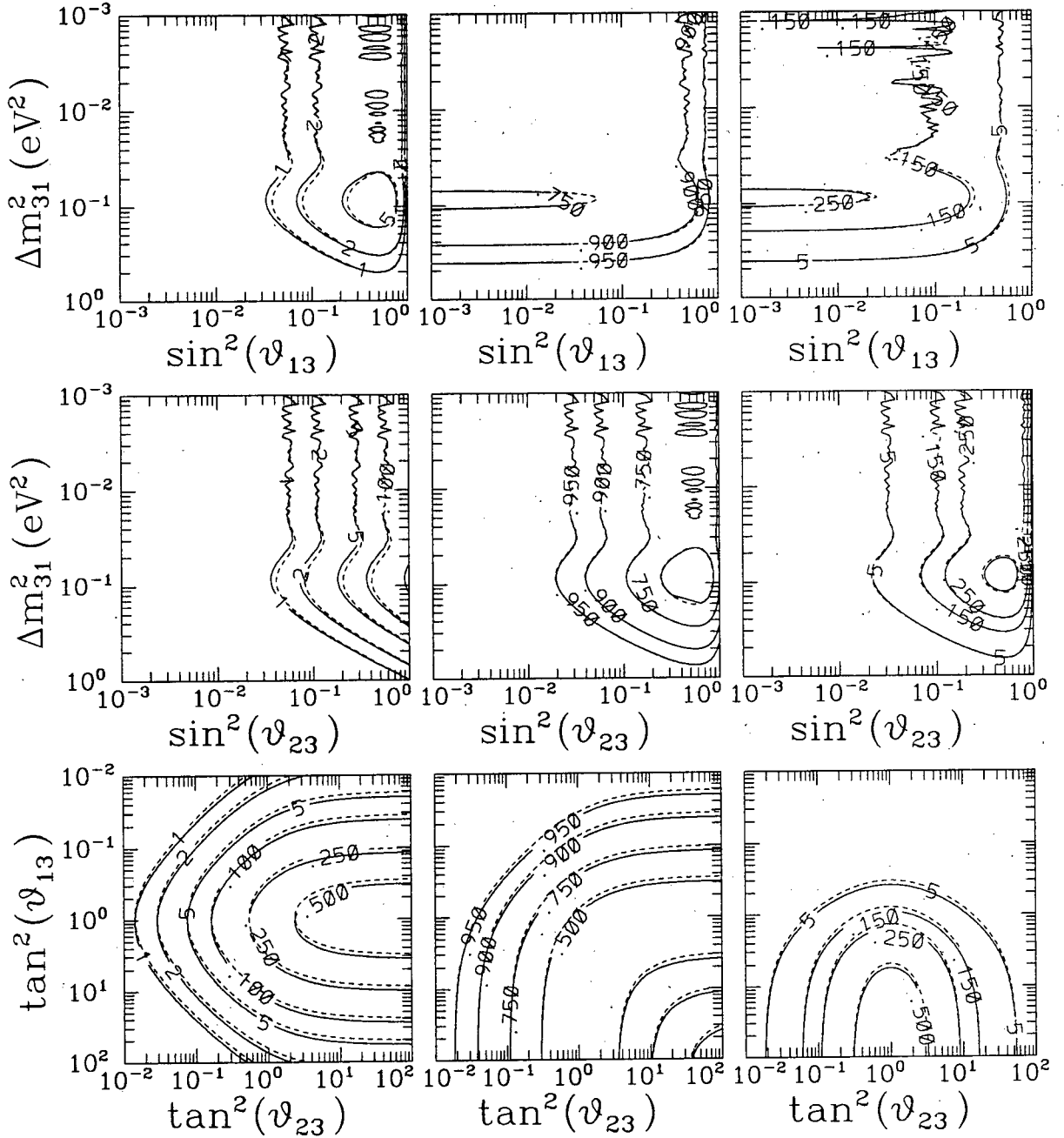


Figure 5.3: Contours of $P_{\mu\alpha}$ (solid lines) and $P_{\mu\bar{\alpha}}$ (dotted lines) on a 250 km baseline in the OMSD-1 scenario. Columns 1, 2 and 3 show $P_{\mu e}$, $P_{\mu\mu}$ and $P_{\mu\tau}$, respectively. Rows 1, 2 and 3 fix $s_{23}^2 = 0.1$, $s_{13}^2 = 0.1$ and $M^2 = 0.01 \text{ eV}^2$, respectively. Initial spectra are given by the reference ν_μ spectra, and calculations are done using the shell method. Note that all contours greater than one are percentages.

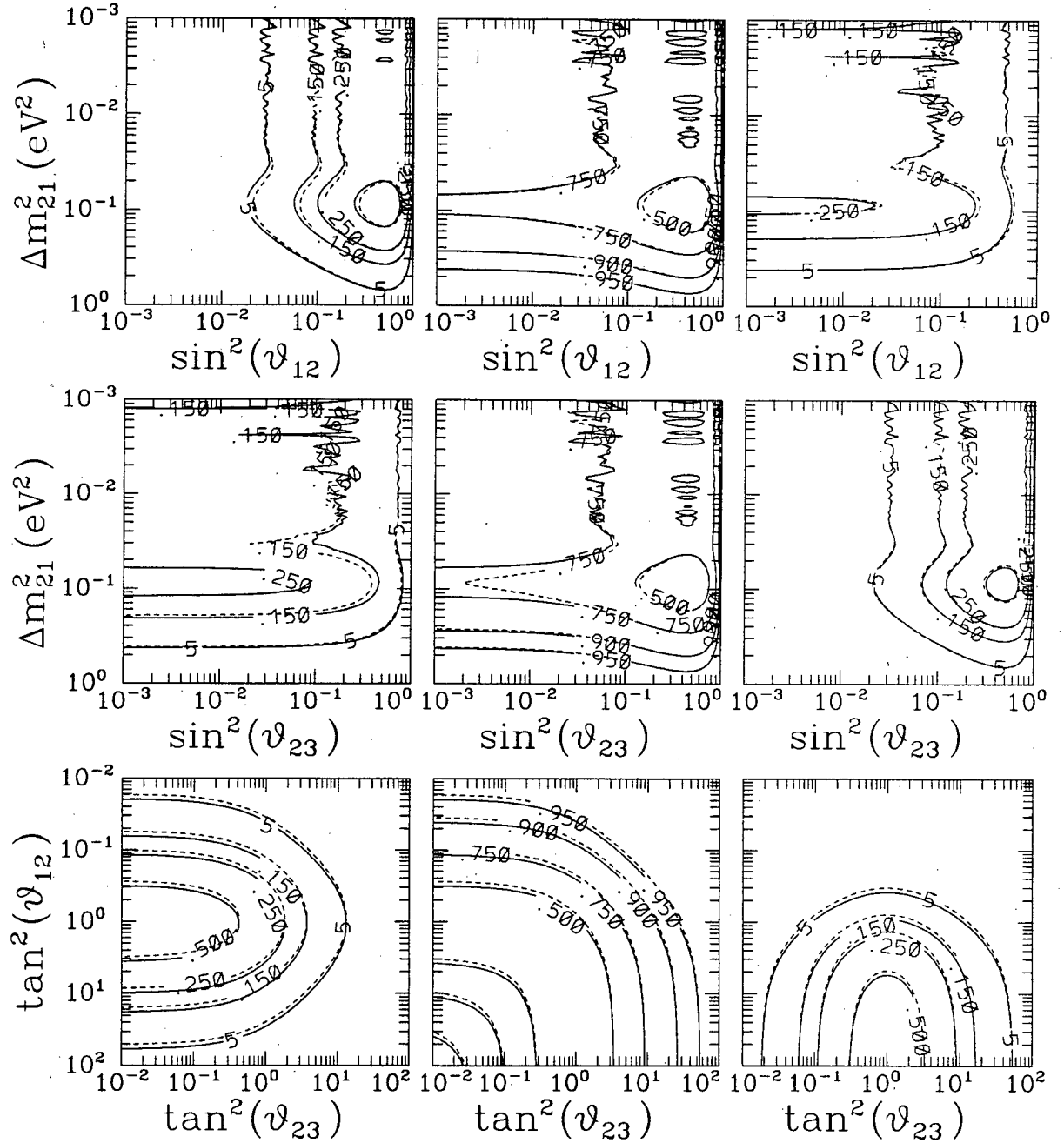


Figure 5.4: Contours of $P_{\mu\alpha}$ (solid lines) and $P_{\bar{\mu}\bar{\alpha}}$ (dotted lines) on a 250 km baseline in the OMSD-2 scenario. Columns 1, 2 and 3 show $P_{\mu e}$, $P_{\mu\mu}$ and $P_{\mu\tau}$, respectively. Rows 1, 2 and 3 fix $\bar{s}_{23}^2 = 0.1$, $\bar{s}_{12}^2 = 0.1$ and $M^2 = 0.01 \text{ eV}^2$, respectively. Initial spectra are given by the reference ν_μ spectra, and calculations are done using the shell method. Note that all contours greater than one are percentages.

shape of $\bar{\nu}_e$ energy spectrum is remarkably similar to the ν_μ reference spectrum except that the energies are three orders of magnitude smaller (MeV instead of GeV). Equation 5.4 clearly shows that matter effects would not be present. The contours in the figures are identical if the mass is scaled so that $\frac{\Delta m^2 L}{E}$ is kept invariant:

$$\Delta m_{PV}^2 = \frac{E_{PV}}{L_{PV}} \frac{\Delta m_{ref}^2 L_{ref}}{E_{ref}} = 0.31 \Delta m_{ref}^2 \quad (5.34)$$

Thus, probability contours for the Palo Verde experiment would be similar to those in figures 5.3 and 5.4 with the mass parameter scaled up by a factor of 1/0.31. Note, however, that this is an approximation since the cross-section would differ.

While the overall matter effects in the 250 km experiment are small, there is a significant first order effect in the second row of the OMSD-2 plot in the first two columns. It occurs here because the theoretical bias assumes that $s_{ij}^2 < c_{ij}^2$.

Matter does not affect s_{23}^2 at first order, and has little effect on c_{13}^2 provided that s_{13}^2 is small ($c_{13,M}^2 = c_{13}^2(1 - 2s_{13}^2 \frac{A}{M^2})$). This rules out matter effects in $P_{\mu\tau}$ while the smallness of s_{23}^2 rules them out in $P_{\mu e}^{OMSD-1}$, leaving $P_{\mu e}^{OMSD-2}$. Having a significant matter effect depends on the term $\bar{s}_{12,M}^2 \bar{c}_{12,M}^2 = \bar{s}_{12}^2 \bar{c}_{12}^2 \left[1 + 2(\bar{c}_{12}^2 - \bar{s}_{12}^2) \frac{A}{M^2}\right]$. The parameter \bar{s}_{12}^2 must be small enough that there is a significant matter effect, but also large enough that there is a measurable oscillation.

Figure 5.5 illustrates the first-order matter effects. It shows that the ratio of probabilities $P_{\mu e}^{OMSD-2}/P_{\bar{\mu}e}^{OMSD-2}$ increases with larger \bar{s}_{12}^2 , passing through unity at $\bar{s}_{12}^2 = 0.5$. Although the individual oscillation probabilities $P_{\mu e}^{OMSD-2}$ and $P_{\bar{\mu}e}^{OMSD-2}$ both reach their maximum magnitudes at that point, they are equal. Thus, a balance with moderately small (or large) \bar{s}_{12}^2 must occur so that oscillations will be measurable, but with a significant difference in the effect of matter on neutrinos and antineutrinos.

Figure 5.6 shows oscillation probabilities for an initial ν_μ ($\bar{\nu}_\mu$) beam with $s_{12}^2 = 0.1$ and $s_{23}^2 = 0.25$ as a function of energy. In mass hierarchies *C* and *D*, $P_{\mu e}$ is enhanced

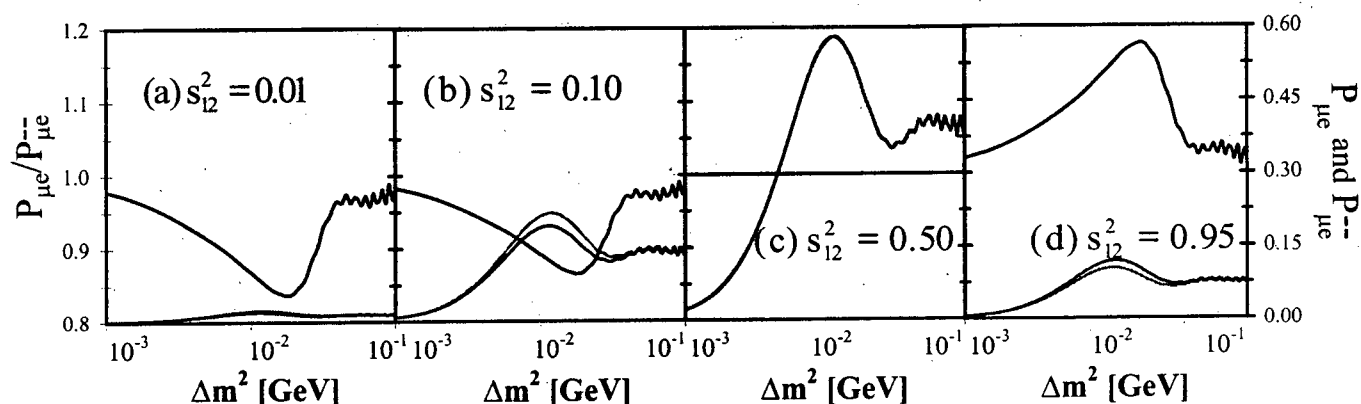


Figure 5.5: Matter effects as a function of Δm^2 for different values of s_{12}^2 . In each plot, the black lines (refer to left axis) show the ratio $P_{\mu e}^{OMSD-2}/P_{\mu e}^{OMSD-2}$, while the dark and light grey lines show $P_{\mu e}^{OMSD-2}$ and $P_{\mu e}^{OMSD-2}$ respectively with ordinates on the right axis.

while $P_{\mu e}$ is inhibited, while in scenarios *A* and *B* the reverse holds true. Thus, if $P_{\mu e}$ corresponds to neutrinos and $P_{\mu e}$ to antineutrinos then the mass structure *D* is in effect, otherwise the neutrinos follow mass structure *A*. Symmetry in the oscillation probabilities showed that hierarchies *A* and *B* are identical under the transformation $s_{23}^2 \leftrightarrow c_{23}^2$, and likewise for *C* and *D*.

In addition, the location of the maxima and minima in the curves will accurately determine the mass difference between the non-degenerate neutrinos. Figure 2.13 in chapter 2 noted that with bin widths of $1/8$ GeV, there would be between 500 and 1000 neutrinos per year in all bins from 0.75 GeV to 3.25 GeV at a 5 kT detector, a result which must be multiplied by six to account for SuperKamiokande's 32 kT fiducial mass.

5.3.5 OMSD solutions with very long baselines

In the very long baseline regime, matter effects become much more important, and the potential for enhancement of neutrino oscillations is much greater. Figures 5.7 and 5.8 show iso-probability contours on a very long baseline—10,000 km. At this length, matter effects are clearly apparent and not surprisingly, the mixing angle s_{13}^2 is the more

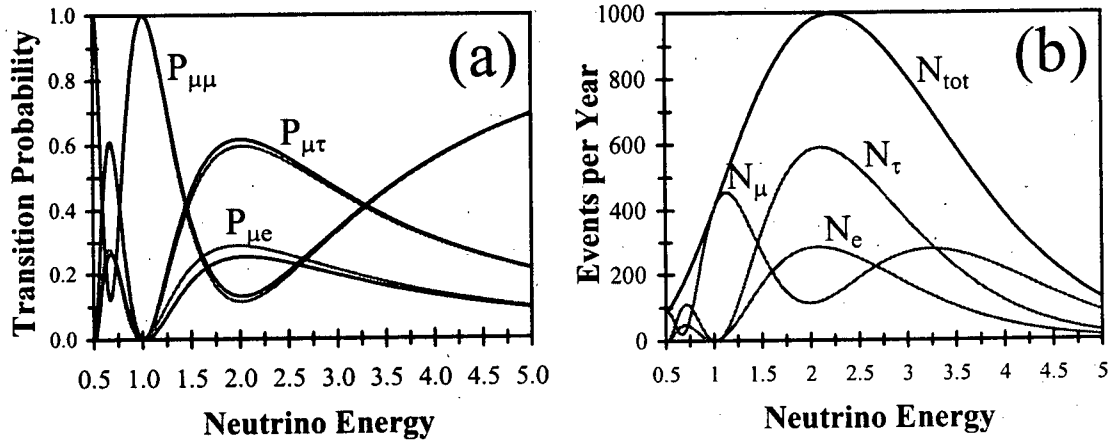


Figure 5.6: Matter effects on the energy spectra of detected neutrinos given vacuum parameters $s_{12}^2 = 0.1$ and $s_{23}^2 = 0.25$. $P_{\mu e}$, $P_{\mu\mu}$ and $P_{\mu\tau}$ are shown in figure (a). Neutrino oscillation probabilities are shown in grey while for antineutrino lines are black. In (b), the reference spectrum for neutrinos is added to show the number of ν_e and ν_{μ} events per year in $1/8 \text{ GeV}$ bins (ν_{τ} events would not be seen below about 4 GeV). Antineutrinos would have about half the number of events as neutrinos due to a smaller cross section.

interesting angular parameter. Matter drives up the $\nu_e - \nu_{\mu}$ and $\nu_e - \nu_{\tau}$ mixing allowing much smaller angles to be probed. On the other hand $\nu_{\mu} - \nu_{\tau}$ mixing (in the last column of the figures) appears to change only when there is a significant reduction in the flux of ν_{μ} 's resulting from large mixing in the $\nu_e - \nu_{\mu}$ sector.

5.4 CP Violation and Neutrino Oscillation

CP violation has already been observed in the quark sector, and with the presence of a third family comes the possibility that it is also violated in the lepton sector through a non-zero complex phase δ in the CKM matrix. Assuming a mass hierarchy with $m_1 < m_2 < m_3$, the effect is proportional to $\Delta m_{21}^2 / \Delta m_{31}^2$. Like the quark sector, CP violation is a very small effect in neutrino oscillations, and will require precision measurements to quantify it. The most likely candidate to see CP would be the KEK

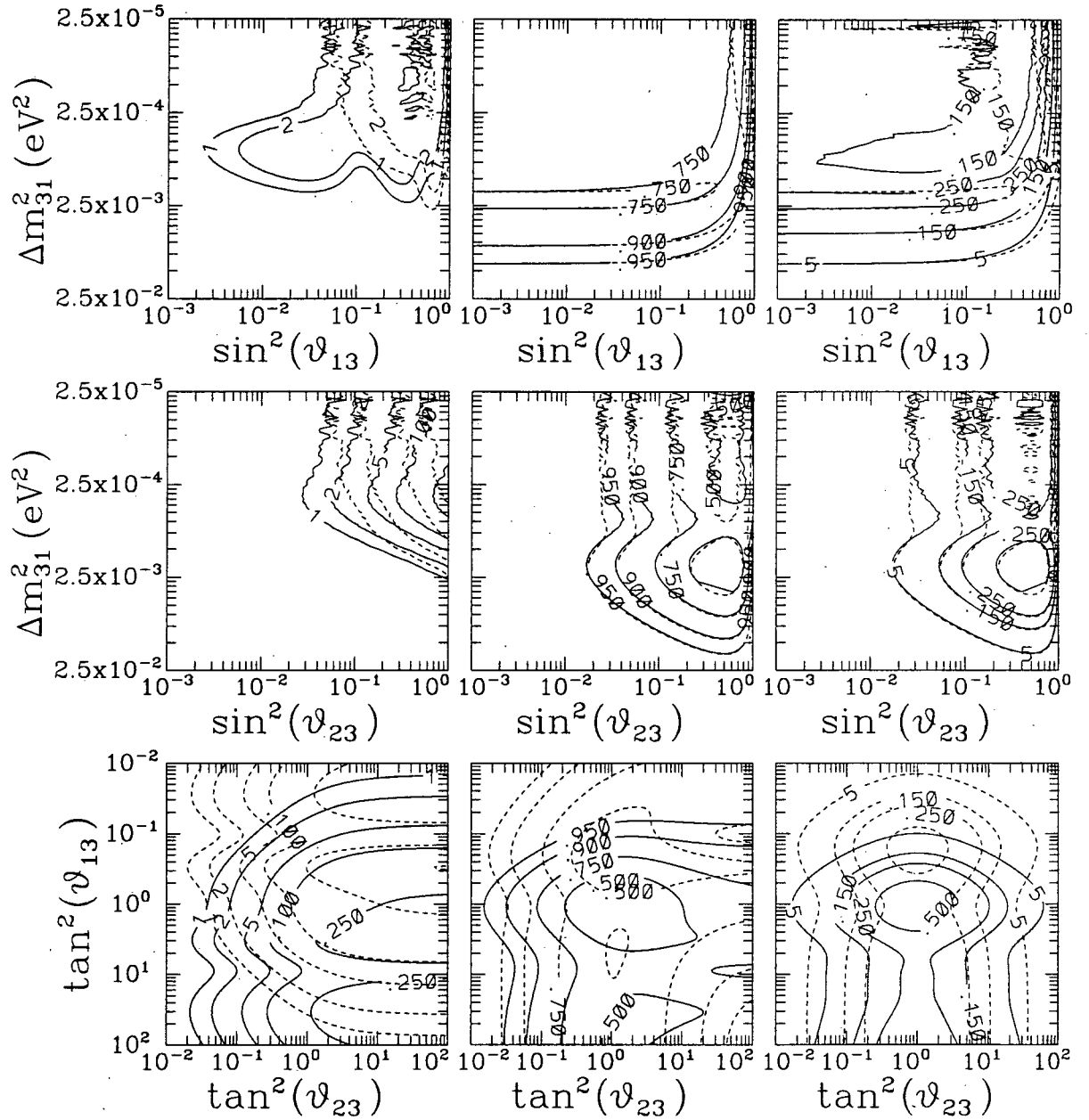


Figure 5.7: Contours of $P_{\mu\alpha}$ (solid lines) and $P_{\bar{\mu}\alpha}$ (dotted lines) on a 10,000 km baseline in the OMSD-1 scenario. Columns 1, 2 and 3 show $P_{\mu e}$, $P_{\mu\mu}$ and $P_{\mu\tau}$, respectively. Rows 1, 2 and 3 fix $s_{23}^2 = 0.1$, $s_{13}^2 = 0.1$ and $M^2 = 0.01 \text{ eV}^2$, respectively. Initial spectra are given by the reference ν_μ spectra, and calculations are done using the shell method. Note that all contours greater than one are percentages.

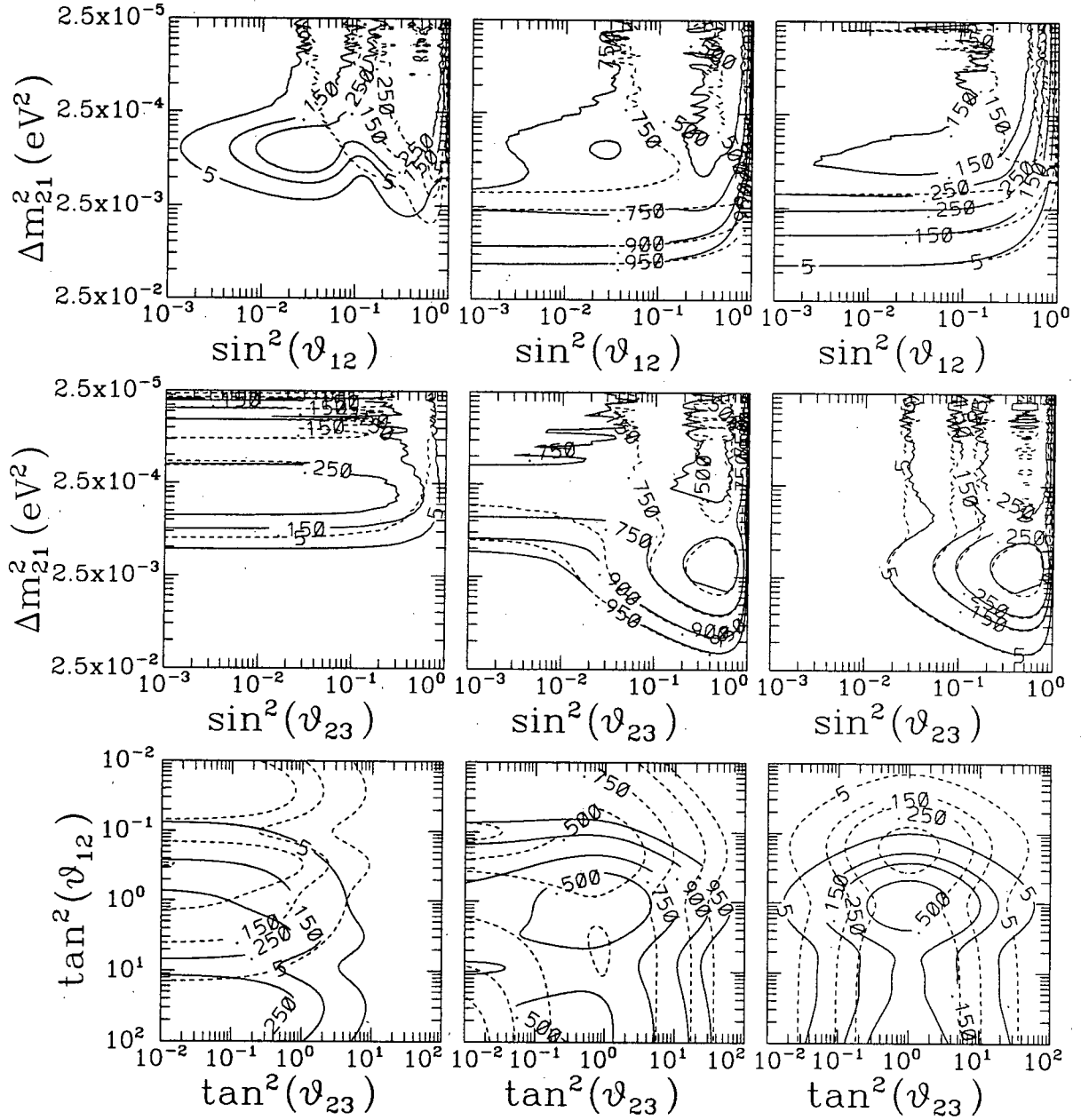


Figure 5.8: Contours of $P_{\mu\alpha}$ (solid lines) and $P_{\bar{\mu}\alpha}$ (dotted lines) on a 10,000 km baseline in the OMSD-2 scenario. Columns 1, 2 and 3 show $P_{\mu e}$, $P_{\mu \mu}$ and $P_{\mu \tau}$, respectively. Rows 1, 2 and 3 fix $\bar{s}_{23}^2 = 0.1$, $\bar{s}_{12}^2 = 0.1$ and $M^2 = 0.01 \text{ eV}^2$, respectively. Initial spectra are given by the reference ν_μ spectra, and calculations are done using the shell method. Note that all contours greater than one are percentages.

to SuperKamiokande long baseline experiment. However, KEK would need a very significant upgrade to produce extremely high fluxes. In addition, the rock surrounding SuperKamiokande would have to be used to increase its effective mass, as has been done in analysing the multi-GeV atmospheric muons, and even then event rates may not be high enough. However, its significance to particle physics makes it an exciting topic.

Theoretically, the CP symmetry can be conveniently studied in vacuum, but it becomes significantly more complex in matter which is not CP invariant. The result is a contamination of measurements which, in practice, is likely to be larger in size than the CP violation itself. Several strategies have been discussed in the literature to sort out these two competing effects, and new ones will be added here. To isolate the CP violating terms in the oscillation probability, both a leading order term and two first order (in small parameter) matter terms must be cancelled. In experimentally feasible scenarios involving oscillations at an accelerator, which would likely measure $P(\nu_\mu \rightarrow \nu_e) - P(\bar{\nu}_\mu \rightarrow \bar{\nu}_e)$, only the leading order term cancels, while the matter terms do not.

Existing work in the literature will be extended by examining long baseline neutrino oscillation experiments using realistic, detailed calculations for two likely to be built experiments. *K2K*, with an upgraded KEK accelerator beam, will produce neutrinos detected at SuperKamiokande at a distance of 250 km and the 10 kT *MINOS* detector will measure a neutrino beam produced 732 km away at FNAL. Methods to tune the energy to reduce the matter effect will be discussed. It will be shown that for reasonable values of the CKM parameters the first order calculations done in the literature are not sufficient to describe the physics analytically and second order results will be presented. In some cases, these will also break down, but exact numerical calculations can still be used to compute the size of CP violating effects. Next, in a novel suggestion for study, it will be demonstrated that it is possible to cancel both the leading order and first order matter terms by combining data from accelerator and reactor experiments. Finally, a

new result will show that CP violating effects may be present in the atmospheric neutrino measurements and the size of that effect will be estimated.

5.4.1 Characterising CP Violation in Vacuum

CP violation in the absence of matter can be characterised in neutrino oscillations by the product of two terms: a constant which depends on the angular parameters in the CKM matrix and an oscillatory term which depends on the neutrino masses. In particular,

$$\Delta^{CP} P_{\alpha\beta} = P(\nu_\alpha \rightarrow \nu_\beta) - P(\bar{\nu}_\alpha \rightarrow \bar{\nu}_\beta) = \pm 4Jf \quad (5.35)$$

for $\alpha \neq \beta$, where $J = s_{12}c_{12}s_{13}c_{13}^2s_{23}c_{23}s_\delta$ is referred to as the Järlskog factor, and the oscillatory term $f = \sin\left(\frac{\Delta m_{21}^2 L}{2E}\right) + \sin\left(\frac{\Delta m_{32}^2 L}{2E}\right) - \sin\left(\frac{\Delta m_{31}^2 L}{2E}\right) = 4\mathbf{S}_{21}\mathbf{S}_{31}\mathbf{S}_{32}$. The sign of $\Delta^{CP} P_{e\mu}$, $\Delta^{CP} P_{\mu\tau}$ and $\Delta^{CP} P_{\tau e}$ are positive in this definition, while $\Delta^{CP} P_{\mu e}$, $\Delta^{CP} P_{\tau\mu}$ and $\Delta^{CP} P_{e\tau}$ are negative.

T violation is defined with the probability difference

$$\Delta^T P_{\alpha\beta} = P(\nu_\alpha \rightarrow \nu_\beta) - P(\nu_\beta \rightarrow \nu_\alpha) = \pm 4Jf \quad (5.36)$$

where the signs are identical to above. T violation extends easily in the presence of matter to $\Delta^T P_{\alpha\beta}^m = \pm 4J^m f^m$ where J^m and f^m are direct analogues of their counterparts in vacuum. CP violation does not translate simply, because the effect of matter on the neutrino oscillation probability is different from the antineutrino oscillation probability.

5.4.2 Review of the Literature

Several authors have begun to look into CP violation using long baseline neutrino oscillation experiments in the last year. Discussions have focussed on where to look for CP violation and how to separate it from matter effects.

Arafune and Sato [152] studied the oscillatory term f when $\Delta m_{21}^2 \ll \Delta m_{31}^2$, and showed that it oscillates regularly with linearly increasing amplitude. They also found oscillatory behaviour when the two mass differences were comparable, and looked at the effect of matter on the Järlskog factor.

Arafune et. al. [143] assumed a small matter effect and a neutrino mass hierarchy in which $A, \Delta m_{21}^2 \ll \Delta m_{31}^2$. They calculated the neutrino probability difference $\Delta^{CP} P_{\mu e}$ to first order in the two small parameters and found that it consists of two matter terms with the factor $\frac{A}{\Delta m_{31}^2}$ and one CP violating term proportional to $\frac{\Delta m_{21}^2}{\Delta m_{31}^2}$. They noted that all three terms oscillated with the same frequency but exhibited different behaviour as the ratio of the baseline to neutrino energy $\frac{L}{E}$ increases: one matter term decreased as $\frac{1}{L/E}$ and the other was constant, while the CP violating term increased linearly with $\frac{L}{E}$.

They suggested that one way to single out the latter term would be to examine the energy dependence of neutrino oscillations. Another way would be to measure $\Delta P_{\mu e}$ at baselines L_1 and L_2 , with energies E_1 and E_2 respectively, such that $\frac{L_1}{E_1} = \frac{L_2}{E_2}$. They showed that the combination $L_1 \Delta P_{\mu e}(L_1, E_1) - L_2 \Delta P_{\mu e}(L_2, E_2)$ cancelled the two matter terms but left the CP violating term intact.

Minakata and Nunokawa [153],[154] also considered the standard mass hierarchy $\Delta M^2 \equiv \Delta m_{32}^2 \simeq \Delta m_{31}^2 \gg \Delta m_{21}^2 \equiv \Delta m^2$. They first assumed that $\Delta M^2 \approx 5 - 100 \text{ eV}^2$ motivated by the dark matter scenarios and $\Delta m^2 \approx 10^{-3} - 10^{-2} \text{ eV}^2$ as suggested by atmospheric neutrino results. In this case the large mass oscillations are very rapid and average out, and oscillation probabilities can be written as

$$P(\nu_\beta \rightarrow \nu_\alpha) = A_{\beta\alpha} + B_{\beta\alpha}(1 - \cos \Delta) + C_{\beta\alpha} \sin \Delta \quad (5.37)$$

where $\Delta = \frac{\Delta m_{21}^2 L}{2E}$ and the third term $C_{\beta\alpha} = 2J$ is the one which violates CP. They suggest placing a second detector at a distance $L/3$ and tuning the energy so that $\Delta = \frac{\pi}{2}$ at $L/3$ and $\frac{3\pi}{2}$ at L . This would eliminate uncertainties in the normalisation of the beam if the

energy is tuned instead. Then by subtracting oscillations at the two detectors the first two terms in equation 5.37 cancel isolating the CP violating term for measurement. They did note, however, that the additional detector would have to be installed at depths of 1.1 km and 9.3 km in the K2K and MINOS long baseline experiments, respectively. The straight path from the point of production to the last detector reaches these depths at $\frac{L}{3}$ and again at $\frac{2L}{3}$ due to the curvature of the earth.

They looked at two mixing angle combinations: small s_{13} , small s_{23} in which the ANP corresponds to $\nu_e - \nu_\mu$ mixing and large s_{13} , arbitrary s_{23} where $\nu_\tau - \nu_\mu$ oscillations solve the ANP. In the former case, they found the matter contamination in $\Delta P_{\mu e}$ was larger than the CP violating effect, but noted that the opposite is true for $\Delta P_{\mu\tau}$. In the latter case, they found that the CP violating term dominated matter and hence it can be more easily studied.

Minakata and Nunokawa also considered the case in which $\Delta M^2 \approx 10^{-3} - 10^{-2} \text{ eV}^2$ accounts for the ANP and $\Delta m^2 \approx 10^{-6} - 10^{-4} \text{ eV}^2$ explains the SNP. They found that the oscillation probability can be written as

$$P(\nu_\beta \rightarrow \nu_\alpha) = \bar{A}_{\beta\alpha}(1 - \cos \Delta) + \bar{B}_{\beta\alpha}\Delta \sin \Delta + \bar{C}_{\beta\alpha}\Delta(1 - \cos \Delta) \quad (5.38)$$

where in this case $\Delta = \frac{\Delta M^2 L}{2E}$ and $\bar{C}_{\beta\alpha} = 2J$. In order to remove the first two terms they suggest building two additional detectors at $L/3$ and $2L/3$, and again tuning the energy so that $\Delta = \frac{\pi}{2}, \pi$ and $\frac{3\pi}{2}$ at distances $L/3, 2L/3$ and L respectively. Then the linear combination $P\left(\frac{3\pi}{2}\right) + 3P\left(\frac{\pi}{2}\right) - 2P(\pi)$ would select out the third, CP violating term.

Tanimoto [155] examined CP violation under the assumption of two mass scales $\Delta M^2 \approx 1 - 5 \text{ eV}^2$ motivated by the LSND indications of neutrino oscillations and $\Delta m^2 \approx 10^{-3} - 10^{-2} \text{ eV}^2$ suggested by the ANP. He considered two mass hierarchies: *HI* has $\Delta M^2 = \Delta m_{32}^2 \simeq \Delta m_{31}^2$, $\Delta m_{21}^2 = \Delta m^2$ so $\nu_\mu - \nu_\tau$ mixing solves the ANP, and *HII* with $\Delta M^2 = \Delta m_{31}^2 \simeq \Delta m_{21}^2$, $\Delta m_{32}^2 \equiv \Delta m^2$ in which $\nu_\mu - \nu_e$ mixing solves the ANP.

In both cases he found a near cancellation in the oscillatory factor f , and the large mass scale oscillations were averaged out. He also considered two regions of CKM parameter space suggested by the ANP: in A , the ν_e has large mixing with the non-degenerate mass eigenstate while the ν_μ has small mixing with it, and in B both of these mixings are small.

The study showed that the CP violating effect in $\Delta P_{\mu\tau}$ was largest, up to about 8 % in HIB , and at most 3 % in the other three regions. In HI , he found the matter effect was always small, while in HII it could be anywhere up to 8 % depending on the value of s_{12} for reasonable test parameters.

5.4.3 Analytical Results

To date, all analyses in the literature make approximations to first order in small parameters. However, that may not always be sufficient. Minakata and Nunokawa [153] estimated one expansion parameter they used to be about 13 % when applied to the K2K baseline of 250 km. That parameter was proportional to the baseline, so they concluded their results could not be applied to the 732 km MINOS experiment. For large neutrino energies or when the larger of the two mass differences is relatively small, second order effects will be apparent.

In calculating $\Delta P_{\alpha\beta}$, the leading order term in the oscillation probability cancels, leaving two matter terms and one CP violating term. The “game” people play is to find ways of cancelling the matter terms to leave only the CP term, using either the energy spectrum or multiple detectors. However, it cannot be assumed that the two small parameters (matter and small mass scale) are necessarily equal in magnitude. Even if the first order matter term is cancelled through a multiple detector configuration or by tuning the energy, the second order mass terms may be as large as the first order mass scale ratio term. The matter effect for a 1 GeV beam traversing the earth’s crust is about

twenty times as large as the lower mass scale predicted by the solar neutrino experiments. Thus, it is necessary to do the expansion to second order.

In what follows, the mass hierarchy $M^2 \equiv \Delta m_{31}^2 \simeq \Delta m_{32}^2 \gg \Delta m_{21}^2 \equiv \Delta m^2$ is assumed. Define two small parameters representing the ratio of the matter effect to the large mass difference and the ratio of the two mass scales as follows:

$$\varepsilon_1 \equiv \frac{2\sqrt{2}G_F N_e E}{M^2} \quad (5.39)$$

$$\varepsilon_2 \equiv \frac{m^2}{M^2} \quad (5.40)$$

The neutrino masses in matter, the CKM matrix angular parameters, the Järlskog factor J and oscillation parameter f , neutrino oscillation probabilities and CP and T violating terms ΔP will be calculated in that order, simultaneously to second order in the two small parameters. The only exception is the CKM mixing parameter s_{12}^2 which will only be calculated to first order as a result of a cancellation of the leading order term in both the numerator and denominator. However, neither s_{12}^2 nor c_{12}^2 appears in the leading order of any term in the oscillation probabilities, so they can all be computed to second order.

Separate calculations were performed for the three cases $\varepsilon_1 = 0$, $\varepsilon_2 = 0$ and $\varepsilon_1 = \varepsilon_2$ to verify the ε_2^2 , ε_1^2 and $\varepsilon_1\varepsilon_2$ terms in each expression. Unitarity and symmetries in the CKM matrix provided additional consistency checks of the calculations, and first order terms were corroborated with results which have appeared in the literature this year.

CKM Parameters to First and Second Order

Zaglaer and Schwarzer's paper uses the general solution of a cubic equation to derive expressions, quoted in Chapter 3, for the masses and all mixing angles in matter in terms of the vacuum values and magnitude of the matter term [132]. Calculating the neutrino

masses to second order in the small parameters ε_1 and ε_2 yields:

$$(M_1^m)^2 = \frac{M^2}{2} [(\varepsilon_1 c_{13}^2 + \varepsilon_2)(1 - \xi) + \varepsilon_1^2 s_{13}^2 c_{13}^2 (\xi \zeta - \xi - 1) + \varepsilon_1 \varepsilon_2 s_{13}^2 \xi (\zeta - 1)] + O(\varepsilon_{1,2}^3) \quad (5.41)$$

$$(M_2^m)^2 = \frac{M^2}{2} [(\varepsilon_1 c_{13}^2 + \varepsilon_2)(1 + \xi) + \varepsilon_1^2 s_{13}^2 c_{13}^2 (\xi - \xi \zeta - 1) - \varepsilon_1 \varepsilon_2 s_{13}^2 \xi (\zeta - 1)] + O(\varepsilon_{1,2}^3) \quad (5.42)$$

$$(M_3^m)^2 = M^2 [1 + \varepsilon_1 s_{13}^2 + \varepsilon_1^2 s_{13}^2 c_{13}^2] + O(\varepsilon_{1,2}^3) \quad (5.43)$$

where the parameters ξ and ζ are defined by:

$$\xi \equiv \left[1 - \frac{4\varepsilon_1 \varepsilon_2 c_{13}^2 c_{12}^2}{(\varepsilon_1 c_{13}^2 + \varepsilon_2)^2} \right]^{1/2} \quad (5.44)$$

$$\zeta \equiv \frac{2\varepsilon_1^2 c_{13}^4 + 3\varepsilon_1 \varepsilon_2 c_{13}^2 (1 - 2c_{12}^2) + \varepsilon_2^2}{\xi^2 (\varepsilon_1 c_{13}^2 + \varepsilon_2)^2} \quad (5.45)$$

Observe that ξ is a positive definite parameter and that $M_{1,M}^2 \longleftrightarrow M_{2,M}^2$ under the transformation $\xi \longleftrightarrow -\xi$. In the limit $\varepsilon_1 \rightarrow 0$, $\xi \rightarrow 1$ and $\zeta \rightarrow 2$, while in the limit $\varepsilon_2 \rightarrow 0$, $\xi \rightarrow 1$ and $\zeta \rightarrow 1$. Also note that the expression $O(\varepsilon_{1,2}^3)$ refers to terms of the form ε_1^3 , $\varepsilon_1^2 \varepsilon_2$, $\varepsilon_1 \varepsilon_2^2$ and ε_2^3 .

Zaglauer and Schwarzer's paper also gives expressions for the CKM parameters. Using the masses above, these can be shown to be:

$$(s_{13}^m)^2 = s_{13}^2 \left\{ 1 + \varepsilon_1 c_{13}^2 [2 + 2\varepsilon_2 s_{12}^2 + 3\varepsilon_1 (c_{13}^2 - s_{13}^2)] \right\} + O(\varepsilon_{1,2}^3) \quad (5.46)$$

$$(s_{12}^m)^2 = \frac{1}{2\xi(\varepsilon_1 c_{13}^2 + \varepsilon_2)} \{ (\varepsilon_1 c_{13}^2 + \varepsilon_2)(1 + \xi) - 2\varepsilon_2 c_{12}^2 + \varepsilon_1 s_{13}^2 [\varepsilon_1 c_{13}^2 (\zeta - 2) + \varepsilon_2 (\zeta - 1)(1 - 2c_{12}^2)] \} + O(\varepsilon_{1,2}^2) \quad (5.47)$$

$$(s_{23}^m)^2 = s_{23}^2 \left[1 + 2\varepsilon_1 \varepsilon_2 \frac{s_{12} c_{12} s_{13} c_{23} c_\delta}{s_{23}} \right] + O(\varepsilon_{1,2}^3) \quad (5.48)$$

$$e^{-i\delta^m} = e^{-i\delta} \left[1 + i\varepsilon_1 \varepsilon_2 \frac{s_{12} c_{12} s_{13} (c_{23}^2 - s_{23}^2) s_\delta}{s_{23} c_{23}} \right] + O(\varepsilon_{1,2}^3) \quad (5.49)$$

Because of the $O(\varepsilon_{1,2}^3)$ term in the denominator, $(s_{12}^m)^2$ only appears to $O(\varepsilon_{1,2}^1)$.

The Järskog Factor and Oscillatory Term

The Järskog factor contains s_{12} and c_{12} among its elements, so it can only be calculated to first order in the small parameters. It is given by

$$\begin{aligned} 4J^m &= 4s_{12}^m c_{12}^m s_{13}^m s_{23}^m c_{23}^m s_{\delta}^m \\ &= 4J \frac{\varepsilon_2}{\xi(\varepsilon_1 c_{13}^2 + \varepsilon_2)} [1 + \varepsilon_1 (s_{13}^2 \zeta + 1 - 4s_{13}^2)] \end{aligned} \quad (5.50)$$

The oscillation factor in matter is equal to

$$\begin{aligned} f^m &= 4S_{21}^m S_{31}^m S_{32}^m \\ &= f \frac{\xi(\varepsilon_1 c_{13}^2 + \varepsilon_2)}{\varepsilon_2} \{1 + \varepsilon_1 [s_{13}^2 (1 - \zeta) + \Omega \cot \Omega (3s_{13}^2 - 1)]\} \end{aligned} \quad (5.51)$$

where $\Omega = \frac{M^2 L}{4E}$. Multiplying these two results gives $\Delta^T P_{\alpha\beta}$, because the effect of matter is the same on the two probabilities in the difference.

$$4J^m f^m = 4Jf [1 + \varepsilon_1 (1 - 3s_{13}^2) (1 - \Omega \cot \Omega)] \quad (5.52)$$

Probabilities to Second Order

Combining the mass differences and CKM parameters in equations 5.41 to 5.49 with the oscillation probabilities in 3.32 to 3.37 yields the neutrino oscillation probabilities to second order. It was previously noted that $P_{\beta\alpha}(\delta) = P_{\alpha\beta}(-\delta)$, and since the matter term is reversed for antineutrinos one can also write that $P_{\bar{\alpha}\bar{\beta}}^m(\delta, \varepsilon_1) = P_{\alpha\beta}^m(-\delta, -\varepsilon_1)$. These two relations, combined with the unitarity condition, allow all eighteen possible neutrino oscillation probabilities to be determined from the six shown below. Notice the additional symmetries $P_{e\mu}^m(s_{23}, c_{23}) = P_{e\tau}^m(c_{23}, -s_{23})$ and $P_{\mu\tau}^m(s_{23}, c_{23}, \delta) = P_{\mu\tau}^m(c_{23}, -s_{23}, -\delta)$ which all stem from the particular form of the CKM matrix. The oscillation probabilities are given by:

$$\begin{aligned} P_{ee}^m &= 1 - 2s_{13}^2 c_{13}^2 (1 - C_{2\Omega}) [1 + 2\varepsilon_1 (c_{13}^2 - s_{13}^2)] \\ &\quad + 4s_{13}^2 c_{13}^2 \Omega S_{2\Omega} [\varepsilon_1 (c_{13}^2 - s_{13}^2) + \varepsilon_2 s_{12}^2] \end{aligned} \quad (5.53)$$

$$\begin{aligned}
P_{\mu\mu}^m = & 1 - 2c_{13}^2 s_{23}^2 (1 - C_{2\Omega}) [1 - c_{13}^2 s_{23}^2 - 2\varepsilon_1 s_{13}^2 (1 - 2c_{13}^2 s_{23}^2)] \\
& - 4c_{13}^2 s_{23}^2 \Omega S_{2\Omega} [\varepsilon_1 s_{13}^2 (1 - 2c_{13}^2 s_{23}^2) \\
& - \varepsilon_2 (c_{12}^2 c_{23}^2 - 2s_{12} c_{12} s_{13} s_{23} c_{23} c_\delta + s_{12}^2 s_{13}^2 s_{23}^2)]
\end{aligned} \tag{5.54}$$

$$\begin{aligned}
P_{\tau\tau}^m = & 1 - 2c_{13}^2 c_{23}^2 (1 - C_{2\Omega}) [1 - c_{13}^2 c_{23}^2 - 2\varepsilon_1 s_{13}^2 (1 - 2c_{13}^2 c_{23}^2)] \\
& - 4c_{13}^2 c_{23}^2 \Omega S_{2\Omega} [\varepsilon_1 s_{13}^2 (1 - 2c_{13}^2 c_{23}^2) \\
& - \varepsilon_2 (c_{12}^2 s_{23}^2 + 2s_{12} c_{12} s_{13} s_{23} c_{23} c_\delta + s_{12}^2 s_{13}^2 c_{23}^2)]
\end{aligned} \tag{5.55}$$

$$\begin{aligned}
P_{e\mu}^m = & 2c_{13}^2 (1 - C_{2\Omega}) \{ s_{13}^2 s_{23}^2 [1 + 2\varepsilon_1 (c_{13}^2 - s_{13}^2)] + 2\varepsilon_2 \Omega s_{12} c_{12} s_{13} s_{23} c_{23} s_\delta \\
& + \varepsilon_1 s_{13}^2 s_{23}^2 [\varepsilon_1 (4c_{13}^2 - 1) (1 - 4s_{13}^2) + 2\varepsilon_2 s_{12}^2 (c_{13}^2 - s_{13}^2)] \\
& - 2\Omega^2 s_{13}^2 s_{23}^2 [\varepsilon_1^2 (c_{13}^2 - s_{13}^2)^2 + 2\varepsilon_1 \varepsilon_2 s_{12}^2 (c_{13}^2 - s_{13}^2) + \varepsilon_2^2 s_{12}^2] \\
& + 2\varepsilon_2 s_{12} c_{12} s_{13} s_{23} c_{23} [\varepsilon_1 s_{13}^2 c_\delta + \varepsilon_1 \Omega (s_\delta - c_\delta \Omega) (1 - 3s_{13}^2) - \varepsilon_2 \Omega^2 c_\delta] \} \\
& + 4c_{13}^2 \Omega S_{2\Omega} \{ - s_{13}^2 s_{23}^2 [\varepsilon_1 (c_{13}^2 - s_{13}^2) + \varepsilon_2 s_{12}^2] + \varepsilon_2 s_{12} c_{12} s_{13} s_{23} c_{23} c_\delta \\
& - 2\varepsilon_1 s_{13}^2 s_{23}^2 (c_{13}^2 - s_{13}^2) [\varepsilon_1 (c_{13}^2 - s_{13}^2) + \varepsilon_2 s_{12}^2] + 2\varepsilon_1^2 s_{13}^4 c_{13}^2 s_{23}^2 \\
& + \varepsilon_2 s_{12} c_{12} s_{13} s_{23} c_{23} [\varepsilon_1 (c_\delta - s_\delta \Omega) (1 - 3s_{13}^2) - \varepsilon_2 s_\delta \Omega] \} \\
& 4\Omega^2 c_{13}^2 \{ s_{13}^2 s_{23}^2 [\varepsilon_1 (c_{13}^2 - s_{13}^2) + \varepsilon_2 s_{12}^2]^2 + \varepsilon_2^2 s_{12}^2 c_{12}^2 c_{23}^2 \\
& - 2\varepsilon_2 s_{12} c_{12} s_{13} s_{23} c_{23} c_\delta [\varepsilon_1 (c_{13}^2 - s_{13}^2) + \varepsilon_2 s_{12}^2] \}
\end{aligned} \tag{5.56}$$

$$\begin{aligned}
P_{e\tau}^m = & 2c_{13}^2 (1 - C_{2\Omega}) \{ s_{13}^2 c_{23}^2 [1 + 2\varepsilon_1 (c_{13}^2 - s_{13}^2)] - 2\varepsilon_2 \Omega s_{12} c_{12} s_{13} s_{23} c_{23} s_\delta \\
& + \varepsilon_1 s_{13}^2 c_{23}^2 [\varepsilon_1 (4c_{13}^2 - 1) (1 - 4s_{13}^2) + 2\varepsilon_2 s_{12}^2 (c_{13}^2 - s_{13}^2)] \\
& - 2\Omega^2 s_{13}^2 c_{23}^2 [\varepsilon_1^2 (c_{13}^2 - s_{13}^2)^2 + 2\varepsilon_1 \varepsilon_2 s_{12}^2 (c_{13}^2 - s_{13}^2) + \varepsilon_2^2 s_{12}^2] \\
& - 2\varepsilon_2 s_{12} c_{12} s_{13} s_{23} c_{23} [\varepsilon_1 s_{13}^2 c_\delta + \varepsilon_1 \Omega (s_\delta - c_\delta \Omega) (1 - 3s_{13}^2) - \varepsilon_2 \Omega^2 c_\delta] \} \\
& + 4c_{13}^2 \Omega S_{2\Omega} \{ - s_{13}^2 c_{23}^2 [\varepsilon_1 (c_{13}^2 - s_{13}^2) + \varepsilon_2 s_{12}^2] - \varepsilon_2 s_{12} c_{12} s_{13} s_{23} c_{23} c_\delta \\
& + 2\varepsilon_1 s_{13}^2 c_{23}^2 (c_{13}^2 - s_{13}^2) [\varepsilon_1 (c_{13}^2 - s_{13}^2) + \varepsilon_2 s_{12}^2] + 2\varepsilon_1^2 s_{13}^4 c_{13}^2 c_{23}^2 \\
& - \varepsilon_2 s_{12} c_{12} s_{13} s_{23} c_{23} [\varepsilon_1 (c_\delta - s_\delta \Omega) (1 - 3s_{13}^2) - \varepsilon_2 s_\delta \Omega] \} \\
& 4\Omega^2 c_{13}^2 \{ s_{13}^2 c_{23}^2 [\varepsilon_1 (c_{13}^2 - s_{13}^2) + \varepsilon_2 s_{12}^2]^2 + \varepsilon_2^2 s_{12}^2 s_{23}^2 \\
& + 2\varepsilon_2 s_{12} c_{12} s_{13} s_{23} c_{23} c_\delta [\varepsilon_1 (c_{13}^2 - s_{13}^2) + \varepsilon_2 s_{12}^2] \}
\end{aligned} \tag{5.57}$$

$$\begin{aligned}
P_{\mu\tau}^m = & 2c_{13}^2 (1 - C_{2\Omega}) \{ c_{13}^2 s_{23}^2 c_{23}^2 (1 - 4\varepsilon_1 s_{13}^2) + 2\varepsilon_2 \Omega s_{12} c_{12} s_{13} s_{23} c_{23} s_\delta \\
& - 2\varepsilon_1 c_{13}^2 s_{23}^2 c_{23}^2 [\varepsilon_1 s_{13}^2 (3c_{13}^2 - 5s_{13}^2) + 2\varepsilon_2 s_{12}^2 s_{13}^2] \\
& - 2\Omega^2 s_{23}^2 c_{23}^2 [\varepsilon_1^2 s_{13}^2 c_{13}^2 (4s_{13}^2 - 1) + 2\varepsilon_1 \varepsilon_2 s_{13}^2 (2s_{12}^2 s_{13}^2 - 1) \\
& + \varepsilon_2^2 (c_{12}^2 - s_{12}^2 s_{13}^2)] - 2\varepsilon_2 s_{12} c_{12} s_{13} s_{23} c_{23} [\varepsilon_1 c_{13}^2 c_\delta (s_{23}^2 - c_{23}^2) \\
& - \varepsilon_1 \Omega s_\delta (1 - 3s_{13}^2) - \Omega^2 c_\delta (s_{23}^2 - c_{23}^2) (\varepsilon_1 (1 - 3s_{13}^2) + \varepsilon_2)] \} \\
& + 4c_{13}^2 \Omega S_{2\Omega} \{ s_{23}^2 c_{23}^2 [2\varepsilon_1 s_{13}^2 c_{13}^2 + \varepsilon_2 (s_{12}^2 s_{13}^2 - c_{12}^2)] \\
& - \varepsilon_2 s_{12} c_{12} s_{13} s_{23} c_{23} c_\delta (s_{23}^2 - c_{23}^2) \\
& + \varepsilon_1 s_{13}^2 s_{23}^2 c_{23}^2 [\varepsilon_1 c_{13}^2 (3 - 10s_{13}^2) + 2\varepsilon_2 (1 - 2s_{12}^2 s_{13}^2)] \\
& + \varepsilon_2 s_{12} c_{12} s_{13} s_{23} c_{23} [\varepsilon_1 (c_\delta (s_{23}^2 - c_{23}^2) - s_\delta \Omega) (1 - 3s_{13}^2) - \varepsilon_2 s_\delta \Omega] \} \\
& + 4\Omega^2 c_{13}^2 \{ 4\varepsilon_1^2 s_{13}^4 c_{13}^4 s_{23}^2 c_{23}^2 - 4\varepsilon_1 \varepsilon_2 s_{13}^2 c_{13}^2 s_{23}^2 c_{23}^2 (c_{12}^2 - s_{12}^2 s_{13}^2) \\
& + \varepsilon_2^2 [s_{12}^2 c_{12}^2 s_{13}^2 + s_{23}^2 c_{23}^2 (1 - s_{12}^2 c_{13}^2 (1 + s_{13}^2))] \\
& - s_{12}^2 c_{12}^2 s_{23}^2 c_{23}^2 (1 + s_{13}^2)^2 - 4\varepsilon_2^2 s_{12}^2 c_{12}^2 s_{13}^2 s_{23}^2 c_{23}^2 c_\delta^2 \\
& + 2\varepsilon_2 s_{12} c_{12} s_{13} c_{13}^2 s_{23} c_{23} c_\delta (s_{23}^2 - c_{23}^2) (\varepsilon_1 s_{13}^2 - \varepsilon_2 c_{12}^2) \}
\end{aligned} \tag{5.58}$$

The leading and first order terms in the expressions above are in the first and fifth line of $P_{e\mu}^m$ and $P_{e\tau}^m$, and in the first, sixth and seventh line of $P_{\mu\tau}^m$.

Probability Differences to Second Order

As noted at the beginning of this section, calculation of the difference between two probabilities, the $\Delta^{CP} P_{\alpha\beta}$ and $\Delta^T P_{\alpha\beta}$, cancels the leading order term. Because the definition of Δ^T includes only neutrinos (or antineutrinos, as opposed to Δ^{CP} which includes both), the effect of matter on the two components is the same and it is much easier to calculate. In fact, $\Delta^T P_{\alpha\beta} = \pm 4J^m f^m$ where J^m and f^m were calculated above.

Thus,

$$\begin{aligned}\Delta^T P_{e\mu} &= P(\nu_e \rightarrow \nu_\mu) - P(\nu_\mu \rightarrow \nu_e) \\ &= 8\varepsilon_2 s_{12} c_{12} s_{13} c_{13}^2 s_{23} c_{23} s_\delta \Omega (1 - \mathbf{C}_{2\Omega}) \times \\ &\quad [1 + \varepsilon_1 (1 - 3s_{13}^2) (1 - \Omega \cot \Omega) - \varepsilon_2 \Omega \cot \Omega]\end{aligned}\quad (5.59)$$

Two other T violating probability differences are identical, $\Delta^T P_{\mu\tau} = \Delta^T P_{\tau e} = \Delta^T P_{e\mu}$, while $\Delta^T P_{\alpha\beta} = -\Delta^T P_{\beta\alpha}$ and for antineutrinos, $\Delta^T P_{\bar{\alpha}\bar{\beta}}(\delta, \varepsilon_1) = \Delta^T P_{\alpha\beta}(-\delta, -\varepsilon_1)$.

The situation is much more complex for the CP violating probability differences $\Delta^{CP} P_{\alpha\beta}$. While the matter term increases the mass of the ν_e and enhances its mixing, it decreases the mass of the $\bar{\nu}_e$ and reduces its mixing. It is possible to compute the expressions, and $\Delta^{CP} P_{\mu e}$ and $\Delta^{CP} P_{\tau\mu}$ are given below. $\Delta^{CP} P_{e\tau}$ can be inferred from $\Delta^{CP} P_{\mu e}$ with the substitutions $s_{23} \rightarrow c_{23}$, $c_{23} \rightarrow -s_{23}$. Note that the first order terms in the expressions below appear in the first two lines.

$$\begin{aligned}\Delta^{CP} P_{\mu e} &= 8\varepsilon_1 s_{13}^2 c_{13}^2 s_{23}^2 (c_{13}^2 - s_{13}^2) (1 - \mathbf{C}_{2\Omega} - \Omega \mathbf{S}_{2\Omega}) \\ &\quad - 8\varepsilon_2 s_{12} c_{12} s_{13} c_{13}^2 s_{23} c_{23} s_\delta \Omega (1 - \mathbf{C}_{2\Omega}) \\ &\quad + 16\varepsilon_1 \varepsilon_2 s_{13}^2 c_{13}^2 \Omega^2 [s_{12}^2 s_{23}^2 (c_{13}^2 - s_{13}^2) + s_{12} c_{12} s_{13} s_{23} c_{23} c_\delta] \\ &\quad + 8\varepsilon_1 \varepsilon_2 c_{13}^2 (1 - \mathbf{C}_{2\Omega}) [s_{12}^2 s_{13}^2 s_{23}^2 (c_{13}^2 - s_{13}^2) (1 - 2\Omega^2) \\ &\quad + s_{12} c_{12} s_{13} s_{23} c_{23} c_\delta (s_{13}^2 - \Omega^2 (1 - 3s_{13}^2))] \\ &\quad + 8\varepsilon_2 c_{13}^2 \Omega \mathbf{S}_{2\Omega} \{ -2\varepsilon_1 s_{12}^2 s_{13}^2 s_{23}^2 (c_{13}^2 - s_{13}^2) \\ &\quad + s_{12} c_{12} s_{13} s_{23} c_{23} [\varepsilon_1 c_\delta (1 - 3s_{13}^2) + \varepsilon_2 s_\delta \Omega] \}\end{aligned}\quad (5.60)$$

$$\begin{aligned}
\Delta^{CP} P_{\tau\mu} = & 16\varepsilon_1 s_{13}^2 c_{13}^4 s_{23}^2 c_{23}^2 (1 - C_{2\Omega} - \Omega S_{2\Omega}) \\
& - 8\varepsilon_2 s_{12} c_{12} s_{13} c_{13}^2 s_{23} c_{23} s_\delta \Omega (1 - C_{2\Omega}) \\
& + 32\varepsilon_1 \varepsilon_2 s_{13}^2 c_{13}^2 \Omega^2 [s_{23}^2 c_{23}^2 (c_{12}^2 - s_{12}^2 s_{13}^2) - 2s_{12} c_{12} s_{13} s_{23} c_{23} c_\delta (s_{23}^2 - c_{23}^2)] \\
& + 8\varepsilon_1 \varepsilon_2 c_{13}^2 (1 - C_{2\Omega}) \{ 2s_{13}^2 s_{23}^2 c_{23}^2 [s_{12}^2 c_{13}^2 + \Omega^2 (2s_{12}^2 s_{13}^2 - 1)] \\
& + s_{12} c_{12} s_{13} s_{23} c_{23} c_\delta (s_{23}^2 - c_{23}^2) (c_{13}^2 - \Omega^2 (1 - 3s_{13}^2)) \} \\
& + 8\varepsilon_2 c_{13}^2 \Omega S_{2\Omega} \{ 2\varepsilon_1 s_{13}^2 (2s_{12}^2 s_{13}^2 - 1) \\
& - s_{12} c_{12} s_{13} s_{23} c_{23} [\varepsilon_1 c_\delta (s_{23}^2 - c_{23}^2) (1 - 3s_{13}^2) - \varepsilon_2 s_\delta \Omega] \}
\end{aligned} \tag{5.61}$$

5.4.4 Strategies to Isolate the CP Violation Parameters

A recent comprehensive study by Fogli et. al. [130] combined all available upward-going muon data from Kamiokande, Baksan, MACRO, IMB and SuperKamiokande with all of the atmospheric data in both the sub-GeV and multi-GeV energy ranges. They plotted allowed regions in the $\tan^2 \psi - \tan^2 \varphi$ plane ($\tan^2 \theta_{23} - \tan^2 \theta_{13}$ in the notation here) for values of Δm_{31}^2 ranging from $3.2 \times 10^{-4} \text{ eV}^2$ to $1.8 \times 10^{-1} \text{ eV}^2$ assuming that Δm_{21}^2 is so small that the oscillation length it induces is greater than the diameter of the earth. They found viable solutions in most of this mass range, noting that the results are still sensitive to the experimental inputs so additional data will be needed to accurately pin down the CKM parameters.

Using the centre column figure six from their paper, five different possible sets of CKM parameters were chosen for the study which will follow. The parameter sets all come from within the 90% confidence levels, but without fine tuning them to optimise CP violation. They are labelled F[a] to F[e] and are shown in table 5.1 along with values of Ω they would produce for three experimental configurations to be studied.

The analytical results so far have found that with a hierarchical mass structure, CP violation in the lepton sector is proportional to the ratio of the squared mass differences

Label	$\Delta M^2 [eV^2]$	s_{13}^2	s_{23}^2	$2\Omega_{250}$	$2\Omega_{732}$	$2\Omega_{1500}$
F[a]	10^{-1}	0.86	0.95	35.3	20.7	212
F[b]	1.8×10^{-2}	0.80	0.96	6.35	3.71	38.1
F[c]	1.8×10^{-2}	0.13	0.90	6.35	3.71	38.1
F[d]	3.2×10^{-3}	0.33	0.83	1.13	0.66	6.77
F[e]	5.6×10^{-4}	0.91	0.67	0.20	0.12	1.18

Table 5.1: Table defining five different CKM parameter sets within the 90 % confidence regions in figure 6 of [130]. Labels in the first column will be used to identify the parameter sets.

$\varepsilon_2 = \frac{\Delta m^2}{\Delta M^2}$. Thus, one expects that schemes F[d] and F[e] in the table will produce the largest CP violating effect.

Most work in the literature has been concerned with differentiating bona fidé CP violation from matter effects which come about in trying to measure $\Delta^{CP} P_{\mu e}$, using energy spectra or tuning the energy at neutrino beams and placing additional detectors at fractions of the distance between the source and detector. For very long baselines, this latter suggestion requires new excavations several kilometres deep into the earth's crust—it is unlikely that two mines of the correct depth already exist at locations exactly one third and two thirds the distance along the line between any potential accelerator and detector pair!

In what follows, detailed calculations of the CP violating effect will be done. Although the analytical work presented in the preceding sections was to second order and helps understand the effects, the numerical work which follows is exact. If conditions are such that the second order approximation breaks down, the computer calculations will still be valid. Neither second order effects nor equivalent numerical computations have appeared in the literature.

Long Baseline Experiments

Several challenges must be overcome to measure CP violation. The signal, which is found by subtracting one oscillation channel from another, must not only be sufficiently large that it can be measured but also dominated by the CP violating terms. Accelerators typically produce beams of ν_μ (and $\bar{\nu}_\mu$) and oscillation signals comparing the rate of appearance of ν_e to $\bar{\nu}_e$ (or ν_τ to $\bar{\nu}_\tau$) at a downstream detector relative to the initial fluxes would be required. If CP violation represents an effect of size ϵ , then on the order of $\frac{1}{\epsilon^2}$ events would be needed to see it.

The next generation of long baseline experiments, K2K and MINOS, combine much higher flux beams with substantially larger detectors than have been available in the past. They will have very high neutrino production rates and long baselines, allowing significant statistical inferences while probing to very low masses. However, as will be shown, CP violation will very likely elude MINOS which has a baseline of 732 km and a 10 kT detector. K2K, at 250 km and with a 50 kT detector, could come much closer so seeing a CP violating effect but will still probably fall short of being able to measure it unless the KEK beam receives a very substantial upgrade and the experiment is able to increase the effective size of the detector by measuring muons produced in the rock surrounding the detector.

Matter presents a second challenge. A 1 GeV neutrino beam traversing the outer crust of the earth with electron density $N_e = 1.34 \text{ mol/cm}^3$ has $\epsilon_1 \approx \frac{2 \times 10^{-4} eV^2}{\Delta M^2}$ according to equation 5.4. This is substantially larger than $\epsilon_2 \approx \frac{10^{-5} eV^2}{\Delta M^2}$ implied by the solar neutrino results. The obvious way to reduce the matter term is to lower the beam energy, but because the neutrinos are come from decaying muons and $m_\mu = 105 \text{ MeV}$, there is a limit to how far this can be done without the beam spreading out. Moreover, the detection cross section scales with energy, so reducing the matter effect in this manner also reduces

the signal. It is also important to note that as E increases and ε_1 gets large, it is the mathematical expansion in small parameters which breaks down, but not necessarily the ability of experiments to measure CP violation.

When the small parameter approximation is valid, the first order terms in equations 5.60 and 5.61 consist of a matter term proportional to ε_1 ($1 - C_{2\Omega} - \Omega S_{2\Omega}$ is often treated as two separate terms $1 - C_{2\Omega}$ and $\Omega S_{2\Omega}$ which have different spectral behaviour), and a CP violating proportional to ε_2 on the second line. In the small Ω -regime, the leading order Ω -dependence in Taylor expansion the matter term is $O(\Omega^2)$, but so is the CP violating term. Going to smaller energy (thus larger $\Omega = \frac{1.27\Delta M^2 L}{E}$) increases the CP term as $1/E^2$, but only increases the matter term as $1/E^1$ because $\varepsilon_1 \propto E$.

Figure 5.9 shows $\Delta P_{\mu e}^{CP}$, expressed as percentages, with $s_\delta = 0.0, 0.5$ and 1.0 for three different sets of conditions. The first two columns, F[d] and F[e] have the CKM parameters given in table 5.1 using the standard reference neutrino spectrum and a baseline of 250 km. The last column, F[ee], has the F[e] CKM parameters, but the energy spectrum is shifted uniformly downward by a factor of two. The last row in the figure shows the difference $100 \times (\Delta P_{\mu e}^{CP}|_{s_\delta=1} - \Delta P_{\mu e}^{CP}|_{s_\delta=0})$ which is a measure of the maximum CP violating effect.

For F[d], the oscillation probability difference is small, on the order of 0.25 %. It came from subtracting two oscillation probabilities of 15 %. Note that $\Delta P_{\mu e}^{CP}|_{s_\delta=0}$ in the upper left plot is dependent on s_{12}^2 , unlike the first order term in equation 5.60, at a level of several percent. This shows that the first order approximation has already begun to break down when $E = 1.8 \text{ GeV}$ and $\Delta m_{31}^2 = 3.2 \times 10^{-3} \text{ eV}^2$. At this point, $\varepsilon_1 \approx 0.11$, $\varepsilon_2 \approx 0.013$ and there are no ε_1^2 terms. However, by computing the magnitudes of the second order $\varepsilon_1 \varepsilon_2$ terms in the equation it becomes apparent that they do contribute several percent to $\Delta P_{\mu e}^{CP}$.

In the middle column the CP violating effect is several times larger because Δm_{31}^2 is

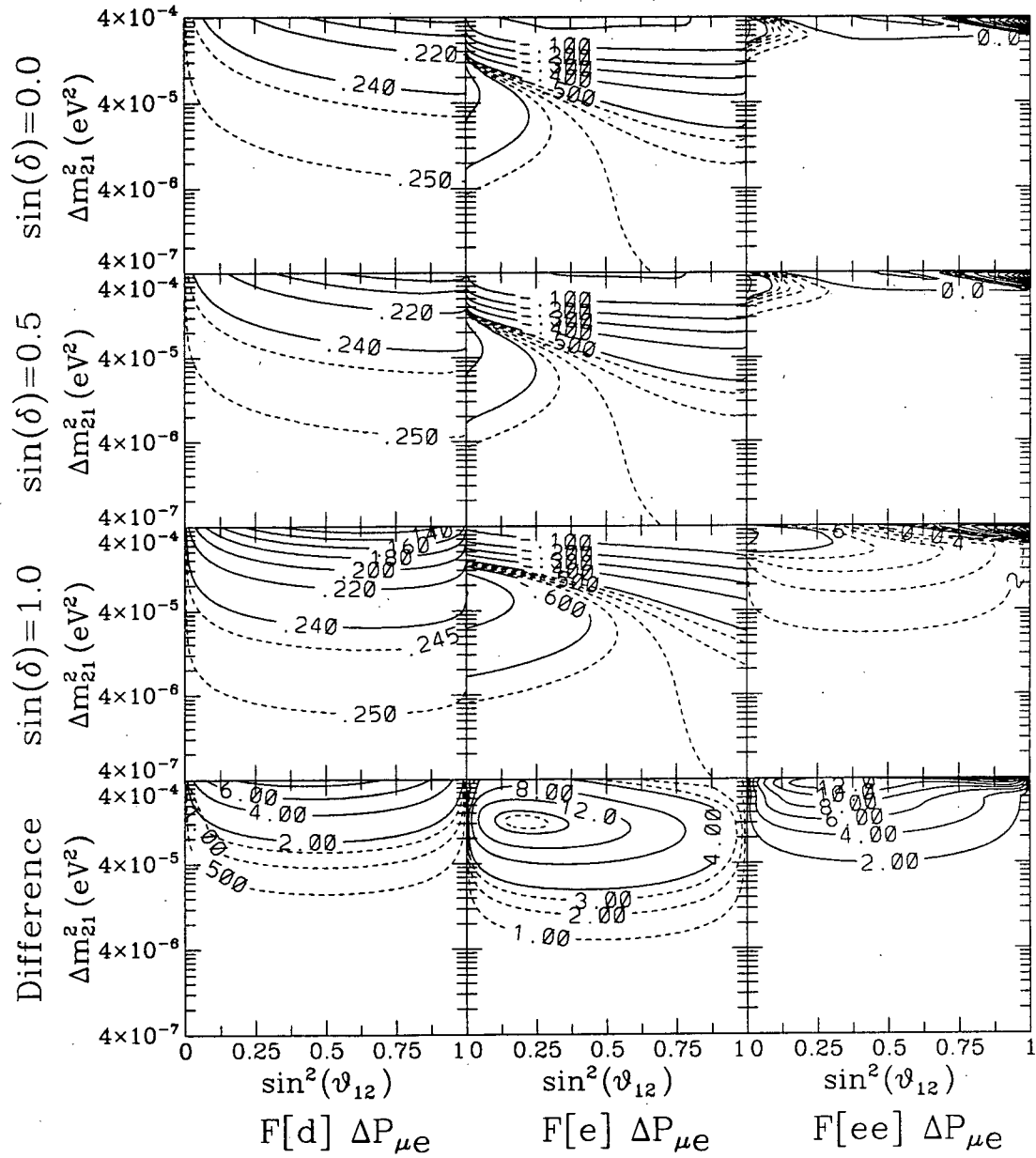


Figure 5.9: Study of CP violation at an experiment with a baseline of 250 km using the reference neutrino spectrum. Contours of constant $\Delta_{\mu e}^{CP} P$ are shown for $s_\delta = 0.0, 0.5$ and 1.0 , expressed as percentages. The bottom row of figures shows the difference between the $s_\delta = 0.0$ and $s_\delta = 1.0$ plots in the column, scaled by a factor of 100. The left and centre columns use the CKM parameter sets $F[d]$ and $F[e]$ and reference spectrum, while the right column uses $F[e]$ with the neutrino energy spectrum scaled down by a factor of two.

smaller and $\varepsilon_2 \propto \frac{1}{\Delta m_{31}^2}$. However the matter parameter $\varepsilon_1 \approx 0.357$ at $E = 1$ GeV, so not only are several of the $\varepsilon_1 \varepsilon_2$ terms in equation 5.60 as large as the ε_2 term, even the third order terms could be expected to contribute to $\Delta P_{\mu e}^{CP}$. At $\Delta m_{21}^2 \approx 10^{-5} \text{ eV}^2$ as suggested by solar neutrino experiments, CP violation of 0.02 % would have to be pulled out of an oscillation difference in the range $\Delta P_{\mu e}^{CP} \approx 0.5 \%$, a 4 % effect.

The situation gets much better in the third column, where the F[e] CKM parameters are used again but the energy spectrum is reduced by a factor of two. Although the magnitude of the CP effect is reduced, the first order matter term declines much farther and $\Delta P_{\mu e}^{CP}$ is almost completely dominated by it. Thus, any measured difference between $P_{\mu e}$ and $P_{\bar{\mu} \bar{e}}$ would be a signal of CP violation. The oscillation probabilities themselves are quite small, about 1.2 %.

Concentrating on a limited range of neutrino energies, either by focussing the beam energy or analysing only data from neutrinos in certain energy bins will also improve the clarity of the CP signal, albeit at the cost of reducing the total number of events. Figure 5.10 shows contours of $\Delta P_{\mu e}^{CP}$ for F[e] in which the region of the asymmetric neutrino spectrum considered is successively decreased. Going from the first to second column, the CP violating signal drops (ie. the "Difference" row) probably partly because cutting out the high energy end of the spectrum decreases the average value of ε_1 . Moving from the second to third column where a still smaller energy region is used, the CP violating signal does not drop significantly but the probability difference does become dominated by it, again making an unambiguous signature for CP.

The MINOS experiment, which has a longer baseline and significantly higher neutrino energies, opens up the possibility of ν_τ appearance in addition to ν_e . Although the CP terms at first order are the same for $\Delta P_{\mu e}^{CP}$ and $\Delta P_{\mu \tau}^{CP}$, the 250 km results above showed that it is necessary to go to second order with both CKM parameter sets F[d] and F[e]. While $\Omega \propto \frac{L}{E}$ decreases for MINOS when compared to K2K, the matter effect grows in

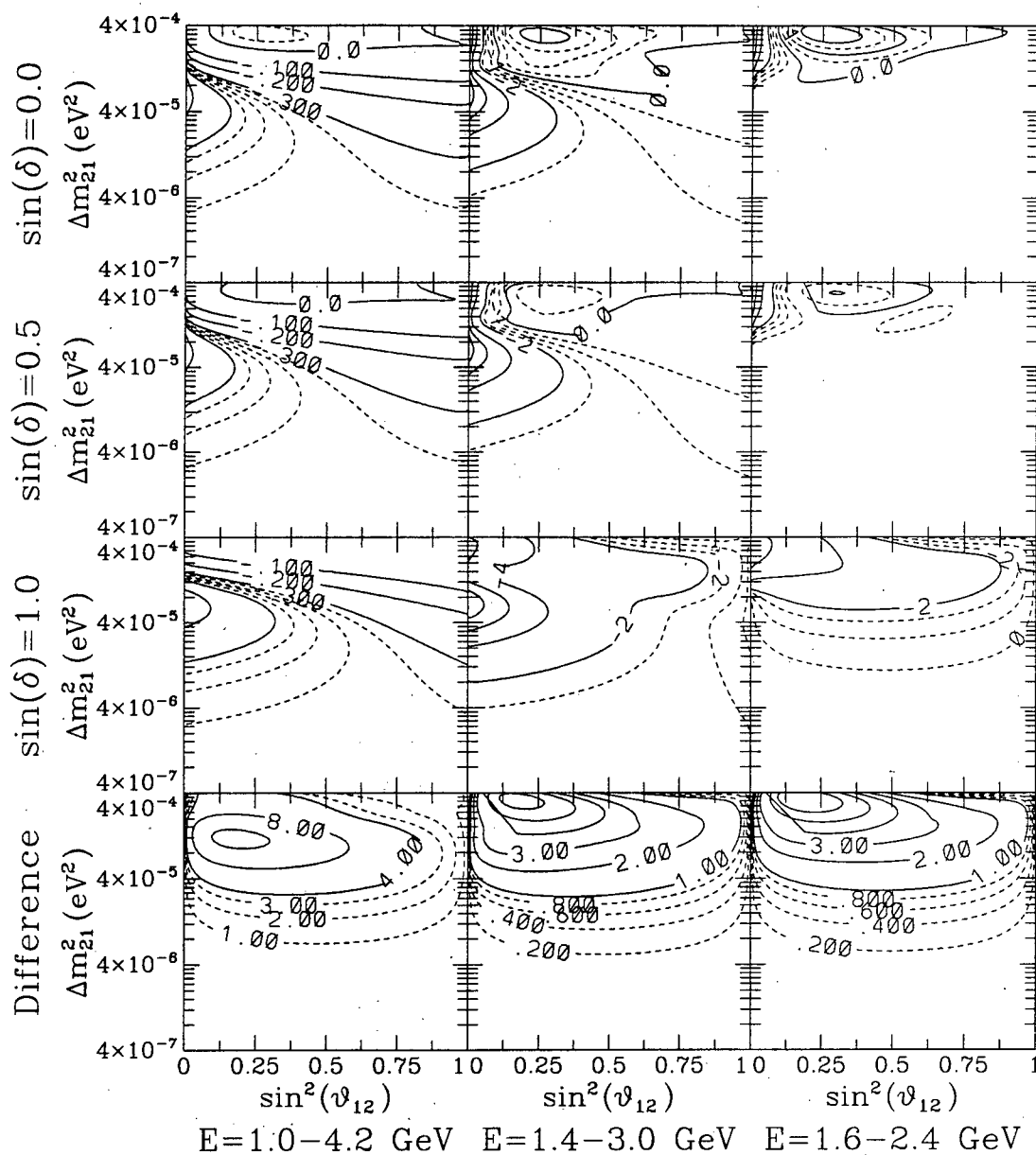


Figure 5.10: Study of CP violation by varying the region of the neutrino reference spectrum used, with a baseline of 250 km. Contours of constant $\Delta_{\mu e}^{CP} P$ are shown for $s_\delta = 0.0$, 0.5 and 1.0, expressed as percentages. The bottom row of figures shows the difference between the $s_\delta = 0.0$ and $s_\delta = 1.0$ plots in the column, scaled by a factor of 100. Moving from left to right, the neutrino energy spectrum is successively compressed.

proportion to energy. However, that larger matter effect will enhance some of the second order CP violating terms in the oscillation probability differences.

Figure 5.11 illustrates what would be seen at MINOS using the reference spectrum scaled upwards by a factor of five and a baseline of 732 km. It shows $\Delta P_{\mu\tau}^{CP}$ using F[d], and both $\Delta P_{\mu\tau}^{CP}$ and $\Delta P_{\mu e}^{CP}$ with the F[e] parameter set. The size of the CP term in $\Delta P_{\mu\tau}^{CP}$ is somewhat larger than in $\Delta P_{\mu e}^{CP}$ for F[d] and the oscillation probability difference is smaller, so it would provide an easier signal to detect. Both $P_{\mu\tau}$ and $P_{\tau\mu}$ are about 27 %.

As expected, the CKM parameter set F[e] produces a larger CP violating term because it has a smaller Δm_{31}^2 . Although $\Delta P_{\mu\tau}^{CP}$ is larger in magnitude than $\Delta P_{\mu e}^{CP}$, it induces a larger violation of CP and the relative contribution of that violation to the oscillation probability difference is about the same—less than $\frac{1}{4}$ %. This ratio is notably less than F[d] in the first column where $\Delta P_{\mu\tau}^{CP}$ was much smaller. However, with only about 20,000 charged current events per year, MINOS will not be able to measure an effect as small as CP violation.

Next, consider an experiment with the standard reference spectrum and a detector 1500 km away. The longer baseline probes to lower values in the mass differences and increases the parameter Ω , which in turn raises the magnitude of the first order CP violating term. Figure 5.12 shows $\Delta P_{\mu e}^{CP}$ for three different cases beginning with the CKM parameters F[d]. The CP term is very small, and much smaller than the oscillation probability differences.

However by tuning the neutrino energy, in this case scaling the reference spectrum downwards by a factor of 0.75, the spectrum peaks at 1.35 GeV. Then at the peak energy, $\Omega \approx 2.33$, and $1 - C_{2\Omega} - \Omega S_{2\Omega} = 0$. The result is that $\Delta P_{\mu e}^{CP}$ drops by about 40 %, while the contribution of CP the violating term is increased by about 50 %. While the effect is not dramatic in this case, it would improve if a smaller region of the spectrum was used

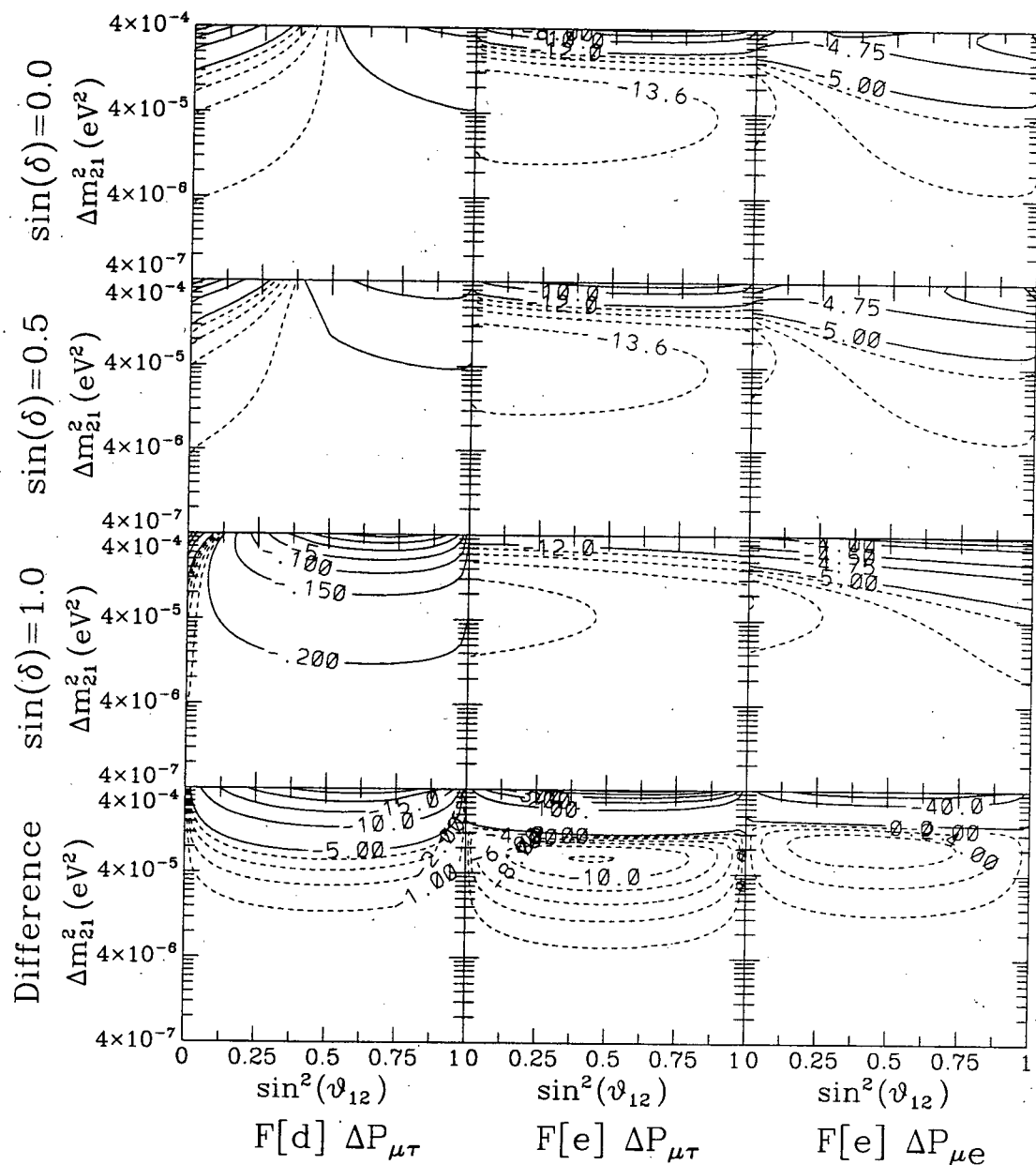


Figure 5.11: Study of CP violation at an experiment with a baseline of 732 km using the reference neutrino spectrum modified by scaling the energy upwards by a factor of 5. Contours of constant $\Delta_{\mu e}^{CP}P$ and $\Delta_{\mu\tau}^{CP}P$ for CKM parameter sets F[d] and F[e] are shown for $s_\delta = 0.0, 0.5$ and 1.0 , expressed as percentages. The bottom row of figures shows the difference between the $s_\delta = 0.0$ and $s_\delta = 1.0$ plots in the column, scaled by a factor of 100.

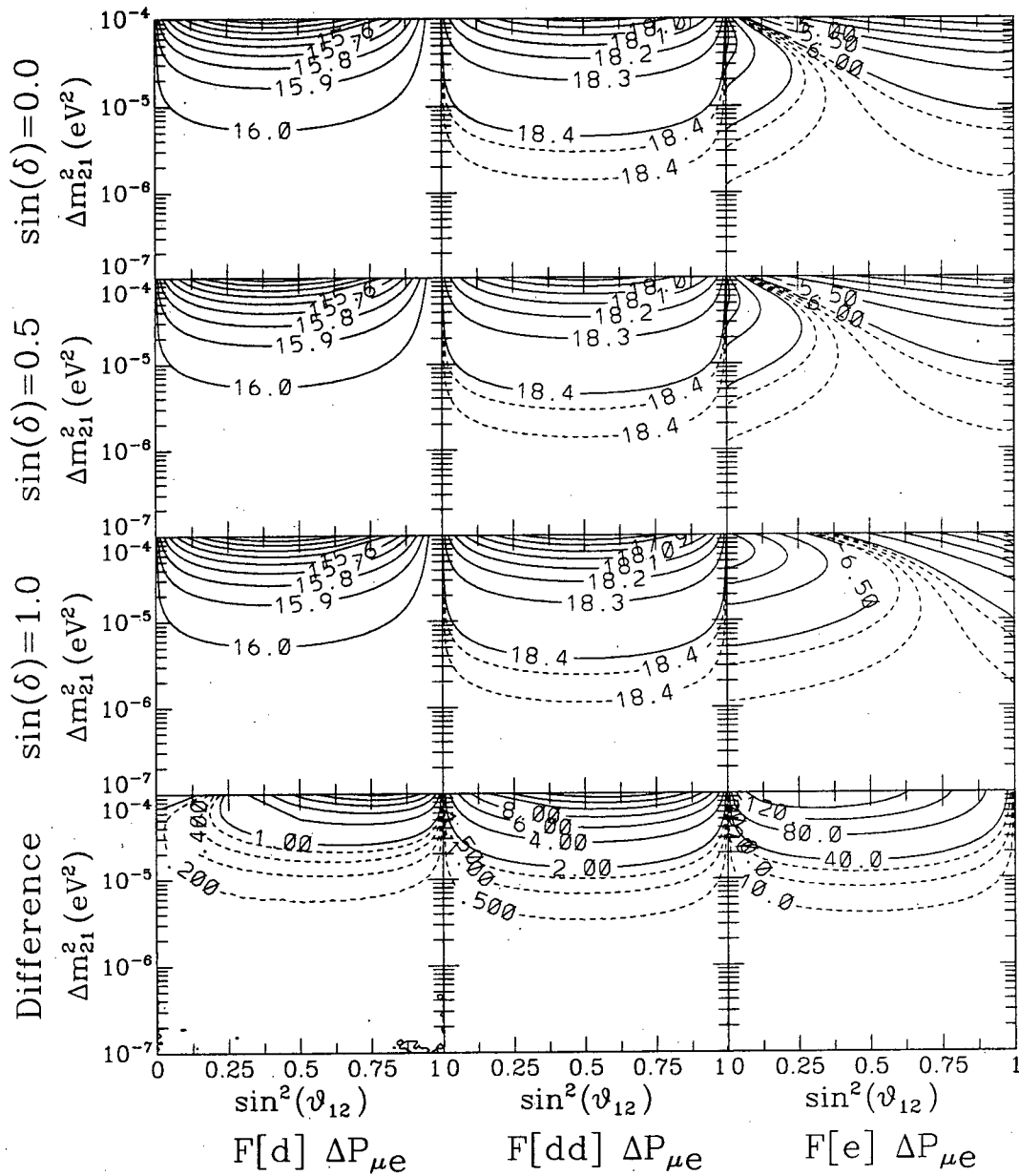


Figure 5.12: Study of CP violation at an experiment with a baseline of 1500 km using the reference neutrino spectrum. Contours of constant $\Delta_{\mu e}^{CP} P$ are shown for $s_\delta = 0.0$, 0.5 and 1.0, expressed as percentages. The bottom row of figures shows the difference between the $s_\delta = 0.0$ and $s_\delta = 1.0$ plots in the column, scaled by a factor of 100. Column 1 uses the CKM parameter set F[d] and the reference neutrino spectrum, while column 2 scales the energy down by a factor of 0.75. In column 3, the CKM parameters defined by F[e] are combined with the reference spectrum.

to increase the region over which the matter term was cancelled.

The third column shows contours of the oscillation probability difference for the CKM parameter set F[e]. Because the baseline is longer, this experiment can probe to lower mass differences. The oscillation probabilities in this case are 12 %, CP violation contributes an absolute magnitude of about 0.2 % which is about ten times as large as was found using a 250 km baseline. However, the number of events falls as the square of the baseline, so the advantage gained in a larger effect is more than lost to reduced statistics.

Finally, figure 5.13 shows the oscillation probability difference spectrum using F[e] for each of the three baselines discussed. In each plot, the upper curve shows $\Delta P_{\mu\alpha}^{CP}$ with $s_\delta = 1$ while the lower curve uses $s_\delta = 0$. Note that ε_1 reaches the value 1 when the neutrino energy is 2.8 GeV, at which point matter begins to dominate the probability.

It is clear that the best signal would be obtained in the low energy region of the 250 km experiment. Here, matter does not play a large part and Ω is relatively small. By going out to 1500 km, Ω becomes large and the oscillatory terms in $\Delta P_{\mu e}^{CP}$ wash out the CP violating signal. Thus, bigger is not necessarily better.

5.4.5 Combining Reactor and Long Baseline Experiments

The last section highlighted the importance of separating matter effects from CP violating effects using long baseline experiments. The reason that most authors calculate the difference $\Delta P_{\mu e}^{CP} = P_{\mu e} - P_{\bar{\mu} e}$ is to cancel the leading order term in the oscillation probabilities. The ε_1^2 terms also cancel because $P_{\bar{\mu} e}(\varepsilon_1, \delta) = P_{\mu e}(-\varepsilon_1, -\delta)$, which is a fortunate side-effect given that ε_1 is probably larger than ε_2 .

A new approach emerges if the two terms are added together instead of subtracted from one another. In that case, both the first order matter terms as well as the first order CP violating terms proportional to s_δ cancel. This leaves the leading order, CP even (in δ) and second order terms. But that leading order term is identical to the one

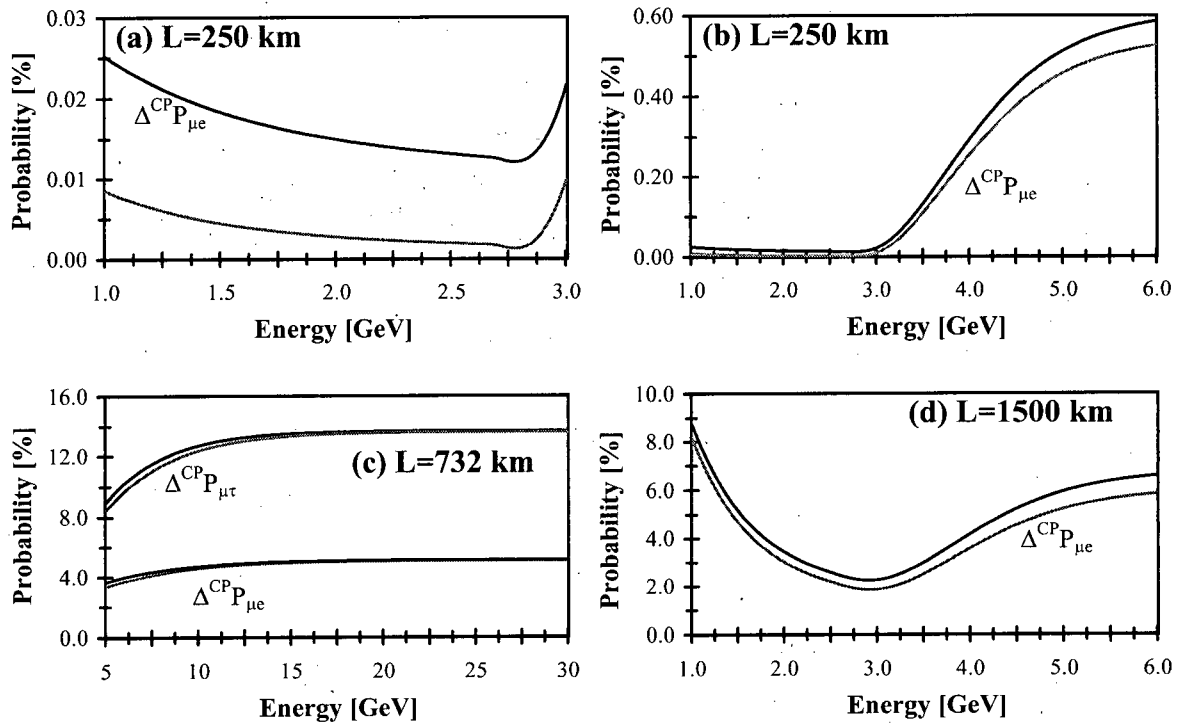


Figure 5.13: Oscillation probability differences $\Delta^{CP}P_{\mu e}$ and $\Delta^{CP}P_{\mu\tau}$ as a function of neutrino energy for baselines of 250, 732 and 1500 km, using the CKM parameter set F[e]. Black curves compare probabilities with $s_\delta = 1.0$ to grey curves with $s_\delta = 0.0$.

in $P_{\bar{\nu}_\mu}$ at a nuclear reactors (even if that's not what is measured). Although they have much lower energy, they have much shorter baselines and typically have similar values of $\frac{L}{E}$. Moreover, the MeV energies of reactor neutrinos reduce the matter effect by three orders of magnitude compared to accelerators, so the matter term can be ignored.

But because reactors measure the disappearance of $\bar{\nu}_e$'s, it is $P_{\bar{\nu}_\mu} + P_{\bar{\nu}_\tau} = 1 - P_{\bar{\nu}_e}$ which will have to be used to cancel the leading order term. This necessitates multiplying the reactor probability by a factor of s_{23}^2 in the expression below. Thus, one can define:

$$\begin{aligned}
\Delta^{A-R}P_{\mu e} &\equiv P_{\mu e}^A + P_{\bar{\mu} \bar{e}}^A - 2s_{23}^2 \left[P_{\bar{\nu}_\mu}^R + P_{\bar{\nu}_\tau}^R \right]_{\varepsilon_1=0} \\
&= 8\varepsilon_2\Omega\mathbf{S}_{2\Omega}s_{12}c_{12}s_{13}c_{13}^2s_{23}c_{23}c_\delta \\
&\quad + 4\varepsilon_1^2s_{13}^2c_{13}^2s_{23}^2\{2\Omega^2(c_{13}^2 - s_{13}^2) + 4\Omega\mathbf{S}_{2\Omega}[s_{13}^2c_{13}^2 - (c_{13}^2 - s_{13}^2)^2] \\
&\quad + (1 - \mathbf{C}_{2\Omega})[(4c_{13}^2 - 1)(1 - 4s_{13}^2) - 2\Omega^2(c_{13}^2 - s_{13}^2)]\} \\
&\quad + 8\varepsilon_2^2\Omega^2c_{13}^2\{s_{12}^2c_{12}^2(c_{23}^2 - s_{23}^2) - 2s_{12}^3c_{12}s_{13}s_{23}c_{23}c_\delta \\
&\quad + (1 - \mathbf{C}_{2\Omega})s_{12}c_{12}s_{13}^3s_{23}^3c_{23}c_\delta\} \\
&\quad + 8\varepsilon_1\varepsilon_2\Omega s_{12}c_{12}s_{13}c_{13}^2s_{23}c_{23}s_\delta(1 - 3s_{13}^2)[s_{13}^2s_{23}^2(1 - \mathbf{C}_{2\Omega}) - \Omega\mathbf{S}_{2\Omega}]
\end{aligned} \tag{5.62}$$

where the superscripts A and R refer to accelerator and reactor, respectively. It is assumed that the probabilities are measured at the same $\frac{L}{E}$.

This type of subtraction, while analytically easy, would be experimentally difficult. It would have to be done over a limited range of energies because the accelerator beam is unlikely to exactly match the shape of the reactor spectrum. The accelerator energy would also have to be tuned so that the ratio $\frac{L}{E}$ is the same for both experiments. Moreover, some systematic errors cancel out in the pure accelerator experiment because the baseline is identical for the ν_μ and $\bar{\nu}_\mu$ and this would not be the case here. Finally, reactors measure the disappearance of $\bar{\nu}_e$ signal, so it is statistically more difficult to measure a small oscillation probability than in an accelerator appearance experiment.

However if these challenges can be overcome, then the three different experimental

measurements (ie. $P_{\mu e}^A$, $P_{\bar{\mu} \bar{e}}^A$ and $P_{\bar{e} \bar{\mu}}^R + P_{\bar{e} \bar{\tau}}^R$) allow the cancellation of both the leading order and $O(\varepsilon_1^1)$ terms. In addition, if s_δ happens to be small, then the first order CP violating effect in the pure accelerator experiment will be negligible. Equation 5.62 measures c_δ in the $O(\varepsilon_1^1)$ term, and this would be close to unity if s_δ is small.

Figure 5.14 plots contours of constant $\Delta^{A-R}P_{\mu e}$ as a function of Δm_{21}^2 and s_{12}^2 and the maximum CP violation, similar to the last section except now c_δ varies in successive rows. The accelerator is assumed to have a 250 km baseline while the reactor neutrinos are detected 500 m from where they are produced. The neutrinos are limited to a small region of their total spectrum for comparison in the plots, although one would expect that in any real experiment the data would all be kept binned by energy.

In the first column, neutrinos in the 2.8 – 3.0 GeV range at the accelerator are combined with 5.6 – 6.0 MeV reactor neutrinos with the CKM parameter set F[c], which has a large $\Delta m_{31}^2 = 1.8 \times 10^{-2} \text{ eV}^2$. Here, both ε_1 and ε_2 are small and the second order terms contribute very little. As a result, $\Delta^{A-R}P_{\mu e}$ is dominated by the first order CP violating term.

The centre column plots the oscillation probability difference using the scheme F[d] with 0.7 – 0.9 GeV and 1.4 – 1.6 MeV neutrinos. As might be expected the magnitude of the CP violation is larger because Δm_{31}^2 is lower. The signal is not as clean because matter terms have $\Delta^{A-R}P_{\mu e}$ has increased, making it more difficult to unambiguously assign a measurable change in it to CP. However, CP violation is about 0.1 % for $\Delta m_{21}^2 = 10^{-5} \text{ eV}^2$.

Finally the last column shows the F[e] CKM parameter set with neutrino energies of 4.8 – 5.0 GeV and 9.6 – 10.0 MeV. The second order matter terms are much more apparent, while the CP violating effect has not increased in the lower regions of the Difference plot. It is, however, still in the range 0.1 %.

Because the magnitude of CP violation for these combined experiments has increased

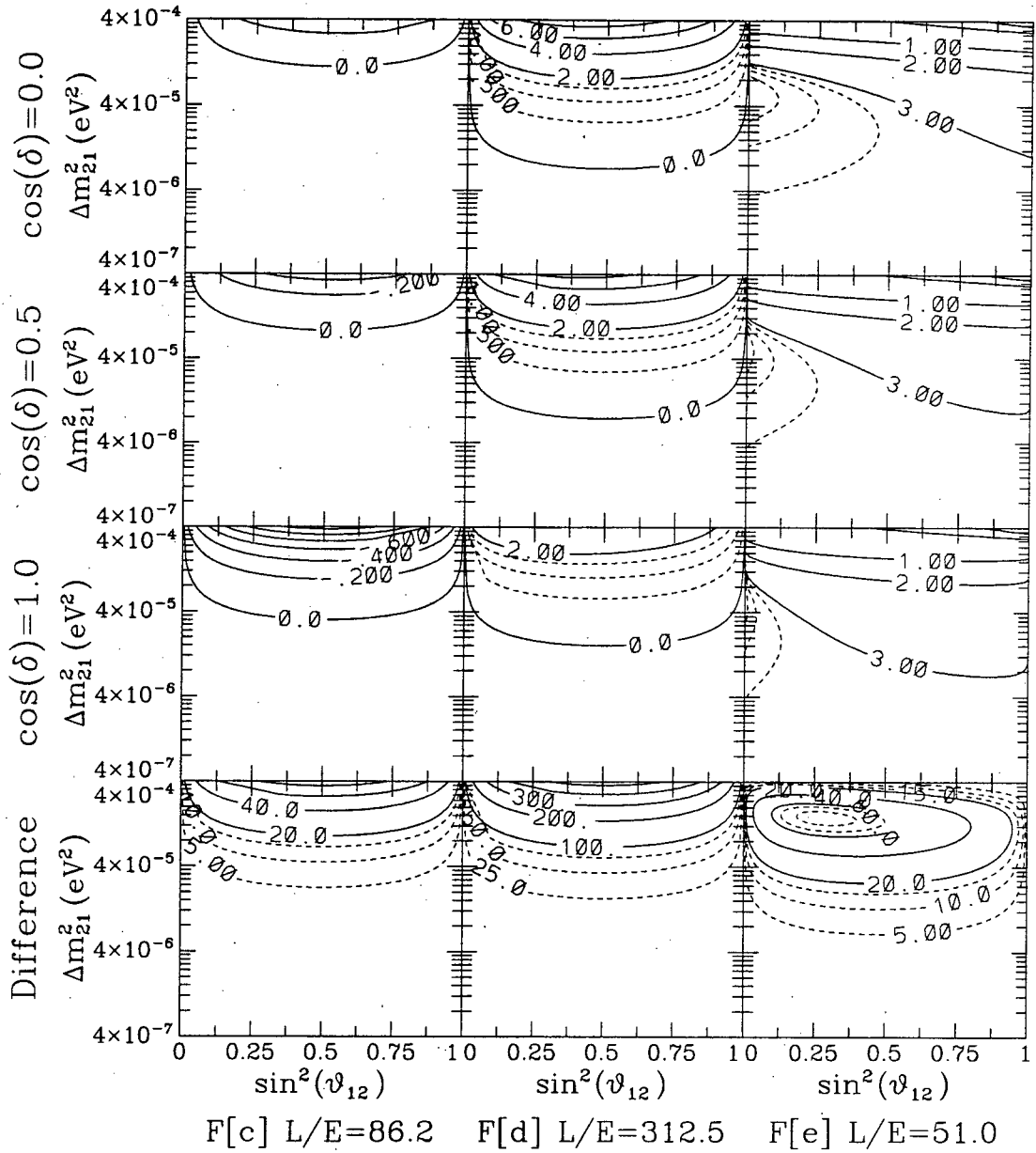


Figure 5.14: Study of CP violation by combining long baseline accelerator and reactor experiments with constant L/E . Contours of constant $\Delta_{\mu e}^{A-RP}$ are shown for $c_\delta = 0.0$, 0.5 and 1.0 , expressed as percentages. The bottom row of figures shows the difference between the $c_\delta = 0.0$ and $c_\delta = 1.0$ plots in the column, scaled by a factor of 100. Each column uses a different CKM parameter set and ratio L/E as labelled.

compared to the purely accelerator case, fewer events would be needed to measure a CP signal. Approximately 10^6 events would be required. However, scaling the baselines at the Chooz and Palo Verde reactor experiments to 500 m would produce one the order of 100 events per day, or about 30,000 per year. Thus, the detectors would have to be scaled up by about an order of magnitude to approach the event rates required to contribute to a measurement of CP violation.

Using reactors to subtract off the leading order terms can also be applied to the dimensions of the MINOS experiment, but with less success. With the higher neutrino energies, ε_1 is relatively larger than ε_2 . Matter effects do not dominate $\Delta^{A-R}P_{\mu e}$ at MINOS in CKM parameter sets F[b] and F[c] but they are large enough to prevent a clean CP violating signal from being seen. F[d] has larger Δm_{31}^2 and the ε_1^2 terms in equation 5.62 are beginning to approach the size of the ε_2^1 terms, so that matter effects again compete with CP violation. In F[e], ε_1 is close to unity so cancelling the first order matter term offers no significant advantage and the approximation breaks down. However the numerical results indicate that CP still does not contribute enough of a signal to be measured.

5.4.6 CP Violation and Atmospheric Neutrinos

At particle accelerators, experimentalists decide whether to produce a beam of neutrinos or a beam of antineutrinos by focussing a beam of either positively or negatively charged mesons. They first produce neutrinos and measure $P_{\mu e}$, then antineutrinos to measure $P_{\bar{\mu} \bar{e}}$. If the two oscillation probabilities differ, it must either be due to a CP violating effect or the presence of matter (which is not CP invariant). In this case, the choice to study either matter or antimatter is explicitly made by the experimenter at the neutrino source.

The situation with atmospheric neutrinos is quite different. There, the “source” consists of four different neutrinos: identical ν_μ and $\bar{\nu}_\mu$ fluxes, combined with ν_e and $\bar{\nu}_e$ fluxes of equal magnitude, but which differ from the ν_μ . However, because the detection processes are dominated by matter they see the four neutrino types differently. In particular, the cross section for detecting a ν_e is different from that of a $\bar{\nu}_e$, and the rate of production of μ^- from ν_μ impinging on nucleons is different from the rate of μ^+ produced by $\bar{\nu}_\mu$.

So, whereas accelerator based experiments can measure CP violation by alternately producing neutrino and antineutrino beams at the source and looking for differences in the oscillation rates, atmospheric neutrino experiments can allow the natural detection processes differentiate the two identical fluxes. It turns out, as will be explicitly calculated, that the experiments need not be able to differentiate μ^- events from μ^+ . CP violation modifies the ratio of e-type to μ -type events.

First, define the four neutrino fluxes and ratio Λ as follows:

$$\Phi_\mu \equiv \Phi_{\nu_\mu} = \Phi_{\bar{\nu}_\mu} \quad (5.63)$$

$$\Phi_e \equiv \Phi_{\nu_e} = \Phi_{\bar{\nu}_e} = \Lambda \Phi_\mu \quad (5.64)$$

Next, make the following definitions about the detection cross sections of the neutrinos and the ratios between them:

$$\sigma_{\nu_\mu} \equiv \sigma \quad (5.65)$$

$$\sigma_{\nu_\mu} \equiv \lambda_\mu \sigma_{\nu_\mu} = \lambda_\mu \sigma \quad (5.66)$$

$$\sigma_{\nu_e} \equiv r \sigma_{\nu_\mu} = r \sigma \quad (5.67)$$

$$\sigma_{\nu_e} \equiv \lambda_e \sigma_{\nu_e} = r \lambda_e \sigma \quad (5.68)$$

Using these definitions, the number of μ -type and e-type atmospheric neutrino events measured by detectors would be given by:

$$\begin{aligned} N_{\nu_e} &= \Phi_{\nu_e} P_{ee} \sigma_{\nu_e} + \Phi_{\bar{\nu}_e} P_{\bar{e}\bar{e}} \sigma_{\bar{\nu}_e} + \Phi_{\nu_\mu} P_{\mu e} \sigma_{\nu_e} + \Phi_{\bar{\nu}_\mu} P_{\bar{\mu}\bar{e}} \sigma_{\bar{\nu}_e} \\ &= \Phi_\mu \sigma r [\Lambda P_{ee} + \Lambda \lambda_e P_{\bar{e}\bar{e}} + P_{\mu e} + \lambda_e P_{\bar{\mu}\bar{e}}] \end{aligned} \quad (5.69)$$

$$\begin{aligned} N_{\nu_\mu} &= \Phi_{\nu_\mu} P_{\mu\mu} \sigma_{\nu_\mu} + \Phi_{\bar{\nu}_\mu} P_{\bar{\mu}\bar{\mu}} \sigma_{\bar{\nu}_\mu} + \Phi_{\nu_e} P_{e\mu} \sigma_{\nu_\mu} + \Phi_{\bar{\nu}_e} P_{\bar{e}\bar{\mu}} \sigma_{\bar{\nu}_\mu} \\ &= \Phi_\mu \sigma [P_{\mu\mu} + \lambda_\mu P_{\bar{\mu}\bar{\mu}} + \Lambda P_{e\mu} + \Lambda \lambda_\mu P_{\bar{e}\bar{\mu}}] \end{aligned} \quad (5.70)$$

Taking the ratio of these two, $\Phi_\mu \sigma$ cancels leaving

$$\frac{N_{\nu_e}}{N_{\nu_\mu}} = (R_{e/\mu})_{data} = \frac{r [\Lambda P_{ee} + \Lambda \lambda_e P_{\bar{e}\bar{e}} + P_{\mu e} + \lambda_e P_{\bar{\mu}\bar{e}}]}{P_{\mu\mu} + \lambda_\mu P_{\bar{\mu}\bar{\mu}} + \Lambda P_{e\mu} + \Lambda \lambda_\mu P_{\bar{e}\bar{\mu}}} \quad (5.71)$$

By substituting for the oscillation probabilities, the ratio can be evaluated. However, even at first order, it is quite complicated and not terribly enlightening for purposes of this discussion. The general form of the ratio is

$$\begin{aligned} (R_{e/\mu})_{data} &= \frac{r(1+\lambda_e)}{(1+\lambda_\mu)} \frac{\Lambda + 2s_{13}^2 c_{13}^2 (s_{12}^2 - \Lambda)(1 - C_{2\Omega})}{1 + 2c_{13}^2 s_{23}^2 (\Lambda s_{13}^2 + c_{13}^2 s_{23}^2 - 1)(1 - C_{2\Omega})} \times \\ &\quad \left\{ 1 + \frac{4c_{13}^2}{[\Lambda + 2s_{13}^2 c_{13}^2 (s_{12}^2 - \Lambda)(1 - C_{2\Omega})][1 + 2c_{13}^2 s_{23}^2 (\Lambda s_{13}^2 + c_{13}^2 s_{23}^2 - 1)(1 - C_{2\Omega})]} \times \right. \\ &\quad [\varepsilon_1 s_{13}^2 (1 - C_{2\Omega} - \Omega S_{2\Omega}) (2c_{13}^2 W_1 (1 - C_{2\Omega}) + X_1) \\ &\quad - \varepsilon_2 s_{12} c_{12} s_{13} s_{23} c_{23} s_\delta \Omega (1 - C_{2\Omega}) (2c_{13}^2 W_2 (1 - C_{2\Omega}) + X_2) \\ &\quad \left. + \varepsilon_2 \Omega S_{2\Omega} (2c_{13}^2 (1 - C_{2\Omega}) (Y_2 + Y_2^\delta c_\delta) + (Z_2 + Z_2^\delta c_\delta)) \right\} \end{aligned} \quad (5.72)$$

where the coefficients W_1 , X_1 , W_2 , X_2 , Y_2 , Y_2^δ , Z_2 and Z_2^δ are functions of Λ , λ_e , λ_μ and the three CKM mixing angles θ_{12} , θ_{13} and θ_{23} . Dependence on the CP violating phase is shown explicitly.

The factor given on the first line of equation 5.72 is the ratio that would be measured by atmospheric neutrino detectors in the absence of matter when the small mass difference is degenerate. The magnitude of the matter and CP effects on the ratio when $\Delta m_{21}^2 \neq 0$

can be estimated by comparing the relative sizes of the respective terms in the square brackets to the "1" in the second line of the equation.

To estimate the likely size of the CP effect, chose $\Omega = \pi$, so that $S_{2\Omega}$ vanishes and $1 - C_{2\Omega} = 2$. The difference contributed by CP term under this condition, compared to unity, is given by

$$\frac{8\pi\epsilon_2 s_{12} c_{12} s_{13} c_{13}^2 s_{23} c_{23} s_\delta (4c_{13}^2 W_2 + X_2)}{[\Lambda + 4s_{13}^2 c_{13}^2 (s_{23}^2 - \Lambda)] [1 + 4c_{13}^2 s_{23}^2 (\Lambda s_{13}^2 + c_{13}^2 s_{23}^2 - 1)]} \quad (5.73)$$

where the functions W_2 and X_2 are given by:

$$W_2 = \frac{1 - \lambda_e}{1 + \lambda_e} s_{23}^2 (\Lambda s_{13}^2 + c_{13}^2 s_{23}^2 - 1) + \frac{1 - \lambda_\mu}{1 + \lambda_\mu} \Lambda s_{13}^2 (s_{23}^2 - \Lambda) \quad (5.74)$$

$$X_2 = \frac{1 - \lambda_e}{1 + \lambda_e} + \Lambda^2 \frac{1 - \lambda_\mu}{1 + \lambda_\mu} \quad (5.75)$$

The ratio of the cross section for production of both e^+ to e^- and μ^+ to μ^- as a function of energy were calculated in Gaisser and O'Connell [156]. At low energies, both λ_e and λ_μ are about $\frac{1}{3}$, while at higher energies they both increase to about $\frac{1}{2}$. The table will use the low energy value for both parameters. The ratio of e-type to μ -type neutrinos in the atmospheric flux is known to be $\Lambda = \frac{1}{1.8}$. Combining these values with the different CKM parameter sets used throughout this section gives an expectation of the CP violating effect on the atmospheric neutrinos. Table 5.2 shows its magnitude in the column labelled "*Estimate 1*" where $s_\delta = 1$ and $s_{12}^2 = 0.5$ have also been assumed.

A second measure of the effect, labelled "*Estimate 2*" in the table, would be to set $\Omega = 2.33$, so that the matter term vanishes completely. Then $1 - C_{2\Omega} = \Omega S_{2\Omega} = 1.69$, and the fractional contribution of CP violation to the ratio is given by

$$\frac{4(1.69)c_{13}^2}{[\Lambda + 2s_{13}^2 c_{13}^2 (s_{12}^2 - \Lambda)(1.69)] [1 + 2c_{13}^2 s_{23}^2 (\Lambda s_{13}^2 + c_{13}^2 s_{23}^2 - 1)(1.69)]} \times \\ [-s_{12} c_{12} s_{13} s_{23} c_{23} s_\delta (2.33) (2c_{13}^2 W_2 (1.69) + X_2) \\ + (2c_{13}^2 (1.69) (Y_2 + Y_2^\delta c_\delta) + (Z_2 + Z_2^\delta c_\delta))] \quad (5.76)$$

Label	Estimate 1	Estimate 2 $\sin(\delta)$	Estimate 2 $\cos(\delta)$	ε_2
F[a]	0.363	0.544	0.803	10^{-4}
F[b]	0.440	0.554	0.857	5.56×10^{-4}
F[c]	1.43	0.998	1.28	5.56×10^{-4}
F[d]	2.34	1.76	2.30	3.13×10^{-3}
F[e]	0.585	1.07	1.05	1.79×10^{-2}

Table 5.2: Estimates of the fractional contribution of the CP violating for three different schemes discussed in the text. The last column shows ε_2 assuming $\Delta m_{21}^2 = 10^{-5} \text{ GeV}^2$. This factor multiplies those in the middle three rows to determine the contribution of CP to the atmospheric neutrino ratio.

where the additional functions in the last line are given by

$$Y_2 = s_{13}^2 (\Lambda - s_{23}^2) (-s_{12}^2 + c_{13}^2 s_{23}^2 + s_{12}^2 s_{13}^2 s_{23}^4) \quad (5.77)$$

$$Y_2^\delta = s_{12} c_{12} s_{13} s_{23} c_{23} \left[-s_{23}^2 c_{23}^2 + s_{13}^2 (\Lambda - s_{23}^2)^2 \right] \quad (5.78)$$

$$Z_2 = s_{12}^2 s_{13}^2 (\Lambda - s_{23}^2) (1 + \Lambda s_{23}^2) - \Lambda c_{12}^2 c_{13}^2 s_{23}^2 \quad (5.79)$$

$$Z_2^\delta = s_{12} c_{12} s_{13} s_{23} c_{23} \left[1 - \Lambda (\Lambda - 2s_{23}^2) \right] \quad (5.80)$$

In the table, two contributions to Estimate 2 are shown. The first, labelled “ $\sin(\delta)$ ” is given by the second line of equation 5.76 with $s_\delta = 1$ and $s_{12}^2 = 0.5$. The other is given by the sum of the contributions of Y_2^δ and Z_2^δ with $c_\delta = 1$ and $s_{12}^2 = 0.5$ and is labelled “ $\cos(\delta)$.”

The table shows that CP could modify the atmospheric neutrino results by as much as fraction of $2\varepsilon_2$, which could be on the order of several percent depending on how small ε_2 is. This provides a novel, new approach to the measurement of CP violation in the lepton sector. Based on accelerator presented earlier, and given that the atmospheric neutrino flux has GeV energies, matter effects would be expected to dominate in the higher energy regions particularly with long path lengths through the earth’s higher density core. The effect would also be difficult to see by detectors with poor energy resolution. However,

with new detectors able to bin the data by azimuthal angle and with sufficient energy resolution, a CP violating signal might be seen in the atmospheric neutrino signal.

5.4.7 Discussion

The CKM parameter sets chosen in this study were based on one particular paper by Fogli, Lisi and Marrone [130], who also noted that their fits are still quite sensitive to changes in the experimental data. As a result, they may yet shift around. The particular choices $F[a]$ to $F[e]$ were somewhat arbitrary, and were not tuned to maximise the CP violating effect but rather to give a wide range of mass differences from the most plausible regions of parameter space in the central figure in that paper.

In practice, the rates for CP violation may increase when better measurements of the other CKM parameters are made, but probably by factors of three or four rather than an order of magnitude. For example, if s_{13}^2 in $F[e]$ was reduced from 0.91 to 0.25, then the CP violating term proportional to $s_{13}c_{13}^2$ would increase by almost 4.5. However, the matter term in $\Delta^{CP}P_{\mu e}$ would increase too, and it is likely that the oscillation probability would as well, so there would be a much smaller total advantage. This study should provide a reasonable estimate on CP violation unless the value of the CKM parameters happen to be "just right."

While the idea of building several detectors (besides the one near the source to calibrate the neutrino beam) at oscillation nodes is theoretically attractive, it is probably prohibitively expensive given that they would need to be placed deep underground. The main tool open to the experimenter is to tune the beam energy and try to adjust the relative sizes of the matter and CP violating terms to best investigate the latter. In addition, high flux experiments can bin observations by energy, and the CP violating term has a different energy dependence than the two matter terms.

K2K shows better potential to isolate CP violation than MINOS for two reasons.

First, the lower energy at K2K makes it easier to separate CP violating terms from matter terms. For reasonable sets of parameters, it may be possible to tune the energy so that the oscillation probability difference is dominated by CP. Second, the longer baseline and smaller detector at MINOS reduce the rate to a level far below that required to quantitatively measure CP violation.

That said, K2K is unlikely to achieve the event rates required to measure CP violation either, unless several factors work in their favour. First, the upgraded flux at KEK would have to be larger than the intense beam used to generate the reference spectrum. Nishikawa et. al. suggested that for a modest cost, KEK could attain about 6×10^{12} protons on target per second, only about 1% of the number delivered to produce the reference spectrum. Thus KEK would need a major upgrade. In addition, the beam would have to be better focussed to reduce the rate at which it spreads out and thus increasing the number of neutrinos which impact the detector. The effective size of the SuperKamiokande could also be increased if the muons produced in the rock surrounding it were also measured. This is already done successfully with the atmospheric neutrinos. Finally, nature would probably have to cooperate too. The magnitude of CP violating effects discussed here could be increased if the CKM parameters were chosen more optimally.

Reactors can be used in a limited way to help quantify CP. Although they measure a CP invariant quantity, it is within a constant factor of the largest term in the oscillation probability. Because the energy is very low, matter corrections are negligible so they measure that leading order term in the oscillation probability very cleanly. As a result, it may be possible to use reactors to subtract off the leading order term from an accelerator data set which has the same $\frac{L}{E}$. However, the systematics of combining the experiments and the disappearance nature of reactor measurements will be challenging to overcome.

Looking beyond standard laboratory experiments, the atmospheric neutrinos should

not be ignored as a potential source to study CP violation. Because the detection process is not CP invariant, the cross sections for neutrinos are different from antineutrinos. Even with identical fluxes of μ -type and (separately) e -type neutrinos, CP violating interactions will change the ratio of the measured events $(R_{e/\mu})_{data}$. With SuperKamiokande binning its data by both azimuthal angle and energy, a statistically challenging but tractable analysis may be able to make a quantitative statement about the magnitude of the CKM phase parameter s_δ .

5.5 Three Neutrino Solar Results

Studies of neutrino oscillation solutions to the solar neutrino problem in the literature generally reduce the system to a three parameter fit: they keep only the small mass difference Δm_{21}^2 and two mixing angles θ_{12} and θ_{13} . The reason for that is partly practical and partly based on experimental evidence. It is much easier, both analytically and conceptually, to study the problem with three parameters instead of four or five. However, the atmospheric neutrino results suggest that Δm_{31}^2 is above the threshold to participate in resonant neutrino oscillations (the MSW effect) in the sun making the reduction at least somewhat justifiable.

Several authors have used this approximation. Harley, Kuo and Pantaleone calculated the neutrino survival probability at the solar surface as a function of Δm_{21}^2 and the CKM matrix elements $|V_{e2}|^2$ and $|V_{e3}|^2$ which are only functions of θ_{12} and θ_{13} [150]. They also fixed $|V_{e3}|^2$ and considered that probability when Δm_{31}^2 is allowed to drop below 10^{-4} eV^2 . Fogli, Lisi and Montanino [144] and more recently Liu and Petcov [157] have employed the approximation

$$P_{3\nu}(\nu_e \rightarrow \nu_e) = s_{13}^4 + c_{13}^4 P_{2\nu}(\nu_e \rightarrow \nu_e) \quad (5.81)$$

where $P_{2\nu}(\nu_e \rightarrow \nu_e)$ is the standard two neutrino survival probability. This is valid when

Δm_{31}^2 is large and s_{23}^2 vanishes.

However, it will be illustrated that these approximations may not be valid for reasonable models of nature, in which there are a total of six independent oscillation parameters. One of these, namely the complex phase δ , will not be studied here. The neutrino is assumed to propagate adiabatically out of the sun, except at resonance(s) where it might jump from one mass eigenstate to another. The jump probability does not depend on δ , and its affect on vacuum oscillation is likely to be weak. Since the experiments measure only $P(\nu_e \rightarrow \nu_e)$ or $P(\nu_e \rightarrow \nu_e, \nu_\mu, \nu_\tau)$ but not $P(\nu_e \rightarrow \nu_\mu)$ or $P(\nu_e \rightarrow \nu_\tau)$ this parameter can be safely dropped.

Whether Δm_{31}^2 is significant to the solar neutrinos depends strongly on its magnitude. If it is larger than about $3 \times 10^{-4} \text{ eV}^2$ no solar neutrinos will be converted to ν_3 in the sun. Because such a mass has an the oscillation length many orders of magnitude less than an astronomical unit, vacuum oscillations between the sun and earth can be averaged out. Whether $\Delta m_{31}^2 = 3 \times 10^{-4} \text{ eV}^2$ or 500 TeV^2 , the result is the same. If, however, Δm_{31}^2 drops below that level, some of the high energy ^8B neutrinos will be converted adiabatically in the sun. While this runs contrary to the strict interpretation of the atmospheric neutrino data, it is only marginally so.

The mixing angle θ_{23} does not affect the jump probability at either of the two resonances possibly crossed by a neutrino leaving in the sun. But that doesn't mean that the detection probability is independent of it. If s_{23}^2 is large, then neutrinos emerging from the sun in the ν_2 mass eigenstate have a second channel into which they can oscillate travelling to earth and as a result, fewer will be converted back to ν_1 . Similarly, s_{23}^2 has the potential modify the regeneration of neutrinos traversing the earth at night, although that effect is not studied here.

In this section, solar neutrinos will be studied as a function of up to five mass differences and CKM parameters. First, the dependence on the detection probability will be

considered assuming that $\Delta m_{31}^2 > 3 \times 10^{-4} \text{ eV}^2$. In this case, all three mixing angles and the small mass parameter affect $P(\nu_e \rightarrow \nu_e)$. Next, the CKM parameter sets defined in table 5.1 and used extensively in the study of CP violation will be shown to generate rather poor fits to the solar neutrino experiments. Finally, Δm_{31}^2 will be allowed to drop to a level where some of the ${}^8\text{B}$ neutrinos can be converted to ν_3 inside the sun. This will be shown to provide a nice solution to the solar neutrino problem because there is a second mechanism to reduce the ${}^8\text{B}$ flux thereby making room for the ${}^7\text{Be}$ neutrinos.

5.5.1 Four Parameter Fits to the Solar Neutrino Problem

Numerical routines calculated the probability that electron neutrinos produced in the sun were still ν_e 's when detected on earth by each of the five experiments, assuming that Δm_{31}^2 is large. Vacuum oscillations between the sun and earth were included, but regeneration inside the earth was not. With the additional data from SuperKamiokande, there are now five independent solar neutrino experiments, compared with four parameters. Figure 5.15 shows 16 plots of "iso- χ^2 " (constant χ^2) contours as a function of Δm_{21}^2 and $\tan^2 \theta_{12}$ (hereafter t_{12}^2). Moving from left to right and bottom to top, s_{13}^2 and s_{23}^2 respectively increase through 0.05, 0.35, 0.65 and 0.95.

The bottom left plot in which both s_{13}^2 and s_{23}^2 are small, best resembles the two neutrino figure in Chapter two. There is a clear trend moving from left to right in the plot. As s_{13}^2 increases, the neutrino survival probability depends less and less on Δm_{21}^2 and t_{12}^2 because it becomes increasingly dominated by $\nu_1 - \nu_3$ vacuum oscillations.

There is also a clear dependence on s_{23}^2 , which is apparent when either of the other two mixing angles gets large. When s_{13}^2 is large, the ν_1 and ν_3 states have a large overlap and can mix freely. However if s_{23}^2 is also large, then the ν_3 also overlaps with the ν_2 , so in a sense, some of the ν_1 's which have oscillated to ν_3 are leaking into ν_2 thereby further reducing the ν_1 content detected on earth. This also washes out the structure

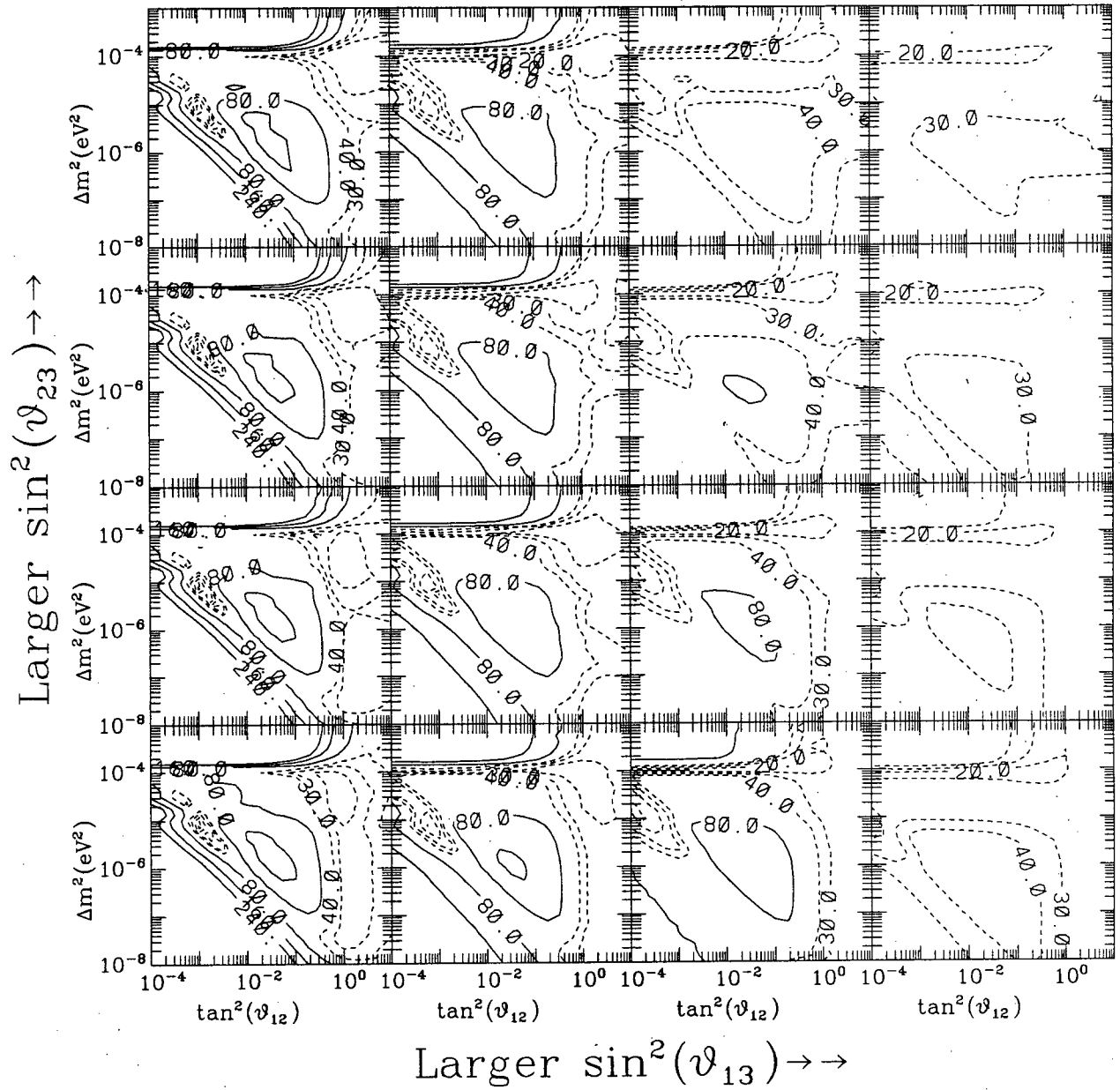


Figure 5.15: Contours of constant χ^2 for four parameter fit to the five solar neutrino experiments. The value of s_{13}^2 in the first through fourth column is 0.05, 0.35, 0.65 and 0.95 respectively. The fourth through first rows have s_{23}^2 equal to 0.05, 0.35, 0.65 and 0.95 respectively. Solid lines show χ^2 of 80, 160 and 240, while dotted contours are at 10, 20, 30 and 40.

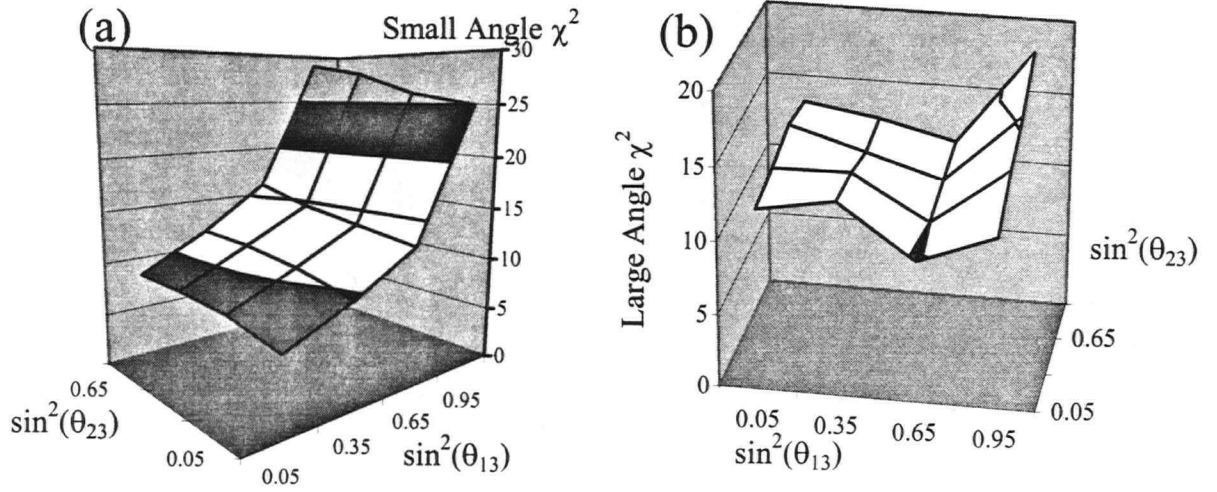


Figure 5.16: Surface plots showing how the minimum value of χ^2 for the small and large angle solar neutrino solutions changes with s_{13}^2 and s_{23}^2 .

of the contour plot, which can be seen in the last column of the figure. A similar but less apparent effect is also seen in the large (t_{12}^2) mixing region of the first column, where increasing s_{23}^2 does shift the contours.

Two solutions are still apparent in most of the plots in figure 5.15. In the bottom left plot there is a small angle solution with $(\Delta m_{21}^2, t_{12}^2)$ equal to $(10^{-5} \text{ eV}^2, 10^{-3})$ and a large angle solution at 10^{-5} eV^2 in which t_{12}^2 cannot be well determined, corresponding to the two neutrino preferred values of the parameters. The small angle solution is quite stable until the other angles get very large and vacuum oscillations take over. The large angle solution moves to larger Δm_{21}^2 and smaller t_{12}^2 relatively quickly.

Figure 5.16 roughly maps out the minimum χ^2 for the two solutions on a 4×4 grid. Numerical study of the χ^2 parameter showed that the small angle solution prefers a smaller value of s_{13}^2 and has a weak preference for small s_{23}^2 . It reached a minimum of $\chi^2 = 7.01$ with $s_{13}^2 = 0.05$ and $s_{23}^2 = 0.05$. While a χ^2 distribution with one degree of freedom would only be expected to be larger in value in about 0.8 % of random trials, the parameter was decreasing with smaller s_{13}^2 and larger s_{23}^2 in the surface plot in figure 5.16,

so this is by no means its minimum. Alternately, s_{13}^2 and s_{23}^2 have not been allowed to vary arbitrarily—both have been restricted to one of four values, so neither one represents a completely free parameter.

The same study found that the best large angle solution in the same 16 trials came when $s_{13}^2 = 0.65$ and $s_{23}^2 = 0.05$. It had $\Delta m_{21}^2 \approx 10^{-4}$ along the adiabatic branch of the MS diagram and $t_{12}^2 \leq 10^0$ could not be exactly determined. The minimum $\chi^2 = 11.5$ occurred at $t_{12}^2 \approx 10^{-3}$, corresponding to a 0.07 % probability by random chance. But again, s_{13}^2 and s_{23}^2 were chosen at the minimum of 16 different trials, not at the actual minimum for the four parameter fit.

Figure 5.17 illustrates the spectra of the $\chi^2 = 7.01$ small angle and $\chi^2 = 9.70$ large angle fits. It is clear that the large angle fit is a vacuum oscillation solution in which neutrinos of all energies are equally likely to survive. By contrast, the small angle fit converts about one half of the high energy ^8B neutrinos and progressively more as the energy drops. The greatest suppression occurs at 1.44 MeV, below which the survival probability increases. The result explains the Kamiokande and SuperKamiokande experiments with a moderately strong suppression of the upper tail of the ^8B flux, and very strong reduction for the rest of the ^8B and the “missing ^7Be ” neutrinos at Homestake. Still lower in the spectrum, in the region of the pp flux, more neutrinos survive thus accounting for the relatively larger rates observed by the gallium experiments.

Figure 5.18 shows the rates and χ^2 for SuperKamiokande, Homestake and the gallium experiments given $s_{13}^2 = 0.05$ and $s_{23}^2 = 0.05$. The small angle fit falls on the non-adiabatic line of the MS diagram for SuperKamiokande, (Kamiokande) and Homestake. There, the ^8B and some ^7Be neutrinos are produced inside the resonance radius in the sun. However, their energy is large enough that many jump across to the ν_1 eigenstate at resonance and thus emerge in the state which is nearly ν_e . Only a few of the pp neutrinos seen by the gallium detectors are produced inside the resonance for conversion in the sun because

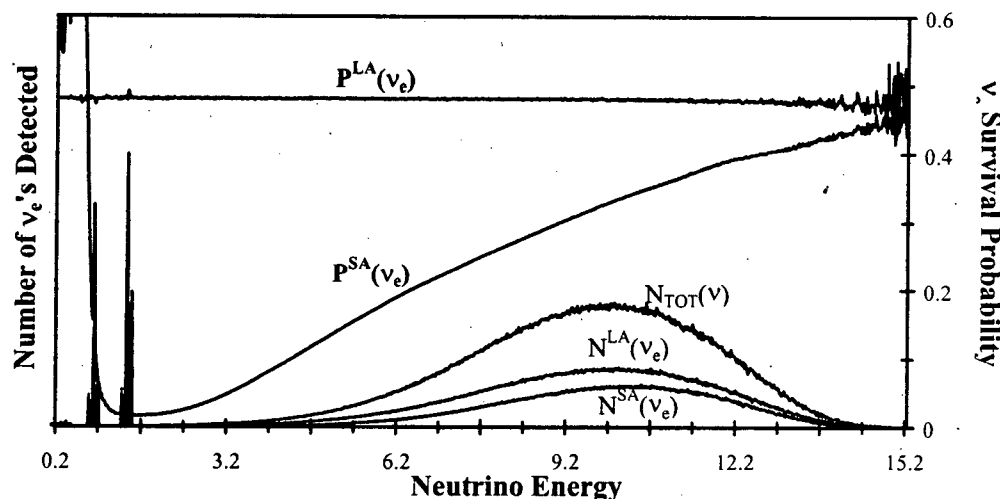


Figure 5.17: Energy Spectra of neutrinos from the small and large angle solutions to the Solar Neutrino Problem. Probabilities are given by the scale on the right axis, while the number of neutrinos are also shown with an arbitrary scale. The small angle (SA) solution corresponds to $\Delta m^2 = 10^{-5} \text{ eV}^2$, $t_{12}^2 = 10^{-3}$ and $s_{13}^2 = s_{23}^2 = 0.05$. The large angle (LA) solution has $\Delta m^2 = 10^{-4} \text{ eV}^2$, $t_{12}^2 = 10^{-3}$, $s_{13}^2 = 0.65$ and $s_{23}^2 = 0.05$.

their energy is so low, but those that do get adiabatically converted to ν_μ .

Finally, figure 5.19 shows the same contours for the large angle solution. Notice that the survival probabilities are reduced by one half or more for all experiments, independent of Δm_{21}^2 or s_{12}^2 . Large mixing between the ν_1 and ν_3 eigenstates converts the neutrinos on the path through vacuum from the sun to the earth. Since there is no energy dependence, all experimental rates are reduced equally.

5.5.2 Combined Atmospheric Best Fit Parameters and Solar Neutrinos

It is worthwhile considering the compatibility of the solar and atmospheric neutrino experiments. Solar neutrino survival probabilities were calculated for the five CKM parameter sets F[a] to F[e] which very recently appeared in the literature as best fit solutions to the ANP. By fixing Δm_{31}^2 , s_{13}^2 and s_{23}^2 there are only two free parameters, so

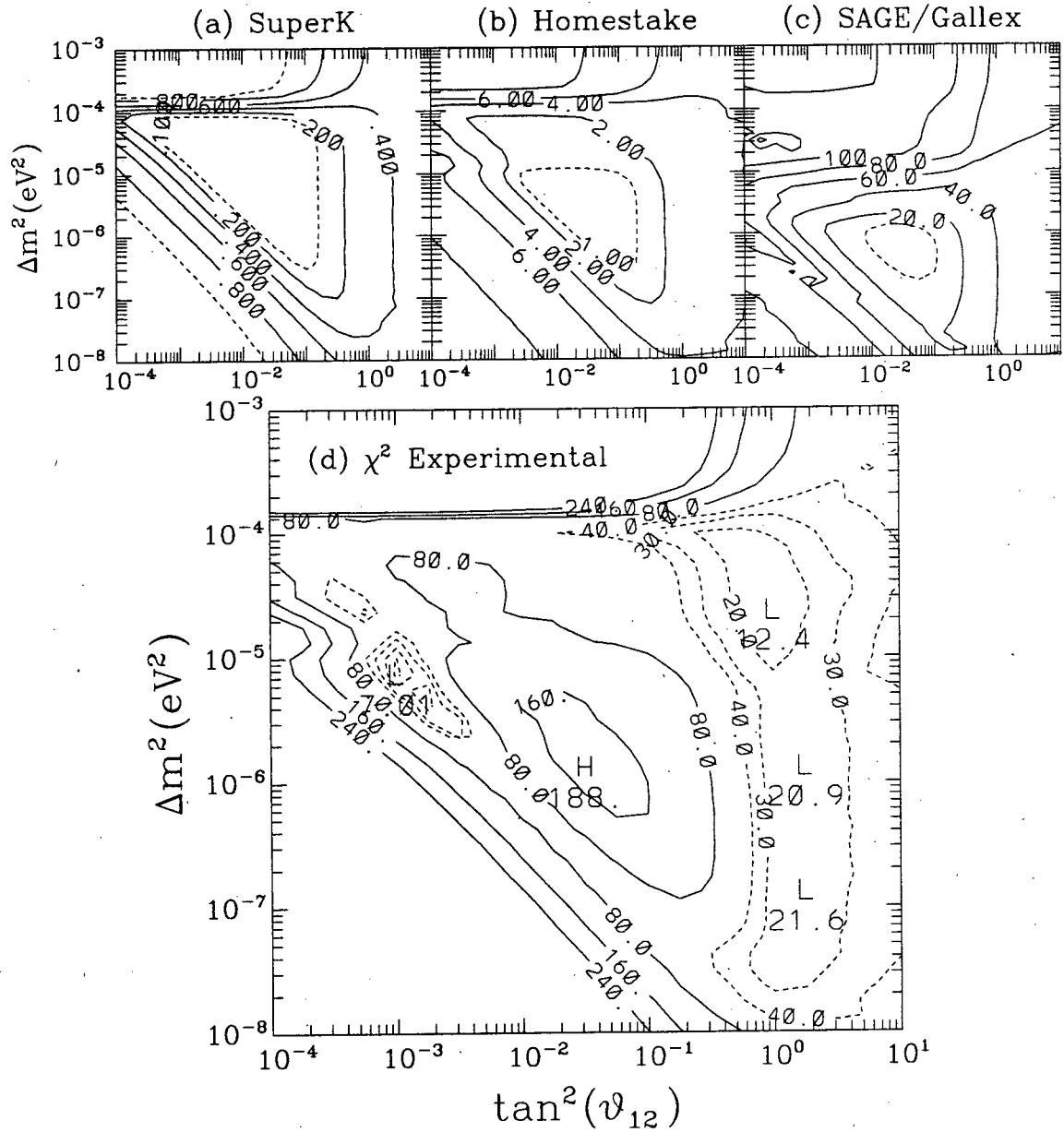


Figure 5.18: Contours of constant probability (SuperK) and experimental rates iso-SNU contours (Homestake and SAGE/Gallex) for the small angle solution to the solar neutrino experiments at the best fit values $s_{13}^2 = 0.05$ and $s_{23}^2 = 0.05$. Kamiokande results would be very close to SuperKamiokande. Bottom plot shows iso- χ^2 contours: solid lines at 80, 160 and 240, and dotted lines at 10, 20, 30 and 40.

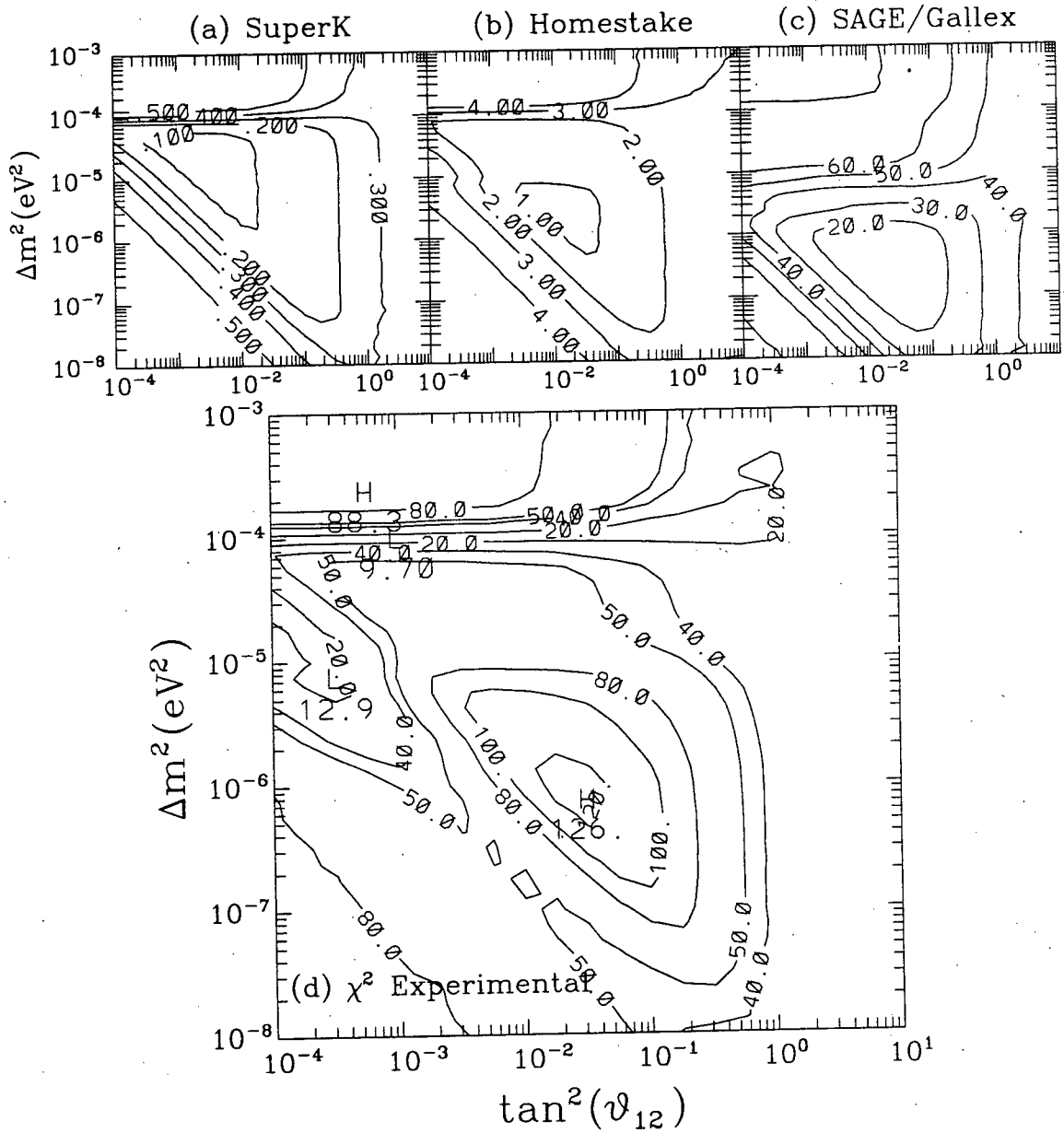


Figure 5.19: Contours of constant probability (SuperK) and experimental rates iso-SNU contours (Homestake and SAGE/Gallex) for the large angle solution to the solar neutrino experiments at the best fit values $s_{13}^2 = 0.65$ and $s_{23}^2 = 0.05$. Kamiokande results would be very close to SuperKamiokande. Bottom plot shows iso- χ^2 contours.

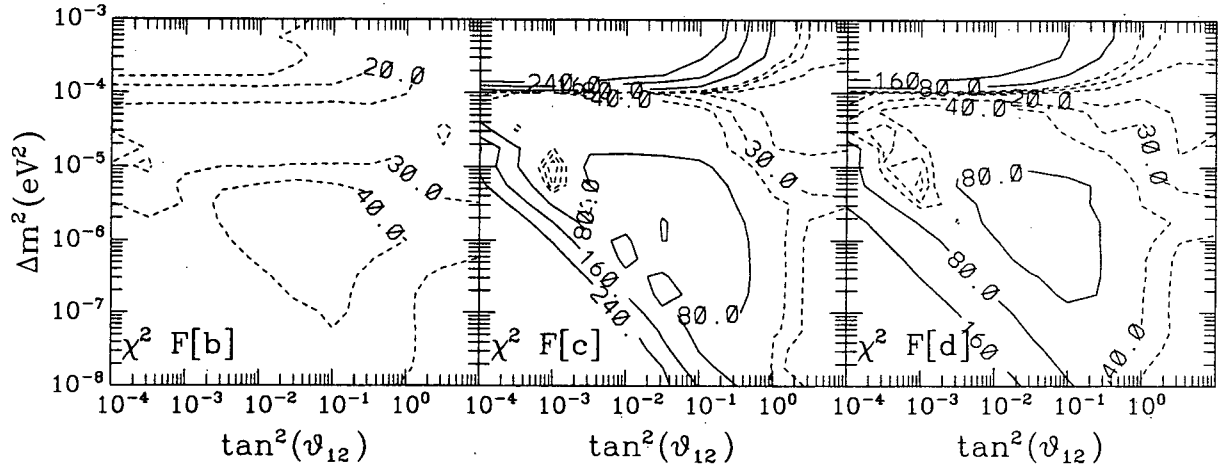


Figure 5.20: Contours of constant χ^2 for five solar neutrino experiments for the CKM parameters sets F[b], F[c] and F[d] defined in table 5.1.

the corresponding χ^2 variate (with five experiments) has three degrees of freedom.

F[a] to F[e] produced minimum values of χ^2 of 13.9, 12.1, 10.1, 12.2 and 18.5 respectively. F[a] and F[e] are extremely poor fits to the data, while a χ^2 variate with three degrees of freedom would randomly give larger values than F[b], F[c] and F[d] in just 0.70 %, 1.8 % and 0.67 % of trials respectively. None of the fits are phenomenally good, but F[d] is slightly better than the two neutrino solution with $s_{13}^2 = s_{23}^2 = 0$, where the same analysis found $\chi^2 = 10.2$. Figure 5.20 plots iso- χ^2 contours for the best three fits F[b], F[c], and F[d].

F[b] and F[d] are large mixing angle solutions, having s_{23}^2 close to unity and $s_{13}^2 \geq \frac{1}{3}$. Both solutions are similar to the large mixing angle solutions illustrated in figure 5.15 with $\Delta m_{21}^2 \approx 10^{-4} \text{ eV}^2$. With its relatively small $\nu_1 - \nu_3$ mixing, the best fit for the parameter set F[c] corresponds to the small mixing solution with $\Delta m_{21}^2 \approx 10^{-5} \text{ eV}^2$ and $t_{12}^2 \approx 10^{-3}$. By fitting the atmospheric data with a parameter set with smaller s_{13}^2 the fit to the solar data would improve.

5.5.3 Solar Neutrinos with Two Small Mass Parameters

While both the large and small angle two neutrino solutions to the SNP do reduce the survival probability, neither one is entirely natural. The large mixing angle solution requires t_{12}^2 to be on the order of unity, which runs counter to experience in the quark sector where the mixing angles are small. While t_{12}^2 drops in the three neutrino extension of the large angle solution, $s_{13}^2 \approx 0.65$ whereas in the quark sector the mixing angle across two families is extremely small. The large angle spectral results also conflict with signals from the experiments: the fit has all neutrino energies are equally suppressed whereas the data suggest an energy dependence.

The small angle two neutrino solution is much better in this regard, admitting a solution with small mixing angle. The mass scale is arranged so that the low energy ^8B and the ^7Be neutrinos are strongly suppressed, the high energy tail of the ^8B flux does not entirely satisfy adiabaticity and often jumps across eigenstates at resonance thus emerging as ν_1 , and the pp neutrinos' resonance occurs deep in the solar interior often inside the radius of production so they are never converted. These phenomena use energy dependence, namely the "pit" in $P^{SA}(\nu_e)$ in figure 5.17, to rationalise the relatively large number of ^8B neutrinos seen at SuperKamiokande against the apparent lack of ^7Be neutrinos seen at Homestake. In a more intuitive solution, however, one might expect a more uniform suppression of neutrinos across the spectrum but still allowing for some energy dependence.

This can be accomplished in the three neutrino scenario, but at a cost. By dropping Δm_{31}^2 to about one one quarter of the lowest value suggested by the atmospheric neutrino results, some of the ^8B neutrinos will be converted to the ν_3 eigenstate at the first of two resonances in the sun. Those produced outside the radius of the first resonance or which non-adiabatically jump to the ν_1 eigenstate may again be converted to ν_2 at the second

resonance. This additional suppression would leave more room in the experimental data for some ${}^7\text{Be}$ neutrinos to emerge. Until the Soudan 2 experiment is able to verify the water Cherenkov atmospheric neutrino results and the theoretical atmospheric neutrino flux calculations converge, this scenario should be considered.

The computer codes discussed in Chapter four again calculated electron neutrino survival probabilities at small steps in Δm_{21}^2 and t_{12}^2 . The large mass scale targetted was from $1 - 2 \times 10^{-4} \text{ eV}^2$ to convert some ${}^8\text{B}$ neutrinos while leaving the ${}^7\text{Be}$ and pp neutrinos unaffected. The mixing parameter s_{13}^2 was kept small, varying from 0.01 to 0.1 but still allowing for large conversions along the adiabatic branch of the MS diagram, while s_{23}^2 was calculated at 0.5 and 0.75. This latter choice does represent large mixing, but only across one generation and in keeping with the preferred values required to explain the atmospheric neutrino data given the requirement of small s_{13}^2 and t_{12}^2 . The s_{23}^2 dependence was, however, very weak due to the low values of both t_{12}^2 and s_{13}^2 .

Figure 5.21 shows contours of constant neutrino survival probability for the solar neutrino experiments as well as iso- χ^2 contours when they are combined. The "large" mass scale was $\Delta m_{31}^2 = 1.5 \times 10^{-4} \text{ eV}^2$, $s_{13}^2 = 0.03$ and $s_{23}^2 = 0.75$. The minimum value of the χ^2 was 3.79 at $\Delta m_{21}^2 \approx 10^{-5} \text{ eV}^2$ and $t_{12}^2 \approx 3 \times 10^{-4}$. A plot with $s_{23}^2 = 0.5$ was almost indistinguishable and gave a minimum of $\chi^2 = 4.01$. Note that this treatment breaks down when the two resonances cross (ie when $\Delta m_{21}^2 \approx 1.5 \times 10^{-4} \text{ eV}^2$) but should be valid at the minimum where they are well separated.

Since s_{23}^2 was determined by the atmospheric neutrino results and the dependence on it is very weak, it is not really a free parameter and the data can be analysed with five experiments fitted by four parameters. A χ^2 parameter with one degree of freedom could be expected to be larger than 3.85 (an approximate mean over the range of externally determined s_{23}^2) by random chance about 5% of the time. Moreover, only a discrete few values of Δm_{31}^2 and s_{13}^2 were surveyed, so a more comprehensive study would probably

lower the minimum χ^2 value somewhat. Even so, this four parameter fit with two mass scales does provide a viable alternative to solve the solar neutrino problem, and which is distinct from the small angle two neutrino solution.

Figure 5.22 compares the spectra produced by this three neutrino solution with the two neutrino small angle one. There is a clear difference. The three neutrino solution suppresses the high energy tail of the ^8B flux with the second resonance crossing. As a result, there is less suppression of the low energy ^8B and ^7Be fluxes, while the low energy behaviour relevant to the pp neutrinos is identical. SuperKamiokande will eventually have enough data to bin their results by energy, and it will be possible to differentiate these two scenarios. Notice that the ^7Be neutrinos are not suppressed as much in the three neutrino fit, while the high energy tail of the ^8B flux is much more strongly suppressed.

5.5.4 Discussion

The three neutrino scenario does provide additional solutions to the solar neutrino data beyond the simplest one in which only s_{13}^2 is added as a free parameter. The mixing angle s_{23}^2 clearly affects the large mixing angle solution to the SNP when the calculation of ν_e survival probability includes vacuum oscillations between the sun and earth. By analogy, when regeneration of neutrinos arriving at night which traverse the earth's core is also calculated, the magnitude of s_{23}^2 will again come into play.

Although the atmospheric neutrino CKM parameter sets chosen did not admit likely extensions for the solar neutrino problem, this was not a complete study. $F[a]$ and $F[e]$ were chosen from the best fits over a wide range of Δm_{31}^2 , and there were other regions of the parameter space which would have given lower χ^2 minima. In particular, by choosing fits to the atmospheric data with smaller s_{13}^2 , better results could be expected. In addition, Fogli et. al. noted in their paper that the best fit regions shown were still sensitive to changes in the experimental data and would probably shift around somewhat

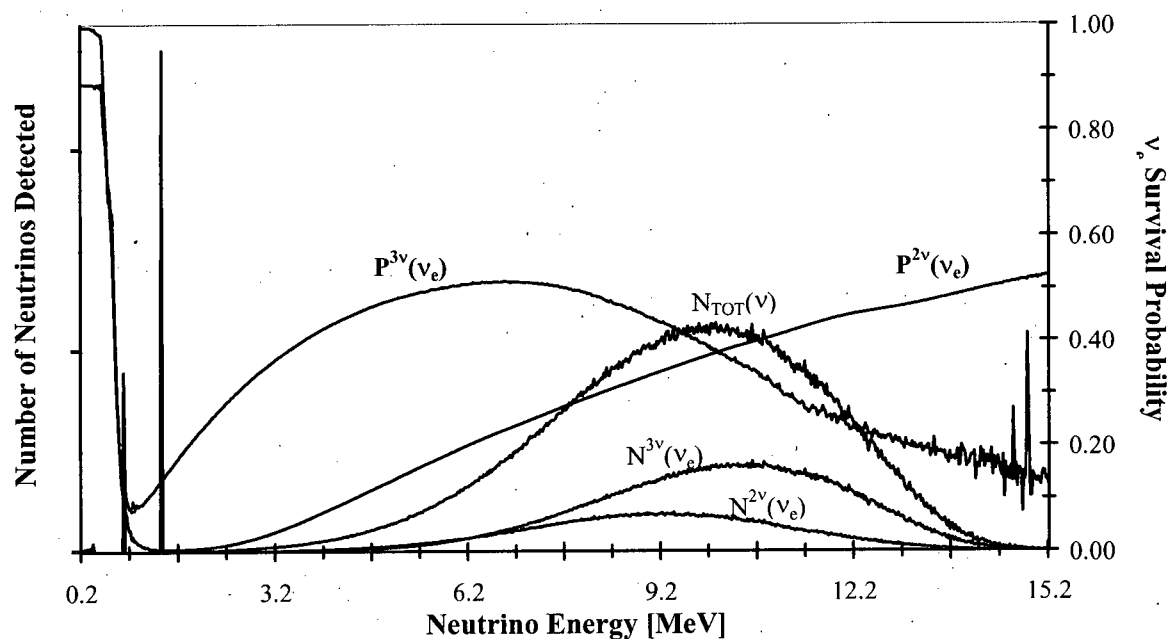


Figure 5.22: Energy Spectra of neutrinos from the two neutrino small angle solution and two mass scale fit to the Solar Neutrino Problem. In the two neutrino (2ν) fit, $\Delta m^2 = 10^{-5} \text{ eV}^2$ and $t_{12}^2 = 10^{-3}$. In the two mass scale fit (3ν) has $\Delta m_{21}^2 = 10^{-5} \text{ eV}^2$, $\Delta m_{31}^2 = 1.5 \times 10^{-4} \text{ eV}^2$, $t_{12}^2 = 10^{-3}$, $s_{13}^2 = 0.03$ and $s_{23}^2 = 0.75$. Probabilities are given by the scale on the right axis, while the number of neutrinos are also shown with an arbitrary scale.

[130].

Most intriguing is the possibility of a second resonance in the sun. The lower limit on Δm_{31}^2 is based on two water Cherenkov experiments which have yet to be confirmed by an iron calorimeter with large statistics. Soudan 2 is now taking data and will either confirm or oppose those results. Then, once the atmospheric neutrino flux calculations are in better agreement, it will be possible to make more definite statements about the ANP and what regions of oscillation parameter space it allows.

By extending the allowed value of Δm_{31}^2 so that some high energy ^8B solar neutrinos are converted, a new solution to the solar neutrino problem becomes possible. In it the high energy tail of the ^8B flux crosses two resonances and becomes more suppressed than in the small angle two neutrino solution. This eases the pressure on the ^7Be line and allows some of the Homestake signal to be assigned to it—thus $P^{3\nu}(\nu_e) > P^{2\nu}(\nu_e)$ at the ^7Be neutrino energies in figure 5.22. At very low energies, this solution is identical to its two neutrino counterpart.

Chapter 6

Conclusions

Neutrinos with finite mass and mixing provide an inviting theoretical analogy with the quark sector. It also offers a possible solution to two major conflicts in particle physics today, the Solar and Atmospheric Neutrino Problems, with a very minimal extension to the Standard Model. The masses and mixings implied to resolve theory with the experiments do not conflict with any other laboratory measurements to date. Early studies of oscillation effects simplified the problem significantly by analysing just two neutrinos. While they did establish the field and show that massive neutrinos could provide viable solutions to the SNP and ANP, they were not accurate models of nature which does have three light neutrinos. The additional complexity of the full parameterisation offers a much richer phenomenology, with new effects discussed throughout this thesis. It provides more ways of explaining the existing results and in the future will be better able to deal with the many new experiments coming on line in the next decade. SNO, Borexino, Hellaz and others will provide additional data on solar neutrinos, while SuperKamiokande and Soudan '2 are currently extending the accuracy of atmospheric neutrino measurements, and the long baseline experiments K2K and MINOS will complement the others. These new experiments will allow physicists to make more precise quantitative statements about the neutrino oscillation parameters, so three neutrino analyses will be absolutely required to interpret them. Chapter one of this thesis discussed two discrepancies between theoretical calculations and experimental measurements, in both the solar and atmospheric

neutrinos, and established the need for additional physics in order to explain them. Moreover, it updated recent arguments which show that the solar neutrino experiments are in conflict with each other under very general assumptions. Chapter two developed the ideas of oscillations with two neutrinos, and applied the results to realistic long baseline experiments and the solar results. The latter included the effect of regeneration of night time neutrinos in the earth which has appeared in the literature in the last few years. Chapter three developed the three neutrino formalism using a CKM matrix identical to that in the quark sector. Several new analytical results, including a complete calculation of the hamiltonian in the weak eigenbasis and exact oscillation probabilities were presented. The second of these was used extensively later. Chapter four outlined the numerical methods used to accurately compute long baseline and solar neutrino oscillations with three neutrinos thus removing the need to make severe approximations. They also correctly computed results even when those analytical approximations broke down. Three detailed studies were produced in Chapter five. The first reduced the oscillation probabilities from Chapter three to four different hierarchies in which the two mass scales are widely separated, the OMSD scenarios. Symmetries between these four scenarios were examined, and an exact relation describing the two-fold degeneracy in accelerator based muon neutrino oscillation experiments already noted in the literature was given. A realistic, detailed study of neutrino oscillation experiments on baselines of 250 km and 732 km showed what regions of parameter space could be studied and where matter effects are likely to be seen. Fluxes which would be measured at a high statistics experiment were also shown to be able to accurately determine some of the CKM parameters. Section four of Chapter five investigated CP violation using accelerator and reactor based experiments. Analytical work extended results from the literature in the last year to include an approximation to oscillation probabilities to second order in both the ratio of the mass scales and the ratio of matter effects to the large mass scale. The first detailed calculations of

neutrino oscillations at the K2K and MINOS experiments showed that neither is likely to have the opportunity to measure CP violation in the lepton sector. K2K does come closer, but would need major upgrades in order to see an effect. Both the first-order and eventually the second-order approximations did break down, but the numerical solutions were able to give accurate quantitative results when they did. Specific strategies unique to each experiment for isolating the effect were outlined. Finally, an analytical calculation showed the effect CP violation would have on the ratio of μ -type to e -type neutrinos in the atmospheric flux. The best estimates of the CKM parameters from the atmospheric neutrino experiments were shown to produce a CP violating effect that may be as large as a few percent. Finally, the survival probability for solar electron neutrinos was calculated in the three family scenario. Results showed that even with one mass scale, the simplest three parameter extension of the two neutrino calculation does not accurately approximate the full system when the mixing angles are large. By allowing the large mass scale to drop below the limit suggested by the water Cherenkov atmospheric experiments a new, statistically viable solution of the solar neutrino problem was found. It reduces the suppression of the ${}^7\text{Be}$ neutrinos so part of the Homestake signal can be assigned to them. Over the next decade, many new experiments will provide additional data on the Solar and Atmospheric Neutrino Problems, as well as related phenomena. Six-parameter three neutrino analyses will have to be performed, not just to correctly interpret those new data, but also to offer legitimate ideas about what additional research should be carried out. What has been presented in this thesis are some numerical techniques and new analytical results to do that, as well as detailed studies on the phenomenology at the next generation of experiments. The challenge to those future experiments will be to either reject or confirm the neutrino oscillation hypothesis as a viable description of nature and, if it is the latter, quantify the parameters which characterise it.

Bibliography

- [1] R.K. Ulrich and A.N. Cox. The Computation of Standard Models. In *Solar Interior and Atmosphere*, edited by A.N. Cox, W.C. Livingston, and M.S. Matthews, The University of Arizona Press, 1991.
- [2] John N. Bahcall and M.H. Pinsonneault. Solar Models with Helium and Heavy Element Diffusion. *Bulletin Board Preprint* hep-ph 9505425, submitted to Reviews of Modern Physics.
- [3] S. Sofia et. al. Pre-Main-Sequence Evolution. In *Solar Interior and Atmosphere*, edited by A.N. Cox, W.C. Livingston, and M.S. Matthews, The University of Arizona Press, 1991.
- [4] Michael Zeilik and Elske v. P. Smith. *Introductory Astronomy and Astrophysics*. Saunders College Publishing, 1987.
- [5] Arthur Eddington. *The Internal Constitution of Stars*. Cambridge University Press, 1926.
- [6] George Gamow. Zur Quantentheorie der Atomzertümmerung. *Zeitschrift Physica* 52:510, 1928.
- [7] H.A. Bethe and C.L. Critchfield. The Formation of Deuterons by Proton Combination. *Physical Review* 54:248, 1938. H.A. Bethe. Energy Production in Stars. *Physical Review* 55:434, 1938. Von C.F. V. Weizsäcker. Über Elementumwandlungen im Innern der Sterne. I. *Physics Zeitschrift* 38:176, 1937.
- [8] John N. Bahcall and Roger K. Ulrich. Solar Models, Neutrino Experiments, and Helioseismology. *Reviews of Modern Physics* 60:297, 1988.
- [9] S. Rosseland. Note on the Absorption of Radiation within a Star. *Monthly Notices of the Royal Astronomical Society* 84:525, 1924.
- [10] W.F. Heubner. Atomic and Radiative Processes in the Solar Interior. In *Physics of the Sun, Volume I: The Solar Interior*, edited by P.A. Sturrock et. al., D. Reidel Publishing Company, 1986.
- [11] Arthur N. Cox, Joyce A. Guzik, and Russell B. Kidman. Oscillations of Solar Models with Internal Element Diffusion. *The Astrophysical Journal* 342:1187, 1989.

- [12] Edward Anders and Nicolas Grevesse. Abundances of the Elements: Meteoritic and Solar. *Geochimica Cosmochimica Acta* 53:197, 1989.
- [13] J.E. Ross and L.H. Aller. The Chemical Composition of the Sun. *Science* 191:1223, 1976.
- [14] L.H. Aller. Chemical Abundances. In *Spectroscopy of Astrophysical Plasmas*, edited by A. Dalgarno and D. Layzer, Cambridge University Press, 1986.
- [15] N. Grevesse and A. Noels. Cosmic Abundances of the Elements. In *Origin and Evolution of Elements*, edited by N. Prantzos, E. Vangioni-Flam and M. Casse, Cambridge University Press, 1993.
- [16] John N. Bahcall and M.H. Pinsonneault. Standard Solar Models, with and without Helium Diffusion, and the Solar Neutrino Problem. *Reviews of Modern Physics* 64:885, 1992.
- [17] Peter D. MacD. Parker. Thermonuclear Reactions in the Solar Interior. In *Physics of the Sun, Volume I: The Solar Interior*, edited by P.A. Sturrock et. al., D. Reidel Publishing Company, 1986.
- [18] E.E. Salpeter. Electron Screening and Thermonuclear Reactions. *Australian Journal of Physics* 7:373, 1954.
- [19] H.J. Assenbaum, K. Langanke, and C. Rolfs. Effects of Electron Screening on Low-Energy Fusion Cross Sections. *Zeitschrift für Physik* A327:461, 1987.
- [20] Claus E. Rolfs and William S. Rodney. *Cauldrons in the Cosmos*, The University of Chicago Press, 1988.
- [21] P.D. MacD. Parker and C.E. Rolfs. Nuclear Energy Generation in the Solar Interior. In *Solar Interior and Atmosphere*, edited by A.N. Cox, W.C. Livingston, and M.S. Matthews, The University of Arizona Press, 1991.
- [22] A. Krauss et. al. Astrophysical S(E) Factor of ${}^3\text{He}(3\text{He}, 2p){}^4\text{He}$ at Solar Energies. *Nuclear Physics* A467:273, 1987.
- [23] M. Hilgemeier et. al. Absolute Cross Section of the ${}^3\text{He}(\alpha, \gamma){}^7\text{Be}$ Reaction. *Zeitschrift für Physik* A329:243, 1988.
- [24] F. Ajzenberg-Selove. Energy Levels of Light Nuclei A = 5-10. *Nuclear Physics* A490:1, 1988.
- [25] C.W. Johnson et. al. The Fate of ${}^7\text{Be}$ in the Sun. *The Astrophysical Journal* 392:320, 1992.

- [26] John N. Bahcall. *Neutrino Astrophysics*, Cambridge University Press, 1989.
- [27] D.C. Hensley. Investigation of a New State in O^{15} Near the $N^{14} + p$ Threshold. *The Astrophysical Journal* 147:818, 1967.
- [28] W. Däppen, J. Keady and F. Rogers. Equation of State and Opacity. In *Solar Interior and Atmosphere*, edited by A.N. Cox, W.C. Livingston, and M.S. Matthews, The University of Arizona Press, 1991.
- [29] C.A. Iglesias and F.J. Rogers. Opacities for the Solar Radiative Interior. *The Astrophysical Journal* 371:408, 1991.
- [30] Anne A. Thoul, John N. Bahcall, and Abraham Loeb. Element Diffusion in the Solar Interior. *The Astrophysical Journal* 421:828, 1994.
- [31] J. Christensen-Dalsgaard. The Structure and Evolution of the Sun. In *The Sun: A Laboratory for Astrophysics*, edited by Joan T. Schmelz and John C. Brown, Kluwer Academic Publishers, 1992.
- [32] R.B. Leighton, R.W. Noyes, and G.W. Simon. Velocity Fields in the Solar Atmosphere. I. Preliminary Report. *The Astrophysical Journal* 135:474, 1962.
- [33] S.V. Vorontsov and V.N. Zharkov. Helioseismology. *Astrophysics and Space Physics Reviews* 7:1, 1988.
- [34] F. Hill, F.-L. Deubner and G. Isaak. Oscillation Observations. In *Solar Interior and Atmosphere*, edited by A.N. Cox, W.C. Livingston, and M.S. Matthews, The University of Arizona Press, 1991.
- [35] J. Christensen-Dalsgaard and G. Berthomieu. Theory of Solar Oscillations. In *Solar Interior and Atmosphere*, edited by A.N. Cox, W.C. Livingston, and M.S. Matthews, The University of Arizona Press, 1991.
- [36] D.O. Gough and M.J. Thompson. The Inversion Problem. In *Solar Interior and Atmosphere*, edited by A.N. Cox, W.C. Livingston, and M.S. Matthews, The University of Arizona Press, 1991.
- [37] J. Christensen-Dalsgaard. Seismic Investigation of the Solar Interior. In *The Sun: A Laboratory for Astrophysics*, edited by Joan T. Schmelz and John C. Brown, Kluwer Academic Publishers, 1992.
- [38] J. Christensen-Dalsgaard, D.O. Gough, and M.J. Thompson. The Depth of the Solar Convection Zone. *The Astrophysical Journal* 378:413, 1991.

- [39] I.-Juliana Sackmann, Arnold I. Boothroyd, and William Fowler. Our Sun. I. The Standard Model: Successes and Failures. *The Astrophysical Journal* 360:727, 1990.
- [40] G. Berthomieu et. al. Standard solar models with CESAM code: neutrinos and helioseismology. *Astronomy and Astrophysics* 268(2):775, February, 1993.
- [41] Sylvaine Turck-Chièze and Ilidio Lopes. Toward a Unified Classical Model of the Sun: On the Sensitivity of Neutrinos and Helioseismology to the Microscopic Physics. *The Astrophysical Journal* 408:347, 1993.
- [42] Charles R. Proffitt. Effects of Heavy-Element Settling on Solar Neutrino Fluxes and Interior Structure. *The Astrophysical Journal* 425:849, 1994.
- [43] V. Castellani et. al. Neutrinos from the Sun: Experimental Results Confronted with Solar Models. *Physical Review* D50:4749, 1994.
- [44] V. Berezinsky, G. Fiorentini, and M. Lissia. The MSW Solution to the Solar Neutrino Problem for Non-Standard Solar Models. *Physics Letters* B341:38, 1994.
- [45] R. Sienkiewicz, J.N. Bahcall, and B. Paczyński. Mixing and the Solar Neutrino Problem. *The Astrophysical Journal* 349:641, 1990.
- [46] W.A. Dziembowski, A.A. Pamyatnykh, and R. Sienkiewicz. Solar Model from Helioseismology and the Neutrino Flux Problem. *Monthly Notices of the Royal Astronomical Society* 244:542, 1990.
- [47] Raymond Davis, Jr. and Arthur N. Cox. Solar Neutrino Experiments. In *Solar Interior and Atmosphere*, edited by A.N. Cox, W.C. Livingston, and M.S. Matthews, The University of Arizona Press, 1991.
- [48] J.K. Rowley, B.T. Cleveland, and R. Davis, Jr. The Chlorine Solar Neutrino Experiment. In *Solar Neutrinos and Neutrino Astronomy*, edited by M.L. Cherry, W.A. Fowler, and K. Lande, American Institute of Physics, 1985.
- [49] B.T. Cleveland et. al. Update on the Measurement of the Solar Neutrino Flux with the Homestake Chlorine Detector. *Neutrino 94 Proceedings in Nuclear Physics Proceedings Supplements* B38:47, 1995.
- [50] John Bahcall and Raymond Davis Jr., Solar Neutrinos: A Scientific Puzzle. *Science* 191:682, 1976.
- [51] Yoichiro Suzuki. Kamiokande Solar Neutrino Results. In *Neutrino 94 Proceedings in Nuclear Physics Proceedings Supplements* B38:54, 1995.

- [52] K. Nakamura. Recent Results from Kamiokande Solar Neutrino Observations. In *Neutrino 92. Proceedings in Nuclear Physics Proceedings Supplements* B31:105, 1993.
- [53] K.S. Hirata et. al. The Kamiokande Solar Neutrino Experiment. In *Inside the Sun*, edited by Gabrielle Berthomieu and Michel Cribier, Kluwer Academic Publishers, 1989.
- [54] K.S. Hirata et. al. Real-time, Directional Measurement of 8B Solar Neutrinos in the Kamiokande II Detector. *Physical Review* D44:2241, 1991.
- [55] Yoichiro Suzuki. Kamiokande Solar Neutrino Results. In *Neutrino 94. Proceedings in Nuclear Physics Proceedings Supplements* B38:54, 1995.
- [56] Reported by Maury Goodman in the "Long-Baseline news", August 1997 edition. <http://www.long-baseline.org>.
- [57] V.A. Kuz'min. Detection of Solar Neutrinos by Means of the $Ga^{71}(\nu, e^-)Ge^{71}$ Reaction. *Soviet Physics Jetp* 22:1051, 1966.
- [58] Thomas J. Bowles and Vladimir N. Gavrin. The Status of the Solar Neutrino Problem. *Ann. Rev. Nucl. Part. Sci.* 43:117, 1993.
- [59] P. Anselmann et. al. Solar Neutrinos Observed by GALLEX at Gran Sasso. *Physics Letters* B285:376, 1992.
- [60] P. Anselmann et. al. First Results from the ^{51}Cr Neutrino Source Experiment with the GALLEX Detector. *Physics Letters* B342:440, 1995.
- [61] O.L. Anosov et. al. Results from the Soviet-American Gallium Experiment. *Nucl. Phys. B Proc. Suppl.* 31:111, 1993.
- [62] V.N. Gavrin et. al. The Baksan Gallium Solar Neutrino Experiment. In *Inside the Sun*, edited by Gabrielle Berthomieu and Michel Cribier, Kluwer Academic Publishers, 1989.
- [63] J.N. Abdurashitov et. al. Results from SAGE (The Russian-American Gallium Solar Neutrino Experiment). *Physics Letters* B328:234, 1994.
- [64] O.L. Anosov. Results from the Soviet-American Gallium Experiment. In *Neutrino 92. Proceedings in Nuclear Physics Proceedings Supplements* B31:105, 1993.
- [65] J.N. Abdurashitov et. al. Results from SAGE. In *Neutrino 94 Proceedings in Nuclear Physics Proceedings Supplements* B38:60, 1995.
- [66] John N. Bahcall. Two solar neutrino problems. *Phys. Lett.* B338(2,3):276, 27 October, 1994.

- [67] M. Spiro and D. Vignaud. Solar model independent neutrino oscillation signals in the forthcoming solar neutrino experiments? *Phys. Lett. B* 242(2):279, 7 June, 1990. S. Degl'Innocenti, G. Fiorentini, and M. Lissia. The pp reaction in the sun and solar neutrinos *Phys. Lett. B* 303(1,2):68, 8 April, 1993. N. Hata, S. Bludman, and P. Langacker. Astrophysical solutions are incompatible with the solar neutrino data. *Phys. Rev. D* 49(7):3622, 1 April, 1994. V. Castellani, S. Degl'Innocenti, and G. Fiorentini. Solar neutrinos and nuclear reactions in the solar interior. *Astron. Astrophys.* 271(2):601, April, 1993.
- [68] Stephen Parke. Status of the Solar Neutrino Puzzle. *Phys. Rev. Lett.* 74(6):839, 6 February, 1995.
- [69] K.S. Hirata et. al. Experimental Study of the Atmospheric Neutrino Flux. *Phys. Lett. B* 205(2,3):416, 28 April, 1988. K.S. Hirata et. al. Observation of a small atmospheric ν_μ/ν_e ratio in Kamiokande. *Phys. Lett. B* 214(1,2):146, 23 April, 1992.
- [70] R.M. Bionata et. al. Contained neutrino interactions in an underground water detector. *Phys. Rev. D* 38(3):768, 1 August, 1988. R. Becker-Szendy et. al. Electron- and muon-neutrino content of the atmospheric flux. *Phys. Rev. D* 46(9):3720, 1 November, 1992. R. Becker-Szendy et. al. Search for Muon Neutrino Oscillations with the Irvine-Michigan-Brookhaven Detector. *Phys. Rev. Lett.* 69(7):1010, 17 August, 1992.
- [71] Giles Barr, T.K. Gaisser and Todor Stanev. Flux of atmospheric neutrinos. *Phys. Rev. D* 39(3):3532, 1 June, 1989. Stephen Barr et. al. Ratio of ν_e/ν_μ in Atmospheric Neutrinos. *Phys. Lett. B* 214(1):147, 10 November, 1988.
- [72] M. Honda et. al. Atmospheric neutrino fluxes. *Phys. Lett. B* 248(1,2):193, 10 November, 1988. M. Honda et. al. Calculation of the Flux of Atmospheric Neutrinos. ICRR-Report-336-95-2. Morihiko Honda et. al. Atmospheric Neutrinos. Bulletin Board Preprint hep-ph/9511223.
- [73] Haeshim Lee and Yoon S. Koh. A New Calculation of Atmospheric Neutrino Flux. *Il Nuovo Cimento* 105B(8-9):883, August-September, 1990.
- [74] E.V. Bugaev and V.A. Naumov. On the interpretation of the Kamiokande Neutrino Experiment. *Phys. Lett. B* 232(3):391, 7 December, 1989.
- [75] T.K. Gaisser. Review of Atmospheric Neutrinos. Bulletin Board Preprint hep-ph/9611301.
- [76] M. Aglietta et. al. Experimental Study of Atmospheric Neutrino Flux in the NUSEX Experiment. *Europhys. Lett.* 8(7):611, 1 April, 1989.

- [77] Ch. Berger et. al. A study of atmospheric oscillations in the Frejus experiment. *Phys. Lett.* B245(2):305, 9 August, 1990.
- [78] Y. Fukuda et. al. Atmospheric ν_μ/ν_e ratio in the multi-GeV energy range. *Phys. Lett.* B335:237, 1 September, 1994.
- [79] W.W.M. Allison et. al. Measurement of the atmospheric neutrino flavour composition in Soudan 2. Bulletin Board Preprint hep-ex/9611007.
- [80] W.A. Mann, T. Kafka and W. Leeson. The atmospheric ν_μ/ν_e anomaly as manifestation of proton decay $p \rightarrow e^+ \nu \nu$. *Phys. Lett.* B291:(1,2):200, 17 September, 1992.
- [81] O.G. Ryazhskaya. Is There an Excess of Electron Neutrinos in the Atmospheric Flux? *Il. Nuov. Cim.* C18(1):77, February, 1995.
- [82] D.H. Perkins. The atmospheric neutrino problem: A critique. *Nucl. Phys.* B399:3, 1993.
- [83] G.L. Fogli and E. Lisi. On the Atmospheric Neutrino Anomaly and its Statistical Significance. Preprint IASSNS-AST 95/21.
- [84] B. Pontecorvo. Neutrino experiments and the problem of conservation of leptonic charge. *Sov. Phys. JetP*, 26(5):984, May, 1968.
- [85] R.M. Barnett et. al. Particle Physics Booklet. From the Review of Particle Properties, *Physical Review D*, 54:1, July, 1996.
- [86] S.M. Bilen'kii and B.M. Pontecorvo. Lepton mixing and neutrino oscillations. *Sov. Phys. Usp.*, 20(10):776, October, 1977.
- [87] T.K. Kuo and James Pantaleone. Neutrino oscillations in matter. *Rev. Mod. Phys.* 61(4):937, October, 1989.
- [88] Lincoln Wolfenstein. Neutrino oscillations in matter. *Phys. Rev. D* 17(9):2369, 5 December, 1977.
- [89] Lincoln Wolfenstein. Neutrino oscillations and stellar collapse. *Phys. Rev. D* 20(10):2634, 20 August, 1979.
- [90] S.P. Mikheev and A. Yu. Smirnov. Resonance enhancement of oscillations in matter and solar neutrino spectroscopy. *Sov. J. Nucl. Phys.* 42(6):913, December, 1985.
- [91] S.P. Mikheyev and A. Yu. Smirnov. Resonance amplification of ν oscillations in matter and solar-neutrino spectroscopy. *Il Nuovo Cimento* 9(1):17, February, 1986. December, 1985.

- [92] S.P. Mikheev and A. Yu. Smirnov. Neutrino oscillations in a variable-density medium and ν -bursts due to the gravitational collapse of stars. *Sov. Phys. JETP* 64(1):4, July, 1986.
- [93] J.F. Cavaignac et. al. Indication for neutrino oscillations from a high statistics experiment at the Bugey reactor. *Phys. Lett. B* 148(45):387, 29 November, 1984.
- [94] A.I. Afonin et. al. Search for neutrino oscillations in an experiment in the reactor of the Rovno nuclear power plant. *Jetp Lett.* 45(5):285, 10 September, 1986.
- [95] G. Zacek et. al. Neutrino-oscillation experiments at the Gösigen nuclear power reactor. *Phys. Rev. D* 34(9):2621, 1 November, 1986.
- [96] R.I. Steinberg. Chooz & Perry: New experiments for long baseline reactor neutrino oscillations. Paper presented at the 5th International Workshop on neutrino telescopes, Venice, March, 1993. DUHEP-9306001.
- [97] Robert H. Bernstein and Stephen J. Parke. Terrestrial long-baseline neutrino-oscillation experiments. *Phys. Rev. D* 44(7):2069, 1 October, 1991.
- [98] Stephen J. Parke. Overview of accelerator long baseline neutrino oscillation experiments. Invited talk at the "Moriond Workshop on Neutrino Physics," January 30 to February 6, 1993 at Villars, Switzerland. Fermilab-Conf-93/056-T. 14 April, 1993.
- [99] Scott Hayward et. al. Investigation of long baseline neutrino oscillations from experiments at KAON. Bulletin board preprint hep-ph 9306282, June, 1993.
- [100] G. Fiorentini and B. Ricci. Old and new interactions in long baseline neutrino experiments. INFN Preprint FE-05-93. K. Nishikawa et. al. Technical feasibility study of the neutrino beam at KEK. KEK Preprint 93-55. I. Chiang et. al. Proposal for a long baseline neutrino oscillation experiment at the AGS. AGS Experiment 889 report, 30 August, 1993. Jean-Pierre Revol. ICARUS: Imaging cosmic and rare underground signals. CERN Preprint CERN-PPE/93-01.
- [101] Scott Hayward. Very long baseline neutrino oscillation experiments. In A. Astbury et. al., editors, *Particle Physics and Cosmology*, World Scientific, 1994.
- [102] Stephen J. Parke. Private communication.
- [103] B. Achkar et. al. Search for neutrino oscillations at 15, 40, and 95 meters from a nuclear power reactor at Bugey. *Nucl. Phys. B* 434:503, 1 October, 1991.
- [104] G.S. Vidyakin et. al. Limitations of the characteristics of neutrino oscillations. *JETP Lett.* 59(6):391, 25 March, 1994.

- [105] C. Athanassopoulos et. al. Candidate events in a search for $\bar{\nu}_\mu \rightarrow \bar{\nu}_e$ oscillations. *Phys. Rev. Lett.* 75(14):2650, 2 October, 1995.
- [106] L. Borodovsky et. al. Search for muon neutrino oscillations $\nu_\mu \rightarrow \nu_e$ ($\bar{\nu}_\mu \rightarrow \bar{\nu}_e$) in a wide band neutrino beam. *Phys. Rev. Lett.* 68(3):274, 20 January, 1992.
- [107] K.S. McFarland et. al. Limits on $\nu_\mu(\bar{\nu}_\mu) \rightarrow \nu_\tau(\bar{\nu}_\tau)$ and $\nu_\mu(\bar{\nu}_\mu) \rightarrow \nu_e(\bar{\nu}_e)$ oscillations from a precision measurement of neutrino-nucleon neutral current interactions. *Phys. Rev. Lett.* 75(22):3993, 27 November, 1995.
- [108] F. Dydak et. al. A search for ν_μ oscillations in the Δm^2 range $0.3 - 90 \text{ eV}^2$. *Phys. Lett.* B134(3,4):281, 12 January, 1984.
- [109] N. Ushida et. al. Limits to $\nu_\mu, \nu_e \rightarrow \nu_\tau$ oscillations and $\nu_\mu, \nu_e \rightarrow \tau^-$ direct coupling. *Phys. Rev. Lett.* 57(23):2897, 8 December, 1986.
- [110] Marco Laveder. The NOMAD Experiment: Status Report. Bulletin Board Preprint hep-ph/9601342.
- [111] Giovanni Rosa. CHORUS: A Status Report. *Nucl. Phys. B Proc. Suppl.* 40:85, 1995.
- [112] B. Zeitnitz. KARMEN: Neutrino Physics at ISIS. In Amand Faessler, editor, *Neutrinos in cosmology, Astro, Particle, and Nuclear Physics*. Progress in Particle and Nuclear Physics, 32:351, September, 1993. Guido Drexlin. KARMEN: Precision Tests of the Standard Model with Neutrinos from Muon and Pion Decay. In Amand Faessler, editor, *Neutrinos in cosmology, Astro, Particle, and Nuclear Physics*. Progress in Particle and Nuclear Physics, 32:375, September, 1993.
- [113] C. Athanassopoulos et. al. Evidence for neutrino oscillations from muon decay at rest. Bulletin Board Preprint nucl-ex/9605001.
- [114] C. Athanassopoulos et. al. Evidence for $\bar{\nu}_\mu \rightarrow \bar{\nu}_e$ from the LSND experiment at LAMPF. Bulletin Board Preprint nucl-ex/9605003.
- [115] J.J. Gomez-Cadenas and M.C. Gonzalez-Garcia. Future ν_τ oscillation experiments and present data. Bulletin Board Preprint hep-ph/9504246.
- [116] R.R. Lewis. Coherent Detection for Low-Energy Neutrinos. *Phys. Rev.* D21(3):663, 1 February, 1980.
- [117] Paul Langacker, Jacques P. Leveille and Jon Sherman. On the Detection of Cosmological Neutrinos by Coherent Scattering. *Phys. Rev.* D27(6):1228, 15 March, 1983.

- [118] H.A. Bethe. Possible Explanation of the Solar-Neutrino Puzzle. *Phys. Rev. Lett.* 56(12):1305, 24 March, 1986.
- [119] Stephen J. Parke. Nonadiabatic Level Crossing in Resonant Neutrino Oscillations. *Phys. Rev. Lett.* 57(10):1275, 8 September, 1986.
- [120] Von L. Landau. Zur Theorie der Energieübertragung. II. *Phys. Z. USSR* 2(1):46, 1 February, 1932.
- [121] Clarence Zener. Non-Adiabatic Crossing of Energy Levels. *Proc. Roy. Soc. of London* A137(A833):696, 1 September, 1932.
- [122] I.S. Gradshteyn and I.M. Ryzhik. *Table of Integrals, Series, and Products*, Academic Press, Inc., 1980.
- [123] S.P. Mikheyev and A.Yu. Smirnov. Resonant Neutrino Oscillations in Matter. *Prog. Part. Nucl. Phys.* 23:41, Pergamon Press, 1989.
- [124] P.I. Krastev and S.T. Petcov. On the Vacuum Oscillation Solution to the Solar Neutrino Problem. Bulletin Board Preprint hep-ph/9510367. Zurab G. Berezhiani and Anna Rossi. Vacuum oscillation solution to the solar neutrino problem in standard and non-standard pictures. Bulletin Board preprint hep-ph/9409464. Naoya Hata. Vacuum Oscillations and Future Solar Neutrino Experiments. Bulletin Board preprint hep-ph/9402311. E. Calabresu et. al. Just so? Vacuum oscillations and MSW: an update. *Astroparticle Phys.* 4:159, 1995.
- [125] V. Barger et. al. Matter effects on three-neutrino oscillations. *Phys. Rev.* D22(11):2718, 1980.
- [126] T.K. Kuo and James Pantaleone. Solar-Neutrino Problem and Three-Neutrino Oscillations. *Phys. Rev. Lett* 57(14):1805, 1986.
- [127] S.T. Petcov and S. Toshev. Three-neutrino oscillations in matter: analytical results in the adiabatic approximation. *Phys. Lett.* B187(1,2):120, 1987.
- [128] J. Pantaleone. Constraints on three-neutrino mixing from atmospheric and reactor data. *Phys. Rev.* D49(5):R2152, 1994.
- [129] James Pantaleone. ν_e appearance for " $\nu_\mu - \nu_\tau$ oscillations in matter. *Phys. Lett.* B292(1,2):201, 1992.
- [130] G.L. Fogli, E. Lisi and A. Marrone. Upward-going muons and neutrino oscillations. Bulletin Board Preprint hep-ph/9708213.

- [131] Haim Harari and Miriam Leurer. Recommending a standard choice of Cabibbo angles and KM phases for any number of generations. *Phys. Lett.* B181(1,2):123, 1986.
- [132] H.W. Zaglauer and K.H. Schwarzer. The mixing angles in matter for three generations of neutrinos and the MSW mechanism. *Z. Phys.* C40:273, 1988.
- [133] S. Toshev. Resonant amplification of three-neutrino oscillations in matter. *Phys. Lett.* B185(1,2):177, 1987.
- [134] A. Acker, A.B. Balantekin and F. Loreti. Three-flavor vacuum oscillations of atmospheric and solar neutrinos. *Phys. Rev.* D49(1):328, 1994.
- [135] C. Giunti, C.W. Kim and J.D. Kim. Atmospheric Neutrino Problem in Maximally-Mixed Three Generations of Neutrinos. Bulletin Board preprint hep-ph/9411219.
- [136] C.W. Kim and J.A. Lee. Maximally-Mixed Three Generations of Neutrinos and the Solar and Atmospheric Neutrino Problems. Bulletin Board Preprint hep-ph/9311317.
- [137] A.S. Joshipura and M.V.N. Murthy. Analytic conditions for three-neutrino resonant oscillations in matter. *Phys. Rev.* D37(6):1374.
- [138] S.T. Petcov. An analytic description of three-neutrino oscillations in matter with varying density. *Phys. Lett.* B214(2):259.
- [139] X. Shi and David Schramm. An update on the solar neutrino problem and the three-family MSW effect allowing for astrophysical uncertainties. *Phys. Lett.* B283(3,4):305, 1992.
- [140] S.M. Bilenky, C. Giunti and W. Grimus. Atmospheric neutrino oscillations among three neutrino flavors and long-baseline experiments. Bulletin Board Preprint hep-ph/9505301.
- [141] Mohan Narayan et. al. Solar and atmospheric neutrino oscillations with three flavours. *Phys. Rev.* D53(5):2809, 1996.
- [142] Mohan Narayan et. al. Atmospheric neutrinos with three flavor mixing. Bulletin Board Preprint hep-ph/9607279.
- [143] Jiro Arafune, Masafumi Koike, and Joe Sato. CP Violation and Matter Effect in Longe Baleline Neutrino Oscillation Experiments. Bulletin Board Preprint hep-ph/9703351.

- [144] G.L. Fogli, E. Lisi and D. Montanino. Comprehensive analysis of solar, atmospheric, accelerator, and reactor neutrino experiments in a hierarchical three-generation scheme. *Phys. Rev. D* 49(7):3626, 1994.
- [145] G.L. Fogli, E. Lisi and D. Montanino. Matter-enhanced Three-flavor Oscillations and the Solar Neutrino Problem. Bulletin Board Preprint hep-ph/9605273.
- [146] G.L. Fogli and E. Lisi. Tests of three-flavor mixing in long-baseline neutrino oscillation experiments. Bulletin Board Preprint hep-ph/9604415.
- [147] G.L. Fogli et. al. Three-flavor atmospheric neutrino anomaly. Bulletin Board Preprint hep-ph/9607251.
- [148] T.K. Kuo and James Pantaleone. Neutrino oscillations in matter. *Rev. Mod. Phys.* 61(4):937, October, 1989.
- [149] T.K. Kuo and James Pantaleone. Three neutrino oscillations and the solar-neutrino experiments. *Phys. Rev. D* 35(11):3432, 1987.
- [150] David Harley, T.K. Kuo and James Pantaleone. Solar neutrinos with three-flavor mixings. *Phys. Rev. D* 47(9):4059, 1993.
- [151] William H. Press et. al. *Numerical Recipes in C*, Cambridge University Press, 1991.
- [152] Jiro Arafune and Joe Sato. CP and T violation tests in neutrino oscillation. *Phys. Rev. D* 55(3):1653, 1997.
- [153] Hisakazu Minakata and Hiroshi Nunokawa. How to Measure CP Violation in Neutrino Oscillation Experiments? Bulletin Board Preprint hep-ph/9606281.
- [154] Hisakazu Minakata and Hiroshi Nunokawa. CP Violation vs. Matter Effect in Long-Baseline Neutrino Oscillation Experiments. Bulletin Board Preprint hep-ph/9905208.
- [155] Morimitsu Tanimoto. Is CP violation observable in long baseline neutrino oscillation experiments? *Phys. Rev. D* 55(1):322, 1997.
- [156] T.K. Gaisser and J.S. O'Connell. Interactions of atmospheric neutrinos in nuclei at low energy. *Phys. Rev. D* 34:822, 1 August, 1986.
- [157] Q.Y. Liu and S.T. Petcov. Three-Neutrino Mixing and Combined Vacuum Oscillations and MSW Transitions of Solar Neutrinos. Bulletin Board Preprint hep-ph/9702400.